



HR EXCELLENCE IN RESEARCH

**Jerzy Haber**

**INSTITUTE OF CATALYSIS AND SURFACE CHEMISTRY**

**POLISH ACADEMY OF SCIENCES**

Agnieszka Winiarska

**Tungsten aldehyde oxidoreductase from  
*Aromatoleum aromaticum* – biocatalyst for  
alcohol production**

PhD Thesis

Prof. dr hab. Maciej Szaleniec

Jerzy Haber Institute of Catalysis and Surface Chemistry, Polish Academy of  
Sciences

Dr hab. Anna Bodzoń-Kułakowska, prof. AGH

Faculty of Materials Science and Ceramics, AGH University of Science and  
Technology in Krakow

**KRAKÓW 2023**

## Acknowledgements

Foremost, I would like to thank my PhD supervisor Prof. Maciej Szaleniec for support of my research and immense knowledge. I am very grateful to my second PhD supervisor Prof. Anna Bodzoń-Kułakowska for many fruitful suggestions.

I would like to thank Prof. Johann Heider for his guidance and introduction to the research topic.

I would like to acknowledge the group of Prof. Heider at University of Marburg, Germany for knowledge exchange and hosting my research stays, especially Dr Fabian Arndt, Dr Iryna Saliı and Dominik Hege.

I would like to thank Dr Jan M. Schuller for his guidance and introduction into the structural studies.

I would like to acknowledge the group of Dr Jan M. Schuller for hosting my research stays and thank Anuj Kumar and Fidel Ramírez-Amador for fruitful collaboration and great help in processing of cryoEM data.

I also thank all my former and current colleagues from Biocatalysis Group at Institute of Catalysis and Surface Chemistry in Kraków for fruitful discussions and scientific collaboration, especially Katarzyna Harażna and Dr Anna Kluza.

I thank Dr Joanna Kryściak-Czerwenka for conducting GC-MS measurements.

I thank Prof. Graham George and Dr Julien Cotelesage for conducting and interpreting EXAFS measurements.

I thank Dr Przemysław Mielczarek for conducting proteomic analysis.

I am deeply grateful to my Husband and Family for their everyday support.

## Funding

This PhD thesis has been completed in the framework of the Program POWER, project No. POWR.03.02.00-00-I004/16, co-financed by the European Union.

The work was partially supported by National Science Centre, Poland grant PRELUDIUM 2017/27/N/ST4/02676.

I acknowledge Poland's high-performance computing infrastructure PLGrid (HPC Centers: ACK Cyfronet AGH) for providing computer facilities and support within computational grants no. PLG/2019/012677, PLG/2020/013784, PLG/2021/014761, PLG/2022/015584.





## Contents

Abstract of PhD thesis of MSc Eng Agnieszka Winiarska .....	11
Streszczenie pracy doktorskiej mgr inż. Agnieszki Winiarskiej .....	13
List of used abbreviations.....	15
<b>LITERATURE REVIEW .....</b>	<b>17</b>
1. Biocatalysis as a modern solution for reductive transformations.....	17
2. Aldehydes as valuable chemicals.....	19
3. Carboxylic acid reduction. ....	22
3.1. Biocatalysts for carboxylic acid reduction.....	22
3.1.1. Carboxylic acid reductases. ....	23
4. Tungstoenzymes.....	25
4.1. Tungsten abundance and chemistry. ....	25
4.2. Tungsten cofactor and enzyme families.....	26
4.3. Aldehyde oxidoreductase family. ....	30
4.4. Imperfections of tungsten cofactor structures.....	35
4.5. Characterization of aldehyde oxidoreductase from <i>Pyrococcus furiosus</i> .....	36
4.6. Theoretical studies of AOR mechanism. ....	37
4.7. Aldehyde oxidoreductase from <i>Aromatoleum aromaticum</i> . ....	39
5. NADH regeneration.....	41
6. Hydrogenases.....	43
6.1. Electron bifurcation. ....	46
7. Cryogenic electron microscopy .....	47
Aims of the work.....	53
<b>MATERIALS AND METHODS .....</b>	<b>54</b>
1. Methods of production of enzymes.....	55
1.1. AOR expression in <i>A. aromaticum</i> SR7 $\Delta$ pdh.....	55
1.1.1. Fermentation of <i>A. aromaticum</i> SR7 $\Delta$ pdh. ....	55
1.1.2. Multi-step purification of native AOR from <i>A. aromaticum</i> SR7 $\Delta$ pdh by FPLC chromatography. ....	57

1.2.	Heterologous expression of AOR in <i>A. Evansii</i> .....	58
1.2.1.	AOR-coding plasmid construction .....	58
1.2.2.	Fermentation of <i>A. Evansii</i> . .....	59
1.3.	Heterologous expression of BaDH in <i>E. coli</i> .....	60
1.4.	Purification of recombinant AOR by affinity chromatography. ....	60
2.	Enzyme characterisation.....	61
2.1.	Determination of protein concentration with the Bradford method.....	61
2.2.	SDS polyacrylamide gel electrophoresis.....	61
2.3.	Proteomic analysis .....	62
2.4.	Thermostability assay.....	63
3.	Catalytic tests .....	63
3.1.	Preparation of chemicals .....	63
3.2.	Chromatographic analysis of aldehydes and alcohols .....	64
3.2.1.	Reversed-phase chromatography and DAD detectors .....	64
3.2.2.	Method for benzaldehyde quantitative analysis.....	65
3.2.3.	Method for benzyl alcohol and benzaldehyde quantitative analysis.....	66
3.2.4.	Method for ( <i>R</i> )-1-phenylethanol quantitative analysis.....	69
3.3.	UHPLC-MS/MS analysis of aldehydes.....	70
3.3.1.	Detection in a triple-quadrupole mass spectrometer .....	70
3.3.2.	Qualitative analysis of aldehydes.....	71
3.3.3.	Quantitative analysis of aldehydes by multiple reaction monitoring .....	73
3.4.	Gas chromatography with mass spectrometer detector (GC-MS) analysis of aldehyde products.....	76
3.4.1.	Sample preparation by solid-phase extraction.....	76
3.4.2.	Gas chromatography method for aldehyde products separation .....	77
3.5.	Spectrophotometric activity assays.....	81
3.5.1.	Assay for AOR activity in aldehyde oxidation .....	86
3.5.2.	Assay for AOR activity in NAD <sup>+</sup> and BV <sup>2+</sup> reduction .....	87
3.5.3.	Coupled enzymatic assay for AOR activity in carboxylic acid reduction .....	88

3.6.	Reactor tests for characterisation of AOR activity. ....	91
3.6.1.	Substrate spectra in acid reduction. ....	91
3.6.2.	Determination of electron donors. ....	92
3.6.3.	Steady-state activities of AOR <sub>Aa</sub> in NAD <sup>+</sup> /benzoate reduction.....	92
3.6.4.	Cascade.....	93
3.6.5.	NADH regeneration.....	94
3.6.6.	Carbon monoxide inhibition test .....	94
4.	Single-Particle Cryo-Electron Microscopy of AOR. ....	94
4.1.	Specimen preparation.....	95
4.2.	Data collection and processing. ....	97
4.3.	Bioinformatic and visualization tools. ....	98
4.4.	Mass Photometry.....	99
5.	Theoretical methods.....	101
5.1.	Quantum mechanics (QM) in modelling of enzyme active site cofactor.....	103
5.2.	Parametrization of W cofactor for AMBER and geometry minimization. ....	106
5.3.	QM:MM modelling.....	107
5.4.	Refinement with W-co model. ....	110
6.	EXAFS .....	110
	RESULTS AND DISCUSSION .....	112
	Part I. Enzyme preparation.....	112
1.	Protein production. ....	112
1.1.	Fermentation of <i>A.evansii</i> in a bioreactor.....	112
1.2.	Protein purification.....	114
2.	Proteomic analysis of purified AOR preparations. ....	116
3.	AOR <sub>Aa</sub> stability.....	120
	DISCUSSION OF PART I.....	121
	PART II. Catalytic characterisation .....	123
4.	Characterisation of AOR activity in aldehyde oxidation.....	123
4.1.	Substrate spectrum in aldehyde oxidation .....	123

4.2. Kinetic parameters of aldehyde oxidation .....	124
5. Characterisation of AOR activity in NAD <sup>+</sup> reduction with hydrogen as an electron donor .....	128
6. Characterisation of AOR activity in carboxylic acid reduction. ....	132
6.1. Electron donors in acid reduction .....	133
6.2. Kinetics of hydrogen-dependent acid reduction .....	133
6.3. Investigation of electron bifurcation hypothesis.....	138
6.4. Isotope enrichment tests .....	140
6.5. Substrate spectrum in acid reduction.....	142
6.6. Characterisation of acid reduction with the coupled assay method. ....	143
6.7. Biocatalytic tests.....	146
6.7.1. AOR and BaDH reactor for benzyl alcohol production.....	146
6.7.2. NADH regeneration system for R-HPED- catalyzed acetophenone reduction. 150	
6.7.3. Carbon monoxide inhibition test.....	151
DISCUSSION OF PART II .....	151
PART III. Structural studies .....	153
7. Structural characterization of AOR.....	153
7.1. Protein homogeneity.....	153
7.2. Reconstruction of AOR <sub>Aa</sub> structure .....	155
7.3. Quaternary structure of the AOR <sub>Aa</sub> complex .....	158
7.4. Electron transfer subunit AorA.....	161
7.5. Structural details of AorC subunit .....	163
7.6. The catalytic subunit.....	166
7.7. Electron transfer chain in AOR <sub>Aa</sub> complex. ....	169
DISCUSSION OF PART III .....	171
PART IV. Studies of W-co.....	173
8. Geometry of W-co.....	173
8.1. QM-only study of W-co .....	174
8.2. QM:MM models of W-co.....	180



8.3. Fit of optimized W-co models to electron density of AORs.....	182
9. EXAFS of AOR <sub>Aa</sub> .....	184
DISCUSSION OF PART IV .....	186
SUMMARY OF THE RESULTS.....	190
References.....	193



### Abstract of PhD thesis of MSc Eng Agnieszka Winiarska

Tungsten-dependent aldehyde oxidoreductases (AOR) are metalloenzymes that catalyze oxidation of wide range of aldehydes. AORs are also the only enzymes that can catalyze the direct reduction of non-activated carboxylic acids to corresponding aldehydes, a low-redox reaction utilized in bacterial whole-cell systems for bioreductions to produce alcohols. AORs are mostly abundant in anaerobic, thermophilic bacteria and archaea and are highly oxygen-sensitive. In this work, a relatively oxygen-resistant AOR from the mesophilic bacterium *Aromatoleum aromaticum* (AOR<sub>Aa</sub>) was characterized as a biocatalyst of high application potential for the production of bioalcohols and other aldehyde derivatives. The enzyme contains a tungsten-metallopterin cofactor in its active site within the AorB subunit, which is connected via a chain of Fe<sub>4</sub>S<sub>4</sub> clusters in the AorB and AorA subunits with a FAD cofactor in the AorC subunit of the enzyme complex.

Similarly to previously characterized AORs, AOR<sub>Aa</sub> was shown to reduce carboxylic acids to aldehydes when coupled with strong reducing agents (Ti(III) or Eu(II) complexes). Surprisingly, AOR<sub>Aa</sub> was found to efficiently utilize the electrons from H<sub>2</sub> oxidation for the reduction of carboxylic acids, establishing it as a new type of hydrogenase. AOR<sub>Aa</sub> was shown to reduce aliphatic, aromatic and heterocyclic acids with hydrogen as an electron donor. AOR<sub>Aa</sub> demonstrated hydrogenase activity also in NAD<sup>+</sup> and BV<sup>2+</sup> reduction. This activity was applied as an NADH-recycling system for a cascade reaction with NADH-dependent benzyl alcohol dehydrogenase from *A. aromaticum* (BaDH). In the cascade, AOR<sub>Aa</sub> simultaneously reduced NAD<sup>+</sup> to NADH and benzoic acid to aldehyde, which was further converted to benzyl alcohol by BaDH at the expense of NADH. The only net reductant for bioalcohol production in this cascade was hydrogen. The simultaneous reduction of benzoate and NAD<sup>+</sup> provoked a hypothesis of AOR<sub>Aa</sub> utilizing electron bifurcation for the reduction of carboxylic acids, which was falsified in a series of experiments. Although the highest activity in the reduction of acid was observed at pH 5.0 and for NAD<sup>+</sup> at pH 8.0, both reactions were still catalyzed at pH 7.0.

As a part of the catalytic characterization of AOR<sub>Aa</sub>, apparent steady-state kinetic parameters for selected electron acceptors in aldehyde oxidation and reductions with hydrogen were determined.

Structural characterization of AOR<sub>Aa</sub> was conducted within this work by cryoelectron microscopy and mass photometry. The study showed that AOR<sub>Aa</sub> has an oligomeric structure of Aor(AB)<sub>n</sub>C, with the highest observed n=5. The structural details provided by the reconstructed density map of AOR<sub>Aa</sub> of 3.3 Å resolution revealed the striking

structural homology of AorB with the known structure of AOR from *Pyrococcus furiosus*. The active site cofactor in both proteins consists of tungsten, coordinated by two metalopterins and other unknown ligands, which identification is crucial for solving AOR catalytic mechanism. Since the coordination of tungsten is not possible to be unambiguously solved by X-ray diffraction or even by spectroscopic methods, theoretical methods were applied to find the most probable ligands. The QM cluster and QM:MM models of different possible coordinations were verified by comparison to the crystal structure of AOR from *P. furiosus*. The study revealed the most probable structure of the oxidized tungsten cofactor. Meanwhile, the identification of tungsten ligands in the reduced enzyme was facilitated by W L<sub>III</sub>-edge EXAFS of AOR<sub>Aa</sub>. The insights gained from the analysis of the binding of a benzoate molecule in the active site derived from structural data of AOR<sub>Aa</sub> and the newly determined composition of oxidized and reduced structures allowed for the formulation of a new mechanistic hypothesis of AOR-catalyzed aldehyde oxidation.

### **Streszczenie pracy doktorskiej mgr inż. Agnieszki Winiarskiej**

Zależne od wolframu oksydoreduktazy aldehydu (AOR) to metaloenzymy, które katalizują utlenianie szerokiego spektrum aldehydów. AOR są również jedynymi enzymami, które mogą katalizować bezpośrednią redukcję nieaktywowanych kwasów karboksylowych do odpowiednich aldehydów, reakcję o niskim poziomie redoks wykorzystywaną w bakteryjnych systemach całokomórkowych do bio redukcji w celu wytworzenia alkoholi. AOR występują głównie w beztlenowych, termofilnych bakteriach i archeonach i są bardzo wrażliwe na tlen. W niniejszej pracy scharakteryzowano względnie odporne na tlen AOR z mezofilnej bakterii *Aromatoleum aromaticum* (AOR<sub>Aa</sub>), jako biokatalizator o znaczącym potencjale aplikacyjnym do produkcji bioalkoholi i innych pochodnych aldehydów. Enzym posiada kofaktor wolframowo-metalopterynowy, w swoim centrum aktywnym znajdującym się w podjednostce AorB, który jest połączony przez łańcuch klastrów Fe<sub>4</sub>S<sub>4</sub> w podjednostkach AorB i AorA z kofaktorem FAD w podjednostce AorC enzymu.

Podobnie do wcześniej scharakteryzowanych AOR, wykazano, że AOR<sub>Aa</sub> redukuje kwasy karboksylowe do aldehydów w obecności silnych reduktorów (kompleksów Ti(III) i Eu(II)). Niespodziewanie odkryto, że AOR<sub>Aa</sub> skutecznie wykorzystuje elektrony z utleniania H<sub>2</sub> do redukcji kwasów karboksylowych, co czyni je nowym typem hydrogenazy. Wykazano, że AOR<sub>Aa</sub> redukuje kwasy alifatyczne, aromatyczne i heterocykliczne za pomocą wodoru jako donora elektronów. AOR<sub>Aa</sub> wykazało aktywność hydrogenazy również w redukcji NAD<sup>+</sup> i BV<sup>2+</sup>. Aktywność ta została zastosowana jako system recyklingu NADH dla reakcji kaskadowej z NADH-zależną dehydrogenazą alkoholu benzyłowego z *A. aromaticum* (BaDH). W kaskadzie AOR<sub>Aa</sub> jednocześnie redukowało NAD<sup>+</sup> do NADH i kwas benzoowy do aldehydu, który następnie był przekształcany w alkohol benzyłowy przez BaDH kosztem NADH. Jedynym reduktorem netto do produkcji bioalkoholu w tej kaskadzie był wodór. Jednoczesna redukcja benzoianu i NAD<sup>+</sup> sprowokowała hipotezę, że AOR<sub>Aa</sub> wykorzystuje bifurkację elektronów do redukcji kwasów karboksylowych, którą sfalsyfikowano w serii eksperymentów. Chociaż największą aktywność w redukcji kwasu obserwowano przy pH 5,0, a dla NAD<sup>+</sup> przy pH 8,0, to obie reakcje były nadal katalizowane przy pH 7,0.

W ramach charakterystyki katalitycznej AOR<sub>Aa</sub> wyznaczono pozorne parametry kinetyczne w stanie stacjonarnym dla wybranych akceptorów elektronów w utlenianiu i redukcji aldehydów wodorem.

W ramach tej pracy przeprowadzono charakterystykę strukturalną AOR<sub>Aa</sub> za pomocą mikroskopii krioelektronowej i fotometrii masowej. Badanie wykazało, że AOR<sub>Aa</sub> ma strukturę oligomeryczną Aor(AB)<sub>n</sub>C, z najwyższym zaobserwowanym n wynoszącym pięć. Szczegóły strukturalne dostarczone przez zrekonstruowaną mapę gęstości AOR<sub>Aa</sub> o rozdzielczości 3,3 Å ujawniły znaczną homologię strukturalną AorB ze znaną strukturą AOR z *Pyrococcus furiosus*. Kofaktor znajdujący się w centrum aktywnym w obu białkach składa się z wolframu koordynowanego przez dwie metalopteryny i inne, nieznane ligandy, których identyfikacja jest kluczowa dla rozwiązania mechanizmu katalitycznego AOR. Ponieważ koordynacja wolframu nie jest możliwa do jednoznacznego rozwiązania za pomocą dyfrakcji rentgenowskiej, ani nawet metodami spektroskopowymi, zastosowano metody teoretyczne w celu znalezienia najbardziej prawdopodobnych ligandów. Zoptymalizowane metodami klastrową QM i QM:MM geometrie modeli kofaktora o różnych możliwych koordynacjach wolframu zostały zweryfikowane przez porównanie ze strukturą krystaliczną AOR z *P. furiosus*. Badania ujawniły najbardziej prawdopodobną strukturę utlenionego kofaktora wolframowego. Tymczasem identyfikacja ligandów wolframu w zredukowanym enzymie została umożliwiona przez otrzymane wyniki z EXAFS krawędzi W L<sub>III</sub> dla AOR<sub>Aa</sub>. Spostrzeżenia uzyskane z analizy wiązania cząsteczki benzoesanu w miejscu aktywnym z danych strukturalnych oraz nowo określony skład struktur utlenionych i zredukowanych, pozwoliły na sformułowanie nowej hipotezy mechanistycznej dla katalizowanego przez AOR utleniania aldehydu.

## List of used abbreviations

AOR - aldehyde oxidoreductase

BaDH - benzyl alcohol dehydrogenase

Bis-Tris - 2-bis(2-hydroxyethyl)amino-2-(hydroxymethyl)-1,3-propanediol

BV- benzyl viologen

CV - column volume

DFT - Density Functional Theory

DMSOR - dimethylsulfoxide reductase

EXAFS - Extended X-Ray Absorption Fine Structure (here used in short as for L(III) edge for W)

FAD - flavin adenine dinucleotide

FDH - formate dehydrogenase

FOR - formaldehyde oxidoreductase

FPLC - Fast protein liquid chromatography

GAPOR - glyceraldehyde-3-phosphate oxidoreductase

HEPES - 4-(2-hydroxyethyl)-1-piperazineethanesulfonic acid

HPLC – high pressure liquid chromatography

MD – molecular dynamics

MES - 2-(N-morpholino)ethanesulfonic acid

Mo-co – molybdenum cofactor

MP – mass photometry

MPT - metallopterin (also molybdopterin)

MRM- multiple reaction monitoring

MS – mass spectrometry

NAD - nicotinamide adenine dinucleotide

NADP- nicotinamide adenine dinucleotide phosphate

OD<sub>600</sub> – optical density (i.e. turbidity) measured at 600 nm

QM:MM – quantum mechanics : molecular mechanics

RT – retention time

SDS-PAGE - sodium dodecyl sulfate-polyacrylamide gel electrophoresis

SOX - sulphite oxidase

SPE - solid-phase extraction

Tris - 2-Amino-2-(hydroxymethyl)propane-1,3-diol

UHPLC – ultra high pressure liquid chromatography

v/v – volume to volume

**W-co – tungsten cofactor**

**WOR4 - archaeal aldehyde oxidoreductases of unknown specificity**

**WOR5 - archaeal aldehyde oxidoreductases of various specificities**

**XO - xanthine oxidize**



## LITERATURE REVIEW

### 1. Biocatalysis as a modern solution for reductive transformations

One of the problems faced by modern science is obtaining fuels and substrates for syntheses from renewable sources using methods of low carbon footprint. Biocatalysis offers alternative synthetic pathways that require lower temperature and pressure in water solutions without toxic reactants<sup>1</sup>. In biocatalysis, isolated enzymes or whole living cells (mainly bacteria, yeast or fungi) are used as catalysts in organic transformations. The use of whole cells assures a simpler process than with isolated enzymes (no need for purification). Although, it usually yields a mixture of products from different pathways<sup>2</sup>. Whole-cell biocatalysis (or biotransformation) allows for the conversion of substrates from renewable sources to value-added products, which is part of a circular economy. The renewable feedstocks preferentially utilize wastes, residues (i.e. lignocellulosic biomass, used cooking oil and waste animal fat) or dedicated crops that do not compete with food crops (such as crops grown on marginal land). The prospective substrate for biotransformations of interest for this thesis are lignocellulosic feedstock and a variety of acids obtained from depolymerisation of lignin, e.g. vanillic acid, ferulic acid, syringic acid, p-hydroxybenzoic acid and acetic acid<sup>3</sup>.

Microbial fermentation of renewable feedstocks to short-chain alcohols is already used in an industrial setup. Used in wine and beer making, yeast *Saccharomyces cerevisiae* is well-studied organism that can be engineered to produce other bioalcohols from conventional and lignocellulosic feedstocks. The reported scope of products available by *S. cerevisiae* fermentation contains butanol, succinic acid and isoprenoids<sup>4</sup>.

Similar process was established by Charles Weizmann, who patented a discovery of strictly anaerobic fermentation of glucose or starch by bacteria from class *Clostridia*, e.g., *Clostridium acetobutylicum* that yields acetone, butanol and ethanol<sup>5</sup>.

A process of fermentation of CO<sub>2</sub> and CO from waste-gases or syngas into fuel-grade alcohols has been applied in an industrial setup by LanzaTech company<sup>6</sup>. The technology uses as industrial biocatalysts strains of *Clostridium autoethanogenum*, which can convert CO<sub>2</sub> and CO to acetyl-CoA and later to ethanol via two alternative pathways, one utilizing aldehyde: ferredoxin oxidoreductase (also called aldehyde oxidoreductase, in abbreviation AOR) to reduce acetate to acetaldehyde with reduced ferredoxin as an electron donor. The electrons fuelling the process come from hydrogen oxidation by NADP-dependent electron bifurcating hydrogenase<sup>7</sup>. The alternative products of CO<sub>2</sub> – fixation by *C. autoethanogenum* are acetate, 2,3-butanediol and lactate.

Production of bioalcohols, including long aliphatic and aromatic alcohols, from carboxylic acids or syngas, was reported for a range of other anaerobic microorganisms i.e. *Moorella thermoacetica*, *Clostridium formicoaceticum*, *Pyrococcus furiosus* (genetically modified) and *Sporomusa ovata*<sup>6</sup>.

*P. furiosus* was genetically modified by the addition of genes of bacterial alcohol dehydrogenases: bifunctional AdhE and monofunctional AdhA, which generate ethanol from acetyl-CoA (AdhE only) and acetaldehyde. The two synthetic pathways generated by the gene insertion were based on the glycolytic conversion of glucose to pyruvate, which is further converted to acetyl-CoA and CO<sub>2</sub> by pyruvate ferredoxin oxidoreductase (POR). Then, the heterologously expressed enzymes AdhE and AdhA reduce acetyl-CoA to ethanol via acetaldehyde as an intermediate (shown in **Figure 1**). Alternatively, acetyl-CoA synthetase (ACS) converts acetyl-CoA to acetate with the regeneration of an ATP, and the acid can be reduced to acetaldehyde by AOR<sup>8</sup>. To obtain a variety of alcohols, the respective organic acids were added exogenously. The biocatalytic pathway utilized electron donors generated from metabolizing glucose, pyruvate, or pyruvate plus H<sub>2</sub> for the reduction of the acids to aldehydes by AOR and for further reduction of the aldehydes to alcohols by either AdhA or AdhE<sup>9</sup>.

When grown at 70 °C the engineered archaeon converted propionate, isobutyrate, valerate, isovalerate, caproate and phenylacetate to the corresponding alcohols, although, the transformation occurred slowly with low yields (highest value was 30 mM of isobutanol after 5 days of fermentation). All acid-reducing fermentations yielded significant concentrations of ethanol and acetate as by-products. The process was improved by adding electron donors of low redox potential for the reaction, i.e., the ferredoxin was reduced by an inserted membrane-bound hydrogenase/carbon monoxide dehydrogenase complex (CODH) from the thermophilic carboxydrotroph *Thermococcus onnurineus*. CODH oxidizes CO to CO<sub>2</sub> and this reaction is coupled to hydride and ferredoxin reduction. This strain, when grown with additional CO gas supply, produced 70 mM isobutanol in 3 days of fermentation (70% conversion) with less acetate as by-product<sup>9</sup>. The main drawback of this process is characteristic of the host microbe, i.e., *P. furiosus* is hyperthermophilic and strictly anaerobic. The archaeon grows optimally at around 90-100 °C and the discussed transformations take place also at elevated temperature of 70 °C<sup>10</sup>.

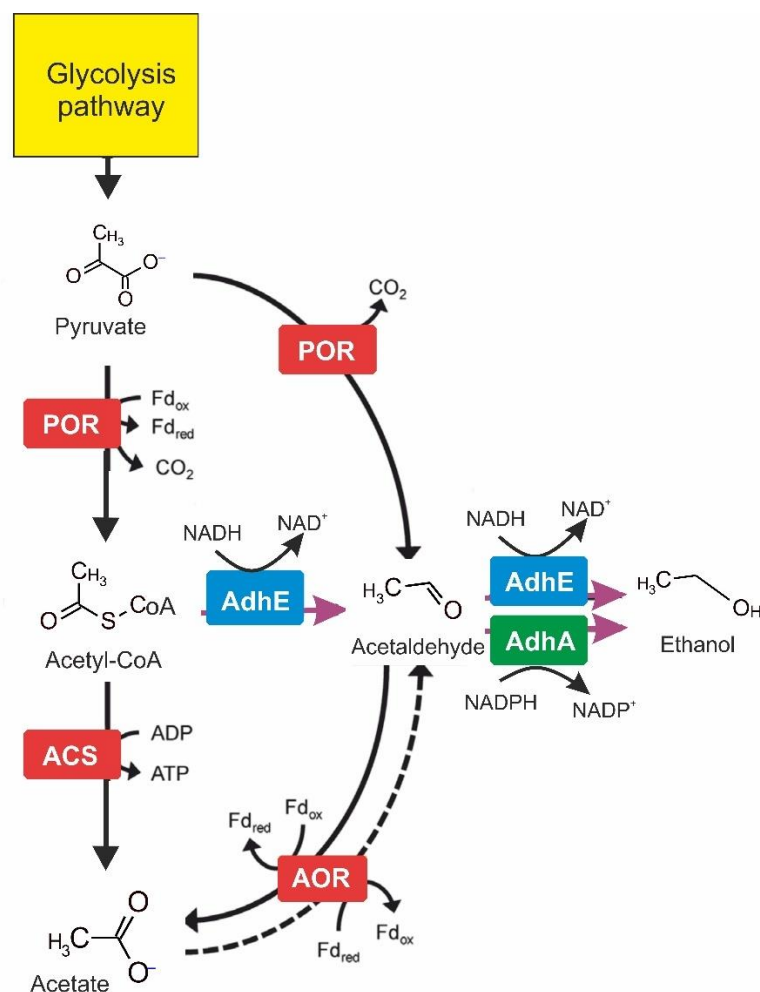


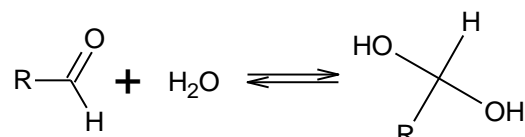
**Figure 1.** Glucose fermentation coupled to alcohol production by engineered strains of *P. furiosus*. The artificial pathway is illustrated by violet arrows; the dashed arrow represents a non-physiological reaction induced by ferredoxin reduced by hydrogenase/carbon monoxide dehydrogenase complex (CODH)<sup>8</sup>.

The direct reduction of carboxylic acid to the corresponding aldehyde presented as a step of the above-described biotransformations is a very uncommon reaction that could have a high application potential for the production of aldehydes from lignin-derived carboxylic acids<sup>6</sup>.

## 2. Aldehydes as valuable chemicals

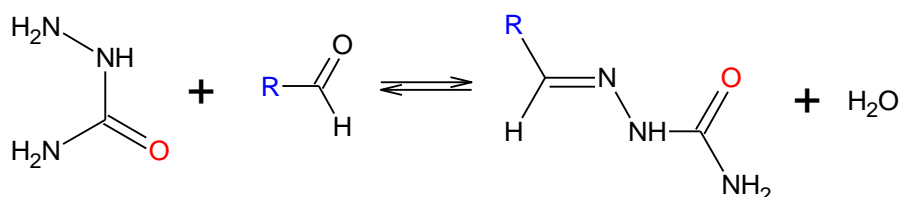
Aldehydes contain a very reactive carbonyl group that can undergo a wide range of reactions, which favours this chemical as an attractive reagent in organic synthesis. The reactivity of the carbonyl group in aldehyde depends on its polarity, which is modified by the hydrocarbon substituent. The groups exhibiting positive inductive effect or mesomeric effect lower carbon atom reactivity toward nucleophilic reactants, but increase the base character of the oxygen atom. For aromatic aldehydes, this effect can

be quantitatively described by the Hammett equation. The carbonyl group is prone to nucleophilic attack, which is the first step of several addition reactions aldehydes undergo. After nucleophilic addition, an intermediate with a negatively charged carbonyl oxygen is formed, which is protonated to form the final product. Nucleophiles that can react with aldehydes are organolithium chemicals, cyanohydrins, hydroxide or alkoxide ions. In aqueous solutions, aldehydes undergo reversible addition of water forming geminal diols according to the following equation<sup>11</sup>:



The equilibrium of this reaction mostly favours the initial state of the aldehyde. However, it depends on the activity of the carbonyl group, with the very active aldehydes being hydrated in a predominant fraction (e.g. formaldehyde, acetaldehyde). Furthermore, the hydration is additionally catalyzed by proton and hydroxyl ions; therefore at acidic or alkaline pH, the equilibrium shifts toward the geminal diol. Finally the hydrated state may be stabilized by the microenvironment present in a protein binding pocket. The geminal diols are unstable and it is impossible to separate most of them from aqueous solutions<sup>12</sup>. This effect is of importance to this thesis as the geminal diol may be a reactive form of the aldehyde oxidized by the AOR enzyme at alkaline conditions.

The nucleophilic addition reaction is the first step in many other reactions of the carbonyl group, including aldol addition or condensation reaction with primary amines to form imines. The latter reaction is used to derivatize the aldehyde prior to detection, for example with semicarbazide to form semicarbazone, which is an example of Schiff base according to **Scheme 1**.<sup>13</sup>.



**Scheme 1.** Reaction of aldehyde group with semicarbazone.

The addition of hydroxide ions (in the presence of hydroxides in alkali water solutions) leads to the disproportionation of aldehydes into corresponding acids and alcohols. However, only aldehydes without hydrogen substituents at the neighbouring carbon to the carbonyl group undergo this reaction efficiently (e.g. benzaldehyde, formaldehyde)<sup>14</sup>.

The high reactivity of the carbonyl group is also a reason for the low stability of aldehydes in bulk or aqueous solutions.

The high reactivity of the carbonyl group is utilized in the polymer industry. Aldehydes are used as a raw material for syntheses and plasticizers in the plastics industry. Formaldehyde is used as a substrate in the production of Bakelite<sup>15</sup> and formaldehyde resins, whereas longer aliphatic aldehydes up to heneicosal can be advantageously used as a modifier preventing gelling and cross-linking of the product in the copolymerization of unsaturated carboxylic acids.

Furthermore, aldehydes are produced by plants and can be obtained as an ingredient of essential oils. Over one hundred aldehydes are admitted as a food flavouring agents in the European Union<sup>16</sup> and the United States of America<sup>17</sup>, with examples such as 4-hydroxybenzaldehyde used for roast taste, benzaldehyde as almond flavour, cinnamaldehyde and vanillin. Their scents and antimicrobial features make them valuable additives in cosmetics and detergents. Benzaldehyde is used as a component of fragrance, antimicrobial and denaturing agents and studies showed it has potential as a drug-action cancerostatic<sup>18</sup>.

Aldehydes are also explored by novel strategies for controlling the growth of infectious bacteria. For example, the growth of multi-drug resistant *Acinetobacter baumannii*, which is a major nosocomial pathogen causing a wide range of clinical conditions, was influenced by the presence of *trans*-cinnamaldehyde in culture medium containing  $\beta$ -lactam antibiotics<sup>19</sup>. Another potential medical application of aldehydes is the use of 4-anisaldehyde in the treatment of dysphagia, a therapy aimed at reducing body weight and reducing blood glucose levels<sup>20</sup>. Aldehydes are applied in pharmaceutical synthesis (drugs and drug precursors), e.g., 4-hydroxyphenylacetaldehyde is intermediate in the production of benzyloquinoline alkaloids (morphine)<sup>21</sup>.

On the other hand, aldehydes naturally present in some food and beverages or contaminating pharmaceuticals can be toxic in higher concentrations. For example, an aldehyde present in balsamic vinegar, fruit juice, biscuits, bread, beer, coffee, and honey, i.e., 5-hydroxymethylfurfural, is cytotoxic, genotoxic, mutagenic, and carcinogenic<sup>22</sup>. High carcinogenicity was also found for short aliphatic aldehydes, present in tobacco fumes, but also in metabolites of alcohol digestion. The short aliphatic aldehydes are thought to be one of the main cancerogens affecting human population<sup>23</sup>.

### 3. Carboxylic acid reduction

Literature provides many methods of obtaining aldehydes directly from derivatives of carboxylic acids, such as acid chlorides, amides or esters. These methods can be divided into chemical and catalytic ones using heterogeneous, homogeneous and enzymatic catalysts, which utilize as reducing agents chemical compounds, hydrogen or electrons (electrochemical methods).

The classic non-catalytic method of carboxylic acids reduction to aldehydes uses metallic lithium or its complexes<sup>12</sup>. For example, the reduction process with lithium wire as a reducing agent of a series of saturated aliphatic acids was carried out in a methylamine solution with an efficiency of 59-84%. The impurity of the reaction was an imine, which was an unhydrolyzed intermediate (constituting about 50% of the products)<sup>24</sup>.

According to the literature, the heterogeneous catalyst used in the reduction of carboxylic acids usually contains palladium. In the most common example of such reduction, the Rosenmund reaction, the catalyst is deactivated to stop over-reduction to alcohols by the addition of barium sulfate<sup>25,26</sup>. In palladium-catalyzed reactions, acids are activated by esterification, or the formation of ethanothioesters or chlorides. In the next step, hydrogen, triethylsilane or organozinc reagents can be used as the reducing agents. Those methods achieve relatively high yields of aldehyde product when applied on a laboratory scale (75-97%)<sup>25,27</sup>.

The alternative routes to aldehyde production utilize the reduction of carboxylic acids (or esters) to alcohols and subsequent oxidation, e.g., by Swern oxidation or with the use of chromium compounds<sup>25,28</sup>. A much less selective method is the ozonolysis of alkenes, where a mixture of aldehydes and ketones is produced<sup>12</sup>. The presented methods all show low selectivity yielding mixtures of aldehydes with the unreacted substrates and side-products (e.g. over-reduced alcohol, unspecific reduction products) contaminated with remains of mostly toxic: solvents, reducing agents and catalysts.

On the other hand, aldehydes can also be obtained from corresponding carboxylic acids in a much more environmentally-friendly manner by biocatalytic methods, i.e., by selective reduction by respective oxidoreductases<sup>29</sup>.

#### 3.1. Biocatalysts for carboxylic acid reduction

The enzymatic reduction of carboxylic acids to corresponding aldehydes can be catalyzed by several enzymes such as L-aminoadipate-semialdehyde dehydrogenase, fatty acyl-coenzyme A reductase, fatty acyl-acyl carrier proteins reductase, aldehyde oxidoreductase and carboxylic acid reductase. However, only two last biocatalysts

exhibit broad substrate spectra which enables their general-purpose industrial application<sup>30</sup>.

The aldehyde oxidoreductases are represented by two distinctive enzyme clades, molybdenum-containing aldehyde oxidoreductases belonging to the xanthine oxidase family and tungsten-containing aldehyde:ferredoxin oxidoreductases. The latter will be discussed in Chapter 4. in more detail. Molybdenum-containing aldehyde oxidoreductases are related to eukaryotic aldehyde oxidases and can oxidize a wide range of aromatic aldehydes to corresponding acids. However, the respective reverse reactions of acid reduction were not observed<sup>31</sup>.

### 3.1.1. Carboxylic acid reductases

The best-studied example of enzymes catalyzing carboxylic acid reduction to aldehydes are carboxylic acid reductases (CAR, E.C. 1.2.1.30). Those oxygen-tolerant enzymes are expressed by plants, fungi and aerobic bacteria<sup>32</sup>. CARs are versatile biocatalysts, reducing a vast range of aliphatic, aromatic (also substituted), polycyclic and heterocyclic acids<sup>30,32</sup>. The reduction is dependent on ATP hydrolysis and irreversible<sup>33</sup>.

The CAR-catalyzed mechanism of reduction consists of three steps. First, the deprotonated carboxylic acid is activated by adenosine 5'-triphosphate (ATP) at the adenylating domain of the enzyme ((1) in **Figure 2.**). Next, the adenosyl phosphate is transferred onto the phosphopantetheine linker where phosphopantetheine thiol binds the substrate as acyl-thioester (2). In this form, the intermediate can dock into the active site of the reductase domain, where the reduction to aldehyde takes place at the cost of oxidation of nicotinamide adenine dinucleotide phosphate (NADPH) (3)<sup>30,33</sup>. To perform reduction, CAR requires one molar equivalent of ATP and NADPH per acid equivalent, whereas the addition of Mg<sup>2+</sup> and dithiothreitol (DTT) increases activity in the assay<sup>30</sup>.

Furthermore, a study of CAR from *Nocardia* sp. NRRL 5646, recombinantly expressed in *Escherichia coli*, showed that CAR is an apoenzyme that requires phosphopantetheinylation for conversion to a fully active holoenzyme. This complicated the expression system in *E.coli*, as the addition of recombinant phosphopantetheine transferase (PPTase) was required. Optimized preparation of purified CAR yielded an enzyme of specific activity in benzoate reduction of 2.1 U mg<sup>-1</sup> protein<sup>34</sup>.

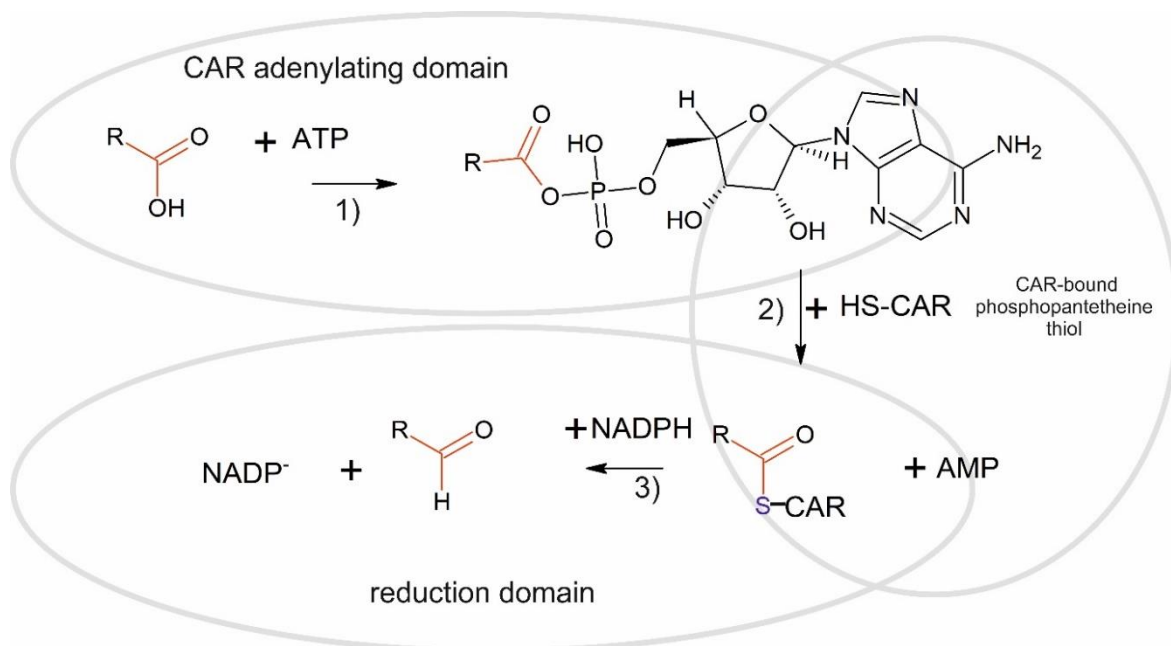


**Figure 2.** Catalytic cycle of CAR in the reduction of carboxylic acids to aldehydes, the scheme of reactions illustrates three domains of CAR, where the specific reaction takes place. Based on Napora-Wijata *et al.*<sup>30</sup>

The preparative aldehyde production by CARs requires the regeneration of two cofactors and special post-transcriptional modifications of protein. Those demands are best met in a whole-cell system. Therefore most tests of CARs activities were conducted in the recombinant expression of the enzyme, i.e. in *E.coli* with co-expressed PPTase<sup>32</sup>. *Nocardia iowensis* NiCAR expressed in *E.coli* is an example that can be used in *de novo* pathway for the preparation of vanillin<sup>35</sup>. *Mycobacterium marinum* MmCAR might be utilized for methyl-branched aliphatic aldehydes production, which are used to introduce savoury flavour in food<sup>36</sup>. When the resting cells of *E.coli* expressing CAR were used, 3.3 g/L of benzoic acid was converted to 0.67 g/L of benzaldehyde and 0.73 g/L of benzyl alcohol in 4 h, and after 24 h to 2.8 g/L of benzyl alcohol with no acid present in the reaction system<sup>37</sup>. This example illustrates the main problem of whole-cell transformation for CAR activity, which is the occurrence of the side reactions, reducing overall yield and the over-reduction of aldehyde to alcohol.

Nevertheless, CARs applied in whole-cell systems can be efficient biocatalysts for aromatic and longer aliphatic alcohols (from aromatic carboxylic acids and medium-chain C5-C10 fatty acids). For 3,4-dihydroxyphenylacetic acid a practical example of a reduction process conducted by engineered *E.coli* expressing heterologous CAR was demonstrated by Horvat *et al.*<sup>8</sup>, yielding 3-hydroxytyrosol (alcohol used as antioxidant cosmetics and food supplements) which was reduced with an endogenous pool of



reducing agents and alcohol reductase. The process was conducted with whole cells from a high cell density culture (optical density - OD<sub>600</sub> 50) and yielded 49.4 mM of the product from 60 mM of the substrate during 21 h of reaction<sup>38</sup>.

## 4. Tungstoenzymes

### 4.1. Tungsten abundance and chemistry

The fact that some enzymes utilize tungsten at their active centre is highly unusual<sup>39</sup>. Tungsten is the heaviest element with a biological function (atomic number 74), and its physiological role and atomic properties are comparable to that of molybdenum (atomic number 42, same group as W). W and Mo are transition metals that share atomic radii and have similar coordination chemistry and a wide range of possible oxidation states (-II to + VI)<sup>40</sup>. Especially the three possible oxidation states, +IV, +V and +VI, are very attractive for biological chemistry, as they lie in the range of redox potential of many physiological reactions<sup>41</sup>. Importantly, the metals can catalyze a two-electron transfer reaction (with the states  $M^{VI+}/M^{IV+}$ ) as well as one-electron oxidation-reduction (utilizing  $M^{V+}$  state) with a simultaneous exchange of a ligand, i.e. oxygen. Tungsten atom forms complexes of a maximum coordination number of 9, with some exceptions up to 13 when bound with  $\sigma$ -bound aromatic ring systems<sup>42</sup>.

The chemical similarities explain the close relation of biological functions of Mo and W; therefore, the latter element should be described in comparison to the former. Both elements are found in small amounts in the natural environment, being only the 53<sup>rd</sup> and 54<sup>th</sup> elements according to their abundance (W and Mo, respectively). Their concentration in Earth's crust is 1.55 mg/kg, but W is primarily present in oxo-rich minerals like scheelite (CaWO<sub>4</sub>) or wolframite ([Fe/Mn]WO<sub>4</sub>), whereas Mo is abundant in soil and seawater<sup>40</sup>. In neutral and acidic pH tungstate salts exhibit poor water solubility. Since tungsten is scarce in freshwater and seawater, its low availability makes any biological function puzzling. The solution to this riddle rests in a few places where the tungsten concentration is significant, i.e., groundwaters coming from weathering of scheelite and wolframite, alkaline thermal waters and lakes in arid zones, and terrestrial hot-spring waters and hydrothermal vents<sup>41</sup>. In those habitats thrive the microbes utilizing tungsten-dependent enzymes (tungstoenzymes). A famous example of such an organism is the hyperthermophilic archaeon *Pyrococcus furiosus*, discovered in geothermally heated marine sediments on the Italian island Vulcano<sup>43</sup>. Apart from such unusual habitats, tungsten-dependent proteins are scarce and present solely in anaerobic bacteria and archaea.

On the other hand, molybdenum is more abundant and is incorporated by a number of enzymes catalyzing oxidation-reduction reactions of key metabolites. Therefore, it is an essential element to a majority of organisms, including humans. An important catabolic enzyme oxidizing toxic sulfite to sulfate is human molybdenum-dependent sulfite oxidase. A rare genetic condition called molybdenum cofactor deficiency, which results in inactive sulfite oxidase, causes severe neonatal neurological problems, which in some cases are fatal<sup>44,45</sup>.

Molybdenum is also present in the nitrogenases, where it forms part of the FeMo cofactor, responsible for catalyzing so-called nitrogen fixation, i.e., the reduction of nitrogen to ammonia, the most important process in the biochemical cycle of nitrogen. Unusually, the Mo is present in FeMoCo at the +III oxidation state and its role in catalysis is unknown<sup>46,47</sup>.

A number of the molybdenum-dependent enzymes can, in the absence of molybdate in media, incorporate available tungsten, resulting in some of those cases in the partially active enzyme. Some of the known tungstoenzymes have their homolog in Mo enzyme families and catalyze the same reaction, e.g., formate dehydrogenases<sup>48</sup>.

Based on those relations of Mo and W an interesting hypothesis was formed and is still discussed by researchers, that the tungstoenzymes are ancestors of molybdoenzymes and dominated the early Earth when sulfidic and anoxic conditions favoured the bioavailability of tungsten. Throughout the ages, the availability of molybdenum increased, while rising atmospheric oxygen levels impeded the growth of tungsten-utilizing organisms (as tungsten enzymes are sensitive to oxygen)<sup>45</sup>.

#### **4.2. Tungsten cofactor and enzyme families**

In tungstoenzymes and most molybdoenzymes, the transition metal forms a mononuclear cofactor with a tricyclic pyranopterin ligand. The structure of this ligand in protein was first reconstructed by X-ray crystallography of tungsten aldehyde ferredoxin oxidoreductase from *Pyrococcus furiosus*<sup>49</sup>.

The ligand chelates the metal by two sulfurs from *cis*-dithiolene group at pyrano ring, which is also substituted with methylphosphate (structure shown in **Figure 3**). The pyranopterin ligand is shortly called MPT and can be modified by the attachment of additional nucleotides (e.g. a guanine dinucleotide moiety to form molybdopterin guanine dinucleotide MGD). The pterin is thought to facilitate intramolecular electron transfer, passing the electrons to other redox cofactors (for tungstoenzymes a proximal iron-sulfur cluster is always present in the structure)<sup>45</sup>. However, the role of MPT in molybdo- and

tungstoenzymes is not yet fully determined and some studies suggest that the structure of the ligand can have a greater role in catalysis than only a scaffold for the metal in the active site and electron “wire”. The dithiolene moiety is usually assumed to be a chelator in the fully reduced tetrahydro form. However, it can be oxidized either by one electron to a radical form or by two electrons to a dihydro form (**Figure 3.E**)<sup>50</sup>. The closed pyrano ring of MPT can be opened in a two-electron oxidized transition state, although the opened form of the cofactor is usually not observed in spectroscopic studies<sup>51</sup>. The fully reduced tetrahydro form of MPT (**Figure 3.D**) can also be oxidized to dihydro-form (at atoms C<sub>4</sub> and N<sub>5</sub>)<sup>45</sup>. The less abundant in spectroscopic studies is a tautomer of dihydro form, a quinonoid form<sup>52</sup>. Nevertheless, the metallopterin is believed not to be redox active during the catalytic cycle, but rather in activation of enzyme<sup>45</sup>.

For molybdenum- and tungsten-containing enzymes the cofactor structure is relevant for the catalytic activity and reflects the phylogenetic relationships between enzymes. Therefore, the structure of the cofactor was set as the criterium for the systematic organization of those enzymes into families: xanthine oxidase (XO) family, sulfite oxidase (SOX) family, dimethylsulfoxide reductase (DMSOR) family and aldehyde oxidoreductase (AOR) family<sup>53</sup>.

Enzymes from the SOX family incorporate molybdenum coordinated by one metallopterin (and other ligands which may differ inside of the family), whereas in the XO family the metallopterin is mostly a cytosine dinucleotide (MCD) <sup>55</sup>.

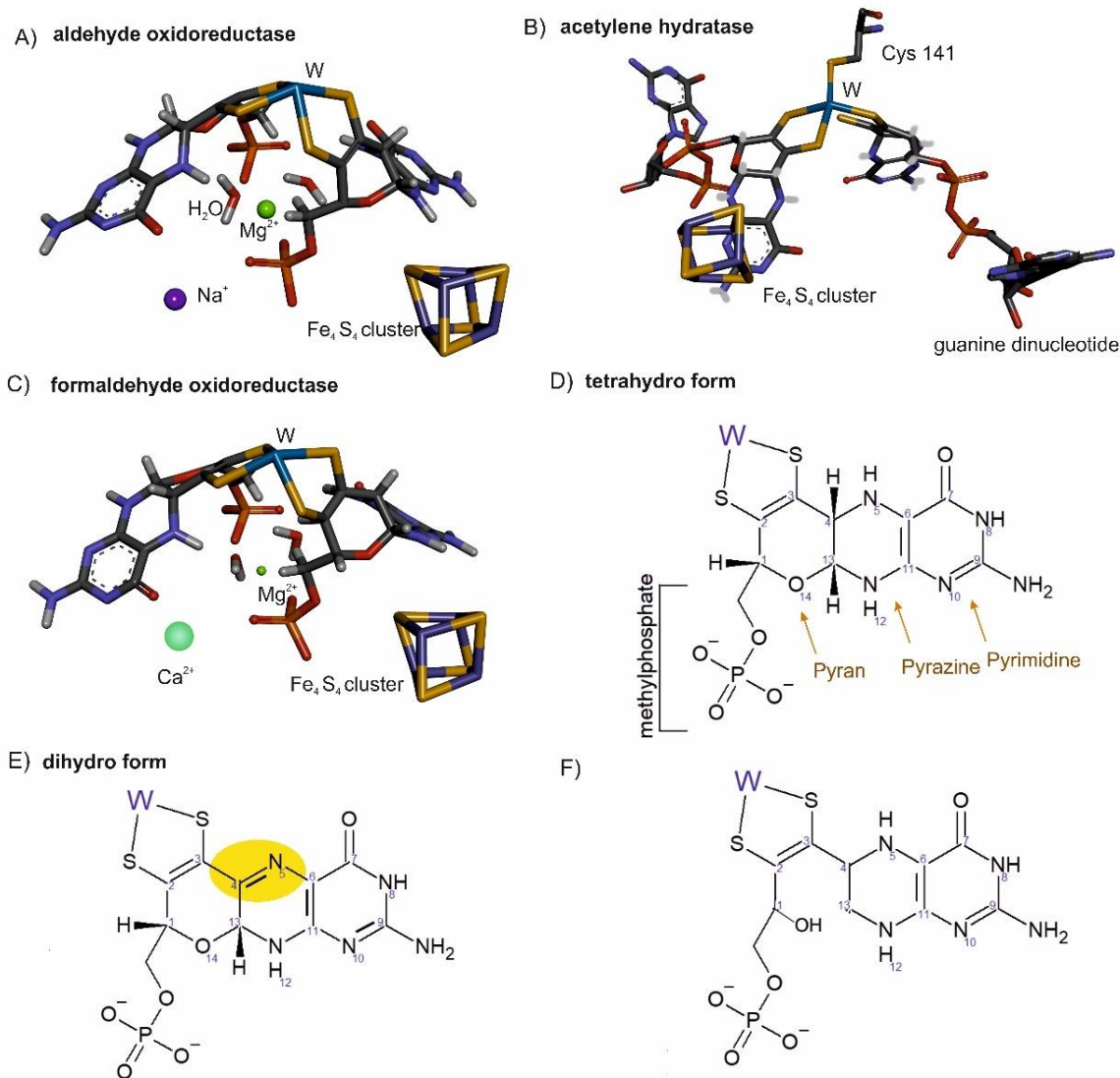


**Figure 3.** Crystal structures of W-co and iron-sulfur cluster ( $\text{Fe}_4\text{S}_4$ ) in the active site of **A)** aldehyde oxidoreductase from *P. furiosus* (Protein Data Bank accession ID 1AOR)<sup>49</sup>; **B)** acetylene hydratase from *Pelobacter acetylenicus* (PDB: 2e7z), tungsten is coordinated by Cys141<sup>54</sup> and bis-molybdopterin guanine dinucleotide; **C)** formaldehyde oxidoreductase from *P. furiosus* (PDB: 1B4N). The W-co has pyramid-like geometry, with a tungsten atom at the top (the structures are missing most ligands above the tungsten atom, for a reason discussed in Chapter 4.1.); Schematic representation of pyranopterin coordinating tungsten **D)** in tetrahydro form; **E)** in dihydro form; **F)** with open pyran ring, a reduced form.

In tungstoenzymes, the metal is always coordinated by two pterin moieties and additional ligands to form a cofactor called shortly W-co. Tungstoenzymes are members of only two families: DMSOR family and AOR family. Enzymes belonging to DMSOR family contain the cofactor where W atom is always coordinated by two metallopterin guanine

dinucleotides (MGD). In enzymes from the AOR family, the cofactor is formed by the metal coordinated by two MPT (*bis*-MPT cofactor) bridged by magnesium. The magnesium ion links both phosphate moieties and also binds the cofactor to the protein<sup>55</sup>. The phylogenetic analysis conducted by Seelmann *et al.*<sup>48</sup> showed that tungsten-containing enzymes constitute a small section of the DMSOR family (as shown in **Figure 4**) with representative examples of acetylene hydratase subfamily and some formate dehydrogenases (FDH). The AOR family constitutes of tungsten-dependent enzymes, except for the Mo-containing YdhV oxidoreductase subfamily of unknown biological function<sup>56</sup>. Many members of the AOR family still have not been isolated and the metal content and biological function of these are unknown<sup>48</sup>.

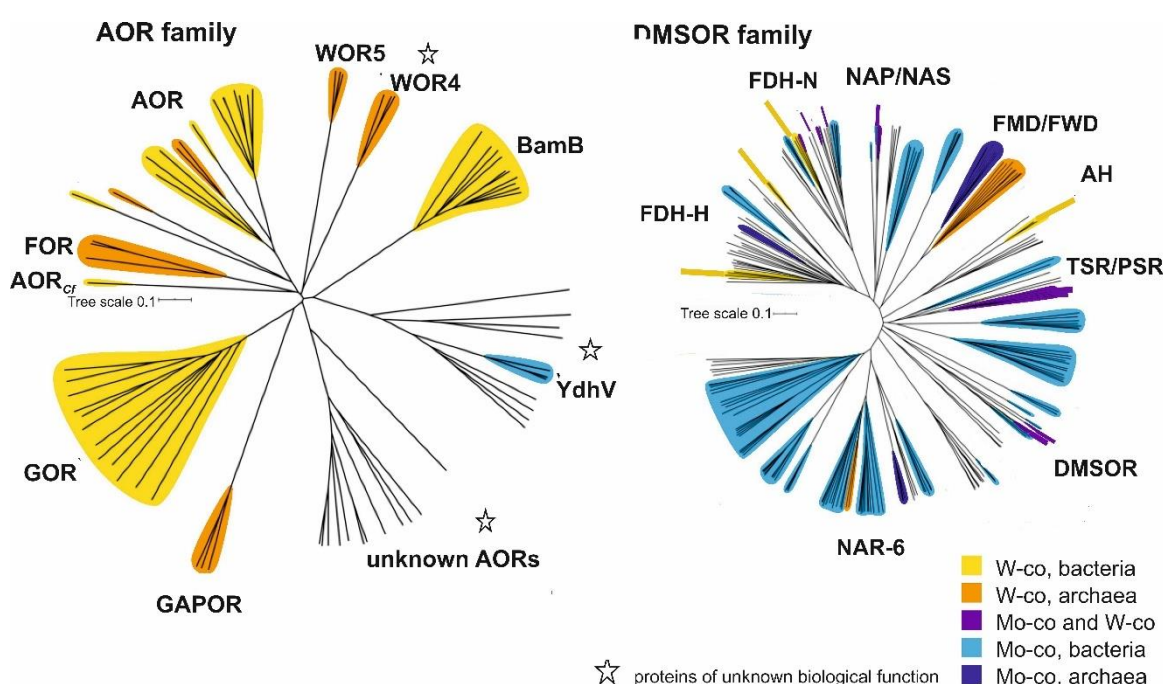


**Figure 4.** Phylogenetic trees of catalytic subunits of enzymes from the AOR family and the DMSOR family. Clades or subclades representing tungsten-containing enzymes are labelled in yellow (found in bacteria) or orange (archaea), whereas enzymes working with either tungsten or molybdenum are highlighted in violet. Molybdenum-containing enzymes are labelled in purple or dark blue (originated from bacterial and archaeal enzymes, respectively).<sup>48</sup>

In W-co, the non-pterin ligands present in the coordinating sphere of metal usually are oxygen atoms (from oxo or hydroxo ligand, water, aspartate or serine) or sulfur atoms (from sulfido ligand, thiolates or thiols) bound directly to tungsten<sup>55</sup>.

If the transition metal in the cofactor is coordinated by six ligands (four thiolate ligands from MPT and two other unknown ligands), the coordination is usually trigonal prismatic

or distorted octahedral. For Mo-DMSOR it was shown that distortion of the geometry of the complex imposed by the protein milieu is tuning its redox potential by destabilising the catalytically active form of the cofactor. Such structural distortion decreases the relative energy of the transition state barrier which results in the catalytic effect<sup>57</sup>.

Most of the tungstoenzymes are involved in low-potential ( $E^{\circ} < -400$  mV) electron transfer reactions with simultaneous transfer of hydrogen, oxygen or sulfur atoms<sup>48</sup>. An exception here is the acetylene hydratase (structurally belonging to the DMSOR family) that catalyzes acetylene hydration and tautomerization to acetaldehyde<sup>58</sup>. The oxidation-reduction reaction is catalyzed by the other members of the DMSOR family: formate dehydrogenase catalyzes the reversible conversion of formate to  $\text{CO}_2$  at  $E^{\circ} = -430$  mV and formylmethanofuran dehydrogenase is responsible for the reversible step of formylmethanofuran conversion to  $\text{CO}_2$  and methanofuran. Further members of the DMSOR family are W-containing isoenzymes of their Mo-dependent versions. For a respiratory nitrate reductase, the substitution of Mo-co with W-co (by depletion of molybdate in medium) yielded a two-fold less active isoenzyme. An exception in a negative impact on activity is the dimethyl sulfoxide reductase where substitution with tungsten yielded more active enzyme in the reduction of DMSO, however, with no activity in the reverse reaction<sup>48</sup>.

The active site of enzymes from the AOR and DMSOR family contains a cubane-type  $\text{Fe}_4\text{S}_4$  iron-sulfur cluster in close vicinity to the W-co (four irons in the structure of the cluster shown in **Figure 4** were colored violet and four sulfurs depicted in yellow). This cluster is bound to protein by four coordinate bonds between iron atoms and sulfur atoms of cysteine (in some rare cases aspartic acid may replace a cysteine ligand). The  $\text{Fe}_4\text{S}_4$  clusters in W- and Mo-dependent oxidoreductases are involved in electron transfer and play a crucial role in the biosynthesis of molybdenum- and tungsten-containing cofactors<sup>59</sup>.

### 4.3. Aldehyde oxidoreductase family

The enzymes of the aldehyde oxidoreductase family are obligatory tungsten-dependent<sup>39</sup>. Based on their biochemical characterisation and phylogenetic analysis, the AOR family was divided into five main clades:

- AOR - *sensu stricto*
- FOR - formaldehyde oxidoreductase
- GAPOR - glyceraldehyde-3-phosphate oxidoreductases
- WOR5 – W-containing oxidoreductase of various specificities
- WOR4 - archaeal aldehyde oxidoreductases of unknown specificity

and the structurally related, but biochemically distinctive BamB, i.e., the catalytic subunit of class II benzoyl-CoA reductase<sup>48</sup>. Most of these clades of AOR (with the exception of WOR4 and BamB) catalyze the oxidation of aldehydes to corresponding carboxylic acids with ferredoxin as an electron acceptor, which in most cases was shown to be a reversible reaction. An exceptional reaction is catalyzed by benzoyl-CoA reductase (BCR): a biological Birch reduction of aromatic rings. The active site subunit of class II BCR (BamB) contains W-co and is an atypical member of the AOR family<sup>60</sup>. The enzymes of the AOR family were shown to be specific to tungsten and not form active molybdenum- or vanadium-containing isoenzymes<sup>61</sup>. Considering the specificity of the tungsten binding, the family is sometimes referred to as tungsten oxidoreductase or WOR family<sup>62</sup>.

Many enzymes of the AOR family are present in archaea (*Thermococcus litoralis*, *Thermococcus paralvinellae*, *Pyrococcus furiosus*), strictly anaerobic bacteria (*Moorella thermoacetica*, *Sporomusa ovata* DSM-2662, *Clostridium formicaceticum*) or facultatively anaerobic bacteria (*Aromatoleum evansii* and *Aromatoleum aromaticum*)<sup>63–66</sup>. The first tungsten-containing enzyme from an obligate aerobe was recently isolated from the bacterium *Brevibacillus massiliensis*<sup>67</sup>.

Examples of each of the five clades of the AOR family can be found in the hyperthermophile *Pyrococcus furiosus*. They were purified and their substrate spectra were characterized, except for WOR4, which did not show any activity with tested aldehydes. The FOR from *P. furiosus* (individual enzymes can be addressed according to the organism of origin, i.e., FOR<sub>Pf</sub>) catalyzes the oxidation of short-chain semi- and dialdehydes (up to C<sub>5</sub>), phenylpropionaldehyde and indole-3-acetaldehyde<sup>66</sup>. The only identified substrate of GAPOR is glyceraldehyde-3-phosphate, which is oxidized by the enzyme to 3-phosphoglycerate<sup>68</sup>. AOR<sub>Pf</sub> and WOR5<sub>Pf</sub> have similar substrate spectra to FOR<sub>Pf</sub>, although they additionally reduce acetic acid<sup>9,69</sup>. WOR5<sub>Pf</sub> was shown to have an additional, unprecedented activity in an oxidative desulfonation of aliphatic sulfonates and subsequent oxidation of the resulting aldehydes<sup>70</sup>.

Only three of the five AORs from *Pyrococcus furiosus* were structurally characterized (AOR<sub>Pf</sub>, FOR<sub>Pf</sub>, WOR5<sub>Pf</sub> structures presented in **Figure 5**). All five enzymes share around 50% amino acid sequence similarity of the catalytic subunit carrying tungsten bis-metallopterin cofactor and one iron-sulfur cluster (Fe<sub>4</sub>S<sub>4</sub>) coordinated by four cysteine residues (except for WOR4<sub>Pf</sub>, which supposedly has a Fe<sub>3</sub>S<sub>4</sub> cluster)<sup>71</sup>. The enzymes can be differentiated by some structural features, including tertiary structure. The homotetrameric FOR<sub>Pf</sub> contains an additional calcium ion of structural role, localized near

the pterin<sup>66</sup>, monomeric GAPOR incorporates two zinc ions per subunit<sup>68</sup>, WOR4<sub>Pf</sub> is a dimer with one calcium ion per subunit<sup>71</sup>. WOR5<sub>Pf</sub> is a heterodimer consisting of one subunit containing a tungsten cofactor and one subunit carrying four Fe<sub>4</sub>S<sub>4</sub> clusters<sup>70</sup>. AOR<sub>Pf</sub> has a dimeric structure with a mononuclear iron site bridging both subunits and a sodium ion placed near pterin<sup>49</sup>. All purified tungsten enzymes from *Pyrococcus furiosus* are oxygen-sensitive but thermostable with high specific activities at temperatures close to the optimal growth temperature of the archaeon (90°C)<sup>66,68,69,71</sup>.

The AOR<sub>Pf</sub> is the best-characterized example of a tungsten enzyme and was first identified in oxygen-deactivated form as a red-coloured, tungsten-iron-sulfur protein (RTP) in 1990<sup>72</sup>. Only after purification in strictly anaerobic conditions the activity of the enzyme was retained<sup>73</sup>.

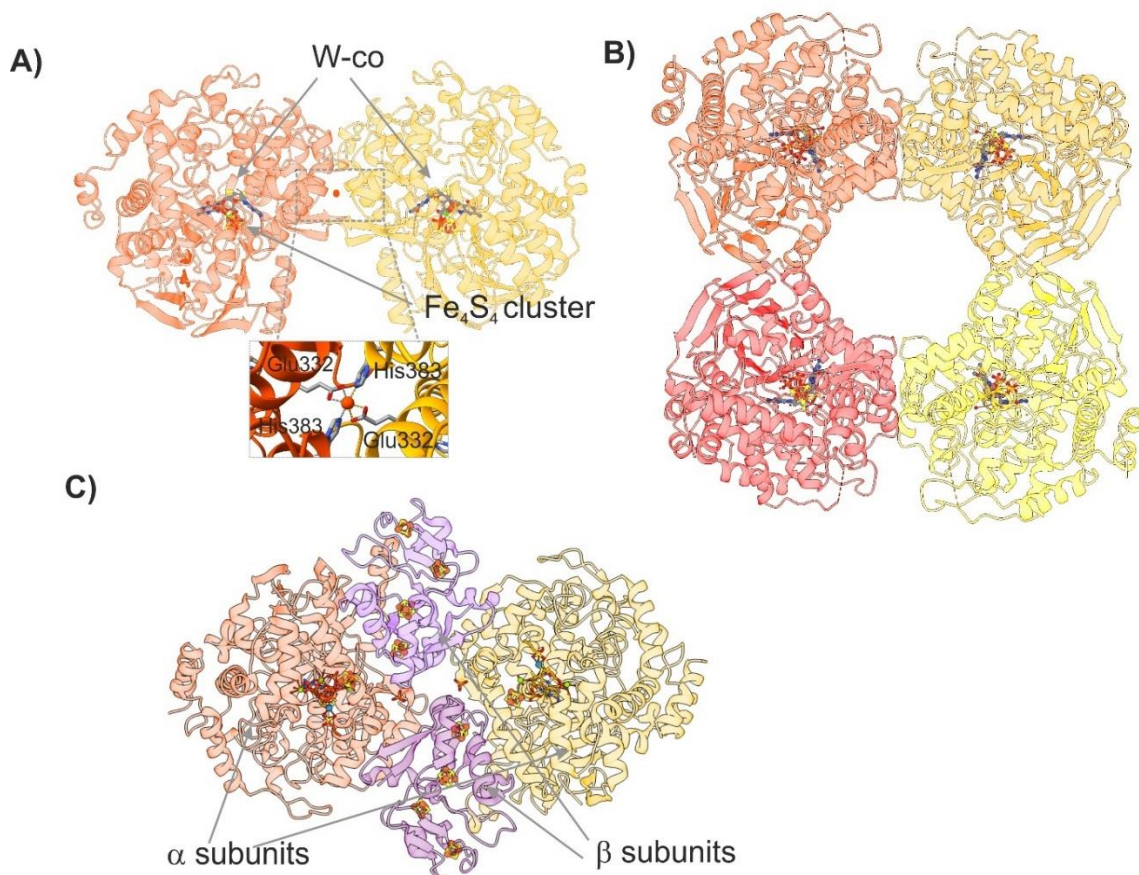


**Figure 5.** Cartoon representation of available crystal structures of enzymes from AOR family (BamB not included). **A)** AOR<sub>Pf</sub> (pdb accession number 1AOR) with W-co and Fe<sub>4</sub>S<sub>4</sub> cofactor atomic structure depicted coloured by a heteroatom, marked with a dashed line is close-up on the single iron binding two subunits; **B)** FOR<sub>Pf</sub> (pdb: 1B25) where each of homotetramers is shown in a different color, the complex do not use the



single iron binding site; **C**) WOR5 (PDB: 6x6u) is a dimer of heterodimers of AorAB- like subunits (previously called  $\alpha$  and  $\beta$  subunits<sup>74</sup>).

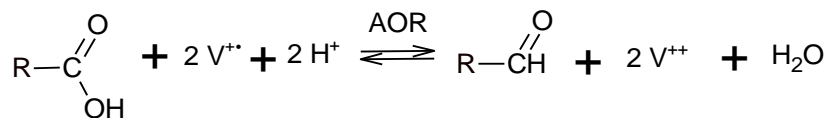
The biochemical characterization of the enzyme showed that cyanide, arsenite, and iodoacetate inhibit the aldehyde oxidoreductase activity of AOR<sub>Pf</sub>. Moreover, substrate inhibition was also noted for concentrations of crotonaldehyde above 200  $\mu$ M. A metal exchange study of tungsten with molybdenum showed that although both could be incorporated in the active site, only the cofactor with tungsten was catalytically active<sup>69</sup>.

The AORs *sensu stricto* are present in many organisms and have been characterized in different complex compositions that impact their substrate and electron mediator spectra. The AOR from archaea, i.e., *Thermococcus parvalvinellae* (AOR<sub>Tp</sub>) and some bacterial AORs, have a similar structure to AOR<sub>Pf</sub> being dimer of 67 kDa subunits and accept viologen dyes and ferredoxin as electron mediators<sup>65</sup>. Heteromeric types of AORs were isolated from bacteria: mesophilic autotrophic acetogen *Clostridium formicaceticum* (AOR<sub>Cf</sub>) and thermophilic acetogen *Moorella thermoacetica* (previously called *Clostridium thermoaceticum*, AOR<sub>Mt</sub>). Most of the mentioned microbes contain more than one operon coding for AOR in their genomes, e.g., for *M. thermoacetica* one AOR containing two types of subunits (AorAB) and one containing three types of subunits (AorABC) were isolated<sup>75,76</sup>. The trimeric complex structures were shown to be dimers of heterotrimers (Aor(ABC)<sub>2</sub>) where the AorB subunit contained the W-Co and Fe<sub>4</sub>S<sub>4</sub> cluster, the AorA subunit carried four more Fe<sub>4</sub>S<sub>4</sub>-clusters, and the AorC subunit a flavine adenine dinucleotide (FAD) cofactor<sup>75,77</sup>. The AorB subunit was shown to be an analogue of the only subunit of homomeric AOR<sub>Pf</sub>. The AorA subunit was thought to be the electron-transfer subunit, while AorC subunit was suggested to facilitate the exchange of electrons with an electron mediator such as NAD(P).

AORs (*sensu stricto*) were shown to be labile in the presence of oxygen. AOR<sub>Pf</sub> and both AORs<sub>Mt</sub> showed a 90% activity loss after 10 min exposure to air<sup>73,78</sup>. The AOR<sub>Cf</sub> was proven to be more stable, although, in a reduced state, it lost 80% of the activity 10 min after exposure to air<sup>76</sup>.

The AOR was first referred to as carboxylic acid reductase containing tungsten, as the enzyme activity was first described in *M. thermoacetica* which resting cells were reducing carboxylic acids to alcohols<sup>78</sup>. The trimeric AOR<sub>Mt</sub> was purified and its activity was tested in both directions. Already then, it was noted that with good stability of the acidic product and higher redox potential of electron mediators, the measurement of aldehyde oxidation activity was far more convenient, and it was used as a routine test for the activity of the enzyme<sup>78</sup>. The carboxylic acid reduction was shown with a spectrum of reduced viologen

dyes and ferredoxin in a reaction where each acid molecule was reduced by the enzyme at the expense of 2 molecules of viologen, as shown in Scheme 2.



**Scheme 2.** Schematic representation of reversible reduction of carboxylic acid coupled to viologen electron donor catalyzed by AOR.

The trimeric AOR<sub>Mt</sub> and AOR<sub>Cf</sub> were active in the reduction of substituted benzoate with reduced 1,1'-carbamoymethyl-viologen<sup>63,76</sup>, whereas AOR<sub>Tp</sub> catalyzed the reduction of acetate with reduced methyl viologen<sup>65</sup>. AOR<sub>Mt</sub> reduced benzoate with a specific activity of 70 U/mg of protein at pH 4.5, less than 10% of its activity in aldehyde oxidation (795 U/mg at pH 9.0)<sup>76</sup>. The activity measurements were conducted with the presence of semicarbazide, which derivatized aldehydes produced in reactions. The presence of reduced aldehyde could impact the acid reduction rates because of low K<sub>m</sub> for aldehydes in the reverse reaction. Derivatization of produced aldehydes aimed at preventing this effect and facilitated detection of a product by liquid chromatography<sup>63</sup>.

Interestingly, several human gut microbes were recently shown to contain W-containing oxidoreductase (WOR) belonging to the AOR family based on phylogenetic analysis and biochemical characterization of selected enzymes<sup>62,67</sup>. The WOR role was suggested to be detoxification of the environment (gut) from aldehydes present in consumed food and secreted by other bacteria. Thus the tungsten-containing enzyme would be important for human health. Two WORs from *Acetomicrobium mobile* (WOR1<sub>Am</sub> and WOR2<sub>Am</sub>) were purified and their substrate spectrum was characterized. WOR1<sub>Am</sub> was shown to convert a wide range of aliphatic and aromatic aldehydes. WOR2<sub>Am</sub> was selective to 4-hydroxybenzaldehyde and some of the aliphatic aldehydes. The detected activity, measured with benzyl viologen as the electron acceptor, was much lower than for WOR1<sub>Am</sub>. WOR2<sub>Am</sub> was characterized to be a dimer consisting of subunits similar to those contained by dimeric AORs<sub>Mt</sub> (AorAB), while WOR1<sub>Am</sub> was isolated as pentamer, containing in addition to AorA- and AorB-like subunits as well as three additional subunits similar to HydABC of a bifurcating FeFe-hydrogenase of *Thermotoga maritima*, however lacking an H-cluster (active site responsible for hydrogen oxidation)<sup>62,79</sup>.

WOR1<sub>Am</sub> was active in aldehyde oxidation only if NAD<sup>+</sup> and ferredoxin were present as electron donors. Authors of the manuscript<sup>62</sup> named this phenomenon 'a bifurcation'. However, the described behaviour of WOR1<sub>Am</sub> did not fulfil the thermodynamic requirements for bifurcation shown by definition (see Chapter 6.1.).

Many of the enzymes from the AOR family have not yet been purified nor further characterized (as presented in **Figure 4**). For example, an electrosynthesising acetogen *Sporomusa ovata* contains genes encoding 6 aldehyde oxidoreductases and fermentation tests showed that the presence of tungstate in media upregulates the expression of two AORs. Moreover, the tungstate addition enhanced fermentative production of ethanol, 1-propanol, and 1-butanol from appropriate acid, indicating the activity of a tungsten-dependent aldehyde oxidoreductase<sup>80</sup>. Nevertheless, those enzymes await further characterization.

#### **4.4. Imperfections of tungsten cofactor structures**

The most important preliminary data for the study of the mechanism relate to the exact structure of the catalytic site, especially the ligands of the tungsten coordination sphere. Resolving the first coordination sphere of the tungsten or molybdenum with the available crystal structures was particularly challenging for a few reasons. The two most important will be discussed here.

A significant aspect to be considered during the assignment of electron density in crystal structures are Fourier termination ripples, which are an unavoidable consequence of a finite range of the collected data. For heavy atoms such as tungsten, these termination ripples can be as intense as if caused by the presence of a light atom and they occur at reasonable distances to imitate a covalently bound atom (ca. 2 Å). Therefore, in most cases, when analyzing the electron density around the tungsten in known W-co structures, the available data are not good enough to unequivocally determine the composition of the cofactor<sup>81</sup>.

Another critical factor lowering the local resolution of the active site in Mo-co- and W-co-containing proteins is the co-crystallization of many different states of cofactor (i.e. oxidized, reduced, inactivated, bound with substrate), which have different geometries and occupations of individual ligands. Achievement of homogenous samples for oxygen-sensitive oxidoreductases is very challenging for simple practical reasons, i.e., exposure to oxygen, inactivation or partial occupancy of metal cofactors. Therefore, the lack of homogeneity results in a blended signal and corrupted bond lengths<sup>81</sup>.

Considering above shortcomings, a common approach for tungstoenzymes mechanistic and structural studies is to use all available methods to identify metal oxidation state, ligands and their geometry. Extended X-Ray Absorption Fine Structure (EXAFS) obtained from X-ray Absorption Spectroscopy and theoretical studies are often applied to aid X-ray crystallography of metalloproteins<sup>82</sup>. Structures of W-co are studied by EXAFS at L<sub>III</sub> edge for tungsten, which is observed in X-ray absorption spectra as an oscillatory

modulation in the region above the absorption edge threshold energy  $E_0$ <sup>81</sup>. Experimental EXAFS is interpreted by comparison with modelled spectra for structures with potential ligands.

In the structure of W-co in FOR<sub>Pf</sub> (1.85 Å resolution), only four sulfurs and one oxygen-containing ligand at a distance of 2.10 Å were identified as ligands of tungsten<sup>83</sup>. In contrast, L<sub>III</sub> EXAFS data from W indicated more atoms binding to tungsten. The four sulfur coordination was identified at an average of 2.41 Å (W-S bond), almost identical to in crystal structure, but EXAFS data revealed additional oxygen ligands. Two populations of oxygen-containing ligands were identified, one W=O (double bond) and W-O (single bond) of 1.72 Å and 2.11 Å length, respectively<sup>81</sup>.

#### **4.5. Characterization of aldehyde oxidoreductase from *Pyrococcus furiosus***

The crystal structure of AOR<sub>Pf</sub> was the first resolved structure of a tungsten-containing enzyme and the first to show the structure of any tricyclic pyranopterin. AOR<sub>Pf</sub> was comprehensively characterized, although most of the achieved results were deteriorated because of the extreme oxygen sensitivity of the enzyme<sup>72,73</sup>.

The structure of AOR<sub>Pf</sub> was resolved with 2.3 Å resolution, which allowed tracking of the sidechains and the recognition of the pterin geometry in the W-co structure<sup>49</sup>. Nevertheless, the local resolution at the W-co was low, probably due to mixed populations of the metal centre, i.e., mixture of the oxidized and reduced state. Moreover, intrinsic spectroscopic properties of the tungsten atom limited the accuracy of measurement<sup>81</sup>. Thus, the deposited W-co in the structure represents an idealized model with only two MPTs as tungsten ligands. The arrangement of the tungsten and the two pairs of dithiolene sulfurs may be described as a distorted square pyramid, with an angle between the planes of the molybdopterin ligands of 97°. Glu313 and His448 residues were found in the vicinity of the tungsten, where the substrate would bind, and those residues could participate in proton transfer in the catalyzed redox reaction.

The EXAFS analysis of the W L<sub>III</sub>-edge of the fully active AOR<sub>Pf</sub> (previously, EXAFS was conducted for red tungsten pterin, i.e., inactive form) together with data from crystal structure yielded a most probable coordination geometry of tungsten according to the interpretation of Pushie *et al.*<sup>84</sup>. The oxidized enzyme (with W<sup>VI</sup>) was fitted with ~3.4 of W-S bonds at 2.40 Å distance (which, according to structural data correspond to pterins), and as additional tungsten ligands: ~1.6 of W=O (oxo ligand) at 1.75 Å, and ~0.6 of W-O at 2.06 Å. The interpretation of the data for the oxidized enzyme gave the best fit for fractional coordination numbers mentioned above, which suggests that this

sample consisted of a mixture of species. The reduced sample appeared to be more homogenous, as the model was fitted with one W=O at 1.75 Å, four W–S bonds at 2.39 Å (complete occupation of pterins), and one W–O at 1.97 Å. According to data from the crystal structure<sup>49</sup> there is no protein-derived ligand at the tungsten coordination sphere. Therefore, the oxygen atom recognized at 1.97 Å should come from a water or hydroxo group.

The difficulties in achieving a homogenous sample were also noted in studies of AOR<sub>Pf</sub> by electron paramagnetic resonance (EPR) and variable-temperature magnetic circular dichroism (VTMCD) spectroscopies<sup>85</sup>. In EPR spectroscopy, only W<sup>V</sup> is visible because of its d<sup>1</sup> configuration, whereas the VTMCD follows a paramagnetic state of the Fe<sub>4</sub>S<sub>4</sub> clusters and tungsten coordination. At least two W<sup>V</sup>-containing cofactor species were identified by redox titration followed by EPR spectroscopy and in spectroscopic studies of the enzyme-substrate complex. One of the species was attributed to a catalytically active enzyme that was able to cycle between W<sup>IV</sup>, the EPR-visible W<sup>V</sup> and oxidized W<sup>VI</sup>. The other species is the W<sup>V</sup> state derived from an inactive cofactor with W<sup>VI</sup> and a terminal S ligand.

According to a review by Hagen, regardless of extensive studies and application of many different approaches, the achievement of a homogenous sample of AOR<sub>Pf</sub> seems to be unreachable<sup>45</sup>. The very oxygen-labile species that are also deactivated by too long incubation with reductant and demanding high-temperature kinetic studies are the main obstacles in the studies. Therefore, other examples of AORs might be worth studying.

#### 4.6. Theoretical studies of AOR mechanism

The mechanism of aldehyde oxidation by W-AOR is not known. Theoretical studies of the related enzymes catalysing the same reaction were conducted before for molybdenum-dependent AOR from *Desulfovibrio gigas*<sup>86</sup> and FOR<sub>Pf</sub><sup>87</sup>. In particular, the catalytic mechanism of the even more interesting reduction of non-activated carboxylic acids by metalloenzymes was not yet explored.

The reaction of aldehyde oxidation catalyzed by the molybdenum-dependent AOR from *Desulfovibrio gigas* has been studied by QM:MM methods. The Mo-AOR belongs to the xanthine oxidase family and is not related to the W-AORs. The Mo ion in the active site is coordinated by two sulfur atoms from a metallopterin cytosine dinucleotide, one sulfide and two oxygen ligands. One of the oxygen species forms a hydrogen bond with Glu869 in the second shell. The result of the study indicated that the Glu869 residue serves as a Lewis base to accept a proton from the Mo-OH and to promote a nucleophilic attack on the substrate's aldehyde carbonyl carbon to generate a tetrahedral intermediate. Next,

the hydride from intermediate diol carbon is transferred to the sulfido group. According to the mechanism, this hydride transfer is a rate-limiting step. The proposed mechanism is shown in **Figure 6**<sup>86</sup>.

On the basis of the above-mentioned catalytic reaction mechanism and the structural data of the Mo-AOR, a similar mechanistic hypothesis was drawn for FOR<sub>Pf</sub>. The available crystal structure of FOR<sub>Pf</sub> with a co-crystallized product glutarate (pdb: 1B4N) shows that the carboxylate is directly bound to the tungsten atom and interacts with the Glu308 residue.

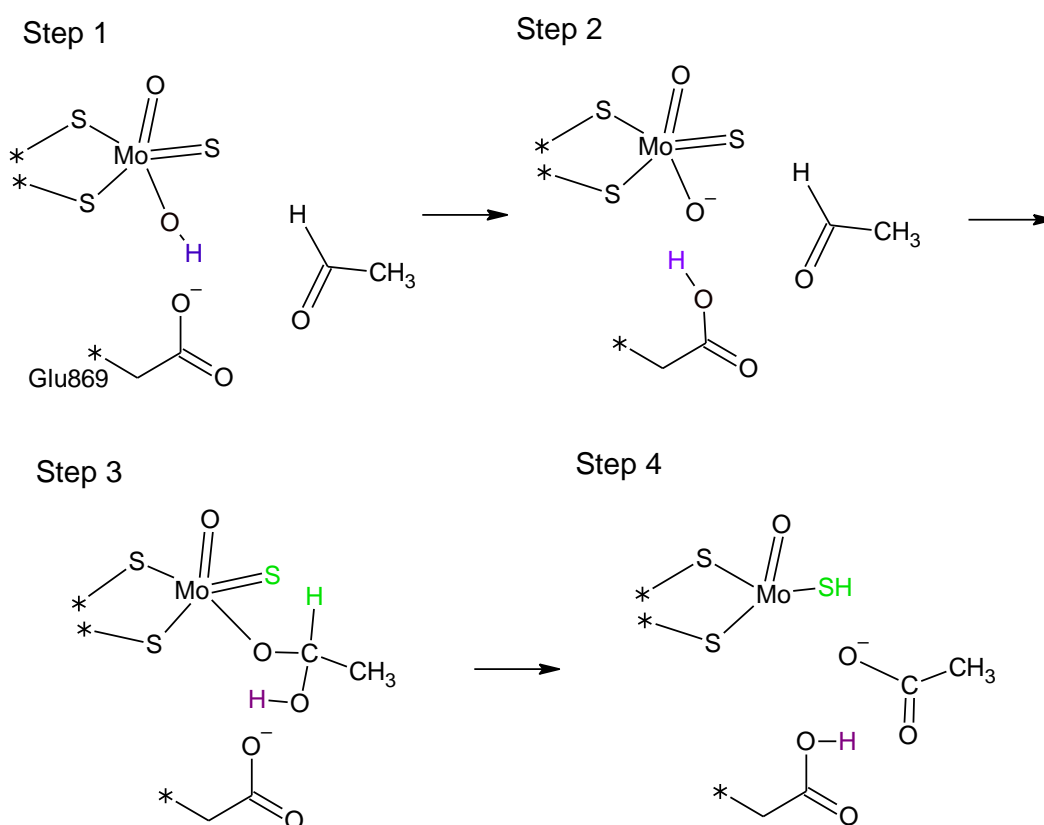


**Figure 6.** Mechanism of aldehyde oxidation proposed for Mo-AOR from *D. gigas*. In the first step, Glu869 accepts the proton from MoCo. Next, a nucleophilic attack of the oxo group on the carbonyl carbon in aldehyde leads to an intermediate bonding of substrate. Hydride transfer to the sulphide group leads to the release of an acidic product. Based on Metz *et al.*<sup>86</sup>, prepared in ChemSketch.

A cluster model (DFT) study elucidated a preferential pathway for the oxidation of formaldehyde (**Figure 7**). The cluster model used in the study depicted the active site: tungsten and its ligands (represented by an oxo group, a water molecule and two 2-methylpyranedithiolenes accounting for metallopterin) and catalytically important residues (Tyr307, Glu308, Ser414, Gly415, Tyr416 and His437). According to

calculations, the most probable pathway involved the direct binding of the formaldehyde in the tungsten's first ligand shell via aldehyde carbonyl oxygen (shown in **Figure 7**). Next, the oxo ligand performs a nucleophilic attack on the formaldehyde carbon resulting in a tetrahedral intermediate. Direct binding to tungsten allows for charge stabilization resulting in lower energy of aldehyde intermediate. Such an effect was also noticed in studies for acetylene hydratase<sup>88</sup>. The following transfer of hydride to Glu308 is coupled with electron transfer from aldehyde to tungsten<sup>87</sup>. The resulting intermediate is the acid bound to W(IV). The next step is the dissociation of formate and the association of ferredoxin, which enables the oxidation of W(IV) in two one-electron steps. The reduced ferredoxin dissociates from the complex and water is associated to the tungsten. The last step before the catalytic cycle is completed is the deprotonation of Glu308 and tungsten ligands and the association of formaldehyde.

In a review by Hagen<sup>45</sup> it was pointed out that these calculations were the only indication of direct binding of the substrate and the product directly to the metal. The study lacked any additional proof for this hypothesis, e.g. the spectroscopic characterisation of respective substrate/product-enzyme complexes.

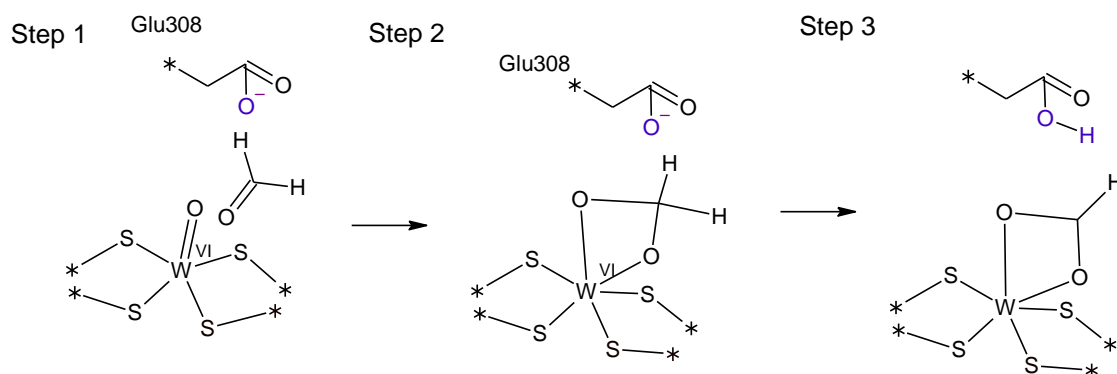


**Figure 7.** Potential reaction pathway for aldehyde oxidation catalyzed by W-FOR from *P. furiosus*.<sup>87</sup>

#### 4.7. Aldehyde oxidoreductase from *Aromatoleum aromaticum*

The mesophilic, denitrifying betaproteobacterium *Aromatoleum aromaticum* can anaerobically degrade aromatic compounds, some of them being common environmental pollutants (toluene, ethylbenzene and phenol)<sup>89</sup>. When growing on phenylalanine, the bacteria produce a range of specialized enzymes (see **Figure 8**) that enables the conversion of the amino acid to phenylglyoxylate and benzoyl-CoA that are degraded via a common pathway<sup>90</sup>. Among the enzymes expressed for the degradation of phenylalanine, two oxidoreductases catalyze the oxidation of phenylacetaldehyde to phenylacetate, i.e., aldehyde oxidoreductase (AOR<sub>Aa</sub>) and phenylacetaldehyde

dehydrogenase (PDH)<sup>90</sup>. PDH is highly substrate-specific and seems to be the main catalyst responsible for the oxidation of phenylacetaldehyde. The AOR<sub>Aa</sub> aldehyde oxidation activity in the cell extract of *A. aromaticum* was observed with benzyl viologen as an electron donor. *A. aromaticum* only expressed the active AOR<sub>Aa</sub> when tungstate was present in the growth media. However, the absence of AOR activity had no impact on the growth on phenylalanine. As the role as the main catalyst in phenylalanine degradation was rejected by this finding, the AOR<sub>Aa</sub> was proposed to play a role in aldehyde detoxification<sup>64</sup>.

AOR<sub>Aa</sub> is expressed by *A. aromaticum* in very low quantities and an alternative method of expression was necessary to isolate the enzyme by chromatographic methods. The first attempt at induction of AOR<sub>Aa</sub> expression was a mutation of *A. aromaticum* eliminating expression of phenylacetaldehyde dehydrogenase. This resulted with construction of a new, streptomycin-resistant strain SR7 $\Delta$ *pdh*<sup>90</sup>. Within only a few generations, the strain SR7 $\Delta$ *pdh* adapted its metabolic pathway to the lack of the main dehydrogenase and expressed AOR<sub>Aa</sub> in high quantities<sup>90</sup>.

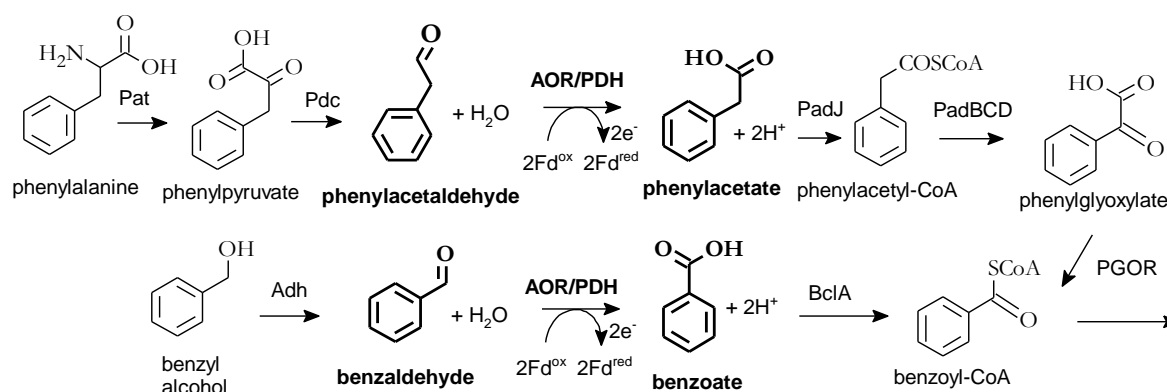


**Figure 8.** Anaerobic degradation pathways of phenylalanine and benzyl alcohol by *A. aromaticum*, adapted from Schmitt *et al.*<sup>90</sup> Enzymes present in the pathway: Pat: phenylalanine aminotransferase; Pdc: phenylpyruvate decarboxylase; AOR: aldehyde:ferredoxin oxidoreductase; PDH: phenylacetaldehyde dehydrogenase; PadJ: phenylacetate-CoA ligase; PadBCD: phenylacetyl-CoA:acceptor oxidoreductase; PadEFGHI: phenylglyoxylate:acceptor oxidoreductase; Adh: benzyl alcohol dehydrogenase; Ald: benzaldehyde dehydrogenase; BclA, benzoate-CoA ligase.<sup>90</sup>

The gene coding for AOR<sub>Aa</sub> active site subunit (AorB, ebA5005) has 50% sequence identity to the well-characterized AOR<sub>Pf</sub> and is organized into an operon of five different genes. Two of the genes encode the other subunits from the isolated AOR<sub>Aa</sub> complex: AorA, a ferredoxin-type subunit with four cysteine binding motifs for Fe<sub>4</sub>S<sub>4</sub> centres and AorC, an NADH oxidoreductase subunit (ebA5007). The two additional genes, *aorD* and



*aorE* sequence, are coding for proteins resembling the Mo-cofactor maturation factor MoaD. These proteins were not found in the purified enzyme but may be involved in the biosynthesis of W-cofactor<sup>91</sup>.

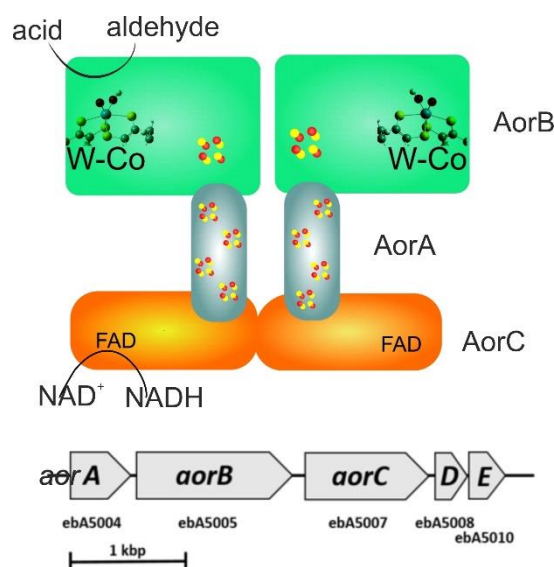


**Figure 9.** (top) Apparent composition of AOR<sub>Aa</sub> with marked positions of catalyzed reactions, (bottom) operon coding for AOR<sub>Aa</sub> subunits and apparent maturation chaperons<sup>74</sup>.

The Ferguson plot analysis showed that the AOR<sub>Aa</sub> has a mass of ca. 280 kDa. Therefore, the AOR<sub>Aa</sub> complex was assumed to have Aor<sub>2</sub>B<sub>2</sub>C<sub>2</sub> composition. In the course of FPLC purification of the AOR<sub>Aa</sub> the enrichment of tungsten was proven through an element analysis (ICP-MS). For purified AOR<sub>Aa</sub>, the presence of 1.8 W, 38 Fe, 6.2 P, and 2.3 Mg per presumed Aor<sub>2</sub>B<sub>2</sub>C<sub>2</sub> holoenzyme was detected without any traces of Mo. This agreed with the elemental content of two W-co and 10 Fe<sub>4</sub>S<sub>4</sub> centres. Based on the above data, the proposed electron-transfer chain begins with the tungsten cofactor linked to FAD via a chain of five Fe<sub>4</sub>S<sub>4</sub> clusters (**Figure 9**). This arrangement of redox centres facilitates the use of NAD<sup>+</sup>, benzyl viologen (BV) and ferredoxin as redox mediators.

AOR<sub>Aa</sub> was proven to be much more stable in contact with oxygen than the archeal AORs. No impact of oxygen atmosphere was shown for AOR<sub>Aa</sub> in cell extract. The isolated AOR<sub>Aa</sub> exhibited a half-life time of 1 h and was almost completely inactivated after 3 h in air contact<sup>74</sup>.

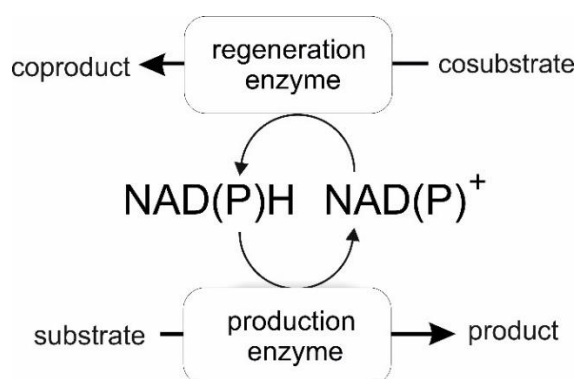
## 5. NADH regeneration

Although the carboxylic acid reduction by AORs is the most interesting activity of this enzyme, a new hydrogenase activity associated with AOR<sub>Aa</sub> shown in this thesis

provides a new application perspective of the enzyme, i.e., for an atom-efficient regeneration system of NADH cofactor.

The NAD(P)H-dependent oxidoreductases are widely used in industrial synthesis<sup>1</sup>. If employed in a reduction reaction, the enzymes utilize an electron donor, usually NADH or NADPH, which in their reduced form are very expensive (in 2011, the cost of bulk NADH was \$2600/mol)<sup>92</sup>. Therefore, any enzymatically-catalyzed reduction process will only be economical if a suitable cofactor regeneration system is used. There are several methods for NAD(P)H reduction, i.e., i) biocatalytic (with dehydrogenases or hydrogenases), ii) electrochemical (on Ti, Au, Cu, glassy carbon electrodes with organometallic redox mediators), iii) photocatalytic (through light-harvesting systems and electron transport chains), and iv) chemical reduction (by reaction with Na<sub>2</sub>S<sub>2</sub>O<sub>4</sub>, NaBH<sub>4</sub>, and 1,4-dihydropyridines)<sup>93</sup>.

Regeneration of the NAD(P)H cofactor is based on the regioselective two-electron reduction at the C4 atom of the nicotinamide ring, and the applicable methods of NAD(P)H regeneration must preserve the active structure of the reduced form. The presence of oxidoreductase substrate in the reaction mixture requires the regeneration system to be selective in the reduction only of NAD(P)<sup>+</sup>. Furthermore, enzymes must generally be used in mild conditions and many biocatalysts are used in whole-cell processes, so the cofactor regeneration method must be compatible with those systems. So far, only enzymatic NADH regeneration methods, due to their high selectivity, catalytic activity, compatibility with whole-cells systems and activity under mild conditions, comply with all those requirements and are prevalent in industrial practice<sup>1</sup>.



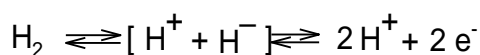
**Scheme 3.** The NADH recycling system comprises NAD(P)H-dependent production enzyme (oxidoreductase) that reduces the substrate and regeneration enzyme, e.g. hydrogenase, alcohol dehydrogenase, that oxidize the cosubstrate and restore the NAD(P)H pool.

The dehydrogenases and hydrogenases used in NADH regeneration can be deployed as: i) a homogenous catalyst - an isolated enzyme or enzyme preparation, ii) an immobilized enzyme as a heterogeneous catalyst, or iii) as part of a whole-cell system<sup>1,93</sup>. When dehydrogenase is used to reduce NAD<sup>+</sup>, a sacrificial substrate has to be oxidized. For example, alcohol dehydrogenases (ADH) convert alcohol to corresponding ketone or aldehyde (a suitable example is 2-propanol converted to acetone), and the reaction is coupled to NAD<sup>+</sup> reduction. Similarly, formate dehydrogenase (FDH) oxidizes formic acid to carbon dioxide, phosphite dehydrogenase yields electrons from phosphite oxidation, and glucose dehydrogenase converts glucose to gluconolactone<sup>94</sup>. There are commercially available dehydrogenases of high thermostability and high specific activity suitable for industrial application<sup>1</sup>. Nevertheless, except for FDH, all dehydrogenases produce byproducts (acetone, phosphate, etc.) that require downstream separation. On the contrary, hydrogenases reduce NAD<sup>+</sup> in a reaction coupled with hydrogen oxidation to protons, giving no side products. Hydrogen gas is an inexpensive reducing agent and the process is 100% atom effective (especially if the protons are eventually consumed in the NAD(P)H-coupled reduction), making this a sustainable system. Interestingly, in 2011 hydrogenase-based NAD(P)H regeneration systems were assessed as not yet developed enough for industrial application.<sup>1</sup>

## 6. Hydrogenases

The structures of active sites and mechanisms of catalyzed reaction of hydrogenases are topics of interest for this review, considering the new activity of AOR<sub>Aa</sub> in hydrogen oxidation shown in this work.

Hydrogenases are a metalloenzyme family present in bacteria, archaea and some eukarya that catalyze the conversion of H<sub>2</sub> to protons and electrons, as well as a reduction of protons to molecular hydrogen<sup>95</sup>. The reaction can be represented by the following equation:



To split the hydrogen, hydrogenases employ specialized metal centers which increase the acidity of the molecule. The heterolytic splitting of hydrogen is possible thanks to the presence of a metal and a base, which can be a basic amino acid (glutamine, arginine, cysteine) or a ligand coordinating metal, e.g., an oxo ligand.

Depending on the type of metal cofactor in the enzyme's active site, three basic groups of hydrogenase can be distinguished: binuclear [NiFe], [FeFe] and mononuclear [Fe] hydrogenases. There are also other metalloenzymes that have the ability to oxidise H<sub>2</sub> to

protons or to reduce protons to hydrogen, such as the molybdenum/copper-containing carbon monoxide CO dehydrogenase from *Oligotropha carboxidovorans* (CODH)<sup>96</sup> and the nitrogenases.

The metal centers in [NiFe], [FeFe] and MoCu hydrogenases are linked by sulfur atom and one of the irons is coordinated by inorganic ligands (e.g. CO and CN<sup>-</sup>), while the other ligands are cysteines (see **Figures 10** and **11**). An open metal coordination site for binding of a hydrogen molecule in [NiFe] and [FeFe] hydrogenases is present on the Ni or Fe atoms, respectively. Hydrogenase structures are optimized for molecular hydrogen and proton transfer and have two respective pathways for those reactants. In [NiFe] and [FeFe] hydrogenases the electrons are transported between subunits by iron-sulfur cluster chains to a flavin cofactor accepting NAD(P)<sup>95</sup>.

The currently proposed mechanism of hydrogen oxidation by [NiFe] hydrogenases is shown schematically in **Figure 10.A**. It begins with the polarization of molecular hydrogen at the Ni and heterolytic cleavage of the H-H bond. The resultant H<sup>-</sup> is captured by the bimetallic center, while the proton is carried by the sulfur of a cysteine, which is coordinating nickel. Together with the proton transfer, one electron leaves the cofactor through a nearby Fe<sub>4</sub>S<sub>4</sub> cluster. The active site is left in a paramagnetic intermediate state with Ni(III). Next, the metals release another proton and an electron, and the catalytic cycle is closed<sup>95,97</sup>.

The active site cofactor of [FeFe] hydrogenases is called H-cluster. In [FeFe] hydrogenases an amine group of a thiol ligand bridging the two irons (as shown in **Figure 10.B**) was proposed to be the most probable base taking part in the catalytic cycle. In order to accept or donate a proton to the reaction, the ligand holding the amine group would be moving during catalysis. Moreover, the Fe<sub>4</sub>S<sub>4</sub> cluster in the vicinity of [FeFe] center was also suggested to be part of catalytic cycle, lending capacity of one electron between oxidized [Fe<sub>4</sub>S<sub>4</sub>]<sup>2+</sup> and reduced [Fe<sub>4</sub>S<sub>4</sub>]<sup>+</sup> states. The catalytic center cycles between the “active oxidized” state H<sub>ox</sub> ([Fe<sub>4</sub>S<sub>4</sub>]<sup>2+</sup>-Fe(I)Fe(II)), the “active reduced state” state H<sub>red</sub> ([Fe<sub>4</sub>S<sub>4</sub>]<sup>2+</sup> Fe(I)Fe(I)) and intermediate state ([Fe<sub>4</sub>S<sub>4</sub>]<sup>+</sup> Fe(I)Fe(I)). The active reduced state of the H-cluster is able to oxidize molecular hydrogen<sup>98</sup>.

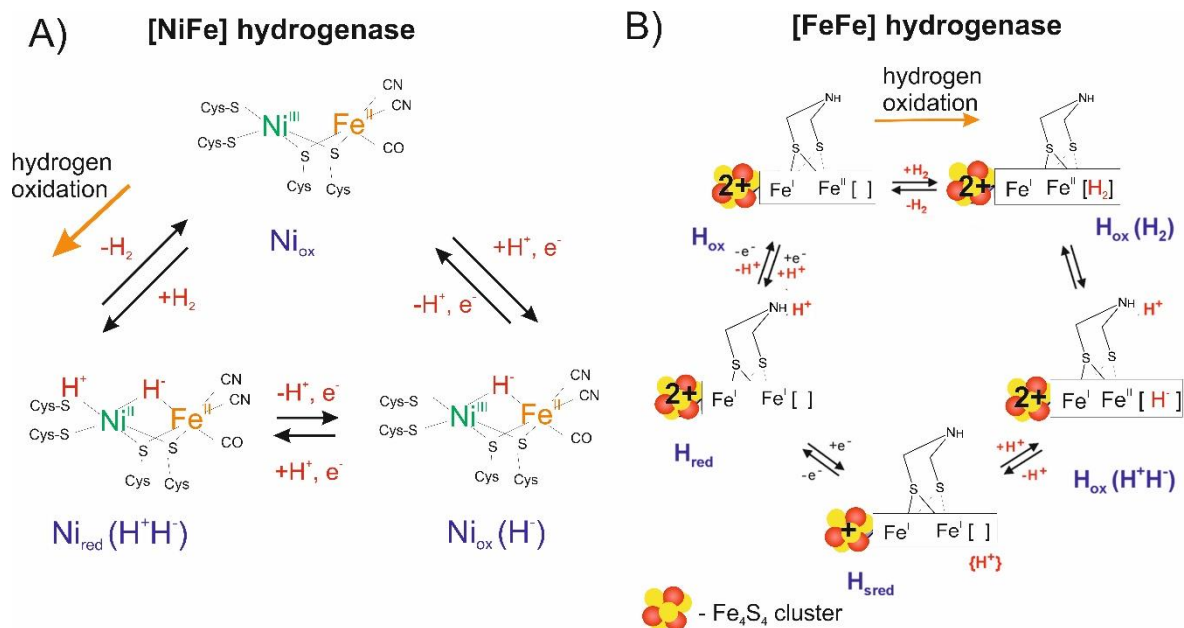


**Figure 10.** Possible catalytic cycle mechanism of **A)** [NiFe] hydrogenase; **B)** [FeFe] hydrogenase, based on Lubitz *et al*<sup>95</sup>. In B, {H<sup>+</sup>} represents a possible binding of the proton on a nearby amino acid.

In contrast to the other hydrogenases the [Fe] hydrogenase employs a mononuclear cofactor in form of the Fe-guanylylpyridinol and contains no iron-sulfur clusters. It catalyzes a non-standard reaction, as it does not reduce electron acceptors like artificial dyes, but hydrogen oxidation reaction is coupled to the reversible reduction of the substrate methenyltetrahydromethanopterin<sup>95</sup>.

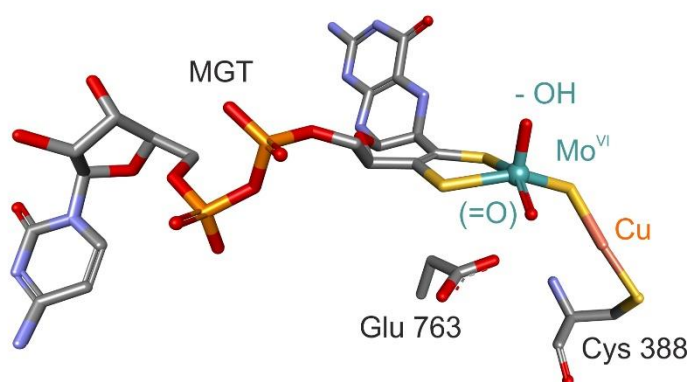


**Figure 11.** The active site of the MoCu-CODH (PDB: 1N5W). The molybdenum atom (shown in teal) is coordinated by two oxygens, metallopterin cytosine dinucleotide and sulfur atom linking it with the copper atom, which is coordinated by Cys388.

The carbon monoxide CO dehydrogenase (CODH) was shown to contain a MoCu binuclear active site (shown in **Figure 11**). The primary activity of CODH is the oxidation of CO to CO<sub>2</sub>, coupled with oxygen reduction ( $k_{\text{cat}}$  of 93 s<sup>-1</sup><sup>99</sup>). Meanwhile, the reduction of MoCu-CODH with molecular hydrogen proceeds at a limiting rate constant of 5.3 s<sup>-1</sup><sup>96</sup>. The active site of the enzyme contains two metals - copper and molybdenum in a unique configuration: the molybdenum is coordinated by one metallopterin cytosine dinucleotide, one oxo- and one hydroxo-ligand and a sulfur atom that forms a bridge between two metals. In the H<sub>2</sub>-dependent catalytic process, the hydrogen is proposed to bind to Cu(I) atom, which results in the reduction of the bimetallic centre from Mo(VI)/Cu(I) to Mo(IV)/Cu(I)<sup>100</sup>.

Hydrogenases are in general oxygen-sensitive. Some of the representatives were reported to be inactivated even by trace amounts of O<sub>2</sub><sup>101</sup>, others needed anaerobic conditions only for activating H<sub>2</sub><sup>96</sup>, and only a few could catalyze reduction with oxygen present<sup>102</sup>. The inactivation by oxygen was shown to be reversible in anaerobic conditions<sup>97</sup>. Most hydrogenases were characterized to have low thermal stability, except those from hyperthermophilic bacteria and archaea<sup>103</sup>.

Hydrogenases are usually inhibited by a higher concentration of hydrogen. For the O<sub>2</sub>-tolerant NAD<sup>+</sup>-reducing hydrogenase from *Ralstonia eutropha* ([NiFe]-hydrogenase) at hyperbaric levels of H<sub>2</sub>, substrate inhibition ( $K_i = 1.46$  mM) was observed<sup>102</sup>. However, the inhibition at high concentrations of hydrogen is not a obstacle for efficient catalysis in case of rapid saturation with the substrate, i.e., for the [FeFe] hydrogenase from *Moorella thermoacetica* apparent  $K_m$  value for H<sub>2</sub> is about 6% in the headspace of the reactor<sup>101</sup>.

Another aspect of hydrogenases sensitivity is inhibition by carbon monoxide. In the case of [NiFe]-hydrogenase inhibition proceeds by binding an exogenous CO ligand to the nickel and the bond can be cleaved only at negative redox potentials<sup>97</sup>.

### 6.1. Electron bifurcation

The effect of electron bifurcation occurs when exergonic and endergonic electron transfer reactions are simultaneously catalyzed (coupled) by the enzyme to minimize the energy loss and overcome thermodynamic barriers for the endergonic reaction. The catalyzed oxidation-reduction reaction can be interpreted as an electrochemical transition and the electron transfer is dependent on the redox potential of the reagents (favouring flow from lower to higher potential).<sup>104</sup>

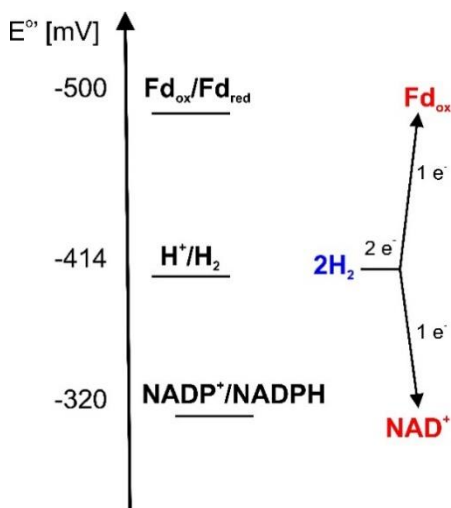
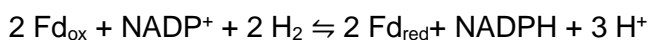


**Figure 12.** Redox potential of reactions catalyzed by [FeFe]-hydrogenase.

An example of an electron-bifurcating enzyme complex is [FeFe] hydrogenase from *M. thermoacetica*. It can catalyze ferredoxin reduction ( $E^\circ = -500$  mV) coupled to  $H_2$  oxidation ( $E^\circ = -414$  mV) only with simultaneous exergonic reduction of  $NAD^+$  ( $E^\circ = -320$  mV) with  $H_2$ . In the absence of  $NAD^+$ , ferredoxin is not reduced. The effect of electron bifurcation is visible when  $NAD^+$  is present in the above reaction. The theoretical explanation of the effect was widely discussed by R. Thauer and M.W.W. Adams (independently<sup>104–106</sup>).

The electron bifurcation can be explained by the example of [FeFe] hydrogenase HytA-E from *Clostridium autoethanogenum*. HytA-E is a cytoplasmic flavin nucleotide-containing complex that stoichiometrically couples the endergonic reduction of ferredoxin with  $H_2$  to the exergonic reduction of  $NADP^+$  with  $H_2$  according to the equation<sup>107</sup>:



The electrons from hydrogen oxidation are split (at a specialized cofactor, here flavin) into one electron of a higher potential (matching the potential of  $NADP^+/NADPH$  couple) and one of a lower potential (the potential of ferredoxin reduction, see **Figure 12**). The efficient reduction of the low-potential substrate (ferredoxin) with hydrogen as an electron donor is possible only with simultaneous  $NADP^+$  reduction<sup>106</sup>.

The mechanism of electron bifurcation has not yet been explained in detail. However, many systems utilizing this effect were identified<sup>106</sup>. All identified reactions involved a reduction of quinone or flavin, which have three consecutive possible oxidation states (hydroquinone, semiquinone and quinone) that can be utilized when splitting the electron pair. The identified low-potential electron acceptors for the system were ferredoxin, flavodoxin, or cytochrome c.<sup>105</sup>

## 7. Cryogenic electron microscopy

Determination of the enzyme 3D structure is key to any mechanistic studies of the catalytic reactions. Although alternative approaches, such as homology modelling or *de novo* structure prediction, were developed to overcome the need for experimental structural study, its hindrance is still a necessity of structural knowledge of similar

proteins based on which either a homolog is built or a machine learning system (e.g. AlphaFold2) is trained. As a result, the experimental structural techniques are still the only solution for new protein folds.

To date, X-ray crystallography is the most widely used technique for solving the structures of proteins at atomic resolution (i.e., below 3 Å). This technique requires a preparative step of crystallization, which for proteins of high mobility and conformational variability frequently turns out to be impossible to achieve. For small, flexible proteins, a structure prediction method utilizing Nuclear Magnetic Resonance and the nuclear Overhauser effect is often used in combination with the computational study. The main limitation of the technique is the size of the protein (for common appliances maximum size is about 35 kDa), which should be improved by higher field magnets to about 100 kDa<sup>108</sup>. Still, with the above techniques, large and flexible protein complexes cannot be resolved.

Fortunately, an alternative method, single-particle analysis cryogenic electron microscopy (CryoEM), has revolutionized protein structural determination. In 2015 Campbell, Carragher, Potter *et al.* achieved a ground-breaking resolution of CryoEM beyond 3 Å in the reconstruction of 20S proteasome (2.8 Å resolution)<sup>109</sup>. The CryoEM allows the recording of a fully hydrated protein in native conditions. Therefore, the proteins that do not crystallize can be studied and for other cases, this technique is beneficiary as it can resolve structure in the hydrated, native form of the complex. The amount of sample needed for the study is much lower than in crystallography and any specimen conformational variability can be observed and solved.

In principle, the CryoEM method can be explained as a study of macromolecules forming a single layer on a supporting grid frozen in cryogenic conditions (**Figure 13**), where 2D micrographs are recorded by transmission electron microscopy (TEM). The principle of TEM function is similar to optical microscopy, where light is replaced with electrons and an optical system with magnetic lenses.



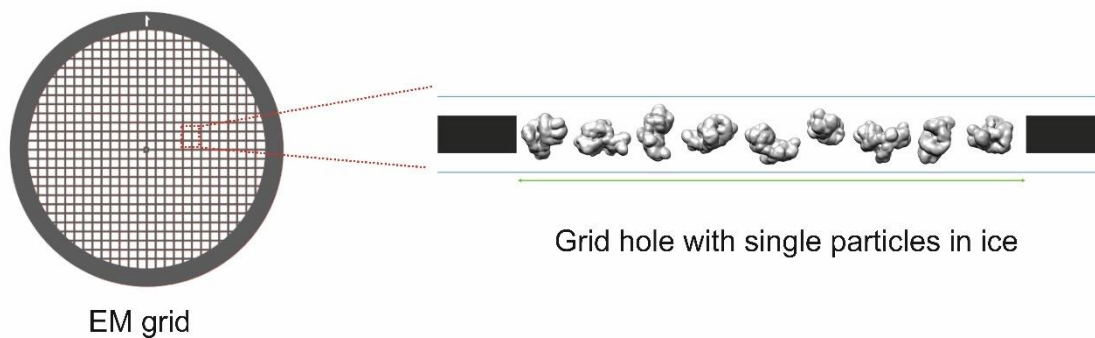


**Figure 13.** Diagram showing EM grid and a close-up of hole cross-sections containing idealized particle and ice behavior zones for single particle cryoEM collection.<sup>110</sup>

The electron beam is directed at the sample and the electrons pass through the sample and diffract, yielding electron image and diffraction patterns<sup>111</sup>. The resulting micrographs are then processed with a single-particle reconstruction algorithm (see Methods Chapter 4.2 for further discussion) to obtain a 3D reconstruction of the particle. The achieved resolution of 3D reconstruction depends on the microscope's limitation and the cryoEM specimen's features. The cryoEM specimen consists of a grid usually made of perforated carbon film supported by a metal frame on which, ideally, a homogenous protein sample forms a randomly-distributed single layer of particles surrounded by thin, amorphous ice.

The electron beam used in EM is of wavelength around 2 pm, which is less than an atom diameter and therefore, there is no limitation in the development of this technique from the type of beam used. The number of problems yet to face are caused by technical limitations of lenses. In recent years the limitation of microscopes changed drastically with each generation, which improved achievable resolution. However, for a given machine, the features of the cryoEM specimen can be optimized to achieve the best results<sup>112</sup>.

Therefore, the first step of the cryoEM study should be the optimization of sample composition (e.g., salt, pH, detergent and protein concentration) based on an assessment of a protein's stability and biochemical activity. The homogeneity of the protein sample can be assessed by sodium dodecyl sulfate-polyacrylamide gel electrophoresis (SDS-PAGE), gel chromatography or dynamic light scattering. Apart from a single species present in the sample, the protein complex must be stable at the concentration used on EM grids. Additionally, at this stage of the experiment, the homogeneity and stability of the complex at low concentrations (similar to those used in EM) can be tested by dynamic light scattering or another recently developed technique, mass photometry (described in Chapter 4.4. of Methods). If the buffer composition

optimization does not yield a stable complex, an additional step of crosslinking the protein may be performed for example, with mild glutaraldehyde fixation using the GraFix protocol<sup>113</sup> or using bis(sulfosuccinimidyl)suberate as a crosslinker. In both approaches, the chemical reacts mainly with an amino group of lysine side chains, forming inter- and intramolecular links in a protein complex. After a homogenous and stable sample is prepared, it may be evaluated by negative stain electron microscopy for the formation of discrete particles of size and shape consistent with previous results.

Once a uniform distribution of particles is confirmed, a cryoEM specimen can be prepared by vitrification of protein on the grid with an automatic or manual plunge freezing device. A grid containing a protein sample is plunged into a cryogenic liquid, such as liquid ethane, which freezes the sample immediately on the contact<sup>114</sup>. This procedure results in the vitrification of water hydrating the protein, preserving the native state of the macromolecule. Moreover, the low-temperature conditions maintained since vitrification minimizes the sample damage by electron irradiation in TEM. A critical feature of the prepared grid is the thickness of ice, which influences contrast with the background and defocus spread. Therefore, the grids should be screened for ice quality and sample distribution using a side-entry Transmission EM and freezing parameters (e.g. length of blotting, filter paper used, sample concentration, etc.) should be optimized in the next iterations of grid preparation. The grids containing evenly distributed particles in the vitrified ice at reasonable density, without overlapping particles, are imaged on a data collection TEM to obtain dose-fractionated 2D projection images of randomly oriented particles. The data obtained in this step are subjected to a single-particle 3D reconstruction to obtain a 3D electron density map of the macromolecule. The procedure of single-particle 3D reconstruction involves steps such as phase Contrast Transfer Function (CTF) estimation and correction, particle picking, 2D and later 3D alignment, averaging and refining the reconstructed density map<sup>115</sup>.

In recent years new techniques were developed to replace the time-consuming step of manual selection from recorded images of hundreds of thousands of particles required for 3D reconstruction. The first methods of particle picking were semi-automated and based on user-selected templates. The user-selected particles were rotationally averaged, and new particles were located by cross-correlating each template image with the entire micrograph<sup>116</sup>. Automated methods include approaches like local comparison of pixel intensity values, quantitative measures of the local image texture/statistics and pattern recognition - edge detection and a sequence of ordered Hough transforms<sup>117</sup>. Among the automated methods are the recent machine learning based methods (like TOPAZ). The TOPAZ procedure (pipeline) is based on a deep neural network learning

by positive-unlabelled classification, which was proved to be an efficient and precise (in a number of false-positives) method of particle picking. The network is trained with few labelled particles (positives) and no labelled negatives. The network can select even difficult, unusually shaped proteins into more representative particle sets and no curation of data is required.<sup>118</sup>

The high-resolution 3D cryoEM structure refinement requires an initial 3D model as a starting point. If no previous 3D models are available for the protein, a new one can be established based on selected particles. All similar particles are grouped to form classes, which are assumed to be different views of the particle. Several of these classes are then manually chosen as input for generating a 3D model. The relative orientations of all of the selected averages are determined using a Fourier common-lines method, which is then integrated to create a 3D initial model<sup>116</sup>.

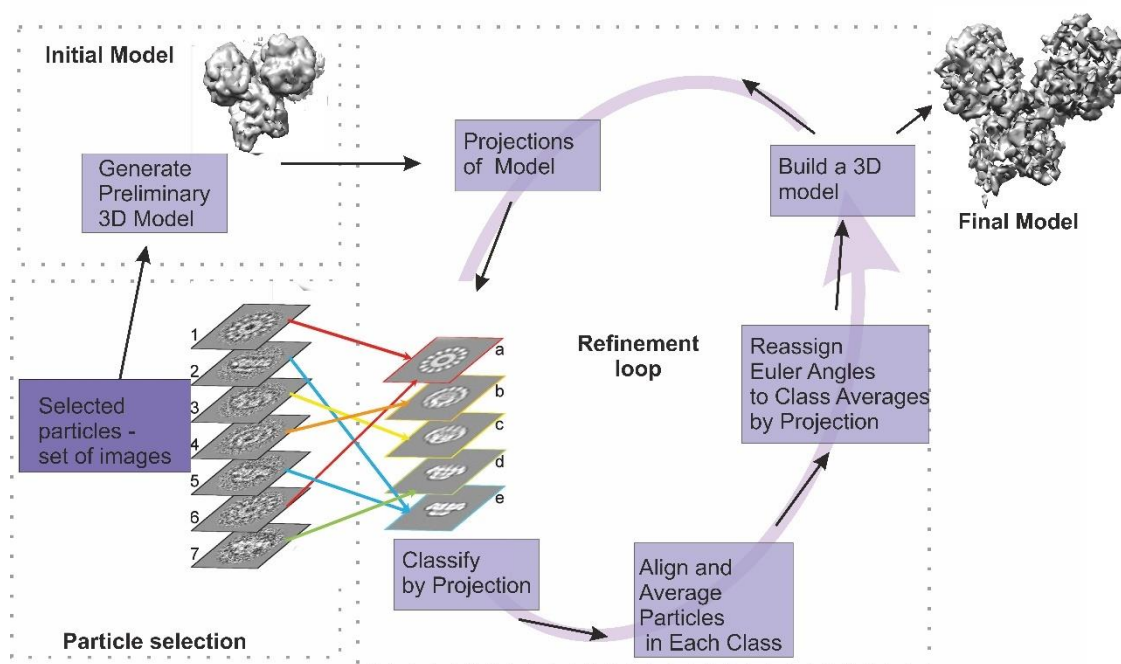


**Figure 14.** Workflow diagram of single-particle reconstruction process implemented by Ludtke *et al.*<sup>116</sup> in EMAN software package. The explanation of classification of selected particles (images 1-7) to projections of a 3D model (a-e).<sup>115</sup>

The next step of data processing is the iterative refinement of a 3D model. Similarly to NMR and X-ray crystallography techniques, direct inversion of the experimental data to create a final 3D structure is impossible. Therefore, iterative refining of a 3D model against the data is applied until achieving convergence, as illustrated in **Figure 14**. The refining procedure begins with the generation of N projections of the model with uniformly distributed orientations. These projections serve as references for classifying

the raw particle data. Each particle is assigned to one of the projections, resulting in N raw particle image classes. The particles in those classes are then mutually aligned and averaged, some particles are excluded and a new class average is produced. The Euler angles<sup>115</sup> of new class averages are redetermined by projection matching, which aligns the data to be used in the new 3D model reconstruction. The 3D model can be used in a subsequent refinement cycle, or if the convergence is reached, it is the final model<sup>116</sup>.

## **Aims of the work**

The presented literature review showed that AORs are good candidates for biocatalysts in carboxylic acid reductions. AOR<sub>Aa</sub>, as a relatively oxygen-insensitive enzyme from mesophilic, facultative anaerobic bacteria, was chosen as a model for the profound characterization of multisubunit AORs, a topic that was overlooked in previous research. The work's general aim was to characterize AOR<sub>Aa</sub> with the intention of solving the aldehyde oxidation reaction mechanism and developing the biotechnological application of the enzyme in carboxylic acid reduction. The two main goals were divided into detailed aims:

**Biochemical characterizaton of AOR<sub>Aa</sub>** - determining how pH and composition of gas atmosphere impact stability and activity of AOR<sub>Aa</sub>.

**Catalytic characterization of AOR<sub>Aa</sub>** - kinetic assays and reactor studies aiming at elucidation of AOR<sub>Aa</sub> substrate spectra, accepted electron mediators and kinetic parameters for both catalyzed reactions - aldehyde oxidation and carboxylic acid reduction.

**Application studies for aldehyde and alcohol production** - AOR<sub>Aa</sub> is a good candidate catalyst for carboxylic acid reduction for the production of aldehydes and in (chemo-)biocatalytic cascades, i.e. for the production of alcohols when appropriate alcohol dehydrogenase is used. A benzyl alcohol dehydrogenase from *Aromatoleum aromaticum* was selected for such a cascade as a preliminary study for whole-cell bioalcohol production with *A. aromaticum* strains.

**Structural characteritization of AOR<sub>Aa</sub>** - determining the quaternary structure of the multisubunit AOR and structural details of each subunit. Although structural homologs of the AorB subunit are known, the details of the active center structure would provide a basis for a directed mutagenesis study aiming to validate the reaction mechanism. The structural characterization of AorA and AorC subunits should elucidate the electron transfer chain.

**Identification of W-co composition and geometry** - intrinsic characteristics of W atom disturb structural studies of W-co, preventing elucidation of the exact structure of the cofactor. A theoretical approach, based on results from spectroscopic studies, aimed at solving the exact structure of W-co in AOR. Additional confirmation of W-co composition could be achieved by enzyme characterisation by EXAFS spectroscopy.

## MATERIALS AND METHODS

The properties of AOR from *Aromatoleum aromaticum* were investigated with protein produced by bacteria and purified by Fast Protein Liquid Chromatography (FPLC) methods. Two types of expression systems of AOR<sub>Aa</sub> were used: i) the engineered native host *Aromatoleum aromaticum* with enhanced expression of AOR<sub>Aa</sub> (Chapter 1.1.) and ii) recombinant AOR<sub>Aa</sub> expression system in *Aromatoleum evansii* (Chapter 1.2.). Cell extracts obtained in both methods were enriched via two different purification protocols.

After executing the respective AOR<sub>Aa</sub> enzyme preparations, the quality of the enzyme batches was routinely assessed by measuring its' concentration by the Coomassie binding method (Chapter 2.1), its activity in benzaldehyde oxidation (Chapter 3.5.1.) and by running it on a SDS-PAGE gel (Chapter 2.2.).

The purity of AOR<sub>Aa</sub> was additionally confirmed by proteomic analysis (Chapter 2.3.). The characterization of the thermal stability of AOR<sub>Aa</sub> was conducted by the *ThermoFAD* method (Chapter 2.4.).

For the catalytic tests conducted during this work, the reaction progress was followed by one of two methods:

- i) Direct detection and quantitation of product (Chapter 3.2.-4.);
- ii) Spectrophotometric assays, where change of absorbance of an electron mediator was measured on a UV-vis spectrophotometer (Chapter 3.5.).

In catalytic tests conducted to determine electron donors used by AOR<sub>Aa</sub> for benzoate reduction, a HPLC-DAD method was used to detect benzaldehyde (Chapter 3.2.2.). The substrate spectrum of AOR<sub>Aa</sub> in the reduction of carboxylic acids (Chapter 3.6.1.) was confirmed by the identification of products (aldehydes) by UHPLC-MS/MS (Chapter 3.3.) or GC-MS (Chapter 3.4.). Steady-state activities of AOR<sub>Aa</sub> in i) aldehyde oxidation (Chapter 3.5.1.) and ii) NAD<sup>+</sup> reduction were measured spectrophotometrically, those in iii) benzoic acid reduction by a coupled assay method (Chapter 3.5.3.) and with a UHPLC-DAD method (Chapter 3.2.3.). In the coupled assay method, benzyl alcohol dehydrogenase (BaDH) from *A. aromaticum* was used. BaDH used in this work was produced recombinantly in *Escherichia coli* and purified by FPLC (Chapter 1.3.).

The structure of AOR<sub>Aa</sub> was reconstructed from a density map obtained from cryoelectron microscopy (Chapter 4.). The characterization of the quaternary structure of the complex was supported by measurements via mass photometry (Chapter 4.4.). The structure of W-co was further investigated by theoretical methods (Chapter 5.). Details on tungsten coordination were provided by EXAFS spectroscopy (Chapter 6.).

## 1. Methods of production of enzymes

The AOR<sub>Aa</sub> enzyme used in this study was produced by expression either in engineered native host *A. aromaticum* containing a knock-out mutation of the *pdh* gene that resulted in induction of AOR<sub>Aa</sub> expression during anaerobic growth on phenylalanine or heterologously in *A. Evansii* carrying respective plasmid. The BaDH was produced by heterologous expression in *Escherichia coli* carrying respective plasmid.

The media for anaerobic bacteria growth were prepared by adding ingredients from stock solutions and buffers for purifications were filtered before use on regenerated cellulose filters of 0.45 µm cut-off size. All solutions were anaerobized by contact with subsequent overpressure of nitrogen and vacuum generated by a pump (3 min for each step, repetitions dependent on the volume of liquid, i.e., 1 L processed for 4 cycles). This procedure was conducted by locking the buffers in bottles with rubber stoppers and accessing the inner atmosphere with needles. Culture media and buffers were sterilized after preparation at 121°C and 1.8 bar pressure. Non-autoclavable media and buffers were sterile filtered (on regenerated cellulose filters with 0.22 µm cut-off size). The culture media were mixed in sterile conditions by handling the liquids with sterile syringes. The purification procedure was conducted on a Fast Protein Liquid Chromatography (FPLC) AKTA (GE Healthcare, Uppsala, Schweden) system connected to an anaerobic glovebox.

### 1.1. AOR expression in *A. aromaticum* SR7Δ*pdh*

#### 1.1.1. Fermentation of *A. aromaticum* SR7Δ*pdh*

The strain *A. aromaticum* SR7Δ*pdh* was obtained from the group of prof. Heider from Marburg University and the engineering approach used to obtain the loss-of-function Δ*pdh* mutation was described by Schmitt *et al.*<sup>90</sup>. The bacteria were grown anaerobically on carbonate-buffered (40 mL/L of 1M NaHCO<sub>3</sub> adjusted with HCl to pH 7.2) minimal medium as shown in **Table 2**, supplemented per 1 L of medium with 1 mL of Vitamins Solution, 1 mL of Trace Elements Solution, 1 mL of W-Se Solution (**Table 1**) and 100 ng/L streptomycin. The only carbon source was phenylalanine, whereas the sodium nitrate was an electron acceptor in an anaerobic environment. Cultures were periodically fed once NO<sub>3</sub><sup>-</sup> and NO<sub>2</sub><sup>-</sup> depletion was determined by nitrate/nitrite test strip [Quantofix, Machery-Nagel, Düren, Germany]. The aliquots of phenylalanine and sodium nitrate were resupplied to the concentration of 1 mM and 4 mM, respectively. Cells were grown in stoppered bottles at 28°C without continuous stirring.

**Table 1.** Ingredients of stock solutions: Vitamins, Trace Elements and W-Se Solution used to prepare media for bacterial growth (adapted from Rabus and Widdel <sup>119</sup>).

Vitamins Solution		Trace Elements Solution	
Ingredients	Amounts	Ingredients	Amount
Vitamin B12	50 mg	HCl (25%; 7.7 M)	10 mL
Pantothenic acid	50 mg	FeCl <sub>2</sub> x 4 H <sub>2</sub> O	1.50 g
Riboflavin	50 mg	ZnCl <sub>2</sub>	70 mg
Pyridoxamine hydrochloride	10 mg	MnCl <sub>2</sub> x 4 H <sub>2</sub> O	100 mg
Biotin	20 mg	H <sub>3</sub> BO <sub>3</sub>	6 mg
Folic acid	20 mg	CoCl <sub>2</sub> x 6 H <sub>2</sub> O	190 mg
Nicotinic acid	25 mg	CuCl <sub>2</sub> x 2 H <sub>2</sub> O	2 mg
Nicotine amide	25 mg	NiCl <sub>2</sub> x 6 H <sub>2</sub> O	24 mg
α-lipoic acid	50 mg	Na <sub>2</sub> MoO <sub>4</sub> x 2 H <sub>2</sub> O	36 mg
p-aminobenzoic acid	50 mg	Distilled water	990 mL
Thiamine hydrochloride·x 2 H <sub>2</sub> O	50 mg		
Distilled water	1000 mL		
W-Se Solution			
Ingredients	Amount		
NaOH	400 mg		
Na <sub>2</sub> SeO <sub>3</sub> ·x 5 H <sub>2</sub> O	4 mg		
Na <sub>2</sub> WO <sub>4</sub> ·x 2 H <sub>2</sub> O	8 mg		
Distilled water	1000 mL		

**Table 2.** Content of mineral base for minimal media used for the growth of *A. aromaticum*.

Minimal media	
Ingredients	Amount (mg/L)
KH <sub>2</sub> PO <sub>4</sub>	500
NH <sub>4</sub> Cl	300
MgSO <sub>4</sub> x 7 H <sub>2</sub> O	500
CaCl <sub>2</sub> x 2 H <sub>2</sub> O	100
NaNO <sub>3</sub>	300
Phenylalanine	150

In order to obtain amounts of cells that would enable the purification of considerable amounts of enzyme, the cultivation was conducted in a 30 L fermenter [Biostat C-plus, Sartorius] at Marburg University. Once the fermenter containing media and supplements was prepared, a 1.8 L-volume of one-week-old preculture (OD<sub>600</sub> = 0.8) was added as inoculum. The fermentor was equipped with an in-line pH electrode, which was



connected to the control unit, that was programmed to add a 15% sulfuric acid to keep pH at 7.2 throughout cultivation. The growth of culture was also monitored with optical density measurement at 600 nm (OD<sub>600</sub>) and culture was checked for NO<sub>3</sub><sup>-</sup> and NO<sub>2</sub><sup>-</sup> depletion and fed as necessary. Cells were harvested after reaching an OD<sub>600</sub> in the range of 6-6.5 by centrifuging the culture in a centrifuge at 17,000 x g at 4 °C for 40 min. After discarding the supernatant containing growth medium the sedimented cells were frozen in liquid nitrogen and stored at -80 °C.

The generation time was calculated based on OD<sub>600</sub> measurements. The dependence of OD<sub>600</sub> on the time of fermentation was plotted for the logarithmic phase, fitted with an exponential curve and generation time was calculated from fitted parameters. For example, for the growth curve shown in **Figure 34** the fit parameters and calculation of doubling time (T<sub>d</sub>) are shown in **Table 3**.

**Table 3.** Parameters of fit of OD<sub>600</sub> dependence on time of fermentation for data from Figure 34.

Model	Exponential
Equation	$y = y_0 \cdot \exp(\mu \cdot x)$
A	0.3586 ± 0.0532
μ	0.0326 ± 0.0017
Reduced Chi-Sqr	0.0055
R-Square (COD)	0.9985
Adj. R-Square	0.9981
T <sub>d</sub> = ln(2)/ μ (h)	21.66

### 1.1.2. Multi-step purification of native AOR from *A. aromaticum* SR7Δpdh by FPLC chromatography.

Frozen cells were thawed anaerobically in the 1: 1 (w:v) ratio of wet cell weight to buffer A (20 mM 2-bis(2-hydroxyethyl)amino-2-(hydroxymethyl)-1,3-propanediol-HCl buffer (Bis-Tris/HCl), pH 6.2, 10% glycerol) containing 0.05 mg/mL DNase I. The bacteria were homogenized by processing them three times with a French press (137 MPa, 4° C). The solution was then subjected to ultra-centrifugation (1 h, 100,000 x g, 4°C) to separate the soluble and membrane fraction. The supernatant from centrifugation, i.e. cell extract, was filtered through a 0.45 μm filter before being applied to the chromatographic column. In the first step, the extract was enriched on a 56 mL Q-Sepharose Fast Flow (XK 26/12 column) preparative column equilibrated with 3 column volumes (CV) of buffer A. The AOR was eluted in a step gradient mode with buffer B (120 mM Bis-Tris/HCl buffer, pH 6.2, 1 M NaCl), started with loading and wash of column (1 CV) with 0 % buffer B, step

gradient to 24% buffer B (for 0.5 CV) and hold for 1 CV when a pool of proteins without AOR activity was eluted, next a step gradient to 33% buffer B (for 3 CV) AOR protein fraction eluted and gradient to 100% buffer B (in 0.5 column volume) to elute residual proteins. The active protein fractions (as tested by UV-vis activity assay with benzaldehyde activity assay from Chapter 3.5.1.) were pooled and desalted using GE-Healthcare HiPres (26/10) column and resuspended in buffer C (5 mM MES/NaOH buffer, pH 6.9, 2 mM CaCl<sub>2</sub>). In the second step, active fractions were separated on a ceramic hydroxyapatite type I column (CV=25 mL, CHT-I, Bio-Rad) equilibrated with 2 volumes of buffer C. After loading the column with desalted pool from the previous step, the column was washed for 1 CV with buffer C and the active fraction was eluted with a step gradient between buffer C and buffer D (5 mM MES buffer, 400 mM potassium phosphate buffer pH 6.8) to a phosphate concentration of 15 mM (gradient for 0.5 CV to 4% buffer D). The collected fractions were concentrated by ultrafiltration on a 30 kDa membrane (Amicon Ultra-15 Centrifugal Filter Units) to a total volume of protein less than 3 mL, which was applied on size exclusion Superdex 200 (120 mL CV (16/60)) column equilibrated with 2 CV volumes of buffer E (100 mM 2-Amino-2-(hydroxymethyl)propane-1,3-diol hydrochloride buffer (Tris/HCl), pH 8.0, 150 mM NaCl). The active protein fractions were collected from the peak at 55 mL, concentrated according to the above method if necessary, aliquoted, frozen in liquid nitrogen and stored at -80°C. All buffers (A-E) contained 10% glycerol as a protein-protecting agent.

## **1.2. Heterologous expression of AOR in *A. evansii***

During the research described in this thesis, a novel expression system was developed by the group of prof. Heider from Marburg University. As the new expression system enabled faster and more efficient production of AOR protein pools of high purity, this method was used as soon as it was available for the research in this work.

### **1.2.1. AOR-coding plasmid construction**

The plasmid and expression strain were prepared by the group of prof. Heider from Marburg University. The genes encoding the AOR protein from *A. aromaticum* (gens EB\_RS13980-14000) were amplified via PCR from chromosomal DNA using the forward 5'AAGCTCTTCAATGTGGAATCGCTTCACATTGACCC3' and reverse primers 5'AAGCTCTTCACCCATTGCTTGCTGCGCTCGTCTG3' and Phusion™ High-Fidelity DNA-Polymerase (Thermo Fisher Scientific, Waltham, USA) according to manufacturer's protocol with minor adaptations.

The amplified DNA fragment was ligated into pEntry via a simultaneous restriction/ligation reaction according to the instructions of the StarGate® cloning system

(IBA Lifesciences, Göttingen, Germany). The sequences of the genes were validated by Sanger sequencing. The obtained plasmid was used in a second restriction/ligation reaction to transfer the genes into the expression vector pASG105\_mob\_ori(-)<sup>120</sup>. The reaction was heat-inactivated (65°C, 20 min) and 0.5 mM ATP and 1 U T4 ligase (Thermo Fisher Scientific, Waltham, USA) were added and the reaction was incubated further for 1 h at room temperature to enhance ligation. The obtained plasmids were transformed into a conjugation strain of *Escherichia coli* (WM3064<sup>121</sup>).

The final plasmid used (pASG\_105\_AOR\_full) was encoding the N-terminally Twin-Strep-tagged<sup>®</sup> AorA (EB\_RS13980), AorB (EB\_RS13985), and AorC (EB\_RS13990) subunits of AOR, as well as the AorD (EB\_RS13995) and AorE (EB\_RS14000) proteins, and the ampicillin resistance gene. The plasmid was then transferred from the donor *E. coli* strain to *A. evansii* by conjugation. The Twin-Strep-tag<sup>®</sup> sequence fused to AorA did not interfere with the activity of the enzyme and allowed fast purification by affinity chromatography. The molecular mass of Twin-Strep-tag<sup>®</sup> sequence is 2.9 kDa and increased the mass of the AorA subunit correspondingly.

### 1.2.2. Fermentation of *A.evansii*.

The bacteria were grown anaerobically on a potassium phosphate-buffered minimal medium of content shown in **Table 4**, supplemented per 1 L of medium with 10 mL of Vitamin Solution, 20 mL Trace Elements Solution, 1 mL W-Se Solution (**Table 1.**), 25 mL of 1.2 M potassium phosphate buffer and 100 ng /L ampicillin. The only carbon source was benzoate, whereas sodium nitrate was an electron acceptor in an anaerobic environment. The cultivation of bacteria was handled as for *A. aromaticum* SR7 $\Delta$ *pdh*, but with the feeding of benzoate (as carbon source, instead of phenylalanine) to 4 mM in medium and potassium nitrate to 10 mM in the medium.

**Table 4** Content of mineral base for minimal media used for the growth of *A.evansii*.

Minimal media	
Ingredients	Amount (mg/L)
NH <sub>4</sub> Cl	530
MgSO <sub>4</sub> x 7 H <sub>2</sub> O	200
CaCl <sub>2</sub> x 2 H <sub>2</sub> O	25
KNO <sub>3</sub>	1000
sodium benzoate	500

The large-scale preparative cultivation was conducted in a 30-litre fermentor [Sartorius] in ICSC PAS, Kraków, according to the protocol described in Chapter 1.1.1, additionally

equipped with a RedOx electrode, with the pH established at 7.7. The fermentation was started by the addition of 1 L inoculum of OD<sub>600</sub> of 0.7 to the final 30 L of the medium. The bacteria were cultivated until OD<sub>600</sub> was in the range of 0.5-0.7, then the temperature was lowered to 18°C and the enzyme overexpression was induced by the addition of anhydrotetracycline to a final concentration of 200 ng/mL in the culture medium. Additionally, Na<sub>2</sub>WO<sub>4</sub> was supplemented to a final concentration of 10 µM. After 20 h of culture, cells were separated from the culture medium by centrifugation at 4500 x g (Hermle Z36HK, 1 h, 4 °C). The supernatant was discarded and sedimented cells were frozen and stored at -80 °C.

### **1.3. Heterologous expression of BaDH in *E. coli***

The plasmid and expression strain were prepared by the group of prof. Heider from Marburg University. The *bdh* gene of *A. aromaticum* strain EbN1 (ebA3166; Rabus et al. 2005) was amplified via PCR from chromosomal DNA using the forward 5'-AAGCTCTTCAATGAAGATTCAAGCCGCAGTAAC-3' and reverse 5'-AAGCTCTTACCCGGCGAGCCTAGGACCGGC-3' primers. The PCR product was cloned into the pASG-IBA103 vector (IBA Lifesciences, Göttingen, Germany) following the manufacturer's instructions. The resulting plasmid codes for a fusion protein of BADH with a C-terminal Twin-Strep-tag®. The plasmid was inserted into *E. coli* BL21(DE3) by transformation. The bacteria were then grown aerobically in 1-L cultures on an LB medium supplemented with 2 % (v/v) ethanol at 37 °C with shaking. Once the culture reached OD<sub>600</sub> of 0.5-0.7, the temperature was lowered to 20 °C and anhydrotetracycline (200 ng/mL) was added to induce protein expression. After 20 h since induction, cells were harvested by centrifugation at 17,000 g and 4 °C for 30 min. The sedimented cells were frozen and stored at -80 °C. BADH activity was exclusively observed in the soluble fraction. The enzyme was later purified by affinity chromatography (as shown in Chapter 1.4.).

### **1.4. Purification of recombinant AOR by affinity chromatography**

Frozen cells of *A. evansii* containing recombinant AOR were thawed anaerobically in the 1: 1 (w:v) ratio of wet cell weight to buffer E (100 mM Tris/HCl, pH 8.0, 150 mM NaCl) containing 0.05 mg/mL DNase I. The cell suspension was then lysed by sonication (Sonics Vibra-Cell VCX500, intermittent cycle, 5 min, amplitude 40%, energy 150,000 J) and centrifuged (1 h, 100,000 x g, 4 °C) to separate the cell debris and insoluble proteins. The supernatant was filtered through a 0.45 µm filter and applied to the Strep-tag® II column (5 mL IBA GmbH), and after rinsing with buffer E. After washing with 5 CV at a flow rate of 1 mL/min of buffer E, the enzyme was eluted with buffer E enriched with 5 mM desthiobiotin. The eluted enzyme was either aliquoted, frozen in liquid nitrogen

and stored at -80 °C (for activity tests) or, if high purity was essential (structural studies), applied to the next column. If the latter was applicable, the 3 mL concentrated (by ultrafiltration on a 30 kDa membrane) pool of eluate from the Strep-tag® II column was applied on the size exclusion Superdex 200 column (120 mL column (16/60)) equilibrated with 2 CV of buffer F (100 mM 4-(2-hydroxyethyl)-1-piperazineethanesulfonic acid sodium hydroxide buffer (HEPES/NaOH), pH 7.5, 150 mM NaCl, 10% glycerol) at a flow rate of 1 mL/min. The AOR fraction eluted as a wide peak at 55 mL.

## **2. Enzyme characterisation.**

The enzyme preparation obtained by the above methods was routinely characterized by establishing the protein concentration by the Bradford method, content analysis by SDS-PAGE, and activity test according to the method shown in Chapter 3.5.1.

### **2.1. Determination of protein concentration with the Bradford method**

The protein concentration in fractions from purification was established with the Bradford method<sup>122</sup>, which utilizes a change in the UV-vis spectrum of the Coomassie Brilliant Blue G-250 dye upon binding to a protein<sup>122</sup>. For calibration, a Bovine Serum Albumin standard solution (BSA, 2 mg/mL, Sigma Aldrich, Saint Louis, USA) was diluted with LC-MS grade water to 20 µg/mL, 40 µg/mL, 60 µg/mL, 80 µg/mL and 100 µg/mL. The protein samples were also diluted to fit the calibration range. A 20 µL of each analyte in 2 repetitions was mixed with 200 µL of Bradford Reagent (Sigma Aldrich, Saint Louis, USA) and incubated at room temperature for 5 min. The absorbance at 595 nm was measured with a microplate reader (EPOCH, BioTek Instruments, Inc, VT, USA) and the sample concentration was calculated from the slope of linear calibration of BSA (as a plot of absorbance vs protein concentration). The error of the estimate was calculated from the errors of linear regression of the calibration curve.

### **2.2. SDS polyacrylamide gel electrophoresis**

The analysis of proteinous sample purity was conducted based on mass separation using sodium dodecyl sulfate-polyacrylamide gel electrophoresis (SDS-PAGE)<sup>123</sup>. In this method, proteins were denatured by SDS and 2-mercaptoethanol (from Laemmli loading buffer), with the former binding to the unfolded macromolecule giving them a negative charge. The sample was subjected to an electric field which induced protein movement through the polyacrylamide gel (7% polyacrylamide in 380 mM Tris/HCl pH 8.8). The samples were examined simultaneously with a prestained protein standard mix (PageRuler™ Plus Prestained Protein Ladder) to enable mass identification. The separation took place for 10 min at 120 V, then at 160 V until the bromophenol from the

loading buffer reached the end of the gel. Finally, the proteins separated in the gel were stained by binding Coomassie Brilliant Blue R-250 dye and the unspecifically bound dye was removed by overnight incubation in water.

### **2.3. Proteomic analysis**

The content of proteins in the 1D SDS-PAGE gel was assayed by a proteomic analysis conducted with AmaZon ETD (Bruker Daltonik) MS/MS by dr Przemysław Mielczarek in the Biochemistry and Neurobiology Department of AGH University.

The selected bands from the SDS-PAGE gel, prepared according to Chapter 2.2., were excised and proteins in retrieved samples were destained by rehydration with 100 mM  $\text{NH}_4\text{HCO}_3$  and subsequent incubation in tubes with acetonitrile added to 50% (v/v) concentration. After 20 min incubation, the destaining solution was removed and gel stripes were dehydrated with acetonitrile and dried in a vacuum. Next, the proteins were reduced by incubation of gels with 10 mM DTT/100 mM  $\text{NH}_4\text{HCO}_3$  for 60 min at 60°C and after discarding the liquid, the proteins were alkylated by soaking in 55 mM iodoacetamide/100 mM  $\text{NH}_4\text{HCO}_3$  solution during 45 min incubation at room temperature in the dark. The gel was then washed with 100 mM  $\text{NH}_4\text{HCO}_3$  vortexing for 15 min, dehydrated with acetonitrile and dried. In the next step the in-gel digestion was started with the reswelling of gel stripes in a solution of 12.5  $\mu\text{g}/\text{mL}$  of trypsin (Trypsin Gold from Promega) in 50 mM  $\text{NH}_4\text{HCO}_3$  for 20 min at 4 °C. Next, for extraction of peptides the solution was exchanged to 50 mM  $\text{NH}_4\text{HCO}_3$  and incubated overnight at 37 °C. The overnight solution was collected and extraction was carried on with successive solutions: i) 50 mM  $\text{NH}_4\text{HCO}_3$  (15 min at 37 °C, shaking every 5 min); ii) 5% HCOOH in  $\text{H}_2\text{O}/\text{acetonitrile}$  (1:1 v/v) (30 min 30 °C); iii) ultrasonication for 30 min in solution as in ii). The collected solutions contained protein fragments and were vacuum-dried and resuspended in water with 0.1% HCOOH.

Protein digests extracted from the gel were separated and examined by nanochromatography combined with tandem mass spectrometry analysis (nanoLC-MS/MS, Proxeon system run by Hystar software, Bruker Daltonics) with a PepMap column (15 cm x 75  $\mu\text{m}$  ID, C18, 3  $\mu\text{m}$  particle size, 100 Å pore size, Thermo-Scientific). The gradient was formed using  $\text{H}_2\text{O}$  with 0.1% HCOOH (A) and ACN with 0.1% HCOOH (B) at a flow rate of 300 nL/min. A gradient was formed from 2 to 35% B at 50 min and up to 90% B at 55 min and then kept until 65 min at 90% B. Fractions eluted from the column were directly deposited with an  $\alpha$ -cyano-4-hydroxycinnamic acid matrix on a MALDI target plate by a Proteineer fc II sample collector (Bruker Daltonics). Fifteen-second fractions were collected, 96 fractions for one sample, and spotted on 384 MALDI

target plate. The mass spectrometry analyzes were performed on ultrafleXtreme (Bruker Daltonics) in positive ion mode. The resulting peak lists was searched against the NCBIInr database using ProteinsScape 3.0 (Bruker).

## **2.4. Thermostability assay**

The enzyme thermostability in the function of pH and buffer content was investigated using the *ThermoFAD* method. This method is a variation of Differential Scanning Fluorimetry method, which exploits fluorescence of flavin cofactor. The principle of this approach is the determination of protein unfolding (here called melting) temperature by monitoring changes in fluorescence signal upon the release of FAD cofactor from AorC<sup>124</sup>. The standard plot of the fluorescence intensity against temperature (thermogram) obtained in such an experiment is a sigmoidal curve and the melting temperature is calculated as the maximum of the first derivative of the curve<sup>125</sup>.

The assay was performed using 2  $\mu$ L of the purified and concentrated enzyme (final concentration in assay 2 mg/mL) and 23  $\mu$ L of the following buffers: 50 mM citrate/Na<sub>2</sub>HPO<sub>4</sub> buffer (pH 4.6–7.0) or HEPES/NaOH, 3-[N-Tris(hydroxymethyl)methylamino]-2-hydroxypropanesulfonic acid sodium hydroxide buffer (TAPSO/NaOH) and Tris/HCl (pH 7.0–8.5). The thermal denaturation curves were collected on Bio-Rad CFX Connect RT PCR by measuring the fluorescence intensities on the FRET channel (450 to 490 nm) and the FAD fluorescence was monitored at 470 nm. The fluorescence emission was followed at the temperature range from 4 °C to 95 °C with a step of 1 °C and 15 s hold before reading. All buffers were tested in the above method at least three times, and the values of melting temperatures ( $T_m$ ) were calculated as the mean values determined from the maximum of the derivatives of the experimental data, shown with the standard error of the mean.

## **3. Catalytic tests**

### **3.1. Preparation of chemicals**

All buffers used in anaerobic tests were anaerobized by contact with subsequent overpressure of nitrogen and vacuum generated by pump (3 min for each step, repetitions dependent on the volume of liquid, i.e. 1 L processed for 4 cycles). This procedure was conducted by locking the buffers in bottles with rubber stoppers and accessing the inner atmosphere with needles. All liquids in anaerobic tests were handled either in a glovebox or with Hamilton gastight syringes.

All buffers used for reaction with H<sub>2</sub> were stored in contact with a gas mixture of 2.5/97.5% H<sub>2</sub>/N<sub>2</sub> (v/v) (if not stated otherwise), for >1 h to ensure proper equilibration and solvation of gas in the liquid phase. For reactions with different gas compositions (D<sub>2</sub>,

different concentrations of H<sub>2</sub>, CO, pure N<sub>2</sub>) the reaction buffer (if possible, containing all reagents that do not initiate the reaction, i.e. without enzymes) was closed in a stoppered vial and the container was flushed by the gas premix for at least 30 seconds. Next, the equilibration was allowed for at least 15 minutes and flushing was repeated.

The carboxylic acids used as substrates in this study were neutralized by an equimolar amount of NaOH, which resulted in stock solutions of sodium salts at concentrations in the range of 0.2-0.5 M. The aldehyde, NADH, NADPH and dithionite stocks used for catalytic tests were prepared daily from pure substances.

Catalytic experiments were conducted with two types of AOR<sub>Aa</sub> batch, thus to standardize the results, the activities of enzyme aliquot were measured:

- An enzyme produced in *A.aromaticum* SR7 $\Delta$ *pdh*, purified by three-step purification of average activity with 1 mM benzaldehyde and 1.6 mM BV<sup>2+</sup> 23.6 U/mg enzyme or with NAD<sup>+</sup> 8.0 U/mg of enzyme, called shortly 'natively expressed AOR<sub>Aa</sub>';
- A recombinantly expressed (in *A.evansii*) enzyme, purified in single-step protocol on a Strep-tag column, of average activity with 1 mM benzaldehyde and 1.6 mM BV<sup>2+</sup> 85.0 U/mg enzyme or with NAD<sup>+</sup> 31.7 U/mg, called shortly 'recombinant AOR<sub>Aa</sub>'.

## 3.2. Chromatographic analysis of aldehydes and alcohols

### 3.2.1. Reversed-phase chromatography and DAD detectors

The detection and quantitation of benzaldehyde, benzyl alcohol and (*R*)-1-phenylethanol was conducted by the High-Performance Liquid Chromatography (HPLC) coupled with a diode array detector (DAD) method.

The HPLC-DAD is a convenient technique in the detection and quantitation of chemicals that absorb light within ultraviolet (UV) and visible (vis) regions of the spectrum in the 190 – 900 nm wavelength range. The DAD enables a fast screening of the peak purity of the target compound by analysing the full spectrum of a peak at one time. This helped during the quantitation of the target chemical to exclude the contribution of co-eluting substances to the measured signal.

In this study, samples consisted of a polar matrix (aqueous buffers, organic salts) and the compounds of interest (benzaldehyde, benzyl alcohol and (*R*)-1-phenylethanol), which were moderately polar chemicals. For such samples, the reversed-phase HPLC was chosen to be the appropriate mode of separation on the chromatographic column.



Aldehydes were detected without a previous step of derivatization, which for these compounds is usually applied in analytical chemistry<sup>76,126,127</sup>. The initial tests of derivatization of aldehydes with 3-nitrophenylhydrazine and cysteine did not give reproducible results for low concentrations of aldehydes and showed that this method is incompatible with the samples matrix (i.e. protein-derived small molecules were also derivatized and coeluted with derivatized aldehyde).

As a general approach, the samples (50-200  $\mu\text{L}$ ) were taken from aqueous reaction mixtures and pipetted into 1.5 ml sample tubes containing the appropriate amount of acetonitrile to precipitate the enzyme (at least 30% of organic phase for AOR-containing mixtures and 50% for *R*-HPED). The samples were centrifuged (4 min, 8000  $\times g$ ) to separate the soluble analytes from the precipitated enzyme and any solid contamination. Multiple samples were taken during the reactor run, with two samples always taken at the same time. Each sample was analyzed by HPLC-DAD with 3 subsequent injections. Concentrations were calculated as an arithmetic average of 3 injections using external standard calibration method.

### 3.2.2. Method for benzaldehyde quantitative analysis

The method was established to detect benzaldehyde in samples from reaction mixtures, where titanium or europium complexes and relatively high concentrations of benzoate ions were also present. Titanium (III) and europium (II) complexes were used as electron donors in catalytic tests and are strong reducing agents. In assays, those complexes were used in stoichiometric surplus, in concentrations of 3 mM, and thus millimolar amounts of the remaining reducing agent could still be present in samples prepared for benzaldehyde quantitation by the HPLC method. The impact of the reducing agent on the column bed is unknown and a change in the backpressure of the column was observed when analysing the samples. Therefore, these samples could not have been analyzed on the UHPLC column.

The samples (30  $\mu\text{L}$  injection) were analyzed on Agilent 1100 HPLC using the LUNA<sup>®</sup> 3u C8 column (100  $\text{\AA}$ , 150  $\times$  4.6 mm, 3  $\mu\text{m}$  bead size, Phenomenex, USA) equilibrated at 40  $^{\circ}\text{C}$  at the 0.75 mL/min flow rate in the isocratic mode with  $\text{H}_2\text{O}/\text{ACN}$  65/45 (v/v) mobile phase. The quantitative analysis was conducted at 245 nm using a DAD detector. The chromatographic method allowed for the separation of benzaldehyde and quantitation according to the calibration shown in **Figure 15**.

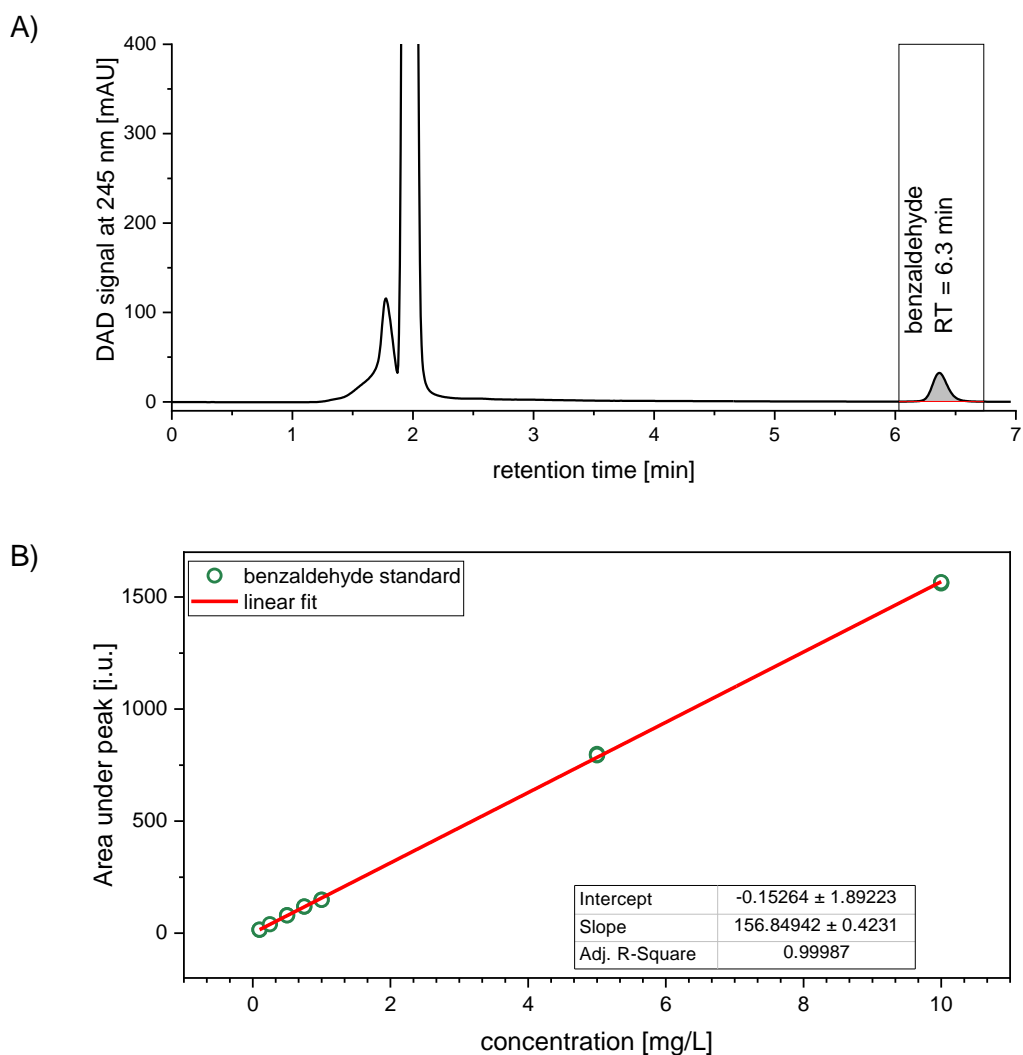


**Figure 15. A)** Chromatogram of the reaction mixture at 245 nm collected according to the method on a DAD detector, peak with a retention time of 6.3 min corresponds to benzaldehyde, and 2.1 min to benzoic acid; **B)** Calibration curve for quantitation of benzaldehyde.

### 3.2.3. Method for benzyl alcohol and benzaldehyde quantitative analysis

An UHPLC method with DAD detection was established to quantitate both benzyl alcohol and benzaldehyde in samples from reaction mixtures. The samples were characterized by a relatively high concentration of benzoic acid (30 mM) and presence of 1 mM  $\text{NAD}^+$ .

The 2  $\mu\text{L}$  of samples were analyzed with Agilent 1260 UHPLC equipped with DAD using the ZORBAX 300 SB-C18 column (RRHD, 2.1x50mm, 1.8  $\mu\text{m}$ , Agilent, USA) at 30  $^{\circ}\text{C}$  and 0.2 mL/min flow rate in the isocratic mode 70/30  $\text{H}_2\text{O}/\text{ACN}$  with a 0.1% formic acid mobile phase. Each sample was analyzed in triplicate. The benzyl alcohol was monitored at 210 nm (retention time (RT): 1.7 min) while benzaldehyde at 250 nm (RT: 3.4 min) as

shown in **Figure 17**. The quantitation of both compounds was conducted based on the external standard calibration curves (**Figure 16**). The limit of detection (LOD) and limit of quantitation (LOQ) were calculated based on the standard deviation of response and slope of the calibration. LOD and LOQ for the method for benzaldehyde quantitation were 4 and 13  $\mu\text{g/L}$ , respectively, and for benzyl alcohol 5 and 15  $\mu\text{g/L}$  (in sample), respectively.

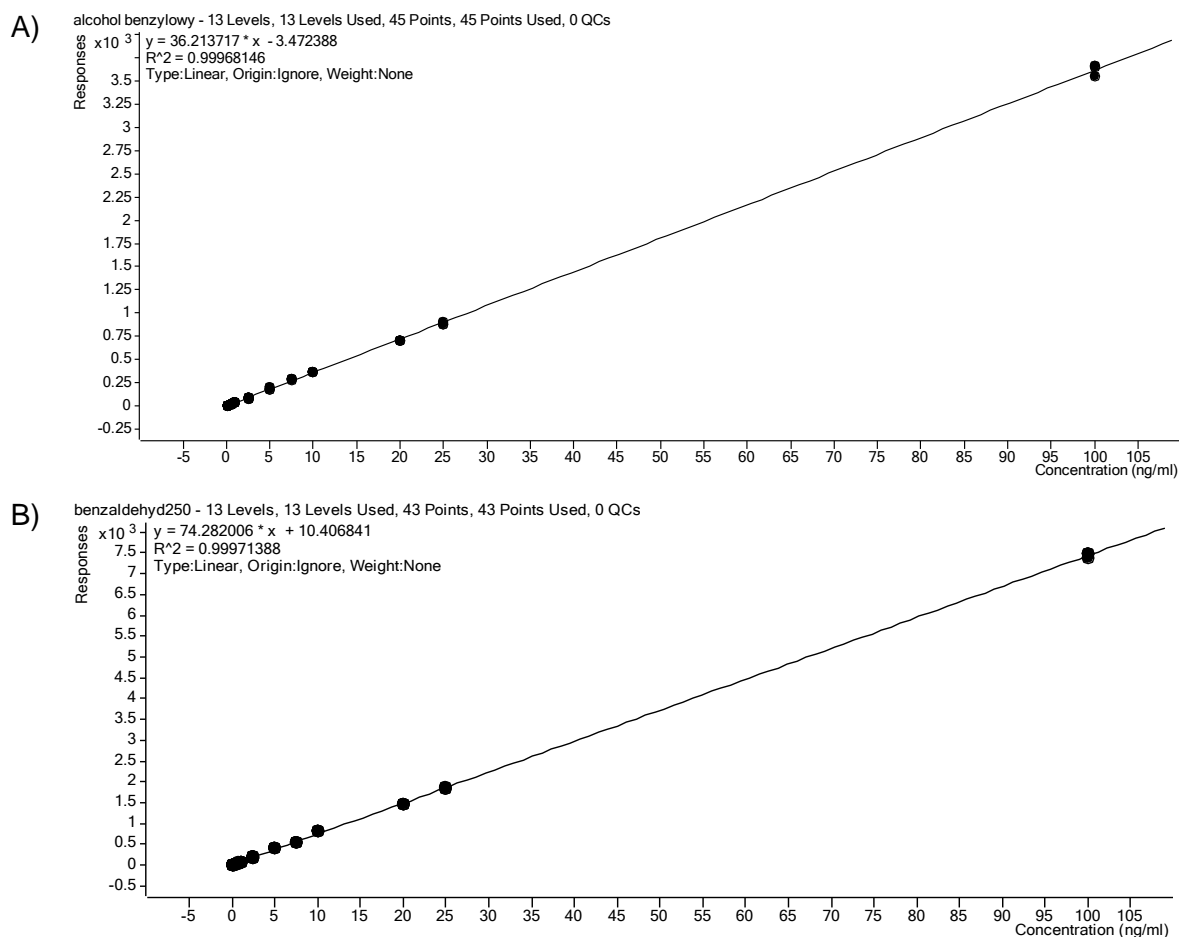


**Figure 16.** DAD calibration curves **A)** for benzyl alcohol quantitation, **B)** for benzaldehyde quantitation on the UHPLC method. Values of concentration are in ng/mL. Each concentration point was measured in triplicate.

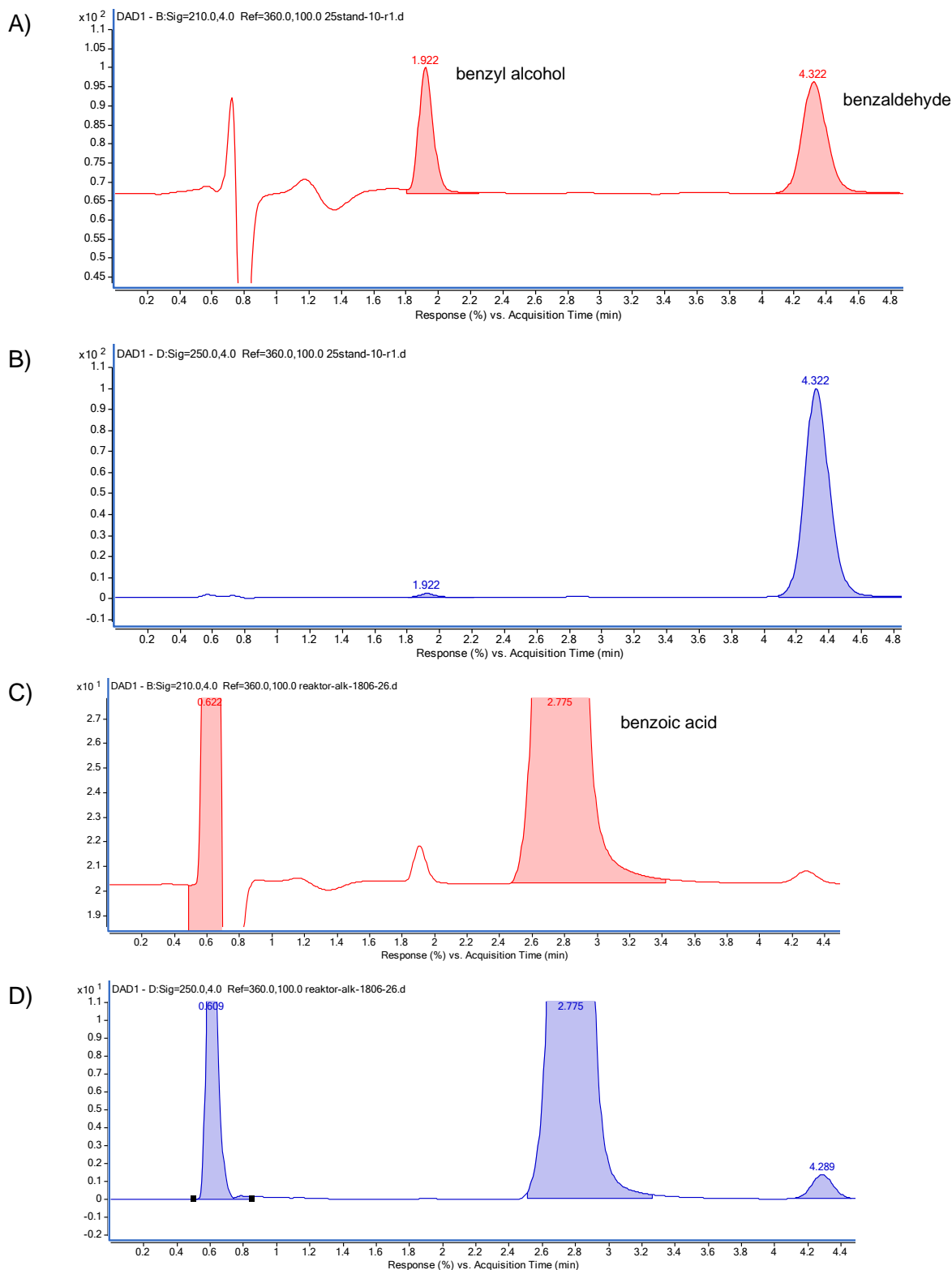


**Figure 17.** Chromatogram of **A)** benzyl alcohol (RT:1.9 min) and benzaldehyde (RT: 4.3 min) standards at 210 nm, peak at retention time 0.6 min corresponds to dead time of the system; **B)** both standards at 250 nm; an example of reaction mixture chromatogram **C)** at 210 nm, peak at RT 1.7 min - benzyl alcohol, RT 2.8 min - benzoic acid; **D)** reaction mixture at 250 nm.

### 3.2.4. Method for (*R*)-1-phenylethanol quantitative analysis

The method was used to detect (*R*)-1-phenylethanol in samples from reactors with present oxidized and reduced NAD, where acetophenone is a substrate. (*R*)-1-phenylethanol concentrations were determined using HPLC Agilent 1100 system equipped with a DAD detector.

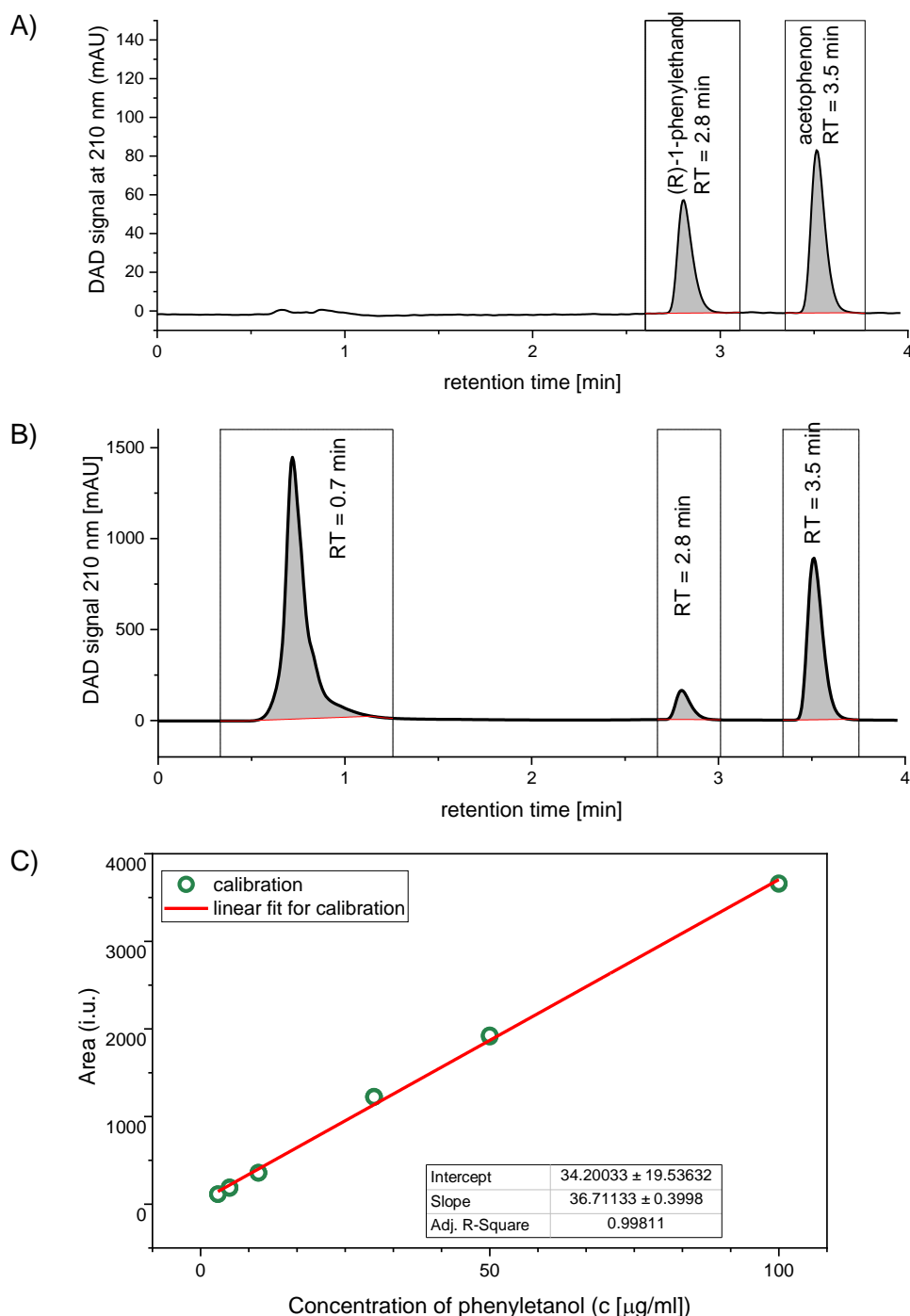


**Figure 18.** Chromatogram of DAD signal at 210 nm of: **A)** standards of (*R*)-1-phenylethanol (RT: 2.8 min) and acetophenone (RT: 3.5 min); **B)** reaction mixture containing NAD<sup>+</sup> and NADH (both visible in the peak of RT: 0.7 min) acetophenone as a

substrate (RT: 3.5 min) and (*R*)-1-phenylethanol as a product; **C**) calibration for (*R*)-1-phenylethanol, fit of a linear function (red line), all points collected in triplicate.

The separations were performed on the Ascentic RP-Amide Express column (75 mm × 4.6 mm, 2.7 μm) at 40 °C mobile phase in the program (A-H<sub>2</sub>O, B-CH<sub>3</sub>CN): 0-0.5 min 20% (v/v) B, 0.5 to 0.8 min gradient to 35% B, 0.8 to 4.2 min isocratic 35%, the flow rate of 1 mL/min and injection volumes of 20 μL. The quantitation of substrate was conducted at 210 nm against external standard calibration (**Figure 18**). The LOD and LOQ for this method were calculated to be 1.75 and 5.32 μg/mL, respectively.

### 3.3. UHPLC-MS/MS analysis of aldehydes

The identification of aldehydes in Ultra High-Performance Liquid Chromatography coupled to tandem mass spectrometry (UHPLC-MS/MS) was used for the quantitation of 4-hydroxybenzaldehyde and benzaldehyde in the initial stage of the project. Unfortunately, the method for simultaneous identification of benzaldehyde and benzyl alcohol in a mixture with benzoic acid in this system was not possible to obtain (choice of solvent) and only detection by a DAD detector was available.

#### 3.3.1. Detection in a triple-quadrupole mass spectrometer

Detection of aldehydes in samples was conducted on Agilent triple-quadrupole mass spectrometer with electrospray ionisation (ESI). The quadrupole mass analyzers consist of four parallel cylindrical metal electrodes that, by inducing oscillating electrical fields, selectively stabilize or destabilize ions, thus allowing to pass only ions with selected  $m/z$  (mass to charge) values. The triple-quadrupole mass spectrometer consists of linearly aligned two quadrupole analyzers and one hexapole in the middle, used as a collision cell. This alignment of analyzers enables the detection of ions formed during initial ionisation in the source (molecular ions, also called precursor ions if they undergo further fragmentation) and ions formed during induced fragmentation in collision cell (product ions). The set of quadrupoles can work in various modes. In simpler modes, only the second quadrupole scans all molecular ions or filters selected molecular ions (i.e. single ion monitoring mode), analogous to single quadrupole spectrometers. In the multiple reaction monitoring (MRM) mode, which was used during the quantitative analysis in this work, the first quadrupole filter the selected precursor ion. Next, the precursor ion enters the collision cell, where it undergoes collision-induced fragmentation by colliding with a neutral gas present in the cell (here, nitrogen gas). Precursor ion is fragmented into product ions. Next, product ions enter the third quadrupole, where selected ions are filtered and allowed to enter the detector. The quantitation of the analyte is based on the amount of product ion of the highest abundance (quantifier). In the MRM method, the

identity of the quantifier ion is assessed by monitoring a constant ratio to another product ion (qualifier) identified in a standard of an analyte.

### 3.3.2. Qualitative analysis of aldehydes

Benzaldehyde and 4-hydroxybenzaldehyde were detected using methanol as solvent and derivatizing agent.

The 4-hydroxybenzaldehyde forms a protonated molecule  $[M+H]^+$  (123 m/z) by the addition of a proton, an apparent form of the complex is shown in **Figure 19**. The  $[M+H]^+$  ion undergoes fragmentation in the collision cell to form product ions of 95 m/z (loss of CO molecule) and phenyl carbocation of 77 m/z (subsequent loss of water).

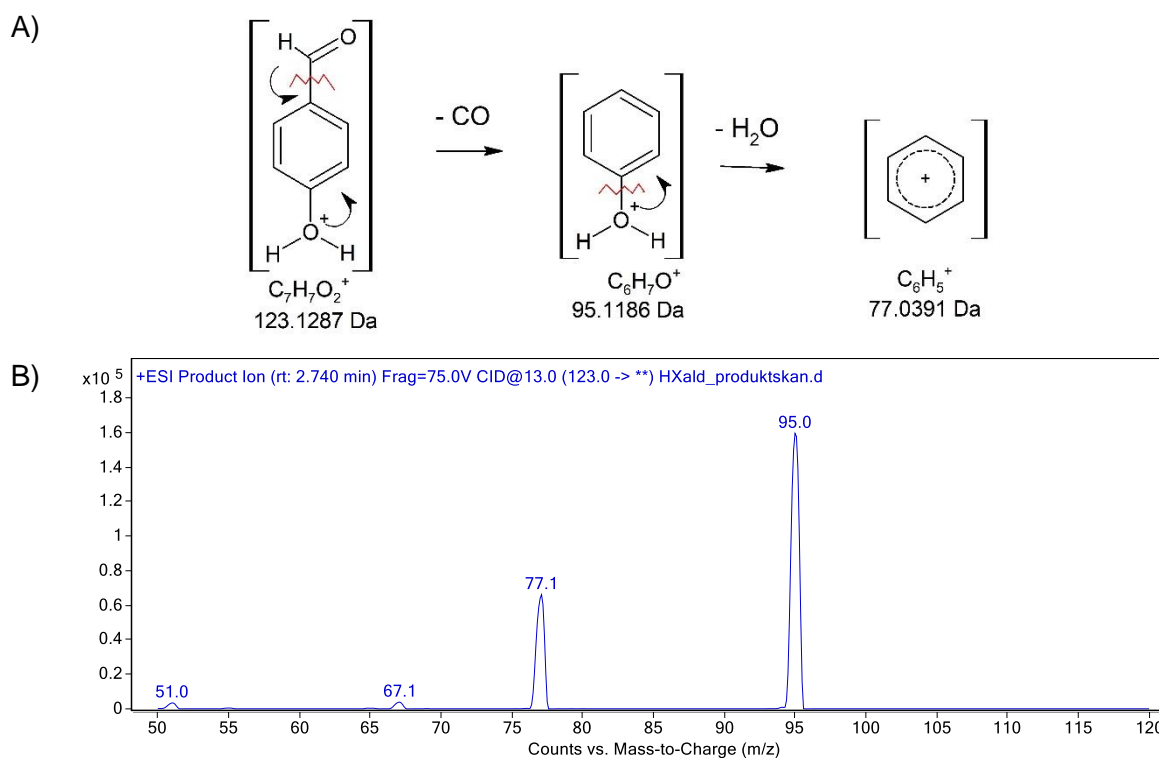


**Figure 19. A)** The apparent fragmentation pathway of 4-hydroxybenzaldehyde in the collision cell. **B)** MS/MS spectrum of Product ion scan (positive) for ion 123 m/z, the parent ion in fragmentation of 4-hydroxybenzaldehyde.

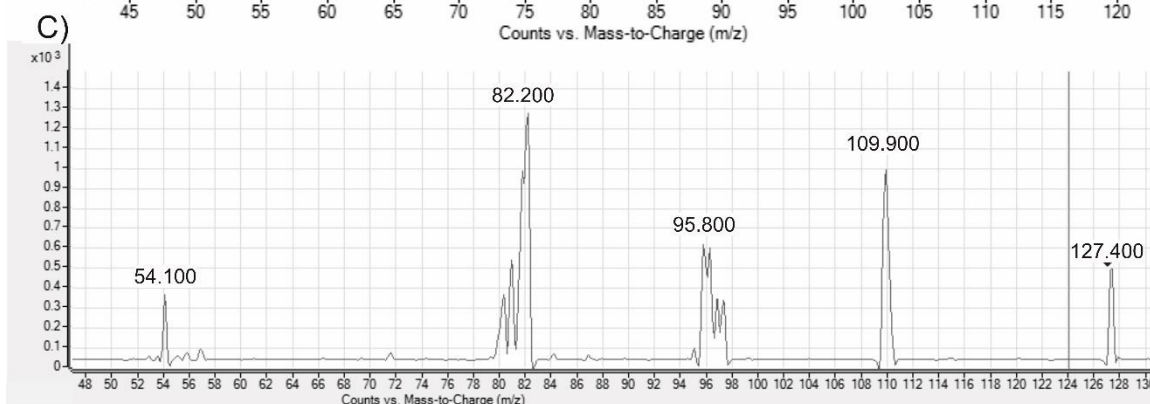
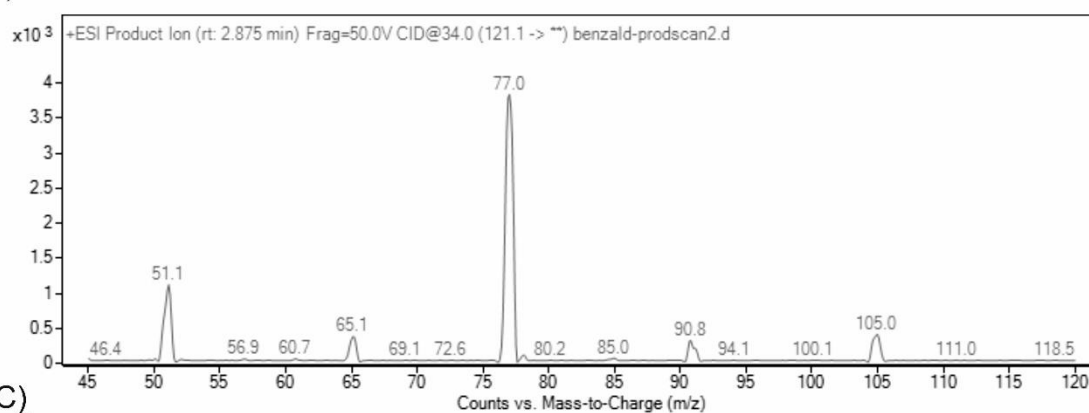
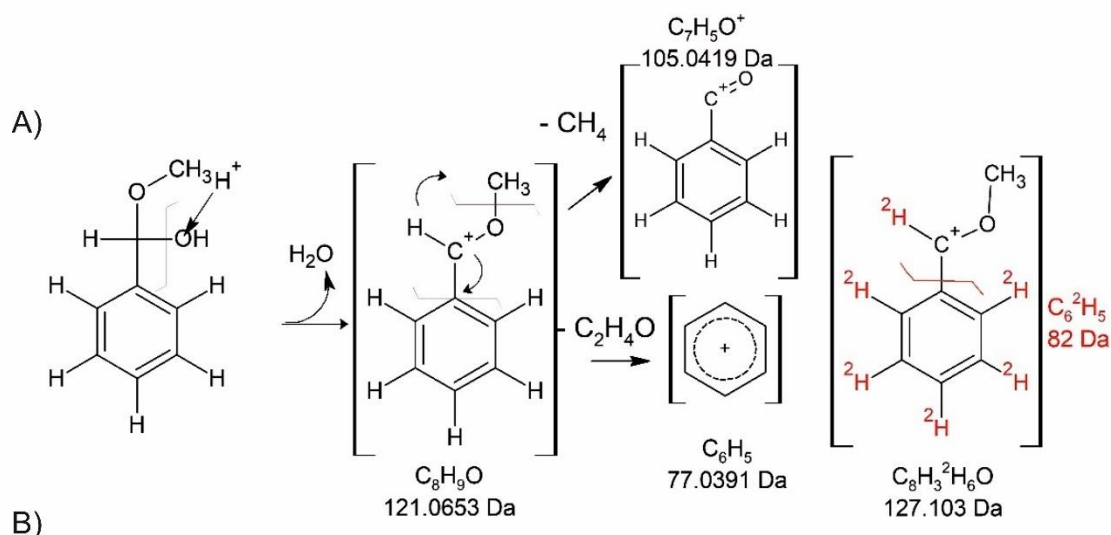


**Figure 20. A)** The apparent fragmentation pathway of benzaldehyde in the collision cell, the structure of deuterated  $d_6$ -benzaldehyde hemiacetal derived ion of  $m/z$  127. **B)** The MS spectrum of benzaldehyde standard acquired by MS/MS is product scan mode for benzaldehyde precursor ion 121.1  $m/z$ . **C)** The MS spectrum of the peak corresponding to  $d^6$ -benzaldehyde (MS/MS in scanning mode).

The benzaldehyde was detected as an ion derived from the hemiacetal formed by aldehyde with methanol (solvent present in the samples as well as in the mobile phase in chromatography). Benzaldehyde undergoes the addition of water and alcohols, although formed derivatives are not stable and cannot be easily isolated. Nevertheless, the rapid



desolvation in electrospray allows the identification of the hemiacetal-derived ions. The benzaldehyde (hemiacetal) of the MW of 138 g/mol upon protonation dehydrates in the ESI source and forms  $[M+H-H_2O]^+$  precursor ion identified at 121 m/z with the apparent structure shown in **Figure 20**. The 121 m/z ion further undergoes fragmentation in the collision cell into the phenyl carbocation (77 m/z) and aldehyde  $[M+H-H_2O-CH_4]^+$  ion (105 m/z). Taking into account the atypical ion formation, the identity of the ions was confirmed by analysis of deuterated  $d_6$ -benzaldehyde, which gave a precursor ion of 127 m/z heavier than in non-deuterated benzaldehyde, which corresponds to 6 deuterons substituting protons. As a result the product ions from 127 m/z were 5 Da heavier than the ions derived from protonated precursor ion, (82 m/z instead of 77 m/z and 110 m/z instead of 105 m/z). These differences in identified m/z values for benzaldehyde and deuterated benzaldehyde align with the masses of ions shown in **Figure 20**.

### 3.3.3. Quantitative analysis of aldehydes by multiple reaction monitoring

The MS MRM method of aldehydes detection and quantitation was established by optimization of source parameters to achieve the highest response for selected fragmentation reactions. The optimization and further analysis were performed for chosen UHPLC separation method. The samples and standards were analyzed by an Agilent 1260 UHPLC equipped with DAD using a ZORBAX 300 SB-C18 column working under parameters shown in **Table 5**. 4-hydroxybenzaldehyde was detected in method LC-MS/MS by a qualifier product ion (123.0  $\rightarrow$  77.1) and quantifier (123.0  $\rightarrow$  95). Benzaldehyde was detected by a qualifier product ion (121.1  $\rightarrow$  77.0) and quantifier (121.1  $\rightarrow$  105). The examples of chromatograms showing the detected products in samples from reaction mixtures are shown in **Figure 21**. The standards of deuterated and protonated benzaldehydes (**Figure 21.C**) elute at slightly different retention times, which is expected from weaker interactions of deuterium with column bed. The calibration curves for both aldehydes detection in this methods are shown in **Figure 21.B,D**. The reaction progress in the samples was stopped by the addition of 50 % of methanol to precipitate the enzyme. To separate the soluble analytes from the precipitated enzyme and any solid contamination samples were centrifuged (4 min, 8000 x g) and water was added to adjust methanol concentration to level in the mobile phase of UHPLC.

**Table 5.** UHPLC and MS/MS parameters of the method used for detection of 4-hydroxybenzaldehyde and benzaldehyde in the reaction mixtures.

HPLC method parameters	4-hydroxybenzaldehyde	benzaldehyde
Column temperature (°C)	30	40
Flow rate (mL/min)	0.2	0.4
Injection volume (μL)	5	5
Flow rate mode and mobile phase	isocratic 85/15 H <sub>2</sub> O/MetOH 0.1% formic acid	Isocratic 80/20 H <sub>2</sub> O/MetOH 0.1% formic acid
Elution time of the chemical of interest (min)	2.4	3.1
MS method parameter	4-hydroksybenzaldehyde	benzaldehyde
Ionization mode	AP-ESI, positive ions	AP-ESI, positive ions
Gas temperature (°C)	300	350
Gas flow (L/min)	11	6
Nebulizer pressure (°C)	25	45
Sheath gas temperature (°C)	300	400
Sheath gas flow (L/min)	10	10
Capillary voltage (V)	3000	3500
Nozzle voltage (V)	1000	500

**Table 6.** MS/MS MRM method parameters used for the detection of characteristic product ions while analyzing the presence of 4-hydroxybenzaldehyde or benzaldehyde in the reaction mixtures.

Detected chemical	Precursor ion (m/z)	Product ion (m/z)	Fragmentor (V)	Collision Energy (V)	Cell Accelerator Voltage (V)	Polarity
benzaldehyde	121.1	77.1	100	30	7	Positive
	121.1	105	100	22	7	Positive
4-hydroxy benzaldehyde	123	95	100	9	7	Positive
	123	77	100	21	7	Positive

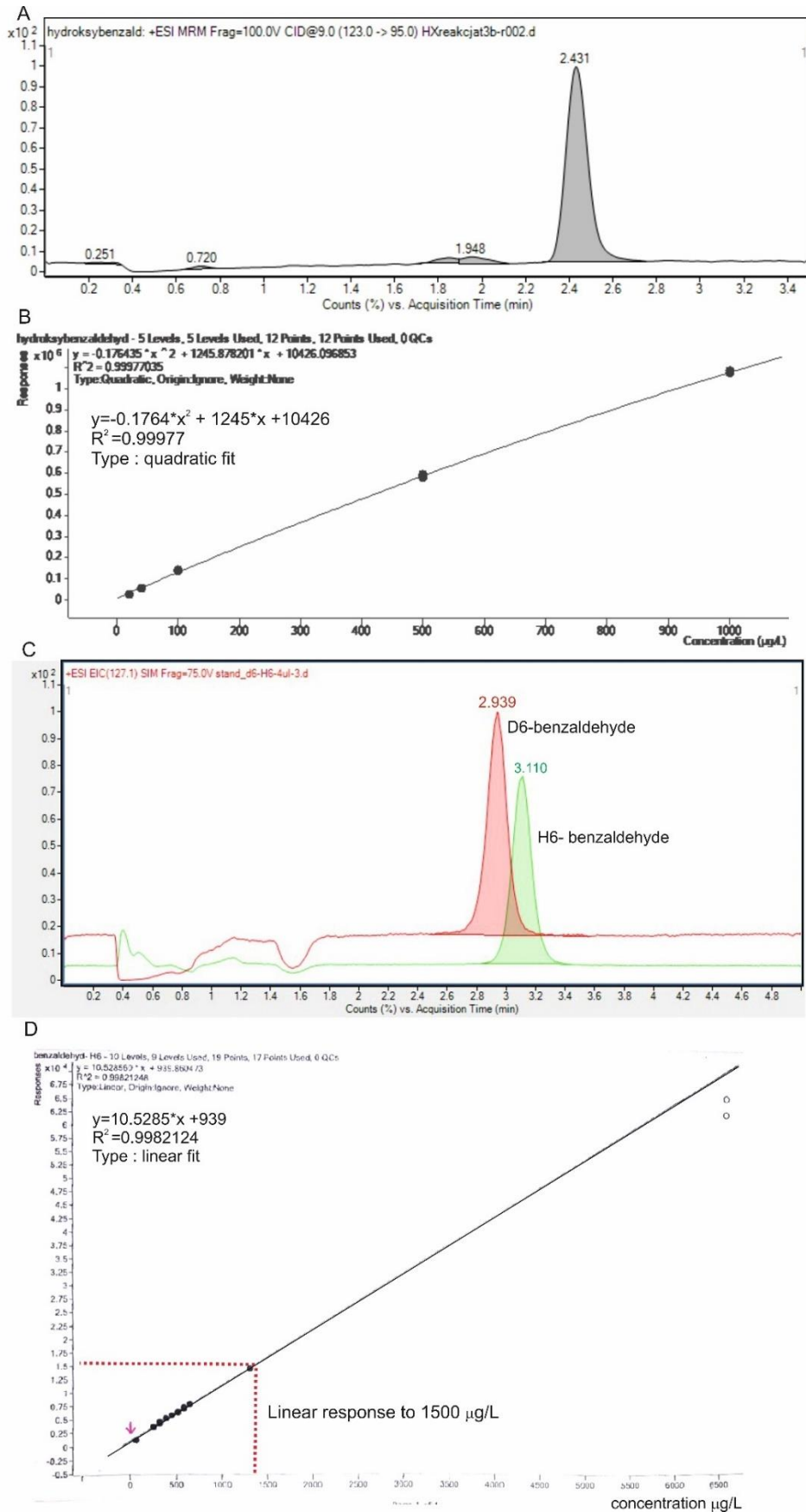


**Figure 21. A)** Chromatogram of the reaction mixture with shown quantifier transition (123 m/z -> 95.1 m/z) signal (percent of counts on the detector), peak at a retention time

of 2.4 min corresponds to 4-hydroxybenzaldehyde; **B)** Calibration curve for 4-hydroxybenzaldehyde; **C)** Chromatogram of standards of H6-benzaldehyde (signal shown is  $m/z$  121) and D<sub>6</sub>-benzaldehyde ( $m/z$  127); **D)** Calibration curve for benzaldehyde.

### **3.4. Gas chromatography with mass spectrometer detector (GC-MS) analysis of aldehyde products**

#### **3.4.1. Sample preparation by solid-phase extraction**

In a screening of AOR<sub>Aa</sub> substrate spectrum in acid reduction, a solid phase extraction (SPE) was used to concentrate and isolate the aldehyde products and exchange the matrix of the sample for one compatible with GC-MS columns (anhydrous, volatile solvent).

The reaction mixtures contained respective acid, buffer, aldehyde product and AOR enzyme and were stopped by the addition of 1 % (v/v) of 1M HCl water stock to precipitate the enzyme. The whole volume of the reaction was then centrifuged and neutralized with 20% ammonia water to pH 9. The substrates (acids) have pK<sub>a</sub> at 4-5; therefore, at pH 9.0, they occur almost only in the carboxylate ion form, which is very polar and do not bind to an SPE column. That approach ensured that the column capacity would not be reached after applying a reaction mixture containing millimolar amounts of carboxylic acid salts. The so-prepared samples were applied on the solid-phase extraction (SPE) column. In the case of the reactions with sodium benzoate, the optimization of the extraction method on a number of SPE columns showed the best recovery (40 %) for the Strata™-X 33µm Polymeric Reversed Phase 100 mg/3 mL columns (Phenomenex). The Reversed-Phase Speedisk™ Octadecyl (C18) 20 mg columns (Avantor™ BAKERBOND) were used for reaction mixtures containing phenylacetic acid, *trans*-cinnamic acid, octanoic acid, nicotinic acid, 4-hydroxybenzoic acid or pentanoic acid salts. The columns were conditioned and equilibrated with solvents, as shown in **Table 7**, and then samples were applied. All solutions were applied at a 2 mL/min flow rate maintained by vacuum in SPE Vacuum Manifold CHROMABOND®. The columns were washed (see **Table 7**) and dried for 30 seconds by the flow of air caused by the vacuum manifold. The analytes were eluted with methanol, and eluates were stored anaerobically at -80 °C until further examination.

**Table 7.** Steps of procedure for solid-phase extraction on SPE columns used in the study.

Step	Speedisk™ C18	Strata™-X
1. Conditioning	0.5 mL methanol	5 mL methanol
2. Equilibration	0.5 mL H <sub>2</sub> O	5 mL H <sub>2</sub> O
3. Sample loading	10 mL	10 mL
4. Washing	0.25 mL H <sub>2</sub> O	1 mL 5% methanol in H <sub>2</sub> O
5. Analyte eluting	0.1 mL methanol	1.5 mL 2% formic acid in methanol

### 3.4.2. Gas chromatography method for aldehyde products separation

The eluates from SPE preparations and respective standards were analyzed using a gas chromatograph coupled with a mass spectrometer (Trace GC/DSQII-MS single quad, Thermo Electron Corporation) equipped with a TRACE™ TR-5MS column (30 m x 0.25 mm ID x 0.25 µm film, Thermo Scientific), using helium as a carrier gas at the flow rate of 1.2 mL/min. Samples of 1 µL were injected in a constant temperature splitless mode at 250 °C and separated according to the temperature program: hold for 2 min at 60°C, a 10 °C/min gradient from 60 to 200 °C, next a gradient from 200 to 290 °C at 30 °C/min and 5 min hold at 290 °C. The MS detector operated in positive ion scanning mode with a mass range of 35-200 m/z, at the electron energy of 70 eV. The ion source and transfer line temperatures were set at 230 °C and 250 °C, respectively. The compounds of interest were identified based on the NIST library and comparison against the MS spectra of an external standards library. The standards in the above method were analyzed before the analysis of samples and the retention times of standards are shown in **Table 8**.

Once a peak of respective retention time was found in the sample chromatogram, confirmation of aldehyde identity was conducted in the generic software from Thermo Electron Corporation that allowed search in libraries and visualisation of fit of detected fragmentation patterns. As an example, a result of a library search for a potential cinnamaldehyde peak is shown in **Figure 20**, which confirms the identity of the chemical against replib and MAINLIB libraries. The diagram in the lower right corner shows residual signals – positive are missing relative abundances in the sample in comparison to the library, and negative are additional signals in the sample.

**Table 8.** The retention time of standards of aldehydes and acids analyzed in the experiment.

Chemical name	RT (min)
Benzaldehyde	5.80
Benzoic acid	9.10
4-hydroxybenzaldehyde	11.80
4-hydroxybenzoic acid	16.70
Phenylacetaldehyde	7.08
Phenylacetic acid	10.37
Octanal	6.25
Octanoic acid	8.82
Pentanal	2.29
Pentanoic acid	4.59
<i>Trans</i> -cinnamic acid	13.10
<i>Trans</i> -cinnamal	10.60
3-pyridine-carboxaldehyde	6.66

The sample spectrum at RT=10.6 min was also compared with the spectrum of the cinnamaldehyde standard, which was measured before the samples. Considering the relatively low concentration of aldehydes in examined samples, the peak purity was additionally confirmed by extracting chromatograms (extracted ion signals EIC) for major signals in the fragmentation pattern ( $m/z=131, 103, 77, 63$ ). The resulting chromatograms were assessed for good separation from other eluates as in the example shown in **Figure 22.A**, all the peaks at RT=10.6 min are baseline separated from other peaks.

The other aldehydes were found in samples from reactions with corresponding carboxylic acids using this approach. The fragmentation pattern of aldehydes depends on the structure of the hydrocarbon residue. The aromatic aldehydes (here cinnamaldehyde and phenylacetaldehyde spectrum shown in **Figures 22** and **23**) fragmentation spectrum usually include signals of 39, 50, 51, 63, and 65  $m/z$  which represent aromatic ring fragmentation. Moreover, signals at 91 and 77  $m/z$  correspond to tropylium and phenyl cation, arising from the aryl group. Furthermore, an abundant molecular ion peak is usually present in the spectra of aromatic aldehydes. Nicotinaldehyde is a heterocyclic compound, however, similarly its MS fragmentation pattern includes abundant molecular ion of 107  $m/z$  and aromatic-derived ions (51, 78  $m/z$ ), as shown in **Figure 24**.

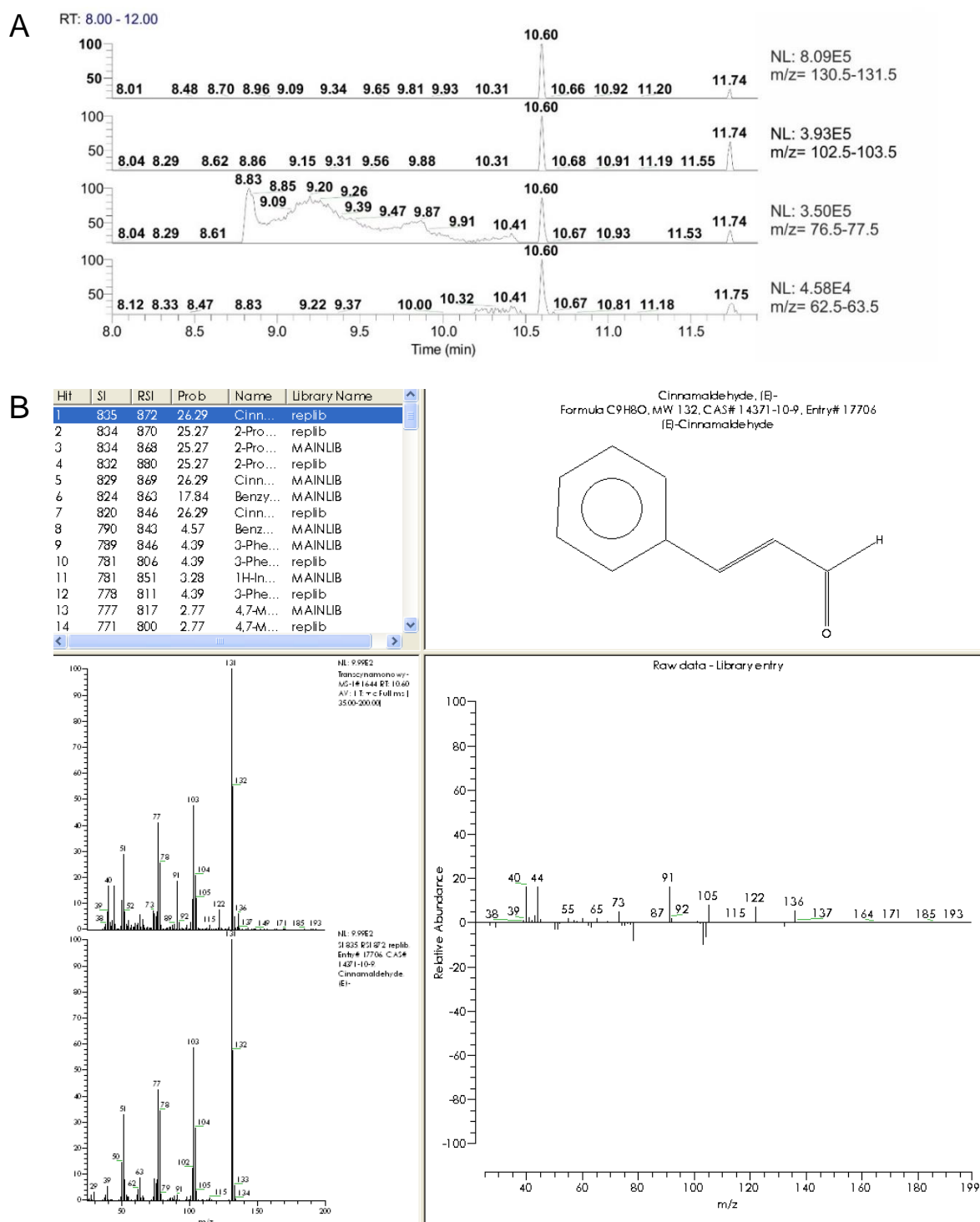


**Figure 22. A)** Chromatogram for signals recognized as main fragmentation peaks of cinnamaldehyde at RT 10.6 min (from top EIC:  $m/z = 131, 103, 77, 63$ ). **B)** Example of library search results: EI spectrum of peak at RT of 10.6 min recognised as cinnamaldehyde, top left: list of compounds recognized in available libraries by the

spectrum. Bottom left: mass spectrum of the chromatogram peak expected as cinnamaldehyde and below mass spectrum of cinnamaldehyde from the database, and differential spectra of the two (right).

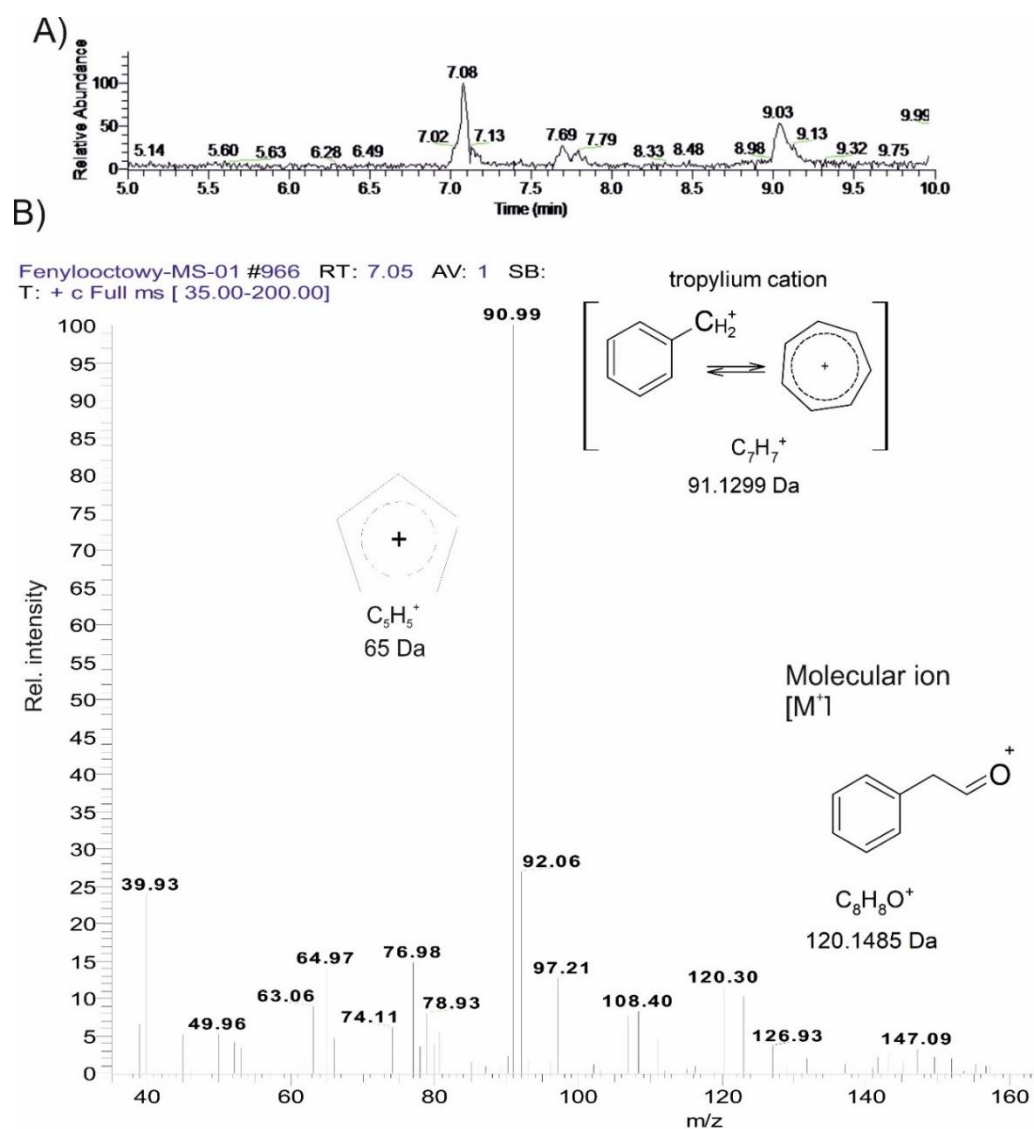


**Figure 23. A)** Chromatogram of  $m/z$  91 corresponding to the base peak in phenylacetaldehyde spectrum, in the sample from the reaction of phenylacetic acid reduction the peak at  $RT=7.08$  min was identified as phenylacetaldehyde based on the **B)** EI spectrum of that peak, shown with expected structural details of fragmentation ions.

The aliphatic aldehydes share one characteristic fragmentation pattern in mass spectrometry, which is MacLafferty rearrangement shown in the example of octanal in **Figure 24.C**<sup>128</sup>. This fragmentation reaction yields, for most of aliphatic aldehydes, in a signal of  $44$   $m/z$ . The other product of the rearrangement has  $m/z$  of  $[M-44]$  depending on the structure of the chemical. Therefore these two signals are characteristic for



aliphatic aldehydes. For reaction samples with octanoic acid, octanal was identified based on abundant peaks of 44 m/z and 84 m/z in the spectrum shown in **Figure 24.B**.

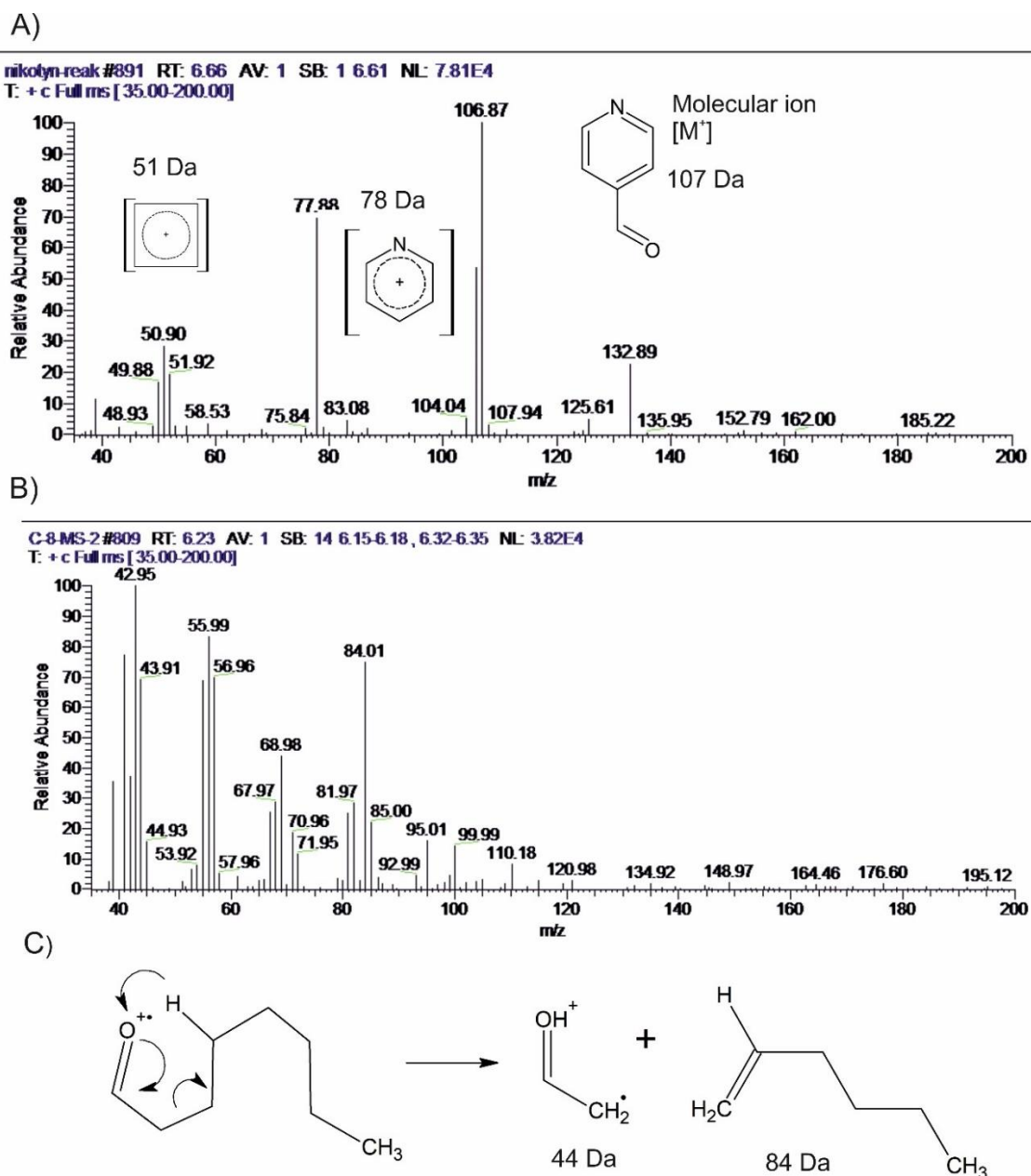


**Figure 24.** MS spectrum of the apparent peak of **A)** nicotinaldehyde (RT=6.66 min) **B)** octanal (RT=6.25 min) in samples from the reaction of reduction of the corresponding acid; **C)** reaction of MacLafferty rearrangement of octanal.

### 3.5. Spectrophotometric activity assays

The steady-state activity of enzymes was measured using a Shimadzu UV-vis spectrometer under anaerobic (UV-1280) or aerobic (UV-2700) conditions in 1.0 mL polystyrene cuvettes with a 10 mm optical pathway. Each reaction assay was conducted

in triplicate. The measurements for reactions with either  $\text{NAD}^+$  or  $\text{BV}^{2+}$  were followed at 340 nm ( $\varepsilon = 6220 \text{ M}^{-1} \text{ cm}^{-1}$ ) or 600 nm ( $\varepsilon = 7400 \text{ M}^{-1} \text{ cm}^{-1}$ ), respectively<sup>90</sup>.

If not stated otherwise, rate values were obtained from the initial phases (0-30 s) of the activity curves which were fitted with linear regression.

The steady-state activity of the enzyme (at a given concentration) was calculated from the linear slope “a” obtained in the linear regression analysis of kinetic data, according to the equation:

$$V_0 = \frac{n}{2} \times \frac{a}{\Delta\varepsilon \times L} \times 10^6$$

Where:

$V_0$  – initial velocity of reaction catalyzed by a given amount of enzyme (in  $\mu\text{M}$  substrate converted per minute);

n – the number of electrons needed for the reduction of one molecule of electron mediator (1 for  $\text{BV}^{2+}$ , 2 for  $\text{NAD}^+$  and  $\text{NADP}^+$ );

a - the slope of the linear fit of the initial part of the progress curve (change of absorbance per minute);

$\Delta\varepsilon$  – a difference in extinction coefficient (between two oxidation states used in the assay) appropriate for the electron mediator at measured wavelength ( $\text{M}^{-1} \text{ cm}^{-1}$ );

L - the optical pathway of cuvette – here 1 (cm).

The obtained plots of reaction velocity in the function of substrate concentration were fitted with the Michaelis-Menten or Hill model by non-linear regression (OriginPro 2019).

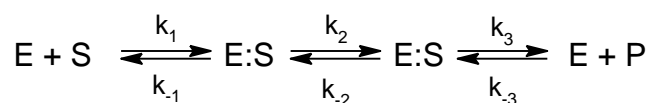
Calculation of specific activity used for comparison of enzyme batches and in some kinetic studies was done according to the equation:

$$A_{spec} = \frac{V_0}{c_{enz}}$$

Where  $A_{spec}$  is specific activity (U/mg of protein) and  $c_{enz}$  is the concentration of enzyme in the reaction mixture (mg/mL).

#### *Dependence of enzyme kinetics on substrate concentration*

The basic and straightforward method to study the mechanism of an enzyme-catalyzed reaction is to analyze its kinetics. The contemporary Henri—Michaelis—Menten model is commonly used to describe enzyme kinetics. The general scheme describing a one substrate reversible enzymatic transformation is following:



This model describes the enzymatic reaction catalysis using several assumptions, simplifying the description. The model assumes a rapid formation of the enzyme-substrate complex (ES) (so-called rapid-equilibrium assumption), which means that the kinetic constant of internal catalytic reaction ( $k_2$ ) is significantly lower than the constant of ES dissociation ( $k_{-1}$ ). The steps following the slowest, catalytic step are assumed as faster and thus not influencing the observed kinetics. The second assumption of the model is large excess of the substrate over the enzyme, which means that the concentration of the free substrate is not significantly changed by the substrate bound in E:S. As a consequence, based on the mass balance equation, the the free enzyme concentration  $[E]_f$  can be described as:

$$[E]_f = [E] - [ES]$$

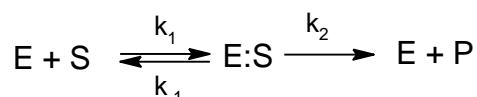
where,  $[E]$  – denotes the total enzyme concentration and  $[ES]$  - the concentration of the E:S complex. The equation describing equilibrium constant of E:S dissociation can be therefore formulated as:

$$K_S = \frac{[E]_f [S]}{[ES]} = \frac{([E] - [ES])[S]}{[ES]}$$

The above equation can be rearranged to describe the unknown concentration of the  $[ES]$

$$[ES] = \frac{[E][S]}{K_S + [S]}$$

Thus, following simplified reaction scheme can be formulated:



All the internal steps associated with catalysis can be described in the simplest case by the first-order rate constant  $k_2$  (assuming a singular elementary catalytic site). On the other hand, multiple elementary steps of the enzymatic catalysis should be taken into account and denoted it with a single composite first-order rate constant  $k_{cat}$ :



In consequence, the rate of product formation is described by the first-order kinetics:

$$V = k_{cat} [ES]$$

When both above equations are combined, the Michaelis-Menten equation in the rapid-equilibrium assumption is obtained:

$$V = \frac{k_{cat}[E][S]}{K_S + [S]} = \frac{V_{max}[S]}{K_S + [S]}$$

where  $K_S$  as an equilibrium constant is the ratio of  $k_{-1}/k_1$ . This description, formulated independently by Henri in 1903 and Michaelis and Menten in 1913 is limited, to rather rare situations when rapid equilibrium indeed is present. The approach is also very useful for the description of the fast kinetics measured with the stopped-flow technique in single turn-over experiments.

The Henri-Michaelis-Menten model was reinterpreted by Briggs and Haldane's derivation that includes a steady-state approximation instead of the rapid formation of the enzyme-substrate complex<sup>129</sup>. Steady-state approximation considers an example of a reaction when  $E:S$  concentration will rapidly approach a steady-state and will be constant during the measurement. This means, that after an initial burst phase,  $[ES]$  concentration will not change appreciably until a significant amount of substrate has been consumed. Briggs and Haldane's derivation also requires several assumptions. Firstly, the initial phase of the progress curve is considered and no other intermediates besides  $E:S$  are formed (no  $E:P$ ). Total enzyme concentration is described by the same equation as in the rapid-equilibrium approach. Furthermore, as previously excess of the substrate over enzyme concentration is assumed (free ligand approximation). Next, as the kinetics is measured only during the initial linear phase of the reaction, product  $[P]$  concentration can be approximated as 0 (the reaction is practically irreversible) and no substrate depletion during the reaction test is assumed ( $[S]_t \sim [S]$ ).

After the burst formation of the  $E:S$  complex the model assumes the steady-state kinetic phase is reached:

$$\frac{d[ES]}{dt} = 0$$

Adding kinetic processes of  $E:S$  formation and decomposition the following equation is obtained:

$$\frac{d[ES]}{dt} = k_1[E][S] - (k_2 + k_{cat})[ES] = 0$$

This equation can be rearranged, so the concentrations are separated from kinetic constants, and as a result, a Michaelis  $K_m$  can be defined:

$$K_m = \frac{k_2 + k_{cat}}{k_1} = \frac{[E][S]}{[ES]}$$

The enzyme velocity under the approximation of steady-state conditions will then depend on substrate concentration according to hyperbolic function:

$$V = \frac{V_{max} \times [S]}{K_m + [S]}$$

Where  $V_{max}$  is the reaction velocity at saturating substrate concentration. If an enzyme would perfectly follow the above model, the substrate versus initial velocity plot should be a rectangular hyperbola (as in **Figure 25**). The  $V_{max}$  can be described as:

$$V_{max} = k_{cat} * [E]$$

The  $K_m$  can be interpreted as the substrate concentration at which the enzyme achieves 50% of the maximum velocity ( $V_{max}$ ) for the catalyzed reaction (or at which half of the enzyme's active sites are filled by substrate molecules). The value is constant for any enzyme concentration and can be used as a measure of the extent of substrate binding affinity of the enzyme. However, it should be highlighted that  $K_m$  very often differs from  $K_s$ , obtained under conditions of rapid equilibrium approximation and is dependent not only on enzyme binding kinetics but also on rate of catalytic transformation. As a result,  $K_m$  should be treated as a kinetic, not thermodynamic, constant.

The value of  $k_{cat}/K_m$  is the apparent second-order rate constant or specificity constant, which defines a measure of the catalytic efficiency of an enzyme-substrate pair. It allows comparison not only of the efficiency of different enzymes to one another but also is considered to be the best measure of substrate specificity for a given enzyme.

#### *Exceptions from hyperbolic function*

Enzymes may contain more than one catalytic subunit with an active site centre binding ligand. For many of such enzymes, reactions are catalyzed independently throughout the complex. However, there are also complexes where the binding of ligands at one active site can increase or decrease the affinity of the other active sites towards the ligand. Such a phenomenon, when ligand binding at one subunit affects the affinity of the other subunit, is called the cooperativity of active sites. The increase in affinity is called positive cooperativity, while the decrease, is negative cooperativity. If there is more than one active site in the enzyme complex, its velocity dependence on substrate concentration can show features of cooperativity and might be then described by the Hill equation:

$$V = \frac{V_{max} \times [S]^n}{S_{0.5} + [S]^n}$$

Where:

$S_{0.5}$  is substrate (S) concentration at which  $V=0.5 V_{max}$  (Hill concentration constant);

$n$  is the Hill coefficient.

When the Hill coefficient value is equal to 1, the equation reduces to the form of the Michaelis- Menten equation (noncooperative binding). The Hill coefficient values above 1 mean positive cooperativity and below 1 negative cooperativity. The value of the Hill coefficient  $n$  depends on the number of active sites and the degree (strength) of cooperativity between them. The impact of cooperativity on enzymes' kinetics is illustrated in **Figure 25**.

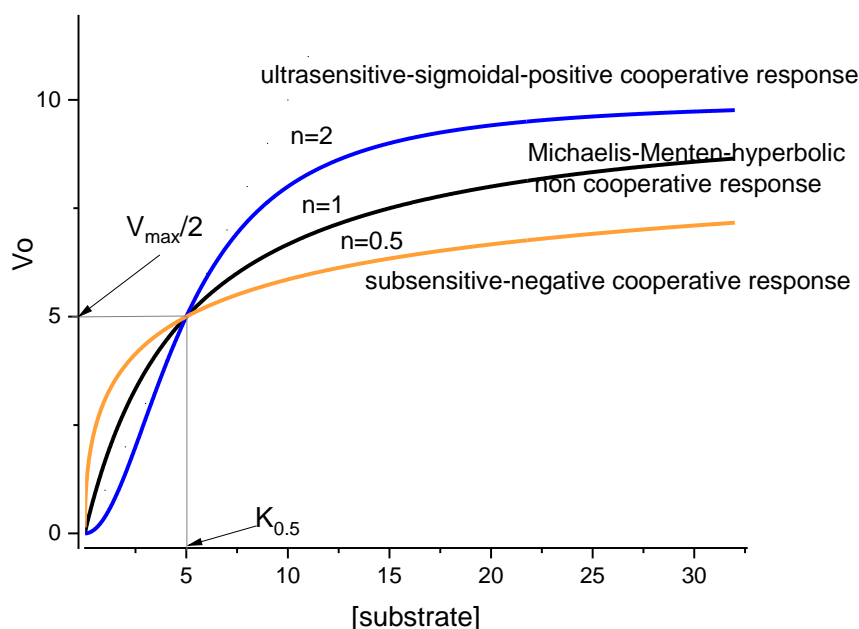


**Figure 25.** The example of a shape of the curve described by the Hill equation for different values of the Hill coefficient for enzymes kinetics, the graph shows the dependency of initial velocity on substrate concentration<sup>130</sup>.

### 3.5.1. Assay for AOR activity in aldehyde oxidation

The AOR<sub>Aa</sub> activity assays in the oxidation of aldehydes were performed with BV<sup>2+</sup> or NAD<sup>+</sup> as electron donors and natively expressed enzyme. The activities with BV<sup>2+</sup> were tested under anaerobic conditions and 20  $\mu$ M Na<sub>2</sub>S<sub>2</sub>O<sub>4</sub> was added to the buffer to get rid of any oxidating agents that might impact stoichiometric BV<sup>+</sup> formation. The activities with NAD<sup>+</sup> were tested aerobically, as AOR<sub>Aa</sub> was proven stable for the first 1 min of reaction in an aerobic buffer, with no drop in initial activity measured. The AOR<sub>Aa</sub> was added with a syringe from stoppered vials. The experiments leading to kinetic curves and

relative activities with a spectrum of aldehydes with  $BV^{2+}$  were done anaerobically in a glovebox with very low hydrogen concentration (due to malfunction of the gassing system). In the presence of residual hydrogen concentrations expected in a correctly working glovebox, a baseline slope of less than 5% of the measured activity with aldehydes was observed and was always subtracted in the calculations of the specific activity. This measured baseline activity was later connected with the hydrogenase activity of  $AOR_{Aa}$  once the hydrogen concentration in the glovebox was increased.

The reactions were conducted at 30 °C in 980  $\mu$ L buffer Tris/HCl pH 8.0 containing 3  $\mu$ g/mL  $AOR_{Aa}$  and 1.6 mM  $BV^{2+}$  or 1.6 mM  $NAD^+$  as respective electron acceptors. The reaction was initiated with the addition of 10  $\mu$ L of aldehyde stock solutions in water or tert-butanol as solvents. It was tested that tert-butanol in low concentrations had no impact on  $AOR_{Aa}$  activity.

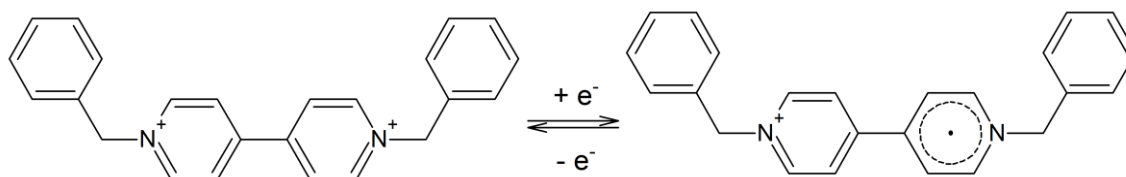


**Figure 26.** Reduction of oxidized benzyl viologen ( $BV^{2+}$ ) to a blue, radical form of the dye ( $BV^+$ , shown on the left).

The reduced form of benzyl viologen under physiological conditions (pH < 12) is generated by the addition of one electron. The reaction of  $BV^{2+}$  reduction (**Figure 26**) can be observed spectrophotometrically following increased absorption of a band at 600 nm. Under conditions used in this work, the normal potential of viologen dyes is independent of pH<sup>131</sup>.

### 3.5.2. Assay for AOR activity in $NAD^+$ and $BV^{2+}$ reduction

The  $AOR_{Aa}$  activity in the reduction of  $NAD^+$  or  $BV^{2+}$  with  $H_2$  was carried out under an anaerobic atmosphere at 30 °C in 1000  $\mu$ L of 100 mM Tris/HCl buffer pH 8.0 containing 1.6 mM  $NAD^+$  or  $BV^{2+}$  as an electron acceptor, and 20  $\mu$ g/mL of  $AOR_{Aa}$ . In assays with  $BV^{2+}$   $Na_2S_2O_4$  was added to final concentration of 20  $\mu$ M to reduce traces of oxygen. The reactions were started with the addition of an electron acceptor. The obtained specific activity was also used to normalize enzyme activity between different batches of enzyme during kinetic studies with hydrogen.

The pH-dependence of  $AOR_{Aa}$  activity in  $NAD^+$  reduction with  $H_2$  as an electron donor was measured in the pH range 5.5-8.0 in 100 mM potassium phosphate buffer and 7.2-8.5 in 100 mM Tris/HCl buffer.

Hydrogen partial pressures (v/v) were converted into molar concentration by assuming a solubility coefficient of  $q = 1.47 \times 10^{-4}$  g of hydrogen in 100 g of water at 30 °C and 1 atmosphere<sup>132</sup>.

### 3.5.3. Coupled enzymatic assay for AOR activity in carboxylic acid reduction

The reaction kinetics could be studied by chromatographic detection of benzaldehyde. However, all methods established for this work had relatively high LOQ and the kinetics could be impacted by product inhibition or thermodynamics of the reaction. Therefore, a coupled assay method was established in which the benzaldehyde production catalyzed by AOR is coupled to further reduction of aldehyde to alcohol by BaDH, which uses NADPH as an electron donor (scheme of the reaction shown in **Figure 27.A**). AOR is not able to use NADPH in either form, i.e. reduced or oxidized. Therefore, all changes in NADPH absorbance measured by UV-vis spectrophotometry can be linked to BaDH activity. In principle, in such coupled assay, the NADPH depletion rate should be equal to the rate of AOR-catalyzed benzoate reduction in steady-state.

In order to study the steady state velocity of benzoate reduction by AOR ( $v_1$ ), this reaction must be rate limiting in the coupled assay setup and benzaldehyde must reach steady state concentration<sup>133</sup>. Under these conditions, benzaldehyde is converted to benzyl alcohol almost instantaneously. The rate of NADPH consumption ( $v_2$ ) is a reflection of the velocity of benzoic acid reduction, what in coupled assay is called the steady state phase. However, this state is not achieved from the beginning of the assay and the preceding phase is called the lag phase. During the lag phase, benzaldehyde is accumulated and  $v_2$  is lower than  $v_1$ . To establish a reproducible and accurate coupled assay method, the lag phase duration had to be minimalized and quantitated. For the reaction according to the scheme:



the lag time, so the time from the beginning of the reaction till the steady-state phase, when  $v_1$  can be measured, can be calculated from an equation derived by Storer *et al.*<sup>134</sup>:

$$t_{99\%} = \frac{\varphi \times K_m^2}{v_1}$$

Where  $K_m^2$  is Michaelis constant for the reduction of aldehyde to alcohol (0.43 mM) and  $\varphi$  is a dimensionless number, a function of the ratios  $\frac{v_1}{V_2}$  and  $\frac{v_2}{v_1}$  that was calculated by Storer *et al.*<sup>134</sup>. The  $V_2$  is a maximum velocity of reaction 2 (transformation of aldehyde to



alcohol) under assay conditions (approx. 30 U mg<sup>-1</sup> for 0.6 mM NADPH, pH 5.5, 100 mM citric buffer, 30 °C), depending on the concentration of the BaDH<sup>133</sup>, whereas  $\frac{v_2}{v_1}$  is a value describing the accuracy of how well  $v_2$  follows  $v_1$ , that for the coupled assay was chosen to be 99% (the value is 0.99).

When designing the assay, one can control the described variables ( $v_1$  and  $v_2$ ) by adjusting the amount of both enzymes. To ensure a short lag time and measurable change in the UV-vis spectrum in the course of the reaction, AOR concentration was chosen to be 0.03 mg/mL and BaDH 0.17 mg/mL. The value of  $\varphi$  (0.012) was calculated by interpolation of data presented in Storer *et al.*<sup>134</sup>. In such a setup, the calculated  $t_{99\%}$  was 30 s for the maximum expected specific activity of AOR assumed as 0.4 U mg<sup>-1</sup>. This means that 30 s after the start of the coupled assay, the measured  $v_2$  can be interpreted as  $v_1$  with 99% accuracy.

The measurements were performed under 2.5% hydrogen in nitrogen (v/v) in the headspace at 30 °C. The principle of the designed coupled assay was tested in a batch reactor consisting of 2 mL citric buffer pH 5.5 with 30 mM benzoate, 0.6 mM NADPH, where the NADPH oxidation to NADP<sup>+</sup> was followed spectrophotometrically. Additionally, the concentrations of both aldehyde and alcohol were measured in samples taken during the reaction by the HPLC method. The resulting concentrations of alcohol, aldehyde and NADP<sup>+</sup>, shown in **Figure 27.B**, behaved in an expected manner. After initial accumulation, benzaldehyde maintained a low quasi-steady-state concentration (approximately 35 μM of benzaldehyde) throughout the assay. Moreover, the NADPH oxidation was followed by a linear increase in the concentration of benzyl alcohol and the reaction rate was constant for about 20 minutes until it slowed down. The slowing down of the reaction might be caused by the decrease of NADPH concentration beyond a level when it did not impact the rate of BaDH-catalyzed reaction ( $v_2$  became the rate-limiting). The validity of the assay was confirmed by the identity of the rate of NADPH consumption and benzyl alcohol production and a stable concentration of benzaldehyde.

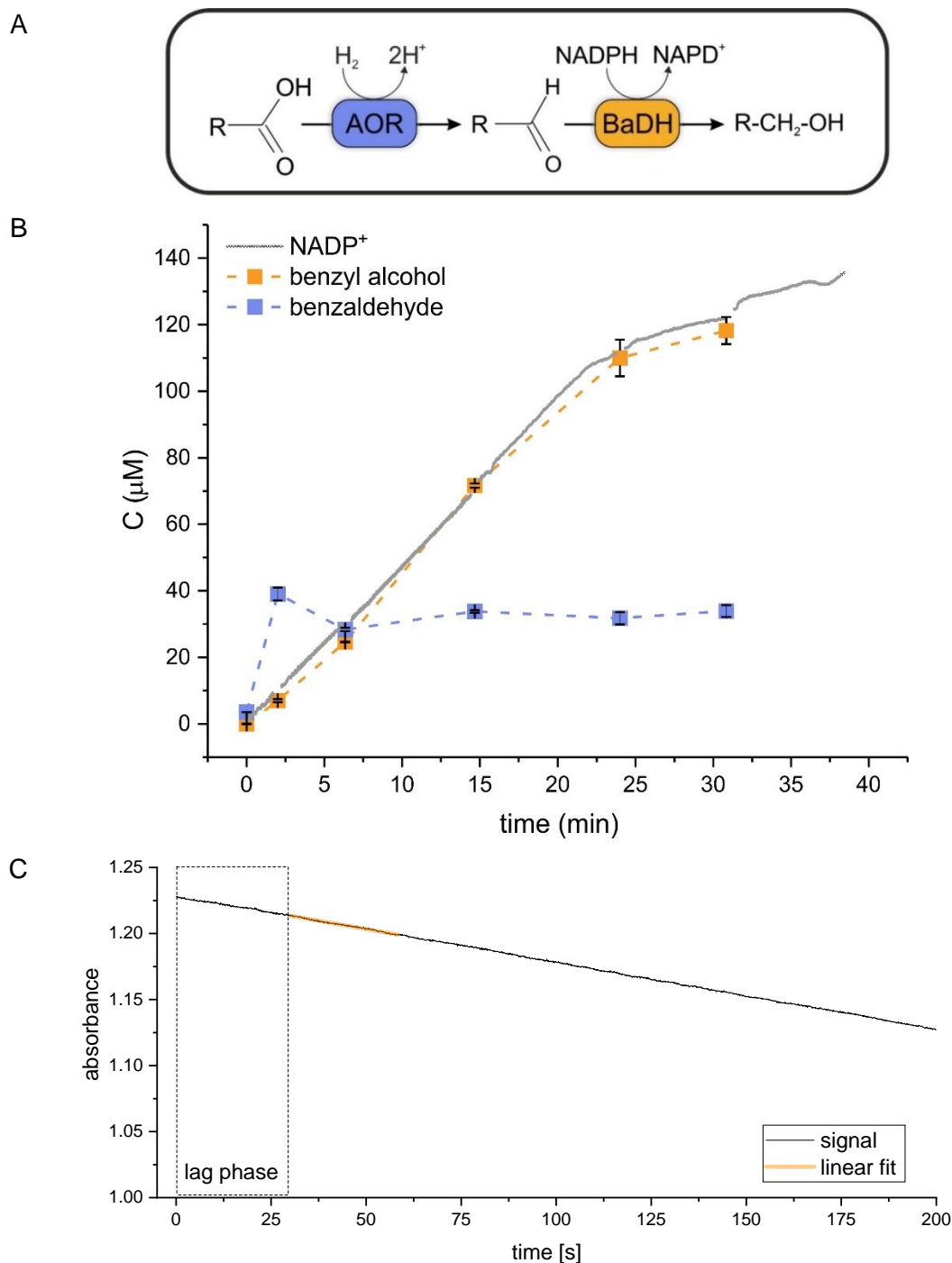


**Figure 27. A)** Scheme of reactions occurring in the coupled assay: reduction of benzoic acid to benzaldehyde by AOR followed by reduction by BaDH to benzyl alcohol coupled to NADPH oxidation. **B)** Progress curve of AOR-BaDH coupled assay cascade conducted at pH 5.5 with 30 mM benzoic acid and 0.6 mM NADPH as substrates. The concentrations of benzyl alcohol (orange) and benzaldehyde (blue) were measured by HPLC, whereas NADP<sup>+</sup> (grey) was derived from UV-vis measurement. **C)** Activity curve for coupled assay with sodium benzoate, 0 min corresponds to the addition of sodium benzoate.

The progress curve of the AOR-BaDH coupled assay presented in **Figure 27.C** shows the principle of fit of activity curves in the coupled assay: the first 30 seconds of the curve are omitted and the rate value is calculated from the linear fit of data obtained in the interval 30-60 s. The linearity of the fragment was assessed based on  $R^2$  of fit of a linear function.

The coupled assay was used to determine the kinetic parameters of AOR<sub>Aa</sub>, pH optimum and impact of hydrogen concentration on benzoic acid reduction. All measurements were performed at 30 °C and, except for the last one, under 2.5% hydrogen in nitrogen (v/v) in the headspace. The reaction mixture in the assay for kinetic parameters determination contained 100 mM sodium citrate buffer pH 5.5, 0.6 mM NADPH, BaDH (170 µg/mL) and recombinant AOR<sub>Aa</sub> (30 µg/mL). The reaction was initiated by the addition of sodium benzoate to concentrations of 4-42 mM in the reaction mixture.

Similarly, the pH optimum of AOR<sub>Aa</sub> for benzoate reduction was determined under the same conditions as above, using 30 mM sodium benzoate and 100 mM sodium citrate buffer in the pH range of 4.5-6.0 or 50 mM potassium phosphate buffer in the pH range of 6.0-7.0.

The impact of hydrogen concentration on benzoic acid reduction was assayed in stoppered cuvettes maintaining the gas mixture contained in the headspace. The different concentrations of gas were obtained from pure nitrogen and hydrogen in a custom gas mixing apparatus and the cuvettes were purged with the gas mixture as described before (Chapter 3.1.). The assay was conducted at pH 5.5, as described before and started by the addition of 30 mM benzoic acid.

### **3.6. Reactor tests for characterization of AOR activity**

#### **3.6.1. Substrate spectra in acid reduction**

Initial tests of hydrogen-dependent reactivity of AOR<sub>Aa</sub> with benzoate were conducted with product detection by LC-ESI(+)-MS/MS method (see Chapter 3.3.). The reaction was conducted in 50 mM MES/NaOH buffer pH 6.5 with 24 mM of sodium benzoate in 2.5% (v/v) hydrogen, at 30 °C, with either 26, 39 or 52 nM AOR<sub>Aa</sub>. The samples were taken during the reaction and the reaction was stopped by the addition of methanol (3:7 methanol: reaction mixture v/v). The sample was centrifuged and applied on LC-MS/MS for benzaldehyde quantification.

The hydrogen-dependent reactivity of AOR<sub>Aa</sub> with benzoate, 4-hydroxybenzoate, phenylacetate, *trans*-cinnamate, nicotinate and octanoate was proven by the detection of

the corresponding aldehydes in the reaction mixture by either LC-ESI(+)-MS/MS (Chapter 3.3) for 4-hydroxybenzaldehyde or by GC-MS for the other aldehydes (Chapter 3.4.). The reactions were performed anaerobically in stoppered vials, flushed with pure hydrogen as described in Chapter 3.1.; the reaction mixture contained 50 mM MES/NaOH buffer pH 5.5, 20 mM of corresponding acid sodium salt (solubilized by an equimolar amount of NaOH) and 0.1  $\mu$ M AOR<sub>Aa</sub> (heterologously expressed, except for benzoate, which was conversed by AOR form native preparation). The reaction mixture was mixed gently for 3 h at 30 °C. The method of how the reaction was stopped and samples were prepared was described in the appropriate detection method.

### 3.6.2. Determination of electron donors

A Ti(III) citrate stock solution was freshly prepared under an anaerobic atmosphere before use from 10.6 mL Ti(III) chloride (30% solution in 10% HCl, Sigma Aldrich, Saint Louis, USA) by addition of 4.4 g solid sodium citrate, 4.7 g NaHCO<sub>3</sub> and 8 mL 100 mM citric acid/NaOH buffer pH 4.5. An Eu(II) complex stock was prepared from EuBr<sub>2</sub> (crystalline powder, anaerobically stored, Sigma Aldrich, Saint Louis, USA) by dissolving the salt anaerobically in an EGTA (ethylene glycol-bis(2-aminoethylether)-N,N',N',N'-tetraacetic acid) containing water solution at a molar ratio of 1:1 to achieve a stock solution of 200 mM Eu(II)-EGTA<sup>135</sup>. The reaction mixture contained 30 mM sodium benzoate in 100 mM citric acid/sodium citrate buffer (pH 5.5) and 0.2  $\mu$ M AOR<sub>Aa</sub> and the respective electron donor. When hydrogen was used as the electron donor, the mixture (without enzyme) was equilibrated overnight in an N<sub>2</sub>/H<sub>2</sub> 97.5%/2.5% atmosphere. In contrast, for the metallic electron donors, 3 mM Ti(III)-citrate or Eu (II)-EGTA were added into closed anaerobic vials under a hydrogen-free N<sub>2</sub> atmosphere. The reactions were started by adding AOR<sub>Aa</sub> and in all samples taken from the reaction the benzaldehyde was detected by the HPLC method (see 3.2.2.). As controls, the mixture of respective metals and benzoate in conditions as in the reaction were incubated for 2 h and tested, showing no benzaldehyde presence.

### 3.6.3. Steady-state activities of AOR<sub>Aa</sub> in NAD<sup>+</sup>/benzoate reduction

The AOR<sub>Aa</sub> activity for the independent or competitive reduction of NAD<sup>+</sup> and benzoic acid with H<sub>2</sub> was assayed in 1.5 mL reactors at 30 °C with the benzaldehyde concentration quantitated by HPLC (Chapter 3.2.3.) and NADH concentration measured spectrophotometrically (Chapter 3.5.2.). The reactions were conducted with 0.02 mg/mL AOR<sub>Aa</sub>. The following setups were tested: reduction with 2.5 % H<sub>2</sub> (v/v) of i) 0.1 mM NAD<sup>+</sup>, ii) 1.0 mM NAD<sup>+</sup>, iii) 30 mM sodium benzoate, iv) 30 mM sodium benzoate and 0.1 mM NAD<sup>+</sup>, v) 30 mM sodium benzoate and 1 mM NAD<sup>+</sup> in either pH 7.0 or pH 5.6

100 mM citric acid/Na<sub>2</sub>HPO<sub>4</sub> buffer. Each reactor test was conducted in two repetitions and for HPLC-DAD, two samples were taken for each experimental point. The reaction progress was followed for 30-80 min. The progress curves for NADH were fitted with a linear function for the initial time of the reaction (0-30 s), while those for benzaldehyde were fitted with the burst-type equation  $[P] = \Pi [1 - \exp(-k_{bt}t)] + V_{ss}$  provided in Origin Pro 2019b by prof. Maciej Szaleniec. The  $V_{ss}$  constant was used to calculate specific activities of the linear phase.

#### *Control reactions for non-catalytic production of benzaldehyde*

In parallel with the enzyme assays mentioned above, control experiments were prepared using the same concentrations of reagents as in samples used for enzyme assays: 2.5 % H<sub>2</sub> (v/v), 30 mM sodium benzoate in 100 mM citric acid/Na<sub>2</sub>HPO<sub>4</sub> buffer pH 5.6:

1. without any protein;
2. with bovine serum albumin (BSA, Sigma-Aldrich, Saint Louis, USA) instead of AOR<sub>Aa</sub> - BSA concentration in the reaction control mixture was 0.02 mg/mL;
3. with inactivated AOR<sub>Aa</sub>: 200  $\mu$ l of purified protein (2 mg/mL) was denatured by incubation at 95 °C and centrifugated - the supernatant was tested for the presence of aldehyde, the precipitated protein was mixed with reagents to a final concentration of protein 0.02 mg/mL.

After 1 h of incubation, samples were taken from control reactions and examined with HPLC-DAD for the presence of products (see Chapter 3.2.3.). There was no benzaldehyde or benzyl alcohol present in any of these controls.

#### *Control without hydrogen*

A capped vial with 2 mL of 100 mM citric acid/Na<sub>2</sub>HPO<sub>4</sub> buffer, pH 5.6, containing 30 mM sodium benzoate was flushed with nitrogen to evacuate hydrogen (residual amounts from sample preparation in the glovebox). AOR<sub>Aa</sub> was added with a syringe to a concentration of 0.02 mg/mL in the control mixture and samples were collected after 1 h of incubation. Samples taken from reactions after 1 h were examined with HPLC (see Chapter 3.2.3.). There was no benzaldehyde or benzyl alcohol present in any of these control samples.

### **3.6.4. Cascade**

The cascade reactions with NAD<sup>+</sup> instead of NADPH were conducted under an anaerobic atmosphere at 30 °C and a pH of either 5.6 or 7.0 (100 mM citric acid/Na<sub>2</sub>HPO<sub>4</sub> buffer) in a 2 mL cuvette containing 0.1 mM NAD<sup>+</sup>, 30 mM sodium

benzoate, 20 µg/mL AOR<sub>Aa</sub> and 75 µg/mL BaDH. The NADH formation was observed spectrophotometrically (see Chapter 3.5.2.), while benzaldehyde and benzyl alcohol concentrations were followed by the HPLC method (see Chapter 3.2.3).

### 3.6.5. NADH regeneration

As shown previously, the crude extract containing recombinant AOR<sub>Aa</sub> was prepared from cell extract obtained for heterologous expression system purification. The cell extract was desalted by repeating 3 times a 5-fold concentration via ultrafiltration (10 kDa membrane, Millipore Amicon Ultra-15 mL) and subsequent dilution with 100 mM Tris/HCl buffer pH 8.0. The reaction was conducted in the above buffer containing 0.5 mM NAD<sup>+</sup>, 2 mM acetophenone and 6 ng/mL of an (*R*)-specific *R*-1-(4-hydroxyphenyl)-ethanol dehydrogenase (R-HPED<sup>136–138</sup>). The mixture was exposed to 2% H<sub>2</sub> under anaerobic conditions and the crude extract was added to a final concentration of 1 mg/mL. The reaction was gently mixed at 20°C and samples were taken during the experiment in duplicate, for each time point the reaction was stopped by mixing with acetonitrile in a 1:1 (v/v) ratio, and the produced (*R*)-1-phenylethanol was quantitated by HPLC-DAD method described in 3.2.4.

### 3.6.6. Carbon monoxide inhibition test

The impact of carbon monoxide on the hydrogenase activity of AOR<sub>Aa</sub> in NAD<sup>+</sup> reduction was tested by a spectrophotometric test at 340 nm. A stoppered 2 mL quartz cuvette containing 1 mL mixture of 0.75 mg/mL crude cell extract with recombinant AOR<sub>Aa</sub> (prepared as in Chapter 3.6.5.) was purged for 2 min with a gas mixture composed of 59% N<sub>2</sub>, 40% CO, 1% H<sub>2</sub>. A control sample was prepared as above without CO (the gas mixture was composed of 99% N<sub>2</sub> and 1% H<sub>2</sub>). The cuvettes were incubated for 1.5 h at 4 °C, then heated to 30 °C and the reaction was started with the addition of NAD<sup>+</sup> to 1 mM concentration in the reaction mixture. The control test and the experiment were conducted in triplicate.

## 4. Single-Particle Cryo-Electron Microscopy of AOR

In crystallization attempts conducted by the prof. Heiders group from Marburg, AOR<sub>Aa</sub> did not form uniform crystals. Therefore, the determination of AOR<sub>Aa</sub> structure with the CryoEM technique was conducted at the laboratory of Dr Jan Schuller in Synmikro (Zentrum für Synthetische Mikrobiologie) at the University of Marburg as a research internship realized during the PhD studies. The pure protein material used in the research was obtained at ICSC PAS, according to the best-established protocol available. The resulting protein sample was characterized by the high occupancy of the tungsten cofactor(s), high enzyme activity and purity.

## 4.1. Specimen preparation

The proteinous sample for CryoEM measurement should be purified to the highest possible homogeneity; therefore, for this study, the AOR<sub>Aa</sub> produced as described in Chapter 1.2. including the step on the size exclusion column. Prior to specimen preparation, the protein was assessed for homogeneity and stability of the particles by mass photometry (see Chapter 4.4.). Moreover, an additional step of crosslinking of protein was also tested with mass photometry according to the protocol shown below.

### *Native sample preparation*

First, the sample of AOR<sub>Aa</sub> without crosslinking (i.e. native unmodified enzyme) was analyzed. The preparation of solution for application on EM grids from the stock of frozen protein was carried out in anaerobic conditions in the glovebox. The frozen stocks containing 4.6 mg/mL AOR<sub>Aa</sub> in 100 mM HEPES/NaOH buffer pH 7.5 with an additional 150 mM NaCl and 10% (v/v) glycerol were thawed on ice. The samples were prepared by dilution of the protein stock with 50 mM HEPES/NaOH buffer pH 7.5, 50 mM NaCl and ultrapure water to levels optimal for EM study yielding a final concentration of 0.7 mg/mL AOR<sub>Aa</sub>, 50 mM HEPES buffer, 75 mM NaCl and glycerol below 2% (v/v).

### *Crosslinked samples preparation*

The cross-linking procedure is used in EM sample preparation if the protein's quaternary structure is unstable at low concentrations (20-100 nM). Mild crosslinking prevents the dissociation of protein subunits while still not significantly influencing their secondary and tertiary structure. A protocol using bis(sulfosuccinimidyl)suberate (BS3, Thermo Scientific™) as a crosslinking agent was previously shown to facilitate studies of oligomeric structures<sup>139</sup>. Therefore, it was a reasonable candidate to be tested for this complex. Stabilization of the protein complex is achieved by the formation of two peptide bonds in the reaction between primary amines (i.e. lysine residues and the N-terminal group of the polypeptide chains ) present on the protein surface and the two ester groups of BS3 linker introducing an 11.7 Å spacer (see **Figure 28**).

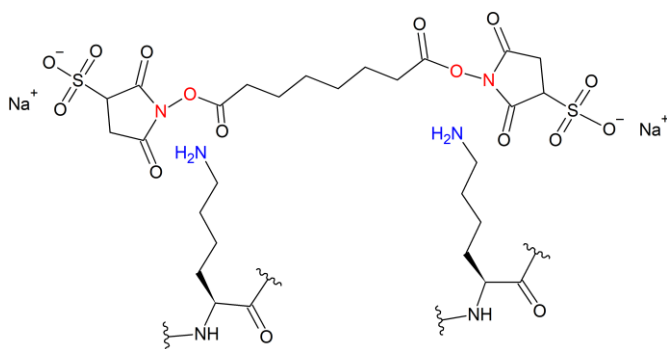


**Figure 28.** The chemical formula of BS3 (top formula) with marked in red bond available for conjugation with amine groups of surface lysines.

The samples prepared with additional crosslinking with BS3 were prepared in the same conditions as native samples. The additional step of crosslinking was optimized by conducting the reaction with BS3 in the range of 0.5-3 mM. The general procedure for crosslinking was started with the preparation of fresh 10 mM stock solution of BS3 in water and then the preparation of crosslinking mixtures with the respective concentration of BS3 (0.5, 1, 1.5 or 3 mM). The crosslinking reaction was started with the addition of 8.7  $\mu$ L AOR to the final concentration of 1 mg/mL. The total volume of each reaction was 40  $\mu$ L. The reaction was incubated for 30 min at 25 °C and subsequently quenched by the addition of 1 M Tris/HCl (pH 7.5) to a final concentration of 30 mM. The quenching reaction was incubated for 15 min at 25 °C. Next, the sample was diluted (as in native sample preparation) to achieve the protein concentration (0.7 mg/mL) required for Cryo-EM analysis.

#### *Preparation of EM grids*

For the preparation of EM grids Quantifoil™ R 2/1 on 200 copper mesh grids (Quantifoil Micro Tools GmbH) were used, immediately after glow discharging in glow discharge cleaning system (PELCO easiGlow) for 25 s with 15 mA current to make the grid more hydrophilic. A series of grids containing AOR<sub>Aa</sub> samples were prepared by vitrification using an automatic plunge freezing device (Vitrobot Mark IV). The sample was kept anaerobic until just before application on the grid, minimizing the impact of oxygen. The only manual step in this procedure is the application of 4  $\mu$ L of sample on a grid, followed by automatic blotting of the sample with filter paper to remove excess moisture and plunging the grid into liquid ethane. The vitrified samples were stored in liquid nitrogen and transported to Frankfurt am Main, Germany, for data collection.



## 4.2. Data collection and processing

Data collection was conducted by technical support staff at the Department of Structural Biology, Central Electron Microscopy Facility, Max Planck Institute of Biophysics on Glacios cryo-TEM (Thermo Scientific). The microscope was working with an accelerating voltage of 200 kV. The camera Falcon 3 in electron counting mode was operating with a raw pixel size of 1 Å, a total exposure dose of 40 e<sup>-</sup> per Å<sup>2</sup> and spherical aberration of 2.7 mm. For the resolved sample, resulting 896 micrographs were processed with cryoSPARC software<sup>140</sup>.

The collected images were corrected for the estimated beam-induced motion and contrast transfer function. Initially, particles were picked with a blob picker, extracted from only 100 micrographs, and subjected to 2D reference-free classification. Selected 2D classes were used to train a model to pick particles from the entire data set using the TOPAZ procedure (more on particle picking in Chapter 7. of the Literature review). The particles selected by TOPAZ were also sorted by reference-free 2D classification and particles selected within the 2D classes were fed again for the TOPAZ training procedure. This was repeated for a total of three iterations of TOPAZ training and particle extraction. As a result, 281,658 particles were extracted by TOPAZ from the whole data set. The best 109,916 particles were selected and subjected to *ab initio* reconstruction resulting in 3 separate classes, which were further utilized to create two 3D reconstructions on entire particle images using homogenous refinement. Both the 3D reconstructions (shown in **Figure 29.A**) were subsequently used for 3D classification using heterogeneous refinements. All classes were used in non-uniform refinement to create a 3D reconstruction of the AOR complex with an overall resolution of 3.3 Å. An in-depth explanation of the 3D reconstruction can be found in a review<sup>141</sup>.

The reconstruction of the protein chain was facilitated by the construction of a homology model of each subunit prepared in AlphaFold<sup>142</sup>, which was then fitted in Chimera<sup>143</sup> to electron density.

The model was fitted into the reconstructed density using COOT<sup>144</sup> and iteratively refined using Phenix Real-space Refinement<sup>140</sup>. Images of density and built model were prepared using UCSF Chimera, UCSF ChimeraX and PyMOL<sup>145</sup>. The model was validated based on the Ramachandran plot. 98%+ residues should have a main chain conformation consistent with the Ramachandran distribution and any outliers should be justified by the strained surrounding (cofactors) and density map.

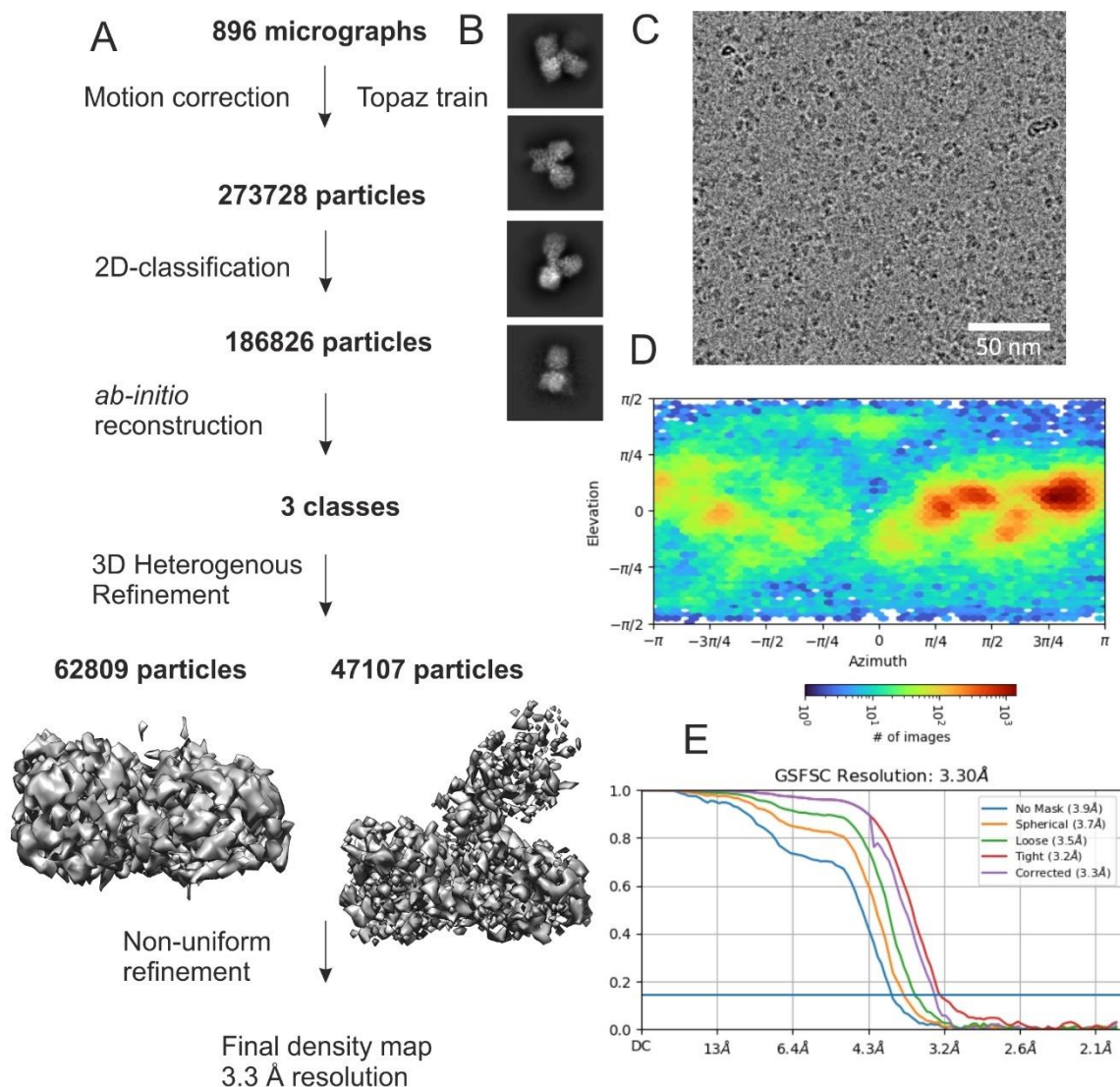


**Figure 29.** Data processing. **A)** Overview of the cryo-EM data-processing scheme; **B)** Reference-free 2D class averages showing AOR in multiple orientations; **C)** Representative cryo-EM micrograph collected on a Glacios Cryo-TEM operated at 200 kV and equipped with a Falcon 3 camera; **D)** Angular distribution of the particles used for the final round of refinement. **E)** Fourier Shell Correlation (FSC) curves of unmasked and corrected 3D maps.

### 4.3. Bioinformatic and visualization tools

The sequence alignments presented through this work were conducted by EMBOSS Needle, available on-line via EMBL-EBI, run with a gap penalty: 5.0, extend penalty: 0.5.

The structural alignments were conducted according to the internal protocol of Biovia Discovery Studio v.18 software. Visualization of structures was conducted with PyMOL<sup>145</sup> PyMOL™ Molecular Graphics System, Version 2.6. or ChimeraX 1.2.5<sup>146</sup>. The interfaces

present in the protein complex were analyzed with PDBePISA, EMBL-EBI on-line tool<sup>147</sup>. The protonation states of residues were estimated by pK<sub>a</sub> values calculated by the PROPKA 2.0 procedure<sup>148</sup>.

The structural similarities of the reconstructed protein subunits were investigated by screening the database of known structures according to the Distance matrix alignment (Dali) protocol available on the Dali web server<sup>149</sup>. The similarity of aligned structures is quantified by a few factors: Z-score, RMSD and LALI. RMSD (root mean square deviation of rigid-body superimposition) is a measure of the average deviation in the distance between aligned C<sub>α</sub> atoms in 3D superimposition. Z-score is Dali's scoring function that, in contrast to RMSD, allows flexible superimposition or plastic deformations. LALI is a number of residues that have an equivalent in the compared structure. About 10 of the best results recognized by the Dali protocol were analyzed, used as a reference for structure-function analysis and selected pairs were described in the Results section.

#### **4.4. Mass Photometry**

The mass photometry method allows for accurate measurement of the mass distribution of biomacromolecules in a sample containing unlabelled protein<sup>150</sup>. The measurement is based on the quantification of light scattering from individual biomacromolecules in a very diluted (<100 nM) solution placed on a microscope cover glass. During measurement, the biomolecules adhere to the cover glass, exchanging water and causing reflectivity changes, which is called a binding event (illustrated in **Figure 30**). The binding events are recorded in time as a movie for about 1 min. The mass photometry contrast of the binding event is proportional to mass of the protein. During data analysis, individual binding events of respective contrast are counted and based on the external calibration, the exact mass of each biomolecule is calculated. The method yields information on the heterogeneity of the sample with good accuracy of mass and single-molecule precision (2% mass error and up to 19-kDa resolution). The time-dependent data may show disassembly processes<sup>151</sup>.

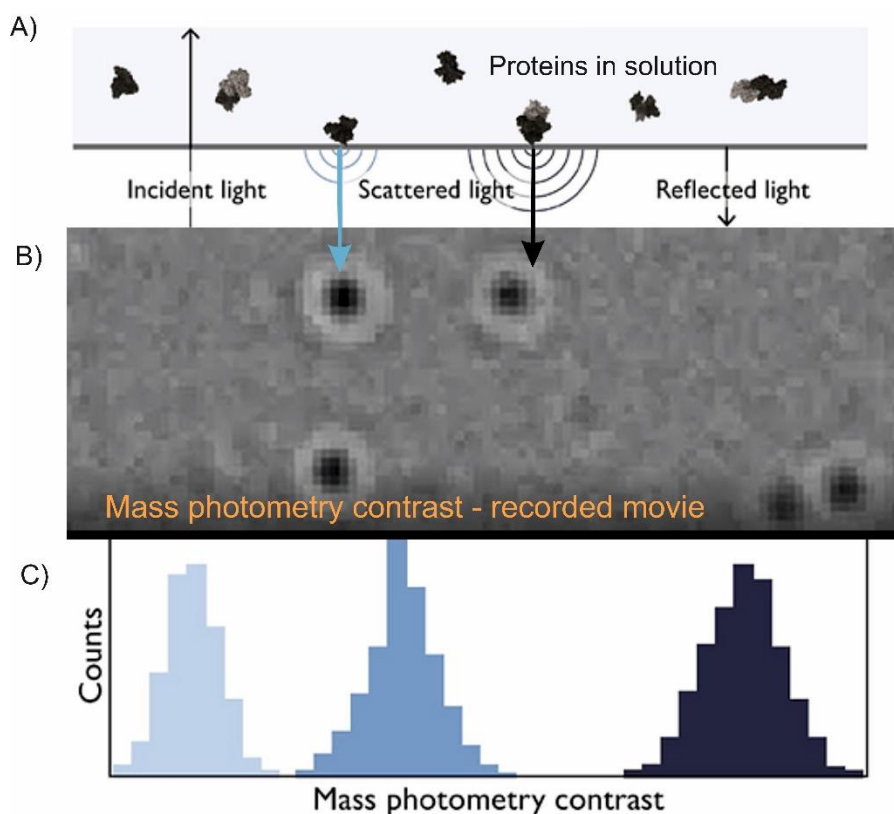


**Figure 30.** Principle of contrast acquisition in mass photometry. *Up* during measurement particles in the solution adsorb on the measurement interface and cause scattering of the laser light. The scattered light creates incident contrast in the movie (*middle*), all incidents of given contrast are then quantitated (*bottom*). Figure adapted from Refeyn Ltd.

The measurements were performed using a OneMP mass photometer (Refeyn Ltd, Oxford, UK), with data acquisition by AcquireMP software (Refeyn Ltd. v2.3). MP movies were recorded at 1 kHz, with exposure times automatically adjusting between 0.6 and 0.9 ms during measurement to maximize camera counts and avoid saturation. Microscope coverslips ( $70 \times 26 \text{ mm}^2$ ) were cleaned for 5 min in 50% (v/v) isopropanol (HPLC grade in ultrapure water) and subsequently in pure ultrapure water and then dried with a pressurized air stream. Silicon gaskets holding the sample drops were cleaned as above and fixed to clean glass slides right before measurement. Right before measurements, the instrument was calibrated using the NativeMark Protein Standard (Thermo Fisher Scientific). To find focus, 18  $\mu\text{L}$  of fresh buffer (10 mM Tris pH 8.0, 100 mM KCl, and 0.1 mM EDTA) was inserted into a gasket well, and the focal position was identified and locked using the autofocus function of the mass photometer. Just before measurement started, 2  $\mu\text{L}$  of the sample was added to the well, resulting in a 10-fold dilution of the sample. The measurement was started right after the addition of the

sample and the measurement procedure was repeated for each sample 3 times and each protein was measured in a new gasket well.

The data analysis was conducted using DiscoverMP software, which converts the contrast values to molecular masses based on calibration. The data were plotted, using Origin2019 software, on histograms with a bin value of 4 kDa, which was chosen based on the noise of measurement. The data were fitted with distribution peaks of the Gaussian function to determine the average molecular mass of the distribution (example of fit shown in **Figure 50**).

## 5. Theoretical methods

Since the structure of AOR<sub>Aa</sub> was not known at the beginning of this project, the structure of AOR from *Pyrococcus furiosus* (pdb accession code 1AOR) was used as a model for theoretical studies of AOR. The AOR<sub>Pf</sub> and AOR<sub>Aa</sub>, albeit with only 49.8% sequence identity, 63.5 % similarity to each other (aligned with EMBOSS Needle), have many important amino acids conserved, especially in the active site cavity.

To analyze the possible coordinations of tungsten in the cofactor identified in AOR from *Pyrococcus furiosus*, which did not contain any identified ligands in the deposited 1AOR structure, the constructed model structures were optimized by theoretical methods and then the electron densities were compared. Shortly, this approach required steps: i) optimization of the initial models in the gas phase (QM-only cluster models) with Density Functional Theory which also enabled parametrization of the cofactors for hybrid QM:MM methods; ii) the QM:MM geometry optimization gave a final structure of cofactor constrained by protein surroundings ; iii) the models were used to prepare the differential density maps allowing assessment of fit of the model to electron density map corresponding to 1AOR. At the end of the project, the electron density map of AOR<sub>Aa</sub> was available and the fit of the selected model to this density could be visually accessed. The optimization of three selected models by the QM:MM method was conducted by prof. Maciej Szaleniec.

Quantum mechanics (QM) methods are employed to describe a system taking into account the electronic structure of molecules. The principle of the QM methods is solving the approximation of the electronic Schrödinger equation for the system in order to find electron densities and energies in a stationary state of a molecule or to characterize transitions between two stationary states<sup>152</sup>. The QM methods are also applied when modelling chemical reactivity, as they allow for modelling bond breaking and bond forming.

The simplest model of molecule used in QM methods describes each electron trajectory in the average field of all others. So-described electron probability distributions are the molecular orbitals of the Hartree-Fock (HF) theory. According to this model, typically only ~99% of total energy can be calculated, and the assessment of remaining energy (called correlation energy) is important for the accuracy of calculations. The correlation energy corresponds to the interactions between electrons, which were omitted due to averaging of the electrons field. The correlation energy is calculated after the molecular orbitals have been found, improving the resulting energy and the overall correction method is called post-HF.

Density Functional Theory (DFT) is an approach where instead of calculation of intermediate many-electron wave function, only the electron density  $\rho(r)$  is calculated to describe the exact ground state of the system. This approach is based on the first Hohenberg-Kohn theorem, which proves that the ground state electron energy is fully determined by the electron density  $\rho(r)$  and the calculated energy is greater than or equal to the real energy<sup>153</sup>.

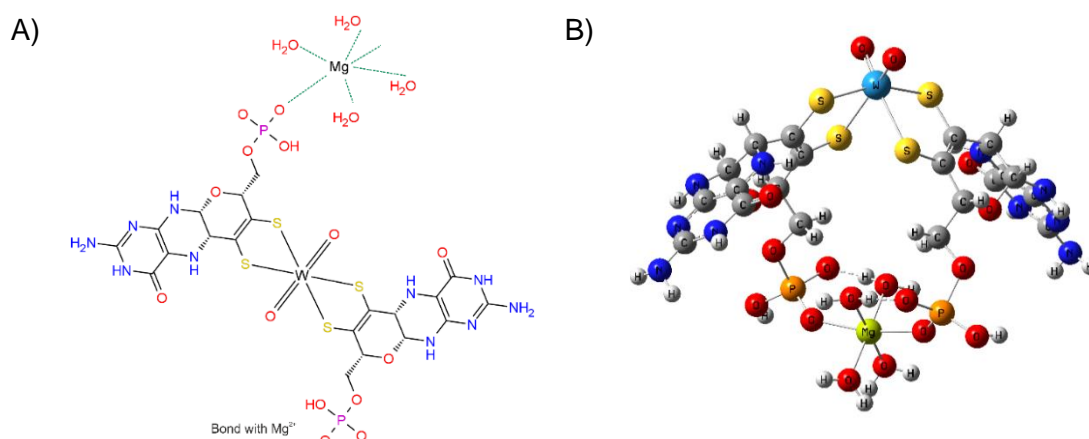
The calculation of energy defined by electron density functional  $\rho(r)$  is based on the Kohn-Sham theory<sup>154</sup>. In this theory, the interactions between electrons are replaced with the concept of Kohn-Sham electrons that do not explicitly interact with each other (but interact with nuclei and the external field) as they move in the effective potential field  $V_0$ . The  $V_0$  potential takes into account the two-electron interactions (Coulomb correlation) and the exchange-correlation (statistical), as well as the correction to the kinetic functional (the difference between the functional for Kohn-Sham electrons and the functional for real electrons) and the correction to reduce the self-interaction energy. The analytical form of exchange-correlation functional is not know and therefore different approaches to estimate its value are used.

The DFT approach simplifies the calculations significantly to the function of only 3 variables, making them less computationally demanding than post-HF methods. Nevertheless, the QM calculations require resource-demanding computations and the computing power demand depends exponentially on the size of the systems. Current computers allow fast optimization of systems built by about 300 atoms. Biological systems, like the studied enzyme, consisting of thousands of atoms (e.g. AorB about 9400 atoms) and QM-only calculations of such a system would be unfeasibly expensive and beyond the limit of available algorithms considering the size of the matrix. Therefore, only the active site cofactor was included in the model QM-only cluster models.

In hybrid methods, the correlation-exchange potential contains Hartree-Fock exchange energy. Many exact energy calculations for metalloenzymes containing transition metals were obtained using hybrid methods proving their robustness<sup>155</sup>. The functional used in this work, B3LYP, contains 20% of HF exchange.

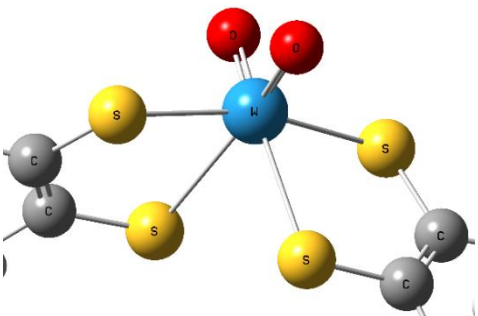
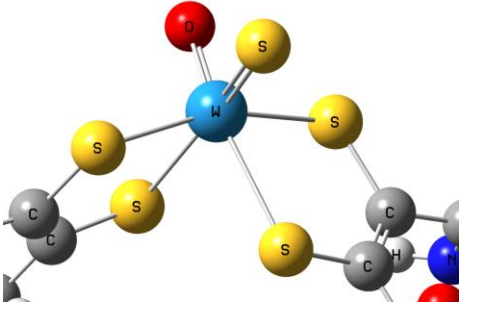
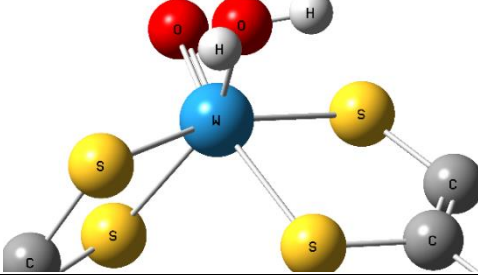
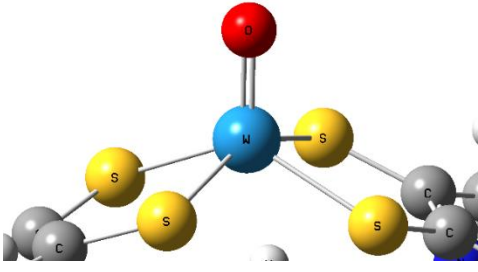
### 5.1. Quantum mechanics (QM) in modelling of enzyme active site cofactor.

The initial geometry of the tungsten cofactor was taken from the crystal structure of AOR from *P. furiosus* (PDB code 1AOR). The first stage of the study was the optimization of possible structures of W-co in the QM-only cluster model. The models included the tungsten atom coordinated by two metallopterins and two other ligands (as described later), magnesium coordinated by two water molecules and the phosphates from the two MPTs. In the enzyme, the negatively charged phosphate groups are neutralized by electrostatic and H-bond interaction with positively charged Arg residues. To account for this, the phosphate groups were protonated with one proton each. Additionally, as shown in **Figure 31**, two amino acids coordinating the magnesium ion with their carbonyl groups were replaced by water, thus providing an octahedral coordination sphere to Mg<sup>2+</sup>. The pterin form was assumed to be tetrahydropterin, as this is the most abundant redox isoform shown in literature for Mo- and W-enzymes<sup>84</sup>. Possible tungsten coordination and oxidation states were deduced from the EXAFS and structural insights (further discussed in the Results section, the models were shown in **Table 9**). The models were built in GaussView 6.0.16 software by the addition of respective atoms at the tungsten coordination sphere, hydrogen atoms and two additional water ligands for magnesium. The overall charge of the model was -2 and calculations were conducted for a singlet state.

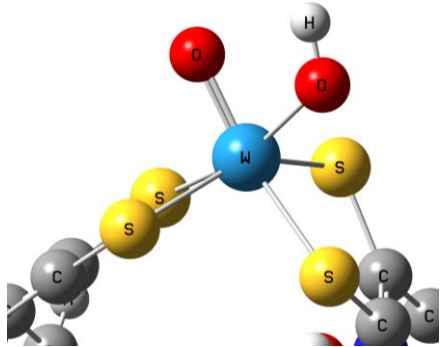
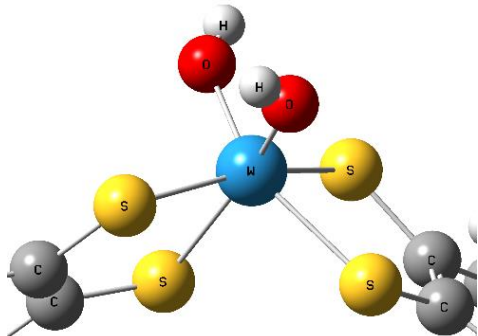


**Figure 31.** A) Representation of tungsten cofactor (example with two oxo ligands) prepared as an input for DFT modelling, B) 3D view and scheme showing atom bonding. Image from GaussView.

**Table 9.** Input models of AOR<sub>Pf</sub> W-co proposed based on spectroscopic data with initial geometry of tungsten coordination. Names of models showed in this table were used throughout the text to simplify description.

Model	Ligand	Image of the tungsten coordination sphere
$[W(VI)(O)_2(MPT)_2Mg(H_2O)_4]^{2-}$	two oxo ligands	
$[W(VI)SO(MPT)_2Mg(H_2O)_4]^{2-}$	one oxo and one thio ligand	
$[W(IV)O(H_2O)(MPT)_2Mg(H_2O)_4]^{2-}$	oxo ligand and water	
$[W(IV)O(MPT)_2Mg(H_2O)_4]^{2-}$	oxo ligand	



$[W(IV)O(OH)(MPT)_2Mg(H_2O)_4]^{2-}$	one oxo ligand one hydroxo ligand	
$[W(IV)(OH)_2(MPT)_2Mg(H_2O)_4]^{2-}$	two hydroxo ligands	

The W-co model structures were optimized by the quantum mechanics method with density functional theory in a vacuum at 0 K in a gas phase, i.e. without the explicit or implicit solvent or protein environment. Optimization of structures was conducted by *ab initio* DFT method using Gaussian09 package<sup>156</sup>. The electron functional was described by the hybrid functional of Hartree-Fock exchange and DFT exchange-correlation the restricted B3LYP<sup>157</sup>. Atomic orbitals were represented using respective basis set: 6-311+G(d) for S, and 6-31G(d,p) for the H, C, N, O, P, Mg atoms and LANL2DZ for valence electrons of W while the core electrons were described by LANL2DZ potential. The above selection of functionals and basis sets has reportedly been used before with accurate results in studies of oxygen-atom transfer reactions in molybdenum and tungsten enzymes from the DMSOR, SO and XO families<sup>57,100,158</sup>. The structure geometry was optimized according to the Berny geometry optimization algorithm<sup>159</sup>. After the geometry optimization reached convergence (**Figure 32**), a vibrational analysis was conducted for each model to confirm that the stationary point was reached. The optimized models were assessed based on their geometry in Discovery Studio and compared to experimental data (EXAFS, structure).

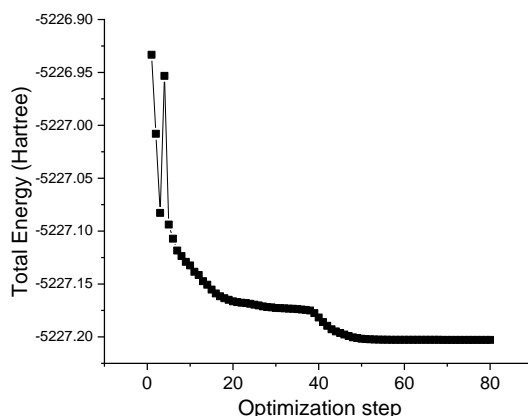


**Figure 32.** Progress of geometry optimization depicting the decrease in total energy of W(IV)O(H<sub>2</sub>O) model.

## 5.2. Parametrization of W cofactor for AMBER and geometry minimization

Molecular Mechanics methods are based on classical mechanics and can be used to describe large systems (hundreds of thousands of atoms) as they are less computationally expensive than quantum mechanics methods. In this method, the potential energy of the system is determined using an appropriate 'force field' i.e., a function, which describes binding and non-binding interaction within the model. In this work, an AMBER force field (ff03) was used in QM:MM calculations. The parameters and functions building the force field come from both experimental measurements and quantum mechanical calculations.

The AMBER (Assisted Model Building with Energy Refinement) force field was used to carry out molecular dynamic simulation in the software package also called Amber 16<sup>160</sup> used in this work in calculations carried out on PLGrid Infrastructure (ACK Cyfronet).

The vibrational analysis of the optimized [W(VI)(O)<sub>2</sub>(MPT)<sub>2</sub>Mg(H<sub>2</sub>O)<sub>4</sub>]<sup>2-</sup>cofactor included the calculation of the Hessian matrix, which carried information on force constants. For all bonds and angles within the first coordination shell of the tungsten atom, the value and respective force constants were calculated based on the Hessian matrix using XYZViever\_097 software provided by courtesy of Sven Marothy according to the method developed by Seminario<sup>161</sup>.

Point charges were computed in the gas phase using the Merz–Kollman electron density calculation method<sup>162</sup> in Gaussian16, followed by the RESP procedure implemented in the ANTECHAMBER program from the AMBER\_TOOLS software package<sup>163,164</sup>.

The RESP procedure derives partial point atomic charges from QM calculations using a least-squares fit of the calculated electrostatic potential on the molecular surface to that of the partial charge model<sup>162</sup>. The ANTECHAMBER assigns atom and bond types based on atomic connectivity<sup>163</sup>. The above parametrization was conducted for tungsten, sulfurs and oxo ligands as non-standard atom types, while the pterin atoms were described with a general Amber force field (GAFF) designed to describe organic ligands<sup>164</sup>. To enable the building of input for AMBER, the W-co was divided at the W atom into three new type ligands: YYB (W and oxo ligands), YYC (from dithiolene whole pterin distal from Fe<sub>4</sub>S<sub>4</sub> cluster) YYD (the proximal pterin to Fe<sub>4</sub>S<sub>4</sub> cluster) and magnesium ion. The partial charges and bond and angle parameters for the Fe<sub>4</sub>S<sub>4</sub> cluster were adapted from Carvalho *et al.*<sup>165</sup>.

The protein was described with the ff03 force field<sup>166</sup>, and the water solvent was described by the TIP3P water model not to add bias to the system, as TIP3P water was used in the parametrization of the ff03 and gaff<sup>167</sup>. Initial coordinates of the protein were taken from the X-ray crystal structure of AOR<sub>Pf</sub> (PDB: 1AOR), with the cofactor exchanged for the respective DFT-optimized model. The protonation states of titrable residues were predicted based on the pK<sub>a</sub> values calculated by the PROPKA 2.0 procedure<sup>148</sup> and pH=8.0, i.e. the optimum pH for the aldehyde oxidation. The protonation state of amino acids was chosen as unprotonated for CYS 291, 288, 295, 494 (binding of Fe<sub>4</sub>S<sub>4</sub> cluster), protonated all lysines and tyrosines, neutral (single protonation at N $\delta$ ) His 128, 335, 362, 383, 435, 568 and doubly protonated His 136, 181, 412, 448, 468. AMBER topology and coordinate files were generated by the LEaP program.

Models were solvated with approximately 15 600 water molecules (TIP3P water model), ensuring a 10 Å radius around the protein. The global charge of the system was -13 and it was neutralized by the addition of 13 Na<sup>+</sup> ions. The positions of waters and sodium ions were initially minimized with AMBER16 using the steepest descent (first 500 steps) and conjugated gradient (subsequent 2000 steps) algorithms for each of the 5 minimization steps in the following sequence. In the first step, only water molecules were minimized (the position of protein atoms was restrained with a force constant of 500 kcal/mol Å<sup>2</sup>). The next four steps of the minimization procedure were performed with decreasing restraints imposed on protein from 500 to 0 kcal/mol<sup>2</sup>.

### 5.3. QM:MM modelling

The computations for two-step geometry minimization by the QM:MM method were conducted by prof. Maciej Szaleniec based on the model prepared within this work.

A solution for accurate and feasible calculations of metalloenzyme structure and properties used in this work was a hybrid QM:MM method. The method used in this work combines expensive QM (<sup>high</sup>) and with a less expensive calculation method, here molecular mechanics (MM) using AMBER force field (<sup>low</sup>) by treating the “model system” (active site environment, where a chemical reaction takes place, called high layer) with the more accurate method, while the MM calculations treat the environment system (low layer). There are different approaches combining both levels in terms of boundary atoms treatment and energy calculation. In this work, the ONIOM (Own N-layer Integrated molecular Orbital molecular Mechanics) designed by Morokuma and coworkers<sup>168</sup> scheme was used to describe the whole system.

The two layered-ONIOM method approximates the energy of the Real System (RS) with a combination of the energies computed by the less computationally expensive methods and the energy of the Small Model (SM) described by a high layer computed at the high QM method.

Therefore, the energy of the model  $E^{\text{high}}(\text{RS})$  is:

$$E^{\text{high}}(\text{RS}) \cong E^{\text{low}}(\text{SM}) + [E^{\text{low}}(\text{RS}) - E^{\text{low}}(\text{SM})] + [E^{\text{high}}(\text{SM}) - E^{\text{low}}(\text{SM})]$$

where the first bracket provides the energy of the low layer calculated with a cheaper method while the second bracket corrects the small model (i.e. high layer) energy calculated with a cheaper method with a more expensive method. As a result, the ONIOM energy is calculated accordingly to the following formula:

$$E^{\text{ONIOM}} = E^{\text{low}}(\text{RS}) + E^{\text{high}}(\text{SM}) - E^{\text{low}}(\text{SM})$$

The main distinction of ONIOM is the treatment of covalent interactions between atoms in the high layer and low layer. When the boundary of the high layer crosses the covalent bonds, they have to be substituted with a hydrogen link atom. This method does not require parametrization of the bond and allows for flexibility of the link atom (bond in question). However, breaking the bond has to be far from the reaction site and should be placed on the non-polarized bond (typically single C-C bonds), which can be, to some extent, approximated by bonding to the H atom.

Another choice to be made when designing ONIOM calculation is how the electrostatic interactions between both layers should be treated. In the chosen approach of electronic embedding<sup>169</sup>, the charge distribution of the low layer interacts with the high layer partial charges. The wave function of the QM part can be polarized by the charge distribution of the low layer. The electronic embedding gives a more accurate electrostatic description

of the system than the mechanical embedding, which accounts only for steric interactions between high and low layers<sup>170</sup>. In this work, the QM:MM geometry optimization protocol utilized mechanical embedding in the first phase, and after reaching convergence, it was followed by geometry optimization using electronic embedding.

The initial geometry for QM:MM minimization was taken from the last minimization step for the parametrized model  $(W(VI)(O)_2(MPT)_2Mg)$  and included a water shell of 5 Å around the protein.

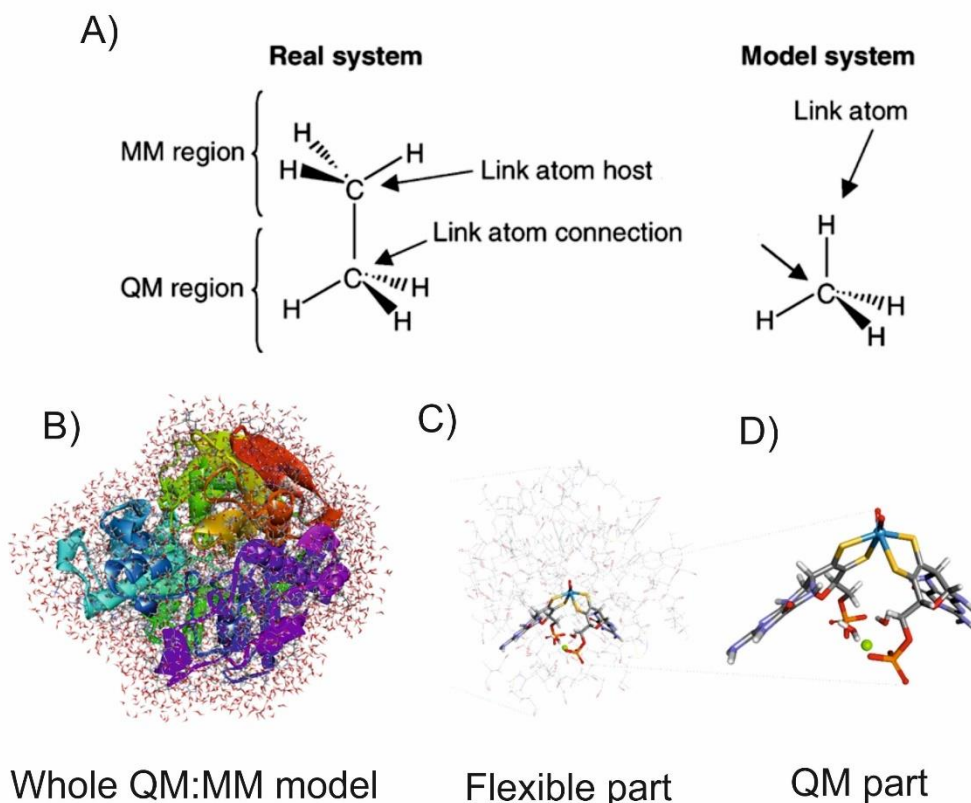


**Figure 33.** **A)** Scheme of link atom treatment of bonds between QM and MM region in QM:MM method; **B)** Whole QM:MM model of AOR<sub>Pf</sub> (one subunit) used for modelling W-co. **C)** Flexible part of the model subjected to geometry optimization, **D)** QM part treated at a quantum chemical level.

The QM part was described by the B3LYP density functional method with the basis set and pseudopotential as for QM-only calculations (see above), and the MM part was treated by the AMBER16 force field. The first structure optimized in QM:MM was with  $[W(VI)(O)_2(MPT)_2Mg]^{2-}$  model cofactor, and later the  $[W(IV)O(OH)(MPT)_2Mg]^{2-}$  and  $[W(IV)O(OH)_2(MPT)_2Mg]^{2-}$ . QM:MM models were built by replacement of the oxo ligand at W atom with OH or OH<sub>2</sub> groups, respectively. The QM part contained the whole W-co: W(VI) atom coordinated by two oxo ligands, two pterins in dihydro form and the Mg<sup>2+</sup> ion

coordinated by two H<sub>2</sub>O ligands and phosphate groups from the pterins. The flexible region subjected to geometry optimization included the QM region and all residues and water molecules of the MM region covering the 12 Å radius of the W atom (**Figure 33**).

The models were not subjected to MD simulations, as those do not reflect conditions for crystallized protein. For [W(IV)O(OH)<sub>2</sub>(MPT)<sub>2</sub>Mg]<sup>2-</sup>, geometry optimization was performed only with mechanical embedding due to the spontaneous dissociation of aqua ligand already at this stage of calculations.

#### 5.4. Refinement with W-co model

The geometries obtained from QM:MM optimization were used to fit with the electron density map of the AOR<sub>Pf</sub> (the map corresponding to PDB structure 1AOR). Fitting was conducted in Phenix v.1.19. Refine, using the deposited structure of AOR<sub>Pf</sub> (1AOR) with the original ligand-less W-co exchanged for the new W-co model and constraints generated from the mentioned above QM:MM analysis of the W-co models. The fit of the models to the 1AOR electron density map was done in two iterations: i) the W-co was fitted to map with a standard Cartesian refinement of model geometry; ii) next, the initial model was superimposed with fitted W-co to choose optimal XYZ for fit and the initial model was used as an input to rigid-body fit with occupancy optimization in Phenix Refine. The second fit iteration resulted in electron density differential maps illustrating the quality of fit of the QM:MM optimized models.

## 6. EXAFS

The protein for this study was heterologously expressed AOR<sub>Aa</sub> produced and purified on the Strep-tag column according to methods shown in Chapter 1.2. The purified protein in 100 mM Tris/HCl buffer pH 8.0 with 100 mM NaCl was concentrated to 111 μM on Centrifugal Filter Unit (Amicon, 10kDa, centrifuged at 3400 x g). Next, the protein was divided into 3 aliquots from which three types of samples were prepared:

- i) Oxidized AOR<sub>Aa</sub> – solid ferrocenium tetrafluoroborate was added to the protein solution as an oxidizing agent to a final concentration of 1 mM;
- ii) Reduced AOR<sub>Aa</sub> - solid sodium dithionite was added to the protein solution as a reducing agent to a final concentration of 1 mM;
- iii) ‘As isolated’ AOR<sub>Aa</sub> – no reagents were added.

Protein was incubated with the reactants for 15 min at room temperature and then packed into specialized plastic holders and rapidly quenched by contact with a metal block cooled in liquid nitrogen (adjustment to conduct freezing in the anaerobic

chamber). The samples were sent on dry ice to Canada and were studied by EXAFS at the W L<sub>III</sub> edge on the Canadian Light Source synchrotron of the University of Saskatchewan by a group of prof. Graham George. Data were fitted with W-co models provided by theoretical research. Samples were handled anaerobically or frozen to maintain the oxidation state of W.

## RESULTS AND DISCUSSION

### Part I. Enzyme preparation.

#### 1. Protein production.

Initially, the protein production was achieved by fermentation of *A. aromaticum* strain SR7 $\Delta$ *pdh* on phenylalanine in a total volume of 35 litres. To achieve high yields of enzyme production, the fermentation was carried out until the end of the logarithmic phase of bacterial growth, which was established after *ca.* four days of cultivation (95 h). Slowing down of bacterial growth was observed after 96 h as illustrated in **Figure 34** representing the dependence of OD<sub>600</sub> on time. The doubling time for *A. aromaticum* SR7 $\Delta$ *pdh* during the fermentation was 21.5 h. After centrifugation, 220 g of wet cell mass was collected. The cells were used to obtain AOR<sub>Aa</sub> via the native purification protocol.

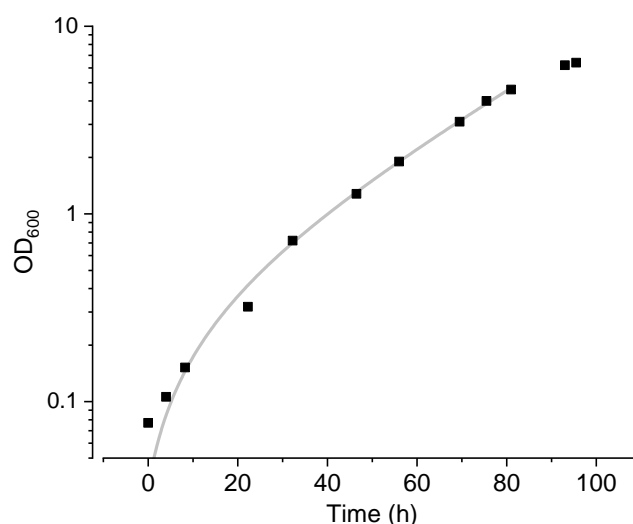


**Figure 34.** *A. aromaticum* SR7 $\Delta$ *pdh* strain growth curve measured during fermentation, points represent measurement of OD<sub>600</sub>, the line represents fit of an exponential curve.

#### 1.1. Fermentation of *A.evansii* in a bioreactor

Fermentation of recombinant AOR-expression strains in 30-litre fermenters was conducted to achieve high amounts of cells containing the target protein. The fermentation of *A.evansii* with plasmid pASG\_105\_AOR\_full was also a proof-of-concept for scaling-up of the manufacturing process of the attractive biocatalyst.

The Sartorius fermenters enable to archive all parameters of cultivation in time and to represent the time course of fermentation of *A.evansii* pASG\_105\_AOR\_full (one of 4 conducted), the most important factors are shown in **Figure 35**. The data on temperature, redox potential and amount of acid added to equilibrate pH to the preset value in **Figure 35** were collected by the fermenter controller and additionally, electron



acceptor concentration and OD<sub>600</sub> values were noted in **Table 10**. When no more nitrate or nitrite was detected by strip test, the culture was resupplied with a mixture of NaNO<sub>3</sub> and sodium benzoate (in 5:2 molar ratio). In the exponential phase of the culture, growth proceeded with a doubling time of about 5 h.

The most interesting parameter turned out to be the redox potential, which can signal oxygen contamination, and its changes during the culture were dependent on the type of microorganism grown<sup>171</sup>. As redox potential depends on the amount of oxygen in media, its value should get lower during the anaerobisation of an anaerobic culture. This phenomenon was indeed observed during the purging step of the fermenter with nitrogen prior to inoculation. For *A. Evansii*, one can identify characteristic changes in the redox value that are most probably linked with the time-dependent depletion of nitrate and nitrite. As shown in **Figure 35**, the fermentation starts with 10 mM NO<sub>3</sub><sup>-</sup> as an electron acceptor and redox potential stabilizes at -70 mV after addition of inoculum. Then at 12 h of fermentation, a first drop of the redox value occurs, however, nitrate is still present (as measured by Quanofix test). At 21 h the next drop of redox value occurs and readings show no more nitrate at 23 h 40 min. Additionally, there are long time slots (i.e. between 12 and 21 h of fermentation) in which sulfuric acid was automatically added at a constant rate to maintain the preset pH value of the medium. The automatic response of the fermentor means that during these time slots, the pH was changing to more basic. These slopes start after the first drop in redox potential and finish when the second drop in redox potential begins. The pH changes were most probably resulting from the reduction of NO<sub>2</sub><sup>-</sup> ions to N<sub>2</sub>O and/or nitrogen.

**Table 10.** Reading of redox potential and pO<sub>2</sub> from electrodes in the fermenter, the reading of nitrate/nitrite test strip (plus means present, minus – not detectable), the measured OD at 600 nm of the culture.

Age of fermentor	Redox (mV)	pO <sub>2</sub> (%sat)	NO <sub>3</sub> <sup>-</sup> / NO <sub>2</sub> <sup>-</sup>	OD <sub>600</sub>	Comments
0 h	-4	0.2	+/+	0.044	Addition of inoculum
4 h 20 min	-74	0.0	+/+	0.118	
20 h 30 min	-217	0.0	+/+	0.830	Start of cooling to 18 °C
23 h 40 min	-282	0.0	-/-	0.942	Induction and feeding
43 h 20 min	-362	-1.4	-/-	1.604	Feeding

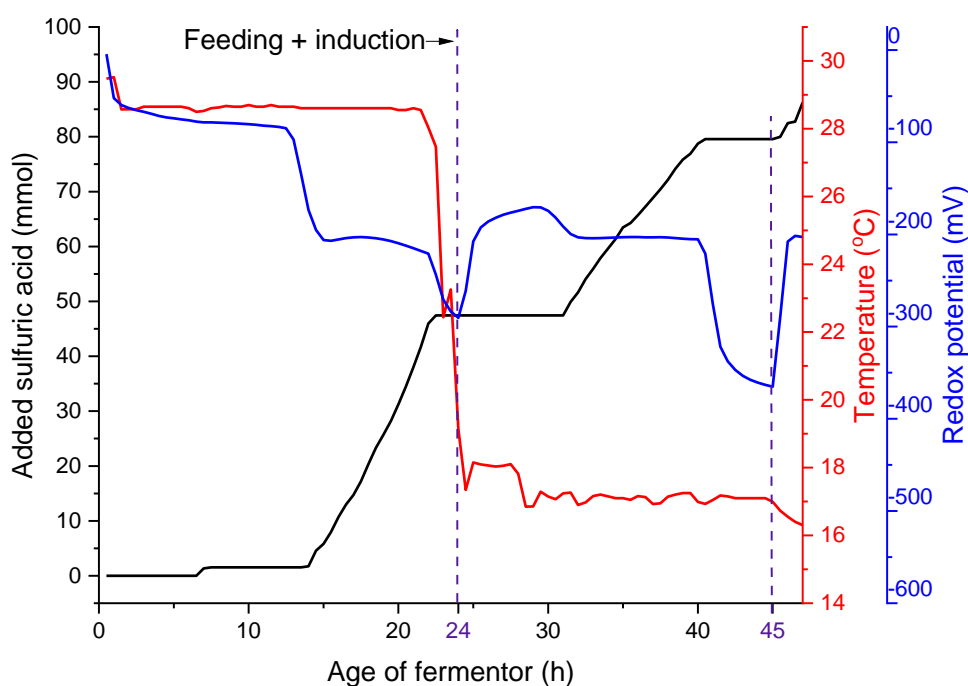


**Figure 35.** The amount of added acid to equilibrate pH (black line), temperature (red) and redox potential (blue) values measured by fermenters electrodes in time of *Aromatoleum evansii* culture. The dashed line at 24 h indicates the first detected depletion of electron acceptor and the first feeding and induction with anhydrotetracycline. The dashed line at 45 h corresponds to the second feeding. At 45 h the centrifugation was started.

After centrifugation of media at 45 h of fermentation, 30 g of wet cell mass was collected. The cell mass was divided into 5 aliquots, that were frozen and kept until purification on affinity chromatography. The final yield of purified AOR<sub>Aa</sub> from this fermenter was a total of 107 mg of active protein.

## 1.2. Protein purification.

The cells from each fermentor were opened by sonication and the protein was purified by the native purification protocol for *A. aromaticum* SR7 $\Delta$ *pdh* cells and by affinity chromatography for the induced cells of *A. evansii* pASG\_105\_AOR\_full. In some cases (i.e. for structural studies), the pools from affinity chromatography were additionally purified on the size-exclusion column (Superdex 200). The pool exhibiting AOR activity eluted in a single, wide peak of retention time (55 min with 1 mL/min flow, shown in **Figure 36**) corresponding to mass 300 kDa, according to calibration of the column.

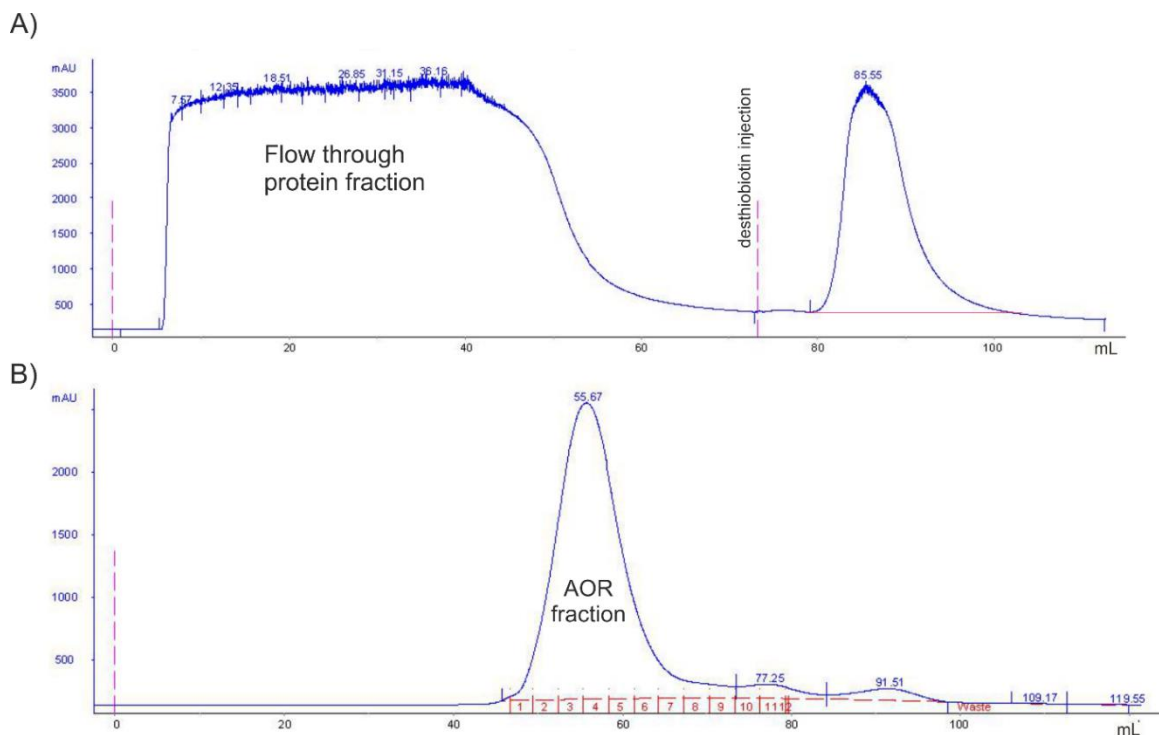


**Figure 36.** Chromatogram of absorbance (mAU) vs. retention volume (mL) for AOR purification steps on A) Strep-tag<sup>®</sup> II column (CV=5 mL); B) gel filtration column (CV=120 mL).

The native purification yielded an “native” AOR<sub>Aa</sub> preparation with the specific activity of 12  $\mu\text{mol min}^{-1} \text{mg}^{-1}$  measured with 1 mM NAD<sup>+</sup>, 1 mM benzaldehyde in 100 mM Tris/HCl pH 8.0 at 30 °C under aerobic conditions (activity measured from anaerobic protein stock). The recombinant AOR<sub>Aa</sub> preparation from the affinity chromatography column yielded samples of specific activity measured with benzaldehyde (as above) of 31.3  $\mu\text{mol min}^{-1} \text{mg}^{-1}$ . The additional step of recombinant AOR<sub>Aa</sub> purification on the gel filtration column resulted in preparations of only 18  $\mu\text{mol min}^{-1} \text{mg}^{-1}$  (conditions as above).

The purity of each AOR<sub>Aa</sub> preparation was accessed by SDS-PAGE analysis and representative results are shown in **Figure 37**. A gradual enrichment of AorA, AorB and AorC (bands of 66, 46 and 17 kDa) can be observed between samples from native purification in order from cell extract (lane 4), after Q-Sepharose column (lanes 2,3) after CHT column (lane 5) to final purity of native AOR<sub>Aa</sub> preparation after gel filtration column (lane 6 and 7). However, in the purified AOR<sub>Aa</sub> sample a substantial amount of other proteins was still present, as other similarly distinct bands are visible in lanes 6 and 7.

The SDS-PAGE analysis showed that the tagged version of the protein was purified to homogeneity by affinity chromatography column and, therefore, can be used in catalytic tests. The presence of relatively faint bands not corresponding to AOR<sub>Aa</sub> subunits

indicated minimal contamination with other proteins, which could, however, pose a problem in structural studies. For this reason, the protein used in structural studies was additionally purified on a gel filtration column.

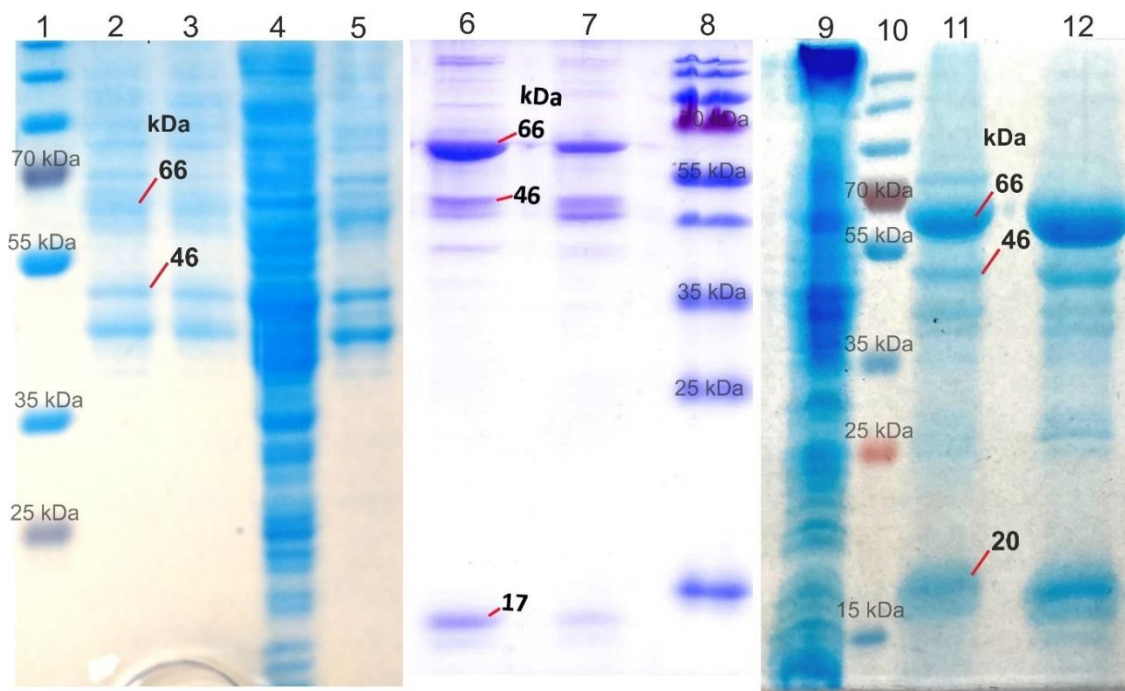


**Figure 37.** SDS-PAGE analysis of the active fractions obtained during AOR<sub>Aa</sub> native purification (1-8) and purification by affinity chromatography of recombinant AOR<sub>Aa</sub> version (9-12). 1,8,10 - protein ladder; 4 - cell extract obtained from *A. aromaticum* SR7Δ*pdh* strain; 2,3 – Q-Sepharose pool of AOR, 5 - ceramic hydroxyapatite column pool which was applied later on gel filtration column and purified to the relatively homogenous pool (6,7). 9 - cell extract obtained from *A. evansii* induced to produce AOR<sub>Aa</sub>; 11 - Strep-tag column pool of AOR activity; 12 - gel filtration column pool of AOR<sub>Aa</sub>. AOR subunits were identified on the gel as bands indicated by masses 66 kDa (AorB), 46 kDa (AorC) and 20 kDa (AorA with Twin-Strep-tag).

The separation of the protein pool after the gel filtration shows additional bands with masses around 40, 38, 26 and 17 kDa, which cannot be identified as AOR<sub>Aa</sub>. The minor (judging by the intensity of bands) impurities are probably proteins expressed by *A. evansii*, bound non-covalently to AOR<sub>Aa</sub>. To test this hypothesis a proteomic analysis of the samples from the presented SDS-PAGE gel was conducted.

## 2. Proteomic analysis of purified AOR preparations

The protein composition of seven bands from SDS-PAGE analysis of purified recombinant AOR<sub>Aa</sub> (pool after gel filtration) was analyzed by proteomic analysis LC-MALDI. For the identification of proteins, the whole genome database of *Aromatoleum*

*evansii* and *Aromatoleum aromaticum* proteins was searched, however, from *A. aromaticum* only the heterologously expressed proteins could be present in the sample.

**Table 11.** Identification of proteins detected in samples from SDS-PAGE gel of purified recombinant AOR<sub>Aa</sub> (pool after gel filtration).

Band (approx. mass from gel)	Protein detected [organism of origin]	Score (sequence coverage)
1 (66 kDa)	Aldehyde:ferredoxin oxidoreductase, tungsten-containing [ <i>Aromatoleum aromaticum</i> (strain EbN1)] <b>AorB</b>	2991.21 (53.9%)
	aldehyde ferredoxin oxidoreductase family protein [ <i>Aromatoleum evansii</i> ] WP_169127012.1	448.48 (12.2%)
2 (46 kDa)	NADH oxidoreductases or NADH oxidases, a potential subunit of aldehyde oxidoreductase [ <i>A. aromaticum</i> (strain EbN1)] <b>AorC</b>	2571.05 (54%)
	FAD-dependent oxidoreductase [ <i>A. evansii</i> ] WP_169127010.1	603.01 (28.8%)
3 (40 kDa)	Benzyl alcohol dehydrogenase [ <i>A. aromaticum</i> (strain EbN1)]	1618.21 (47.8%)
4 (38 kDa)	unidentified*	
5 (26 kDa)	unidentified*	
6 (20 kDa)	Iron-sulfur cluster-binding protein potential subunit of aldehyde oxidoreductase [ <i>A. aromaticum</i> (strain EbN1)] <b>AorA</b>	1219.28 (80.4 %)
7 (17 kDa)	Iron-sulfur cluster-binding protein potential subunit of aldehyde oxidoreductase [ <i>A. aromaticum</i> (strain EbN1)] <b>AorA</b>	467.88 (44.30 %)
	4Fe-4S dicluster domain-containing protein [ <i>A. evansii</i> ] WP_169127014.1	236.90 (17.7 %)

\*- no protein of correct mass was identified; signals referring to all AOR<sub>Aa</sub> subunits are present.

The analysis of the recombinant AOR<sub>Aa</sub> sample expressed in *A. evansii* confirmed the presence of AOR<sub>Aa</sub> in bands corresponding to masses 66, 46 and 20 kDa. In the bands at 66, 46 and 20 kDa another protein was also identified with high probability, namely all

three hypothetical subunits of AOR from *A. evansii* (AOR<sub>Ae</sub>). Moreover, an additional band of mass of about 17 kDa was identified as AorA from AOR<sub>Aa</sub> or an AorA from AOR expressed natively by *Aromatoleum evansii* (organism used for expression of AOR<sub>Aa</sub>). Considering that the heterologously expressed AorA contained a Twin-Strep-tag of mass about 3 kDa and was identified at another band, one has to assume that it is AorA from *A. evansii*. AOR<sub>Ae</sub> and AOR<sub>Aa</sub> sequences were aligned and compared in **Figure 38**. The overall sequence identity of each subunit is 92% for AorA, 83% for AorB and 85% for AorC. Both bacteria, *A. evansii* and *A. aromaticum*, belong to genus *Aromatoleum*<sup>172</sup>, and therefore are closely related; thus the identity of AORs is not surprising. The sequence identity could be a reason for the mismatch of peptide identification during the database search. However, it was confirmed that there are also fragments unique only to one of identified AORs. The highly similar sequence of both AORs could also imply a similar fold and thus the presence of analogous binding sites responsible for forming of heterotrimer (or higher super-structure, binding explained in more detail in Chapter 7). Both proteins are expressed in *A. evansii* strain used in sample preparation, AOR<sub>Aa</sub> is expressed heterologously after induction and AOR<sub>Ae</sub> is apparently expressed under used growth conditions and both proteins might have an opportunity for exchange of subunits of the formed complexes in the living microbe or during purification. The binding of AOR<sub>Ae</sub> subunits to AOR<sub>Aa</sub> complex equipped with the tag may explain why the proteins are coeluting in both affinity chromatography and at the size-exclusion column.

The other bands visible in SDS-PAGE analysis of AOR<sub>Aa</sub> purified sample have masses of about 40, 38 and 26 kDa. The protein identified at 40 kDa was benzyl alcohol dehydrogenase (BaDH) from *A. aromaticum*, which could not come from a strain of *A. evansii* used for AOR<sub>Aa</sub> production. BaDH was purified on the same column (Strep-tag) before the AOR<sub>Aa</sub> preparation was made, therefore the impurity might have originated from to the column and eluted during the AOR<sub>Aa</sub> purification. The bands of 38 and 26 kDa masses were not recognized as any of the proteins possibly present in *A. evansii* cell extract, except for the subunits of AOR<sub>Aa</sub> which represent unspecific signal identified in all analyzed bands. This base signal might be a result of the high concentration of sample used for the SDS-PAGE analysis, which were overloaded for the purpose of proteomic analysis. The amount of proteins in bands of 38 and 26 kDa masses could be too low for analysis or the proteins were not expressed by *A. evansii*. If the latter is true, the impurities might originate from previous purifications on Strep-tag column conducted in our laboratory, similarly as in the case of contamination with BaDH. In this case, the potential enzymatic activities of the impurities were of minor concern as the enzymes bound to the column for an extended time denature with time.

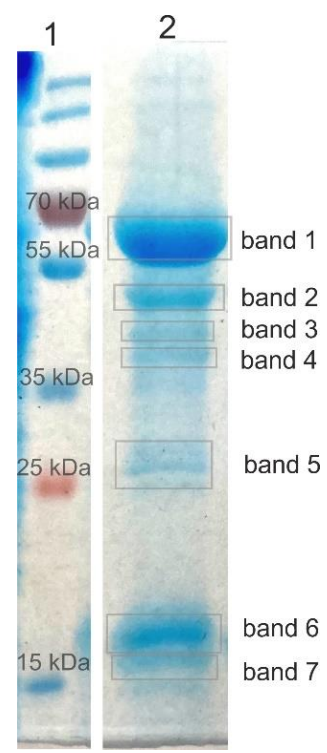
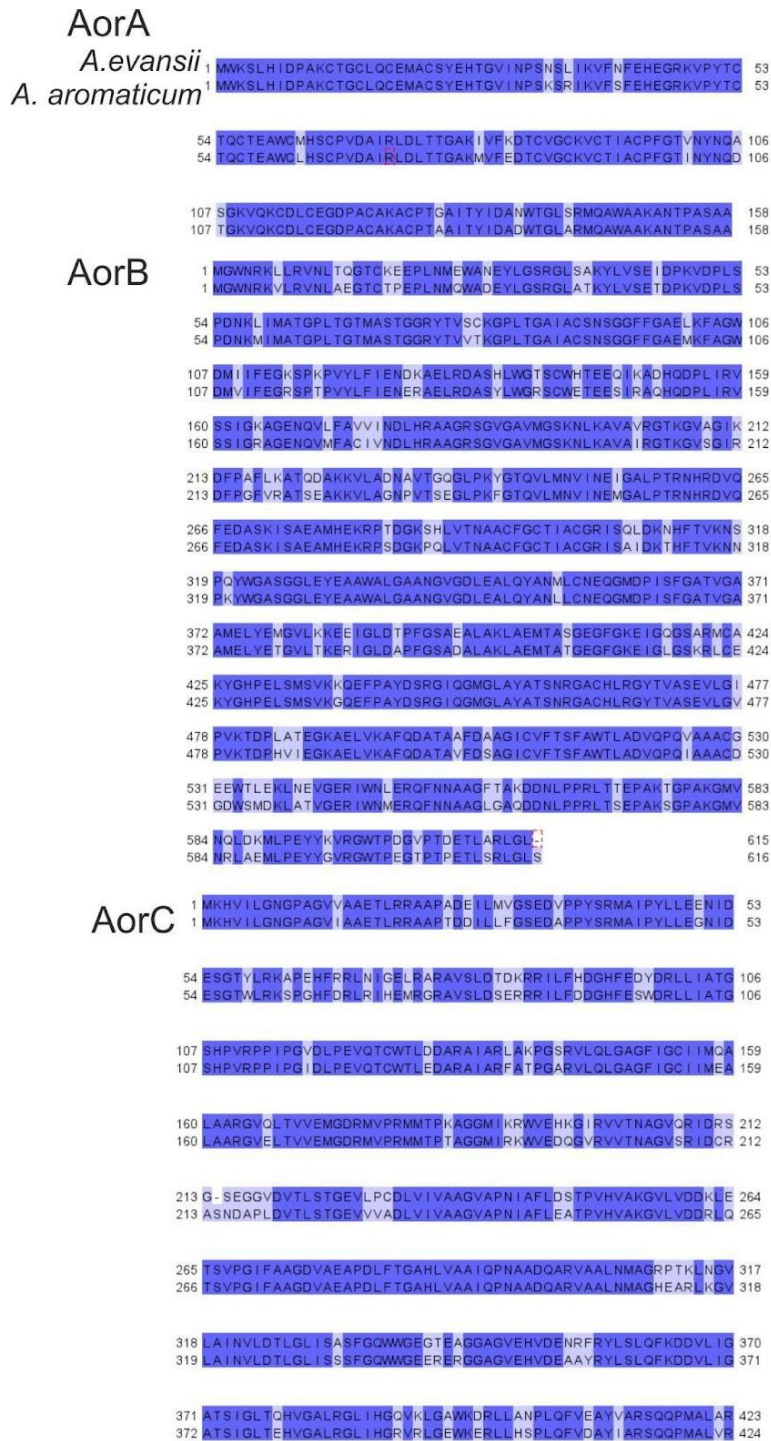


**Figure 38.** Sequence alignment of AOR from *A.aromaticum* and *A.evansii*; dark blue are amino acids that are identical. SDS-PAGE of AOR<sub>Aa</sub> with marked bands extracted for proteomic analysis.

### 3. AOR<sub>Aa</sub> stability

AOR<sub>Aa</sub> stability was assayed by the *ThermoFAD* method in a selection of buffers of a wide pH range. The stability was assessed based on the measured melting temperature ( $T_m$ ) of the AorC subunit (which contains FAD) and the results were shown in **Figure 39**. In the pH range of 4.5 to 7.0 maintained by citrate buffer, the measured  $T_m$  was stable at around 65 °C. Similar results were obtained for malonate and

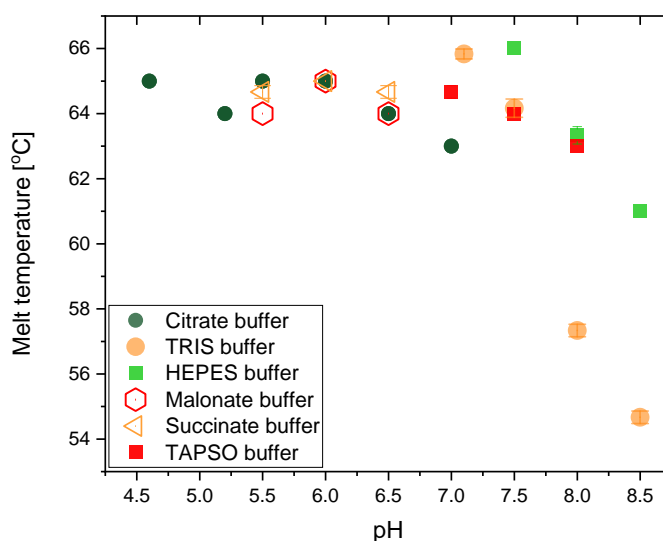


**Figure 39.** Dependence of  $T_m$  of AOR<sub>Aa</sub> on buffer range of 5.5 – 6.5. type and pH, assayed by *ThermoFAD* method.

A negative impact of pH above 7.5

on AorC stability was shown for all types of buffers used, especially in Tris buffer, where the  $T_m$  decreased from 65 °C at pH 7.5 to 57°C at pH 8.0 and at pH 8.5 to 55°C.

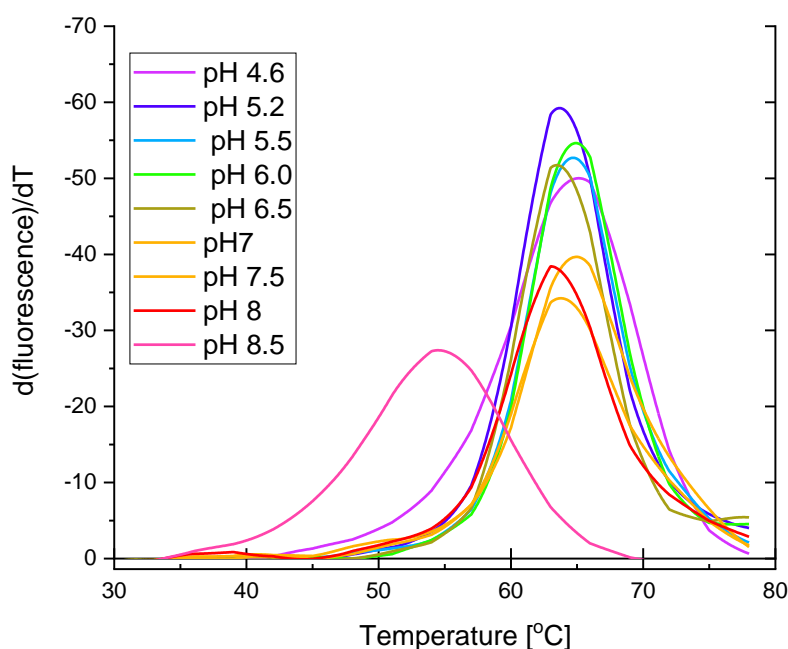


**Figure 40.** The derivative of fluorescence value in respect to temperature versus temperature in *ThermoFAD* assay. Each line correspond to one protein sample assay in given pH in citrate buffer (pH 4.6-7.0) or Tris buffer (pH 7.5-8.5).

The value of the  $T_m$  is estimated as the temperature corresponding to the peak of the function of the derivative of fluorescence value with respect to time versus temperature.



Other features of this function are the onset of the change in fluorescence and the value of the fluorescence derivative. The former value might reflect the stability of the fraction of molecules, however, preferentially, the temperature corresponding to peak of derivative of fluorescence is interpreted as  $T_m$ . The intensity of fluorescence can be influenced by many factors, e.g., by the type of buffer, therefore is not interpreted. Nevertheless, the shape of the function plot was also verified and an example was shown in **Figure 40**. The onset temperature of change of fluorescence is lower for samples in pH 4.6 (citrate/ $\text{Na}_2\text{HPO}_4$  buffer) and pH 8.5 (Tris/HCl) than for other conditions. On the other hand, the peak of derivative of fluorescence for protein in pH 8.5 (Tris/HCl) corresponds to lowest  $T_m$  detected in whole range, while for pH 4.6 (citrate/ $\text{Na}_2\text{HPO}_4$  buffer) much higher  $T_m$  was detected. This bias illustrates the drawback of this method in assessment of protein stability. Based on the  $T_m$  value, the enzyme was assumed to be stable at pH 4.6, while the value of onset temperature of the fluorescence change seems to indicate that the stability at pH 4.6 is, in fact, worse than for pH 5.2-7.0.

One aspect to be discussed in the interpretation of this assay is the dependence of the pH of buffers on temperature. The buffer  $\text{pK}_a$  depends on temperature, pressure and ionic strength, and the pH of the buffered solution is affected accordingly. The  $\text{pK}_a$  changes with temperature are described by the Gibbs free energy, which depends on the change of enthalpy ( $\Delta H$ ) and heat capacity of the chemical. These intrinsic characteristics of each buffer and experimental data were shown in Samuelsen *et al.*<sup>173</sup> and can help interpret the accuracy of measurement. Carboxylic acid buffers are least affected by temperature changes ( $\Delta H$  close to 0). Thus the pH of citrate, malonate and succinate buffer should not be influenced by the temperature change in the range of 25 to 65 °C and results obtained for those buffers should be precise. On the other hand, Tris/HCl buffer of pH 8.0 at 25°C will have pH of 7.0 at 65 °C (after reaching equilibrium)<sup>174</sup>. Therefore, the protein stability in higher pH values observed with Tris/HCl buffer might be in reality worse than the data suggest (due to the drift of pH with the elevation of the temperature). The value of HEPES  $\text{pK}_a$  is less impacted by the temperature than for Tris.

## DISCUSSION OF PART I

The protein used in this thesis was prepared by two different protocols that yielded two separate types of  $\text{AOR}_{Aa}$  preparation, which constituted of proteins of different purity and activity. The type of  $\text{AOR}_{Aa}$  preparation used was noted for each experiment in this thesis.

The use of two types of AOR<sub>Aa</sub> preparations was a consequence of studies done in parallel to the development of a new expression system for AOR<sub>Aa</sub> conducted at Marburg University. Despite the fact, that the change of AOR<sub>Aa</sub> preparation makes the presented results somewhat less transparent, it also allows to present improvement in biocatalyst production as a process and proof that both systems result in practically the same protein characteristic (except for the level of activity).

Without providing this general insight into biocatalyst production, the idea of the commercial value of this product should not be considered, as non-continuous fermentation processes are not easily applicable in the industrial setting. The presented example of the AOR-expression strain of *A.evansii* fermentation provides preliminary data that could lead to full automation of the fermentation process and allows to access the volume of fermentation needed for future production of the biocatalyst.

The fermentation of *A.evansii* is conducted for only 45 h in contrast to *A. aromaticum* (95 h). However, based on OD<sub>600</sub> (1.3 vs. 7, respectively) *A. aromaticum* fermentation yield a higher amount of bacterial cell mass from the same volume of fermentation. The native purification protocol was conducted over three days and protein had to be stored twice overnight at 4 °C. The purification by affinity chromatography for the heterologous system allows achieving similar purity of AOR<sub>Aa</sub> preparation with just a one-column purification protocol, which can be conducted in one day. If a higher purity of AOR<sub>Aa</sub> preparation is necessary, the addition of an additional column to the protocol extends the protocol for one day. Theoretically, higher purity AOR<sub>Aa</sub> should give the higher specific activity of the enzyme. This is not evident in the results, on the contrary, the pool of recombinant protein after gel filtration had lower specific activity than after the affinity column (18 and 31.3  $\mu\text{mol min}^{-1} \text{mg}^{-1}$ , respectively). The drop in the specific activity can be caused by prolonged incubation of the enzyme at 4 °C during the extended protocol and slow deactivation in these conditions or dissociation of the enzyme oligomers during the excessive dilution taking place during the SEC chromatography (more conclusions regarding oligomeric state in Chapter 7). Therefore, the shortened one-column purification protocol is the best solution for the production of active biocatalysts.

The proteomic analysis of AOR<sub>Aa</sub> preparation showed that the protein is not homogenous and structurally similar subunits of AOR<sub>Ae</sub> are present in the preparation. This observation led to a hypothesis that the subunits in heterologously expressed AOR<sub>Aa</sub> could be partially exchanged in the AOR<sub>Aa</sub> complex by subunits from homologously expressed AOR<sub>Ae</sub>. The amount of AOR<sub>Ae</sub> subunits mixed into AOR<sub>Aa</sub> should be relatively low, judging from the much higher intensity of the SDS-PAGE band at 20 kDa, i.e., AorA

from AOR<sub>Aa</sub>, than the band at 17 kDa, i.e., AorA from AOR<sub>Ae</sub>. Moreover, the heterologously expressed AOR<sub>Aa</sub> should be produced in larger quantities than a homologously expressed AOR<sub>Ae</sub> (if the production of homologous AOR is similar in *A.evansii* as in *A.aromaticum*, where native bacteria produced very low quantities of AOR<sup>64</sup>).

The AOR<sub>Aa</sub> stability assay by ThermoFAD method proved that the protein is stable in wide range of pH (4.5-7.5). This range includes higher pH values (7.5) corresponding to the pH optimum of most FAD-dependent oxidation reactions and pH values below 7.0 previously has been shown to be optimal for catalysis of carboxylic acid reduction by AORs<sup>63</sup>. The study identified HEPES and TAPSO buffers as enhancing the protein stability in a basic environment in contrast to Tris/HCl buffer, although the data are biased by the pH change with temperature.

## **PART II. Catalytic characterisation**

### **4. Characterisation of AOR activity in aldehyde oxidation**

The AOR<sub>Aa</sub> activity in aldehyde oxidation was initially characterized by the group of prof. Heider<sup>64,74,90</sup>. This characterisation was continued in this study by broadening the substrate spectrum and determination of the kinetic parameters for catalyzed reactions.

#### **4.1. Substrate spectrum in aldehyde oxidation**

The previously determined substrate spectrum is shown in Arndt *et al.*<sup>74</sup>. The substrate spectrum was determined by measuring the AOR<sub>Aa</sub> activity in the oxidation of 1 mM aldehyde with 1.6 mM BV<sup>2+</sup> as an electron donor. The results were shown as relative activity to the activity in benzaldehyde oxidation (as % of this activity, **Table 12**). The substrate spectrum of AOR<sub>Aa</sub> was broadened with heterocyclic aldehydes such as furfural and 2-thiophenecarboxaldehyde. A range of 4-substituted benzaldehyde derivatives was tested and in all cases AOR<sub>Aa</sub> turned out to be active. Surprisingly, the enzyme was active in the oxidation of aldehydes with large substituents in the benzene ring, such as bromine. Similarly, a wide substrate spectrum was also shown for other AORs from *M. thermoacetica* and *T. paralvinellae*<sup>65,76</sup>, however, 4-bromobenzaldehyde or furfural have not been tested before.

The values of specific activity with 1 mM substrate concentration are only approximate measures of enzyme activity, as only studying the full dependency of reaction velocity in a function of a substrate concentration enables comparison the enzyme affinity toward the substrate. In this study, however, the kinetic parameters were determined only for selected representatives of substrates, i.e. for acetaldehyde, as an aliphatic aldehyde,

phenylacetaldehyde, as an alkylaromatic aldehyde, and for benzaldehyde, as an aromatic aldehyde.

**Table 12.** Screening of the activity of AOR in the oxidation of aldehyde substrates (1 mM) with 1.6 mM BV<sup>2+</sup> as an electron donor.

Substrate	Relative activity (%)	Specific activity with std. error of mean (U/mg protein)		
Benzaldehyde	100%	23.61	±	0.67
4-methylbenzaldehyde	50%	11.81	±	0.27
4-fluorobenzaldehyde	46%	10.83	±	2.09
Furfural	40%	9.52	±	0.25
4-hydroksybenzaldehyde	39%	9.31	±	0.30
4-anisaldehyde	29%	6.85	±	0.30
2-thiophenecarboxaldehyde	28%	6.59	±	0.27
4-chlorobenzaldehyde	9%	2.02	±	0.23
4-bromobenzaldehyde	5%	1.29	±	0.09

#### 4.2. Kinetic parameters of aldehyde oxidation

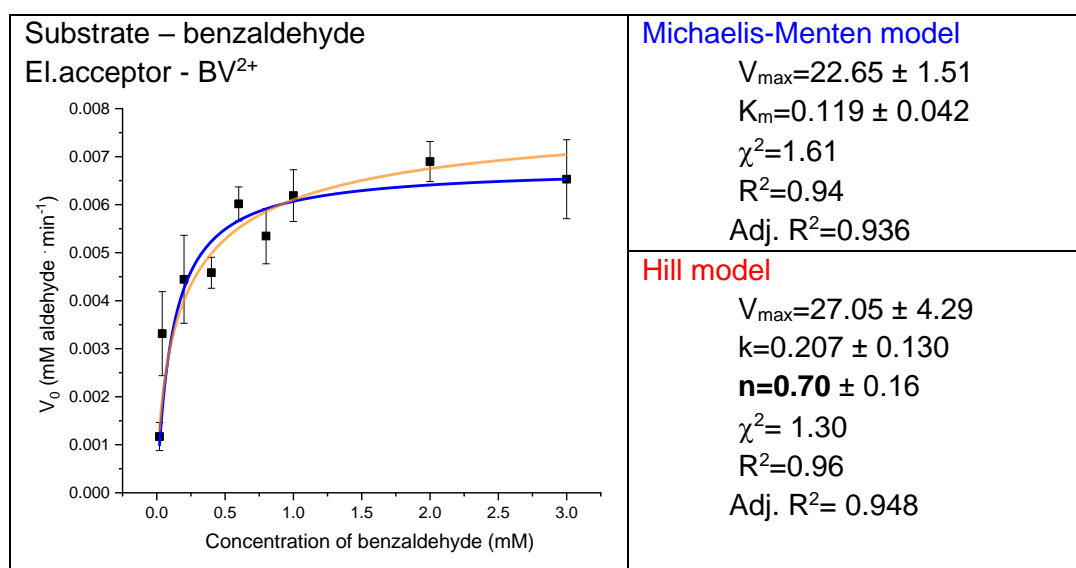
The dependence of initial rates of reaction on the concentration of benzaldehyde, phenylacetaldehyde and acetaldehyde was measured in steady-state kinetic tests with 1.6 mM of NAD<sup>+</sup> or BV<sup>2+</sup>. Two models of enzyme kinetics (the Michaelis-Menten and the Hill model) were fitted to all data sets and the model's quality was assessed by two statistical parameters of fit,  $\chi^2$  and R<sup>2</sup>.

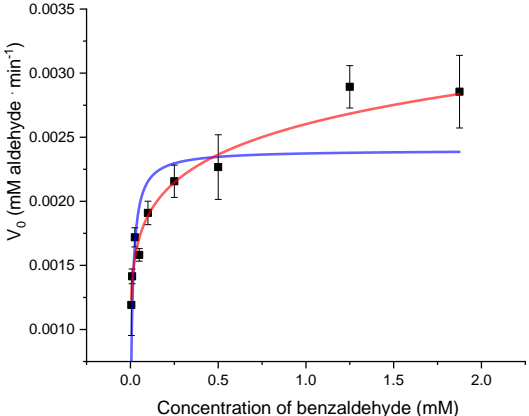
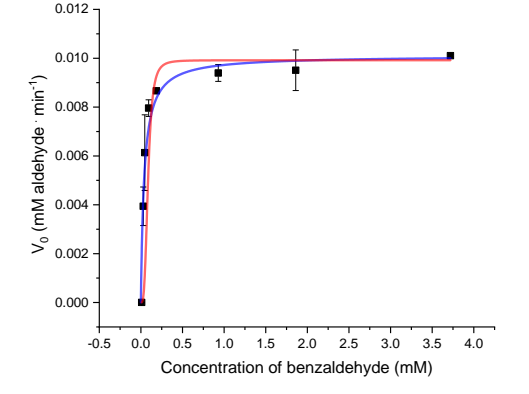
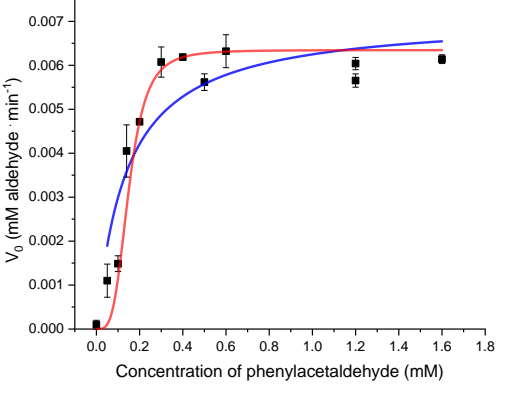
In most cases, data was fitted with the Michaelis-Menten model with satisfactory accuracy and the Hill model did not show relevant improvement in the statistical parameters. However, results for specific activity dependence on phenylacetaldehyde concentration with BV<sup>2+</sup> as an electron acceptor did not fit well the Michaelis-Menten model. Based on residual  $\chi^2$  of fit with the Michaelis-Menten and Hill models the best result was achieved with the latter model with a cooperativity coefficient of  $3.5 \pm 0.6$  (fits shown in **Table 13**). The value of the coefficient shows positive cooperativity of substrate binding. Hence one aldehyde bound to the active site increases the affinity of the other active sites for substrate binding in the multisubunit assembly. Moreover, if this effect occurs the protein is likely to form a functional multimeric complex (see the result of structural analysis, Chapter 7). This reasoning can be questioned, as the kinetics studied so far did not show clearly the dependence for concentrations of the substrate below K<sub>m</sub>. That region strongly influences the Hill coefficient, which for AOR<sub>Aa</sub> cannot be easily

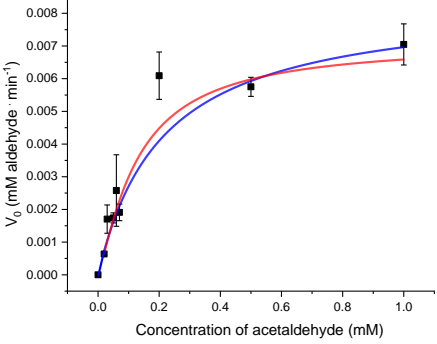
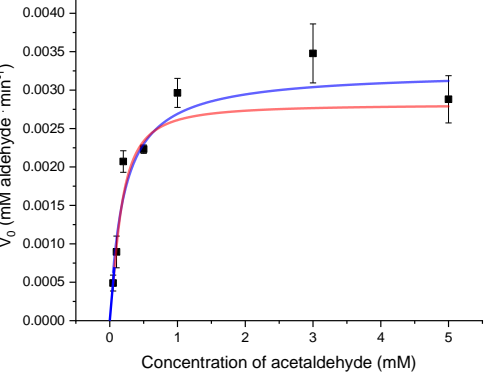
studied, as the values of  $K_m$  towards aldehydes are very low. The observed features of the kinetic curves could also be explained as a result of weak substrate inhibition, especially as this phenomenon was already reported for enzymes from the AOR family<sup>65</sup>. Considering the described ambiguities in the recognition of the mechanism, the interpretation of data was done based on the simpler, Michaelis-Menten model.

For acetaldehyde and benzaldehyde as substrates AOR<sub>Aa</sub> exhibited a 2 and 2.7-fold higher apparent maximal turnover rate with BV<sup>2+</sup> than with NAD<sup>+</sup> as an electron acceptor, respectively. Natively expressed AOR<sub>Aa</sub> converts all measured substrates with BV<sup>2+</sup> with similar  $V_{max}$  of about 22-24 U/mg of protein and with NAD<sup>+</sup> with 11 and 8 U/mg of protein for acetaldehyde and benzaldehyde, respectively. The heterologously expressed enzyme exhibits about 4-fold higher activity in benzaldehyde oxidation with NAD<sup>+</sup> as an electron acceptor than the AOR<sub>Aa</sub> expressed in native bacteria.

**Table 13.** Achieved kinetic curves for the dependence of initial rates of reaction on the concentration of substrate with BV<sup>2+</sup> or NAD<sup>+</sup>. Data from measurement (black dots with standard deviation range) was fitted with Michaelis-Menten (blue curve) and Hill (red curve) model.  $V_{max}$  is the maximum velocity calculated from fit parameters to U·mg of protein<sup>-1</sup>;  $K_m$  is shown in mM.



<p>Substrate – benzaldehyde El.acceptor - NAD<sup>+</sup></p>  <p>Detailed description: A plot of initial velocity (V<sub>0</sub>) in mM aldehyde · min<sup>-1</sup> versus the concentration of benzaldehyde in mM. The y-axis ranges from 0.0010 to 0.0035, and the x-axis ranges from 0.0 to 2.0. Data points are shown as black squares with error bars. Two curves are fitted: a blue Michaelis-Menten curve and a red Hill curve. The Hill curve provides a better fit to the data points.</p>	<p><b>Michaelis-Menten model</b></p> <p><math>V_{max} = 7.36 \pm 0.42</math>  <math>K_m = 0.010 \pm 0</math>  <math>\chi^2 = 11.11</math>  <math>R^2 = 0.298</math>  Adj. <math>R^2 = 0.299</math></p>
<p>Substrate – benzaldehyde El.acceptor - NAD<sup>+</sup> *Heterologously expressed enzyme</p>  <p>Detailed description: A plot of initial velocity (V<sub>0</sub>) in mM aldehyde · min<sup>-1</sup> versus the concentration of benzaldehyde in mM. The y-axis ranges from 0.000 to 0.012, and the x-axis ranges from -0.5 to 4.0. Data points are shown as black squares with error bars. Two curves are fitted: a blue Michaelis-Menten curve and a red Hill curve. The Hill curve provides a better fit to the data points.</p>	<p><b>Michaelis-Menten model</b></p> <p><math>V_{max} = 33.76 \pm 1.18</math>  <math>K_m = 0.039 \pm 0.006</math>  <math>\chi^2 = 12.96</math>  <math>R^2 = 0.912</math>  Adj. <math>R^2 = 0.908</math></p>
<p>Substrate – phenylacetaldehyde El.acceptor - BV<sup>2+</sup></p>  <p>Detailed description: A plot of initial velocity (V<sub>0</sub>) in mM aldehyde · min<sup>-1</sup> versus the concentration of phenylacetaldehyde in mM. The y-axis ranges from 0.000 to 0.007, and the x-axis ranges from 0.0 to 1.8. Data points are shown as black squares with error bars. Two curves are fitted: a blue Michaelis-Menten curve and a red Hill curve. The Hill curve provides a better fit to the data points.</p>	<p><b>Michaelis-Menten model</b></p> <p><math>V_{max} = 23.73 \pm 1.30</math>  <math>K_m = 0.138 \pm 0.029</math>  <math>\chi^2 = 8.33</math>  <math>R^2 = 0.829</math>  Adj. <math>R^2 = 0.823</math></p>
<p><b>Hill model</b></p> <p><math>V_{max} = 20.18 \pm 0.42</math>  <math>k = 0.123 \pm 0.005</math>  <b><math>n = 3.51 \pm 0.61</math></b>  <math>\chi^2 = 3.07</math>  <math>R^2 = 0.938</math>  Adj. <math>R^2 = 0.933</math></p>	

<p>Substrate – acetaldehyde El.acceptor - BV<sup>2+</sup></p> 	<p><b>Michaelis-Menten model</b></p> $V_{\max} = 22.68 \pm 1.65$ $K_m = 0.117 \pm 0.041$ $\chi^2 = 2.24$ $R^2 = 0.970$ $\text{Adj. } R^2 = 0.965$
<p>Substrate – acetaldehyde El.acceptor - NAD<sup>+</sup></p> 	<p><b>Michaelis-Menten model</b></p> $V_{\max} = 11.24 \pm 0.54$ $K_m = 0.189 \pm 0.039$ $\chi^2 = 1.526$ $R^2 = 0.904$ $\text{Adj. } R^2 = 0.900$
	<p><b>Hill model</b></p> $V_{\max} = 21.11 \pm 1.78$ $k = 0.115 \pm 0.025$ $n = 1.52 \pm 0.54$ $\chi^2 = 12.470$ $R^2 = 0.822$ $\text{Adj. } R^2 = 0.802$
	<p><b>Hill model</b></p> $V_{\max} = 9.36 \pm 0.36$ $k = 0.161 \pm 0$ $n = 1.4 \pm 0$ $\chi^2 = 3.535$ $R^2 = 0.931$ $\text{Adj. } R^2 = 0.931$

The highest apparent  $K_m$  value was recorded with NAD<sup>+</sup> for acetaldehyde and the lowest for benzaldehyde with the same electron acceptor. AOR<sub>Aa</sub> exhibits the best catalytic efficiency with benzaldehyde, however, this value is at least several-fold lower than those observed for other AORs, i.e. AOR<sub>Mt</sub> and AOR<sub>Tp</sub> (**Table 14**). The difference between the catalytic efficiencies ( $k_{\text{cat}}/K_M$ ) of the enzymes is due to higher maximal turnover and lower  $K_m$  reported in the literature. However, the higher maximal turnover values for AOR<sub>Mt</sub> and AOR<sub>Tp</sub> can easily be explained because these enzymes are from thermophilic organisms<sup>2</sup> and have been assayed at higher measurement temperatures (40 and 85 °C, respectively).

**Table 14.** Kinetic parameters of AOR<sub>Aa</sub> from two expression systems (produced in *A. aromaticum* and from heterologous expression) in aldehyde oxidation shown with the error of standard deviation, compared with literature data for other AORs,  $k_{cat}$  was calculated for AOR<sub>Aa</sub> mass Aor(AB)<sub>2</sub>C= 218 kDa, measured at 30 °C.

Enzyme	Substrate	EI. acceptor	$k_{cat}$ (s <sup>-1</sup> )	$K_M$ (μM)	$k_{cat}/K_M$ (s <sup>-1</sup> μM <sup>-1</sup> )
AOR from <i>Aromatoleum aromaticum</i> (native expression)	benzaldehyde	BV <sup>2+</sup>	82 ± 5	119 ± 42	0.69
	acetaldehyde		82 ± 7	117 ± 38	0.70
	phenylacetaldehyde		86 ± 5	138 ± 29	0.62
	benzaldehyde	NAD <sup>+</sup>	30 ± 1	10 ± 2	3.0
	acetaldehyde		41 ± 2	190 ± 40	0.21
AOR from <i>Aromatoleum aromaticum</i> (heterologous expression)	benzaldehyde	NAD <sup>+</sup>	123	39.3 ± 6.6	3.1
AOR from <i>Moorella thermoacetica</i> <sup>a</sup>	benzaldehyde	CAV <sup>2+</sup>	-	9	127
	acetaldehyde		-	10	114
AOR from <i>Thermococcus paralvinellae</i> <sup>b</sup>	benzaldehyde	BV <sup>2+</sup>	720	57	13
	acetaldehyde		343	16	22
	phenylacetaldehyde		960	76	13

<sup>a</sup> measured at 40 °C in 0.85 ml 0.1 M Tris/HCl pH 9.0 containing 1.2 mM CAV<sup>2+</sup>, data from Huber *et al.*<sup>76</sup>

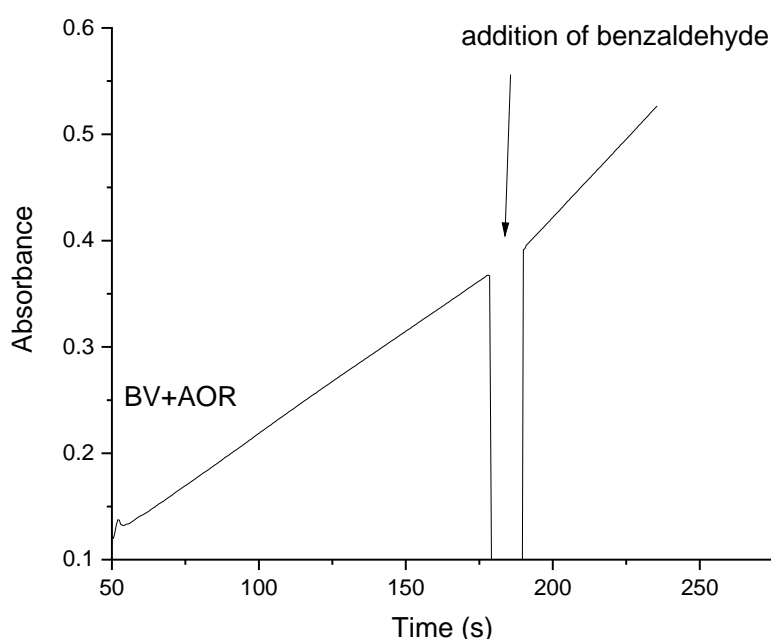
<sup>b</sup> at 85 °C in 0.1 M EPPS buffer pH 8.4 with 1.6 mM BV<sup>2+</sup>, data from Heider *et al.*<sup>65</sup>

## 5. Characterisation of AOR activity in NAD<sup>+</sup> reduction with hydrogen as an electron donor

W-containing aldehyde oxidoreductases can reduce NAD<sup>+</sup> in a reaction coupled to aldehyde oxidation, which was demonstrated for the studied enzyme. However, when the above reaction was studied under anaerobic atmosphere (in a glovebox containing 2.5% hydrogen in nitrogen), a significant baseline activity was observed, with only



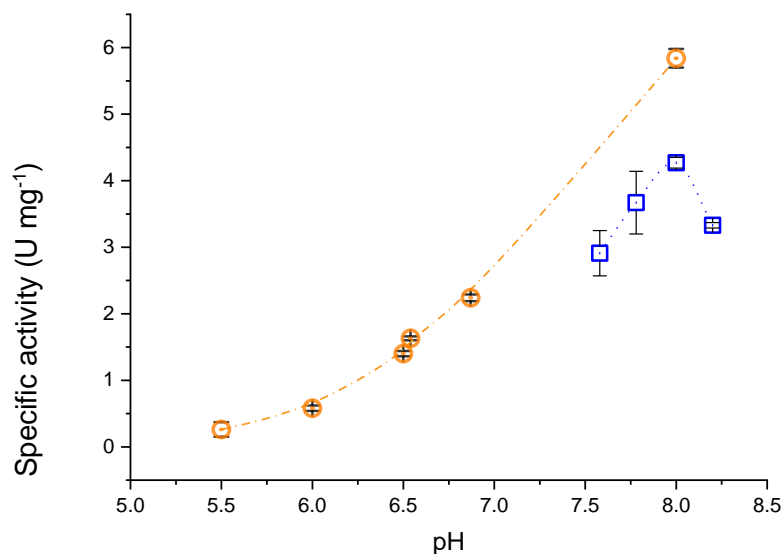
purified AOR<sub>Aa</sub> and NAD<sup>+</sup> (or BV<sup>2+</sup>) present in the reaction mixture (see **Figure 41**). The occurrence of this baseline activity was not observed in tests with NAD<sup>+</sup> conducted under aerobic conditions nor in a pure nitrogen atmosphere, which clearly pointed at the impact of hydrogen. One possible explanation of this activity could have been the presence of hydrogenase in AOR<sub>Aa</sub> preparation. However no genes coding such enzymes are present in the genomes of *A. aromaticum* or *A. evansii* used for the expression of the AOR<sub>Aa</sub>. In light of this evidence, it was assumed that the observed NAD<sup>+</sup> reduction is a reaction coupled to hydrogen oxidation, which was not observed before for AORs. To test this theory, further characterization of hydrogen oxidation by AOR<sub>Aa</sub> was performed as a part of this thesis.



**Figure 41.** An example of UV-vis assay for AOR<sub>Aa</sub> activity in aldehyde oxidation with BV<sup>2+</sup> with 2.5% hydrogen in the headspace. The time of 0 s marks the addition of AOR<sub>Aa</sub> to the reaction mixture containing 1 mM BV<sup>2+</sup>, the observed activity from that point to the addition of benzaldehyde is a background activity (presumably with H<sub>2</sub>), and measurement of activity in aldehyde oxidation is initiated after the addition of benzaldehyde (at 175 s).

The pH dependence of hydrogen oxidation with NAD<sup>+</sup> as electron acceptor was measured in direct UV-vis measurement of absorption at 340 nm, with 1 mM NAD<sup>+</sup> and 2.5% of hydrogen in the headspace, in 50 mM K<sub>2</sub>HPO<sub>4</sub>/KH<sub>2</sub>PO<sub>4</sub> buffer (pH range 5.5-8.0) and 100 mM Tris/HCl (pH 7.6-8.0). The highest activity was noticed for the reaction conducted at pH 8.0, which is the same value as for aldehyde oxidation. The specific activity of AOR<sub>Aa</sub> (shown in **Figure 42**) has a very strong dependency on pH, with a

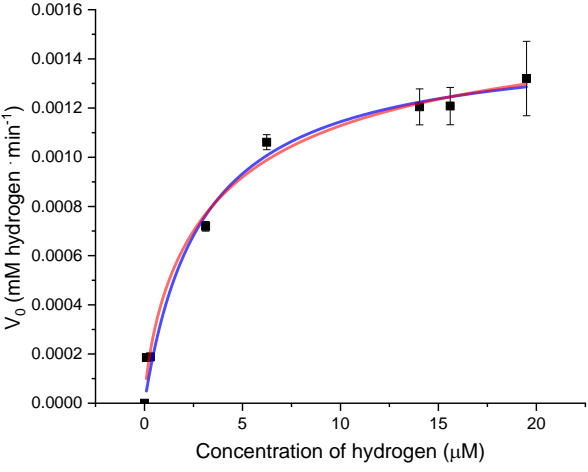
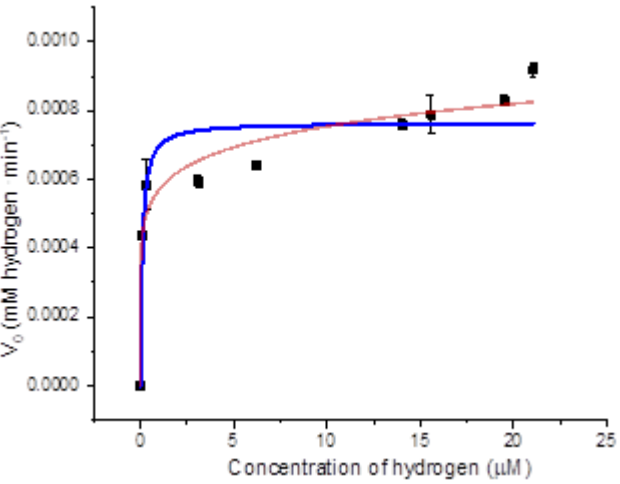
reaction rate 20 times higher at pH 8.0 than at pH 5.5 (0.28 vs. 5.84 U mg<sup>-1</sup>, respectively, in K<sub>2</sub>HPO<sub>4</sub>/KH<sub>2</sub>PO<sub>4</sub> buffer).



**Figure 42.** The pH-dependence of AOR<sub>Aa</sub> activity in NAD<sup>+</sup> reduction with H<sub>2</sub> as an electron donor. Orange circles represent measurements conducted in K<sub>2</sub>HPO<sub>4</sub>/KH<sub>2</sub>PO<sub>4</sub> buffer, blue squares – Tris/HCl buffer; error bars represent standard deviations of measurements.

To determine the apparent kinetic parameters for those reactions, the steady-state kinetics of NAD<sup>+</sup> or BV<sup>2+</sup> reduction coupled to molecular hydrogen oxidation was studied (**Table 15 and 16**). The assays were performed at optimal pH of 8.0, either with constant NAD<sup>+</sup> or BV<sup>2+</sup> concentration (1 mM) and varied hydrogen concentrations (0-2.7%) or at a constant concentration of hydrogen (2.5%) and varied NAD<sup>+</sup> concentrations (0-2 mM). Among tested reduction reactions, AOR<sub>Aa</sub> exhibited the highest turnover number ( $k_{cat}$ ) of 17.9 s<sup>-1</sup> in H<sub>2</sub> oxidation coupled to the reduction of BV<sup>2+</sup>. The apparent  $k_{cat}$  values for NAD<sup>+</sup> reduction were 10.2 s<sup>-1</sup> at constant 1 mM NAD<sup>+</sup> and 13.4 s<sup>-1</sup> at 2.5% H<sub>2</sub>, which represent 8.3% to 10.5% of the apparent  $k_{cat}$  observed for benzaldehyde-dependent NAD<sup>+</sup> reduction (123 s<sup>-1</sup>). To date, there has been no report of such H<sub>2</sub>-dependent reduction of enzymes from the AOR family. From the related enzymes, only a Mo-enzyme (CO dehydrogenase) was shown to be reduced with H<sub>2</sub> at 5% rate of the CO-dependent rates (i.e. 5.1 s<sup>-1</sup>) for the ultimate reduction of quinones or methylene blue<sup>175</sup>. Notably, the observed turnover rates for hydrogen-dependent BV<sup>2+</sup> reduction by AOR<sub>Aa</sub> represent the highest hydrogen-oxidation rate shown to date for any Mo- or W-enzyme<sup>96</sup>.

**Table 15.** Kinetic curves for the dependence of AOR<sub>Aa</sub>-catalyzed reaction velocity of BV<sup>2+</sup> or NAD<sup>+</sup> reduction at different concentrations of H<sub>2</sub> in the reaction medium and with a constant concentration of hydrogen and varied concentration of NAD<sup>+</sup>. Data from measurement (black dots with standard deviations) were fitted with the Michaelis-Menten (blue curve) or Hill (red curve) models; K<sub>m</sub> is shown in μM.

<p>BV<sup>2+</sup> reduction with variable concentration of hydrogen</p> 	<p><b>Michaelis-Menten model</b></p> <p><math>K_m = 2.937 \pm 0.553</math></p> <p><math>\chi^2 = 0.093</math></p> <p><math>R^2 = 0.957</math></p> <p>Adj. <math>R^2 = 0.955</math></p>
<p>NAD<sup>+</sup> reduction with variable concentration of hydrogen</p> 	<p><b>Michaelis-Menten model</b></p> <p><math>K_m = 0.14 \pm 0.045</math></p> <p><math>\chi^2 = 0.03817</math></p> <p><math>R^2 = 0.9292</math></p> <p>Adj. <math>R^2 = 0.9213</math></p> <p><b>Hill model</b></p> <p><math>k = 0.0001 \pm 0.0001</math></p> <p><math>n = 0.141 \pm 0.0196</math></p> <p><math>\chi^2 = 0.04908</math></p> <p><math>R^2 = 0.9996</math></p> <p>Adj. <math>R^2 = 0.9995</math></p>

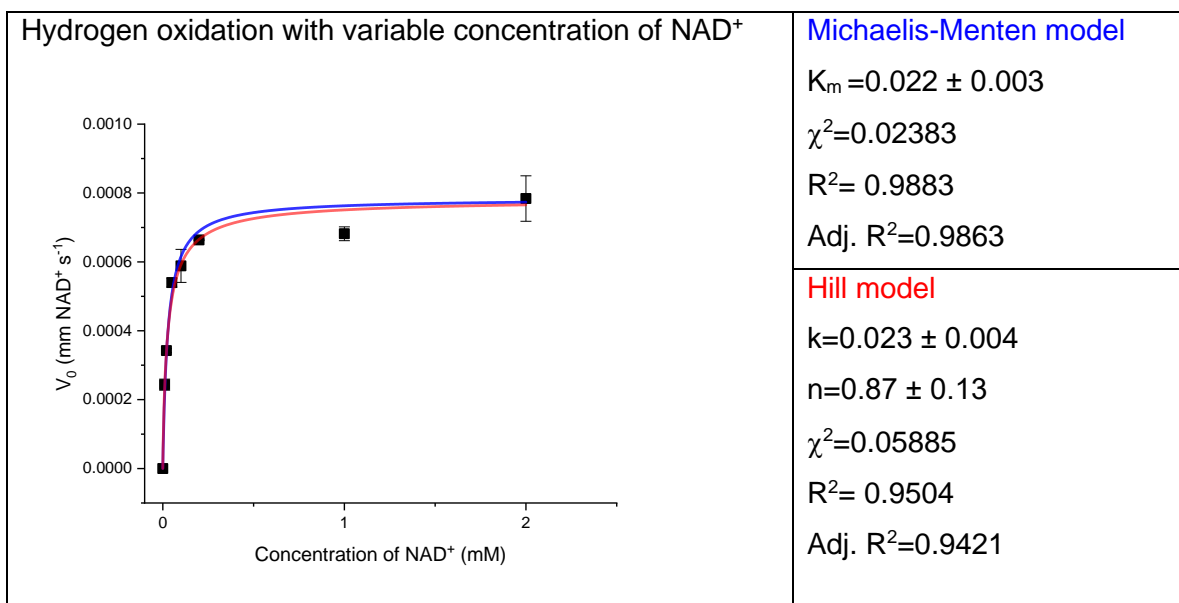


**Table 16.** Apparent kinetic parameters of AOR<sub>Aa</sub>; the  $k_{\text{cat}}$  was calculated for the mass of the complex Aor(AB)<sub>2</sub>C of 218 kDa.

[A]	[B] <sub>const</sub>	V <sub>max</sub> (U/mg)	K <sub>M</sub> ( $\mu\text{M}$ ) or (%)*	k <sub>cat</sub> (s <sup>-1</sup> )	k <sub>cat</sub> / K <sub>M</sub> ( $\mu\text{M}^{-1}\text{s}^{-1}$ )
NAD <sup>+</sup>	H <sub>2</sub>	3.7 ± 0.1	21.7 ± 2.7	13.4	0.6
H <sub>2</sub>	BV	4.94 ± 0.26	2.9 ± 0.6 [0.38 ± 0.08]*	17.9	6.4
H <sub>2</sub>	NAD <sup>+</sup>	2.82 ± 0.19	0.14 ± 0.3 [0.037 ± 0.034]*	10.2	72.9

\*hydrogen concentration in  $\mu\text{M}$  was calculated from H<sub>2</sub> pp% according to the solubility of gases in water. Constant given for 30 °C and the pressure of the gas plus that of the water vapour is 760 mm:  $q = 0.0001474$  g hydrogen in 100 g of water.

The calculated apparent  $K_m$  values of either H<sub>2</sub> or NAD<sup>+</sup> were very low at about 0.3  $\mu\text{M}$  H<sub>2</sub> and 21  $\mu\text{M}$  NAD<sup>+</sup>, respectively, which may indicate that the reactivity of AOR<sub>Aa</sub> with H<sub>2</sub> is physiologically relevant. Considering low  $K_m$  values for H<sub>2</sub> and NAD<sup>+</sup> and relatively high turnover numbers, the AOR-catalyzed reduction of NAD<sup>+</sup> has potential use in the common hydrogenase application – an NADH recycling system.

## 6. Characterisation of AOR activity in carboxylic acid reduction.

The characterisation of AOR<sub>Aa</sub> as a catalyst for the reduction of carboxylic acids was covered in this work in the following parts: i) identification of electron donors for acid reduction, ii) identification of substrate spectra, iii) impact of pH on activity, iv) kinetic characterisation of catalyst.

## 6.1. Electron donors in acid reduction

The proof of reduction of carboxylic acids by AOR<sub>Aa</sub> was first demonstrated in a study by Arndt *et al.*<sup>74</sup>. In the preliminary qualitative study not covered by this work, the reduced methyl viologen ( $E^{\circ}$  (MV/MV<sup>+</sup>) = -440 mV)<sup>65</sup> was shown not to be working as electron donor, whereas the use of titanium (III) citrate ( $E^{\circ}$  (Ti<sup>3+</sup>/Ti<sup>4+</sup>) = -800 mV) led to reduction of benzoic acid. In conclusion, the reaction was suspected to be working only with low redox potential electron donors. Therefore, the titanium (III) citrate and europium (II) EGTA complexes were tested as electron donors. In addition, I also tested hydrogen, which was newly discovered as a reducing agent acting with AOR<sub>Aa</sub> in NAD<sup>+</sup> reduction, as an electron donor in carboxylic acid reduction.

The reaction was catalyzed by 192 nM purified, heterologously expressed AOR<sub>Aa</sub> in pH 5.5 maintained by 100 mM citric buffer, with 30 mM sodium benzoate as substrate and either 3 mM of the Ti(III)-citrate or Eu(II)-EGTA under anaerobic conditions (100% N<sub>2</sub>) or with 2.5% H<sub>2</sub> in headspace as an electron donor. In reactions with Ti(III)-citrate or Eu(II)-EGTA the yields of benzaldehyde after 2 h of reaction reached considerable amounts of 11.3 ± 0.6 and 33.1 ± 0.5 μM, respectively. Surprisingly, the example with hydrogen as an electron donor also showed a reduction of benzoate, with a similar yield as in the experiment with Ti(III)-citrate (10.4 ± 2.6 μM after 2 h). The reduction assays with Ti(III)-citrate and Eu(II)-EGTA were not investigated further, as the remains of reactive metal species were a hazard for the integrity of the HPLC system and column. Moreover, these electron donors have low applicability because of their high cost and contamination of the reaction mixture by heavy metals and high concentration of salts.

The reduction of carboxylic acids with hydrogen as an electron donor is surprising as the redox potential of hydrogen oxidation ( $E^{\circ}$ (H<sup>+</sup>/H<sub>2</sub>) = -414 mV) is higher than the other studied electron donors and even higher than the benzoic acid reduction potential ( $E^{\circ}$ (benzoic acid/benzaldehyde) = -505 mV). As this was the first report of such activity for any enzyme, this reaction was studied in more detail and was used for further characterization of AOR<sub>Aa</sub> as a catalyst for the reduction of carboxylic acids.

## 6.2. Kinetics of hydrogen-dependent acid reduction

According to the literature, the carboxylic acid reduction by AORs was studied widely with viologen dyes as electron donors and the reaction was shown to depend on millimolar concentrations of carboxylic acids and have optimum pH around 5.5<sup>63,65</sup>.

### Optimization of conditions for repeatable kinetic tests

The first series of tests of acid reduction were conducted with millimolar benzoic acid concentration with benzaldehyde detection by LC-MS/MS method. Because several of the experiments gave poor reproducibility of the results due to low concentrations of the product, only one example will be discussed here. A series of reactors with concentrations of AOR<sub>Aa</sub> of 26, 39 and 52 nM were run with 24 mM sodium benzoate as substrate in a 2.5 % hydrogen atmosphere and the concentration of benzaldehyde was determined during 5 h of reaction. These initial experiments demonstrated very low yields of reaction (below 100  $\mu\text{M}$  of product, which is less than 1% conversion, as shown in **Figure 43**). A rate of acid reduction during initial linear phase (0-60 min) for 52 nM AOR<sub>Aa</sub> was about 1  $\mu\text{M}/\text{min}$ . In reactors with lower concentration of catalyst the linear phase was shorter.

After two hours of reaction, a drop in benzaldehyde concentration in samples was observed. This effect might have been caused by three possible phenomena: firstly, enzyme activity may drop after reaching the steady-state phase, secondly, benzaldehyde may be degraded under the reaction conditions (which happened due to known reactions of spontaneous oxidation or condensation of aldehyde<sup>176</sup>), and thirdly, the phenomenon might be caused by the difference of rates between reactions when hydrogen is depleted from the liquid phase and gas-liquid equilibration of hydrogen concentration, causing its gradual decrease in reaction conditions.

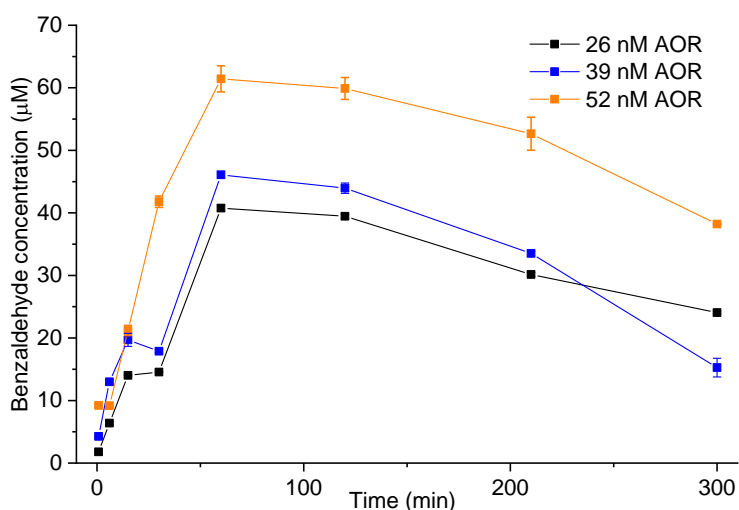


**Figure 43.** Progress curves of benzaldehyde synthesis from 24 mM benzoate and H<sub>2</sub> (2.5% in headspace) in 50 mM MES buffer at pH 6.5 with 26, 39 or 52 nM AOR<sub>Aa</sub>. Analytical repetition average, the error bars represent SD.

Based on the results of this experiment, an optimal window for kinetic measurements was established within the first one hour of the reaction and a minimal concentration of the enzyme of 52 nM to be added to the reaction mixture to achieve measurable concentrations of benzaldehyde. Moreover, the decomposition of benzaldehyde during the reaction and in samples observed additionally during measurements not included in this work, was also addressed by minimizing the time between reaction and measurement of aldehyde concentration. The direct measurement of benzaldehyde concentration was conducted only if other methods were not applicable, i.e., experiments showing saturation phase or study of reaction thermodynamics. For other experiments, a method of kinetic measurements with aldehyde being converted to more stable benzyl alcohol was established (Chapter 6.6.).

#### *Experiment showing saturation phase*

The acid reduction was also tested with a higher concentration of enzyme (240 nM) in pH 5.5 maintained by 100 mM citric acid/ $\text{Na}_2\text{HPO}_4$  buffer and the reaction progress is shown in **Figure 44**.

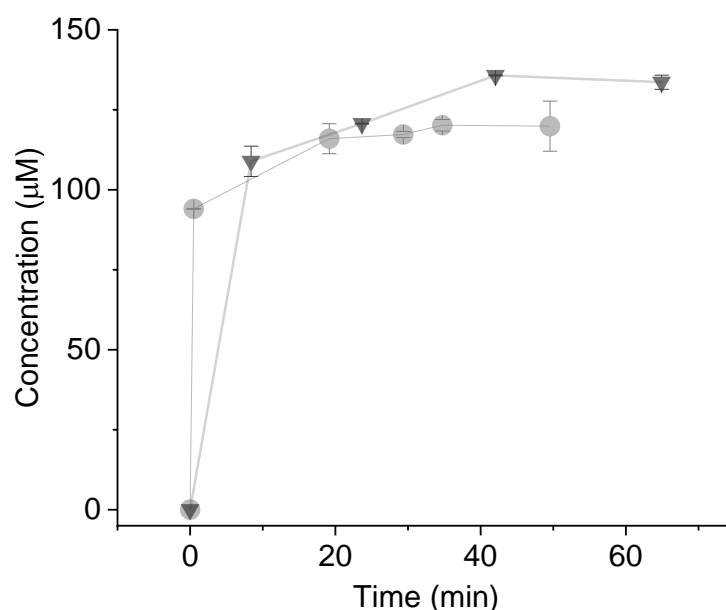


**Figure 44** Exemplary progress curves of benzaldehyde synthesis from 30 mM benzoate and  $\text{H}_2$  (2.5% in headspace) in 100 mM citric acid/ $\text{Na}_2\text{HPO}_4$  buffer at pH 5.5 with 240 nM  $\text{AOR}_{Aa}$ . Analytical repetition average, the error bars represent SD.

A rapid accumulation of product was observed in this reactor and activity could be studied from collected data. Already at 30 s of reaction, the concentration of benzaldehyde reaches 90  $\mu\text{M}$  and slowly rises in next measurements. After 20 min, the concentration of benzaldehyde reached around 120  $\mu\text{M}$  and stabilized for the next 30

min of the assay, which can be recognized as the saturation phase. Once this phase is reached, we can assume that the rates of benzoate reduction and benzaldehyde re-oxidation cancel each other out. The value of product equilibrium concentration was very low ( $127.3 \pm 7.3 \mu\text{M}$ ) in comparison with substrate concentration (30 mM benzoate). This is to be expected as the reaction thermodynamics are indeed unfavourable for the reduction of acids.

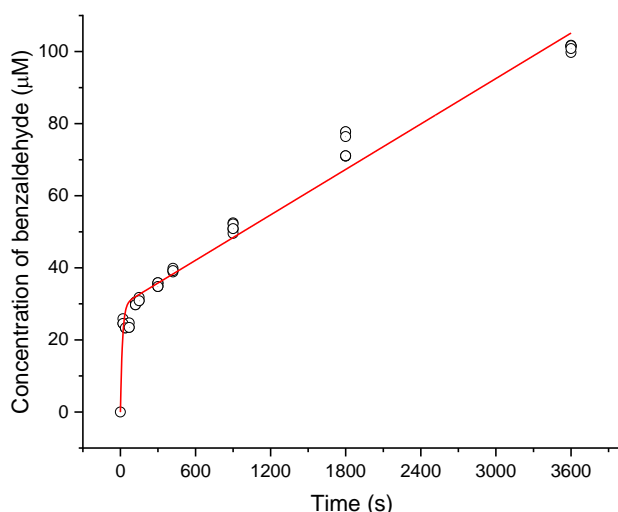
#### *Initial activity in acid reduction*

To quantitate the initial rate of AOR-catalyzed  $\text{H}_2$ -dependent carboxylic acid reduction, a series of reactors was conducted with benzoate as substrate and with the detection of benzaldehyde by means of HPLC-DAD. The reactors were set up with 30 mM benzoate and 2.5% hydrogen in the headspace in 100 mM citric acid/ $\text{Na}_2\text{HPO}_4$  buffer of two different pH values: 5.6 to test the acidic pH and 7.0 to test if a reaction occurs in physiological pH.

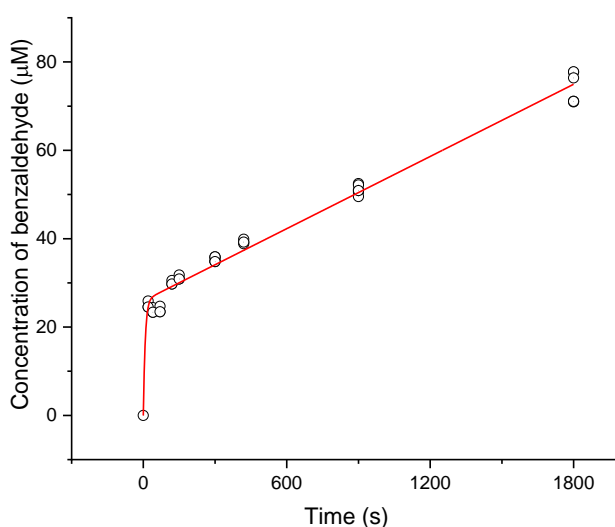
Reactors with 60 nM  $\text{AOR}_{Aa}$  were sampled at the beginning of the reaction every minute, then with longer intervals to show progress curves of the reaction until 30 minutes. In such a direct assay of reaction velocity, the product appearance profile for an enzyme-catalyzed reaction at the beginning should follow approximately linear dependence<sup>133</sup>. Surprisingly, the dependence of benzaldehyde concentration on time was not linear at the beginning of the reaction (see **Figure 45**), but after the first minutes of measurement showed a linear dependency.

This may be interpreted as an initial burst of rapid reaction preceding the linear steady state phase of the reaction, which is called burst phase kinetics. In enzymes, burst kinetics can be caused by one of the reasons: i) severe product inhibition; ii) time-dependent conformational change of the enzyme structure caused by substrate binding; iii) limitation by a slow release of the product from the EP complex; iv) forming of a covalent intermediate, which undergoes slower steady-state decomposition to products<sup>133</sup>.





Fit parameters:  
 $\Pi = 29.47 \pm 0.96$   
 $k = 0.063 \pm 0.014$   
 $V_{ss} = 0.021 \pm 5.76E-4$   
 $\chi^2 = 18.1$   
 $R^2 = 0.976$   
 $\text{Adj. } R^2 = 0.975$



Fit parameters:  
 $\Pi = 25.93 \pm 0.57$   
 $k = 0.127 \pm 0.035$   
 $V_{ss} = 0.027 \pm 6.478E-4$   
 $\chi^2 = 5.29$   
 $R^2 = 0.984$   
 $\text{Adj. } R^2 = 0.984$

**Figure 45.** Progress curves of benzaldehyde synthesis from 30 mM benzoate and H<sub>2</sub> (2.5% in headspace) in 100 mM citric acid/Na<sub>2</sub>HPO<sub>4</sub> buffer at pH 5.6 with 60 nM AOR. The measured values (circles) were fitted with the burst-type kinetic equation  $[P] = \Pi [1 - \exp(-k_b t)] + V_{ss} t$  (red curves).

The burst phase kinetic can be described by an equation:

$$[P] = \Pi [1 - \exp(-k_b t)] + V_{ss} t$$

where  $\Pi$  is the burst amplitude and  $V_{ss}$  is the velocity of the reaction in a steady-state. The burst amplitude depends on the amount of enzyme catalyzing the reaction<sup>177</sup>.

The  $V_{ss}$  was used to calculate the specific activities of the enzyme in reactors according to the same equation as for the initial rate of reaction. The specific activity of AOR<sub>Aa</sub> in benzoate reduction in pH 5.6 was  $72.42 \pm 1.5$  mU/mg, whereas at pH 7.0, the activity was 8 times lower ( $9.33 \pm 0.72$  mU/mg). The interesting result is the activity in an acid

reduction in neutral pH, which suggests that the reaction may also occur in the physiological environment in bacterial cells.

### 6.3. Investigation of electron bifurcation hypothesis.

The AOR<sub>Aa</sub> is able to catalyze the reduction of carboxylic acids as well as NAD<sup>+</sup> with molecular hydrogen as an electron donor. The NAD<sup>+</sup> reduction half-reaction has a standard redox potential of -320 mV, whereas the hydrogen oxidation half-reaction has a lower potential ( $E^\circ(\text{H}^+/\text{H}_2) = -414 \text{ mV}$  for pH 7), which makes the catalyzed reaction feasible. On the other hand, the acid reduction half-reaction has an even lower redox potential ( $E^\circ(\text{benzoic acid/benzaldehyde}) = -505 \text{ mV}$ ) and the hydrogen-dependent reaction must be “pushed” by high substrate concentrations. When the redox potentials of these two reductions are considered, one can notice that the redox potential of H<sub>2</sub> is about halfway between those half-reactions. This creates the possibility for electron bifurcation to occur when electrons from hydrogen oxidation would be split into one electron of higher potential (matching the NADH/NAD<sup>+</sup>) and one of lower potential (the level of benzoic acid/benzaldehyde half-reaction) to minimize free energy loss.

One of the assumptions of the electron bifurcation model in the enzymatic system is that the lower-redox reduction cannot be catalyzed without the simultaneous and stoichiometric reduction of the higher-redox substrate. For the discussed reaction, it would mean no activity in acid reduction unless NAD<sup>+</sup> is available for the enzyme. We did observe the reduction of acid as a sole substrate, however, there is a factor that may facilitate this reaction. As shown for the benzoic acid reduction, the reaction progresses only until an equilibrium is reached that is substantially low and thermodynamically favourable. Therefore, the electron bifurcation, in this case, would be visible in the acceleration of the acid reduction when NAD<sup>+</sup> is also present in the reaction mixture and both reactions should occur with the same velocity.

To test this hypothesis, a range of reactor tests were conducted where apparent initial activities of benzoate and NAD<sup>+</sup> reduction were measured with hydrogen as an electron donor. The substrates for reduction were tested and compared separately or simultaneously in different concentrations of NAD<sup>+</sup>: 0.1 mM (value near  $K_m$ ) or 1 mM (saturated condition) and with 30 mM of benzoate (value near  $K_m$ ). Two different pH values were tested, 5.6 and 7.0, to approach the respective optima for acid (5.0) or NAD<sup>+</sup>(8.0) reduction while retaining the significant activity of the other reaction. The results of this experiment are shown in **Table 17**.

**Table 17.** Specific activities of benzoate and NAD<sup>+</sup> reduction by AOR<sub>Aa</sub> in individual experiments. Calculations of specific activities were based on the V<sub>ss</sub> values obtained from the burst kinetics models.

Reaction set-up	Specific activity in reduction of benzoate (mU/mg)		Reaction set-up	Specific activity in reduction of NAD <sup>+</sup> (mU/mg)	
	pH 5.6	pH 7.0		pH 5.6	pH 7.0
Benzoate	72.42 ± 1.5	9.33 ± 0.72	0.1 mM NAD <sup>+</sup>	16.0 ± 0.1	1300 ± 3.5
			1 mM NAD <sup>+</sup>	71.8 ± 6.5	1 559.8 ± 84.0
Reaction set-up	Specific activity in reduction of benzoate (mU/mg)		Specific activity in reduction of NAD <sup>+</sup> (mU/mg)		
	pH 5.6	pH 7.0	pH 5.6	pH 7.0	
0.1 mM NAD <sup>+</sup> + benzoate	48.04 ± 4.35	14.0 ± 1.00	7.3 ± 0.9	1013.5 ± 4.0	
1 mM NAD <sup>+</sup> + benzoate	6.18 ± 0.36	n.d.	49.3 ± 1.5	1702.5 ± 167.5	

In pH 5.6, acid reduction was 30% slower with 0.1 mM NAD<sup>+</sup> than the control without NAD<sup>+</sup> and 10-fold slower if 1 mM NAD<sup>+</sup> was present in the reactor. On the other hand, in pH 7.0, no impact of the addition of 0.1 mM NAD<sup>+</sup> to the reactor on apparent acid reduction rates was detected, however the acid reduction rate before total NAD<sup>+</sup> conversion could not be quantitated considering a rapid NADH formation. On the contrary, in analogous reactor with 1 mM NAD<sup>+</sup> no activity in acid reduction was detected.

The NAD<sup>+</sup> reduction rates were also influenced by the presence of the second substrate. In pH 5.6, both reaction rates with 0.1 mM NAD<sup>+</sup> and 1 mM NAD<sup>+</sup> were about 2-fold slower if benzoate was present in the reactor. On the other hand, in pH 7.0 presence of benzoate had a negligible impact on activity.

The AOR<sub>Aa</sub> activity in acid and NAD<sup>+</sup> reduction did not show any synergistic effects when both substrates were present. Moreover, the reactions were not stoichiometric, neither did the activities follow stoichiometric changes. Instead, the effects observed clearly show competition between both reductions when the addition of NAD<sup>+</sup> slowed down the

reaction at pH 5.6. These observations falsified the hypothesis that AOR<sub>Aa</sub> might use bifurcation to reduce acids with hydrogen as the electron donor.

#### 6.4. Isotope enrichment tests

The novelty of the hydrogen oxidation reaction by AOR<sub>Aa</sub> opens the question of where the reaction is catalyzed and if the proton required for the reduction of the carboxyl group comes from the electron donor or from water. To gain insight into the mechanistic details of benzoate catalytic reduction with H<sub>2</sub> a series of reactors with deuterated substrates was conducted and the isotopic pattern of the produced benzaldehyde was analyzed based on mass spectra. The reactors contained 100 nM of recombinant AOR<sub>Aa</sub> and 20 mM sodium benzoate in a solution buffered by 50 mM MES to pH 6.5 and as electron donor and solvent, respectively: i) D<sub>2</sub> in H<sub>2</sub>O, ii) H<sub>2</sub> in D<sub>2</sub>O, iii) H<sub>2</sub> and Eu(II) complex in D<sub>2</sub>O, and as a control, iv) H<sub>2</sub> in H<sub>2</sub>O. The samples with D<sub>2</sub>O as solvent contained 5% of H<sub>2</sub>O from the enzyme and buffer. The isotopic pattern of benzaldehyde extracted from reaction mixtures after the reaction is shown in **Table 18**.

**Table 18.** The isotopic pattern of benzaldehyde in standard and samples recorded on GC-MS. The relative abundance was calculated relative to the highest signal.

Mass signal (m/z)	Standard		Sample			
	benzaldehyde	d <sup>1</sup> -benzaldehyde	H <sub>2</sub> /H <sub>2</sub> O	H <sub>2</sub> /D <sub>2</sub> O	D <sub>2</sub> /H <sub>2</sub> O	H <sub>2</sub> /Eu(II)/D <sub>2</sub> O
	<b>absolute abundance</b>					
105	49 823 744	5 815 266	37 013	38 490	98 622	129 194
106	48 108 800	567 066	28 922	25 033	77 815	31 715
107	3 835 817	5 840 551	2 230	5 297	6 542	83 429
108	222 776	446 076	90	918	1 039	77 05
	<b>relative abundance</b>					
105	100.00%	99.6%	100.00%	100.0%	100.0%	100.0%
106	96.56%	9.7%	78.14%	65.0%	78.9%	24.5%
107	7.70%	100.0%	6.02%	13.8%	6.6%	64.6%
108	0.45%	7.6%	0.24%	2.4%	1.1%	6.0%
d <sup>1</sup> -benzaldehyde (%)	<b>0.00%</b>	<b>100.0%</b>	<b>0.00%</b>	<b>27.3%</b>	<b>9.1%</b>	<b>77.6%</b>

When the benzoate is reduced to benzaldehyde, a proton addition occurs at the C1 position. As a result, the deuterated product is d<sup>1</sup>-benzaldehyde. The theoretical isotopic pattern for a [M]<sup>+</sup> = 106 m/z (benzaldehyde) yields singals of m/z 106:107:108 of relative

abundance of 1:0.077:0.004 (calculated by Agilent Isotope Distribution Calculator). Unfortunately, the spectrum is complicated by  $[M-H]^+$  fragmentation ion (105 m/z for benzaldehyde), thus the interpretation of isotopic pattern change by enrichment of  $d^1$ -benzaldehyde from an experiment is not straight forward. The MS isotopic pattern of benzaldehyde and  $d^1$ -benzaldehyde standards in mass signals (m/z) 106:107:108 is 1:0.08:0 and 0.1:1:0.08, respectively. The deuteration of benzaldehyde is most clearly visible from the enrichment of 108 m/z mass signal. Therefore, the fraction of deuterated benzaldehyde was estimated based on the intensity of the 108 m/z signal relative to its occurrence in deuterated or non-deuterated benzaldehyde standards ( $[M+1]^+$  and  $[M+2]^+$ , respectively).

In the sample, where acid was reduced by  $H_2$  in  $H_2O$  the relative abundance of 108 m/z is lower than in the benzaldehyde standard, showing no  $d^1$ -benzaldehyde in the negative control. To calculate the content of  $d^1$ -benzaldehyde a simplified dependence of the amount of  $d^1$ -benzaldehyde on relative abundance was assumed. The relative abundance of 108 m/z signal was described as a sum of the relative abundance of signal from both benzaldehyde and  $d^1$ -benzaldehyde:

$$RA = 7.6 * x + (1 - x) * 0.45$$

Where RA- is the relative abundance of 108 m/z signal [%], x is the content of  $d^1$ -benzaldehyde, 7.6 is RA of pure  $d^1$ -benzaldehyde, 0.45 is RA of pure benzaldehyde.

For the benzoate reduction in  $H_2O$  with  $D_2$  as electron donor enrichment with deuterium was low, reaching only 9.1% of  $d^1$ -benzaldehyde in the total product. The higher content of  $d^1$ -benzaldehyde (27.3 %) was detected in samples reduced by  $H_2$  in  $D_2O$ , whereas when Eu(II) complex was added to such reaction as a second electron donor, the deuterium enrichment was significant, reaching 77.6% of the deuterated product. The second electron donor was added to prove that deuteration of benzaldehyde is possible (positive control). Although in reaction with  $D_2$  as an electron donor the  $d^1$ -benzaldehyde content is low, its presence implies that the acid reduction and hydrogen oxidation reactions take place in close vicinity enabling the transfer of a proton from  $D_2$ , probably on the same cofactor – W-co. However, the hydride that is transferred to the carbonyl atom of benzoate in reaction with  $D_2$  does not come directly from the gaseous electron donor. Apparently, there is an exchange of protons with water molecules present in the active site and as the pool is enriched by the deuterons from  $D_2$ , a small fraction of the product is  $d^1$ -benzaldehyde. Similarly, the high enrichment of benzaldehyde with deuterium (27.3%) in the reaction conducted in  $D_2O$  suggests that protons from hydrogen oxidation are also released and exchanged with deuterons from deuterated water molecules present in the active site. However, the fraction is not analogous as in

the reverse experiment (9.1% D<sub>2</sub> with H<sub>2</sub>O suggesting deuteration in this experiment), because the enzyme is already solvated by H<sub>2</sub>O (from stock). This reasoning leads to such hypothesis of reaction mechanism: H<sub>2</sub>/D<sub>2</sub> is oxidized on *W-bis*-MPT cofactor and protons/deuterons are dissociated after reducing the metal from the W(VI) to the W(IV) state. Subsequently, the benzoic acid is being reduced with a transfer of hydride either bound at *W-co* or from protonated amino acid in the active site.

### 6.5. Substrate spectrum in acid reduction

AOR<sub>Aa</sub> substrate spectrum in the reduction of carboxylic acids was established by the detection of product in test reactors using hydrogen as an electron donor. The reaction was conducted in anaerobic reactors flushed with 100% hydrogen with 10 mL of a mixture consisting of 20 mM respective acid sodium salt in 50 mM MES buffer pH 5.5 and 0.1 μM AOR<sub>Aa</sub>. The reactors were stopped and the product was extracted on SPE columns. Considering low concentrations of benzaldehyde in previous experiments, the chosen protocol for this study was supposed to ensure the rising of concentration of the product to the level detectable in GC-MS.

**Table 19.** Identification of product based on the GC-MS detection of appropriate peaks.

Substrate	Product	GC-MS signals of detected product [m/z] with the shown structure of detected ion
benzoic acid	benzaldehyde	106 [M] <sup>+</sup> , 105 [M-H] <sup>+</sup> , 77 [M-CHO] <sup>+</sup> , 51
cinnamic acid	cinnamaldehyde	132 [M] <sup>+</sup> , 131 [M-H] <sup>+</sup> , 103 [M-CHO] <sup>+</sup> , 77 [M-C <sub>2</sub> H <sub>2</sub> CHO] <sup>+</sup> , 51
phenylacetic acid	phenylacetaldehyde	120 [M] <sup>+</sup> , 91 [M-CHO] <sup>+</sup> , 77 [M-CH <sub>2</sub> CHO] <sup>+</sup> , 65
octanoic acid	octanal	100 [M+H-CHO] <sup>+</sup> , 84 [M-C <sub>3</sub> H <sub>8</sub> ] <sup>+</sup> , 110, 69, 56, 44
nicotinic acid	3-pyridine-carboxaldehyde	107 [M] <sup>+</sup> , 106 [M-H] <sup>+</sup> , 78 [M-CHO] <sup>+</sup> , 51

The identification of isolated reaction products was carried out using mass spectroscopy coupled with gas chromatography. The observed [M]<sup>+</sup> MS signals and characteristics for aldehydes fragmentation patterns in GC-MS (shown in **Table 19**) allowed identification of the products of reduction of the following carboxylic acids: benzoic acid, phenylacetic acid, *trans*-cinnamic acid, octanoic acid and nicotinic acid. The identity of the aldehyde

products was additionally confirmed by the same retention time of the standards. No aldehyde product was detected in mixtures containing 4-hydroxybenzoic acid and pentanoic acid salts, suggesting that those acids are not substrates for AOR<sub>Aa</sub>. That result was surprising, as 4-hydroxybenzaldehyde is oxidized by AOR<sub>Aa</sub>, similarly to all aldehydes that were detected in this set of experiments. The test could have had a false negative result, caused by a low recovery of the sample from the SPE column and a concentration of analyte below the limit of detection by the MS method. Therefore, a different detection method was tested. An LC-MS/MS detection method was established for 4-hydroxybenzaldehyde and the samples from the reaction mixture with 4-hydroxybenzoic acid were analyzed. A [M+H]<sup>+</sup> quasi-molecular parent ion and characteristic MRM transitions in LC-MS/MS for 4-hydroxybenzaldehyde were detected in the aforementioned samples, which proved that 4-hydroxybenzoic acid is an AOR<sub>Aa</sub> substrate. Unfortunately, for a low molecular mass pentanal, the LC-MS/MS detection method could not be established.

### **6.6. Characterisation of acid reduction with the coupled assay method**

The study of kinetic parameters of acid reduction by AOR<sub>Aa</sub> with identified electron acceptors was not possible in the direct spectroscopic measurement of absorbance. Titanium (III) complexes used in experiments have very high absorbance in visible spectra and easily precipitate. Europium (II) complexes are very expensive and could not be used in the more extended study. A set-up with hydrogen as an electron donor, was also tested to see if the difference in absorption between benzoic acid and benzaldehyde is visible in UV-vis spectrometry, but the low conversions of benzoic acid in the AOR-catalyzed reaction gave no change in UV-vis spectra. Therefore, a coupled assay method was developed, in which the benzaldehyde production catalysed by AOR<sub>Aa</sub> is coupled to further reduction of aldehyde to alcohol by BaDH, which is using NADPH as electron donor. The NADPH oxidation is observed by UV-vis spectrometry. Considering the low equilibrium concentration of benzaldehyde in the coupled assay, this test also allows for the quantitation of reaction rates of acid reduction by AOR<sub>Aa</sub> without the impact of product inhibition.

The pH dependency of the specific activity of AOR<sub>Aa</sub> in benzoate reduction, shown in **Figure 46.A** was examined by an established coupled assay method in either citric buffer (pH 4.5-6.0) or potassium phosphate buffer (pH 6.0 – 7.0) with 30 mM benzoate as substrate.

The results show a strong preference for more acidic pH, with a decrease in activity at 4.5. The activity measurements at pH 4.5 had a very standard deviation of

measurement, which was probably caused by the precipitation of enzymes. The precipitation was observed by an increase of baseline absorption in the UV-vis spectrum in the range of 250-500 nm (data not shown). At pH 7.0 no activity was detected, in contrast to previous experiments where produced benzaldehyde was detected. This result indicates that the rate of acid reduction was below the limit of detection of the coupled assay method.

The highest activity was noted for pH 5.0. Nevertheless, the kinetic parameters examination and reactor tests were conducted at pH 5.5 to ensure that any possible precipitation does not influence activity. These results show that the pH has a strong impact on AOR<sub>Aa</sub> activity in carboxylic acid reduction. The fact, that the enzyme is favouring acidic pH suggests that the reaction occurs with protonated carboxylic acid rather than a carboxylate ion, since the pK<sub>a</sub> of benzoate in water is 4.2.

The coupled assay was also used to analyze the kinetics of H<sub>2</sub>-dependent acid reduction at constant hydrogen concentration (2.5% in the headspace of reaction) and varied concentrations of benzoate (4-60 mM) in 100 mM citric acid/citrate buffer pH 5.5 (30 °C). The dependency of the steady-state rate of the reaction catalyzed by 0.03 mg/mL AOR<sub>Aa</sub> on the concentration of benzoate could be fitted with good accuracy (R<sup>2</sup>=0.95) to Michaelis Menten model as shown in **Figure 46.C**. Fit of data with Hill model gave n=1 which is equivalent to Michaelis-Menten model. The data fit yielded an apparent K<sub>m</sub> of 33.8 mM benzoate and a maximum reaction rate V<sub>max</sub> of 0.011 mM min<sup>-1</sup> corresponding to k<sub>cat</sub> value of 1.4 s<sup>-1</sup> (calculated for the complex mass of 218 kDa). The affinity of AOR<sub>Aa</sub> towards benzoate is significantly lower than for benzaldehyde (with almost a thousand times lower K<sub>m</sub> of 39 μM benzaldehyde) and the reduction is around a hundred times slower with k<sub>cat</sub> for benzaldehyde oxidation of 123 s<sup>-1</sup>.

The kinetic parameters of acid reduction by aldehyde oxidoreductases have been shown in literature with reduced viologen dyes as electron donors (TMV<sup>+</sup>, CAV<sup>+</sup> and MV<sup>+</sup>) for AOR<sub>Cf</sub>, AOR<sub>Mt</sub> and AOR<sub>Tp</sub><sup>65,76,178</sup>. From the comparison shown in **Table 20**, one can state that the low affinity towards benzoate is a common feature of AORs and the reduction of a nonactivated carboxylic acid is catalyzed with low turnover numbers.

The comparison was extended to carboxylic acid reductases, although it should be noted that the catalysis by this enzyme includes an additional step of formation of acyl adenylated intermediate. The affinity of AOR towards benzoate is significantly lower than those observed for CAR enzymes (K<sub>m</sub> of 0.9 mM for *Nocardia* sp. NRRL 5646 CAR<sup>8</sup>) and the reaction occurs with a lower turnover number (1.4 s<sup>-1</sup> for AOR and 6.6 s<sup>-1</sup> for CAR).



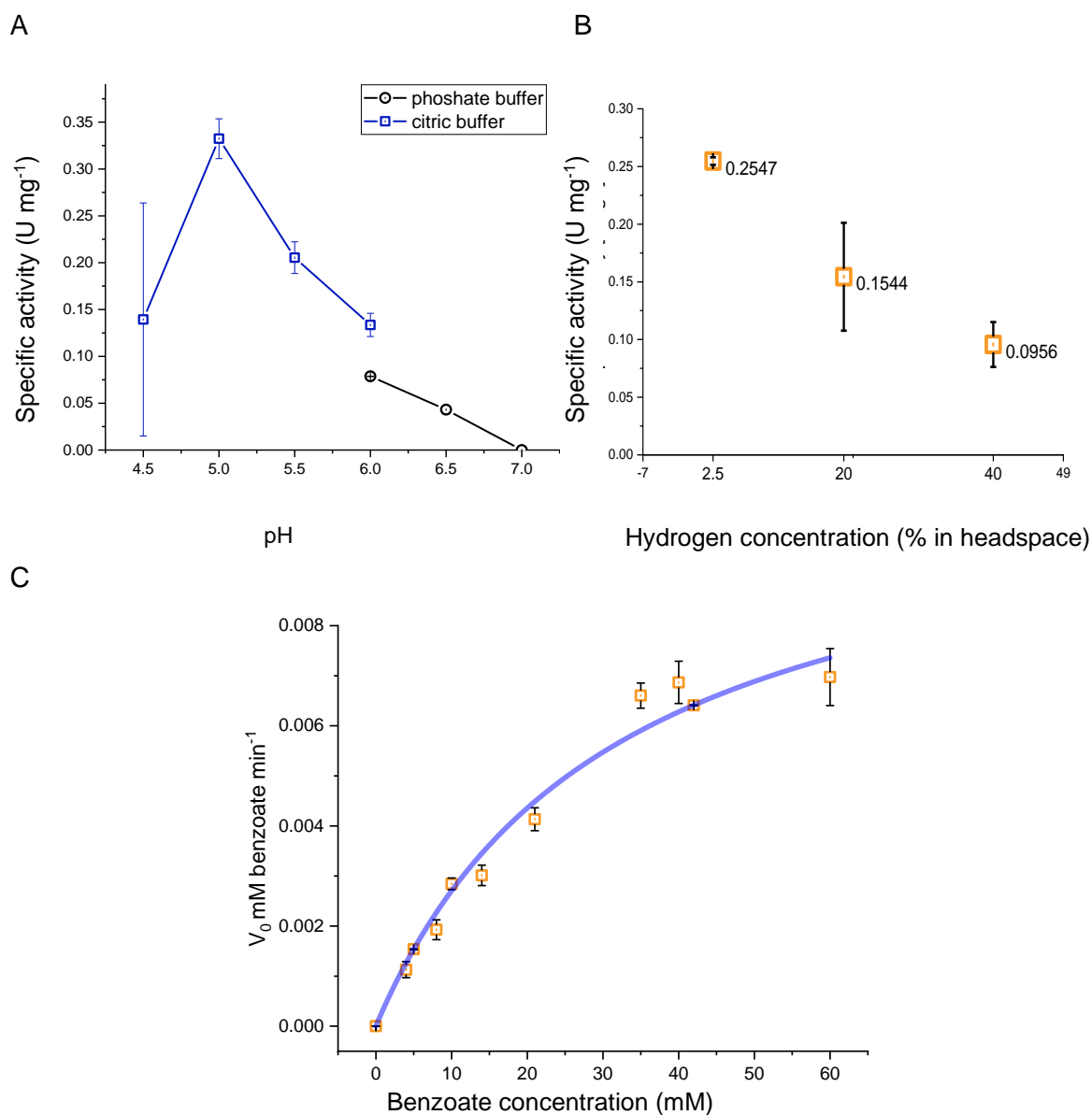


**Figure 46.** Dependency of specific activity of AOR in benzoic acid reduction **A)** on pH, measured with the coupled assay in either sodium citrate buffer (pH 4.5-6.0) or potassium phosphate buffer (pH 6.0 – 7.0), **B)** on hydrogen concentration; **C)** Michaelis-Menten kinetic curve fits for AOR activity with variable benzoate concentrations at constant H<sub>2</sub> (2.5 %).

Surprisingly, when activity in acid reduction was tested according to coupled assay method, with higher hydrogen concentrations than in standard tests (20% and 40% of hydrogen in headspace instead of 2.5%) the observed reaction rate was significantly lower (**Figure 46B**). With a 2.5% hydrogen reaction rate was 0.25 U mg<sup>-1</sup>, while with 20% hydrogen in the headspace, the activity was only 0.15 U mg<sup>-1</sup> and further doubling the fraction of hydrogen resulted in only 38% of activity in the standard test

(0.096 U mg<sup>-1</sup>). Even though those data are not detailed enough to discuss the mechanism of inhibition by hydrogen, such an effect was also observed in many hydrogenases (i.e. *Ralstonia eutropha* [NiFe]-hydrogenase)<sup>102</sup>.

**Table 20.** Kinetic parameters of AOR<sub>Aa</sub> in benzoic acid reduction, compared with literature data for other AORs,  $k_{cat}$  was calculated for AOR<sub>Aa</sub> mass Aor(AB)<sub>2</sub>C= 218 kDa, measured at 30 °C.

Enzyme	Substrate	El. Donor	$K_{cat}$ (s <sup>-1</sup> )	$K_m$ (mM)	$k_{cat}/K_m$ (mM /s)
AOR from <i>Aromatoleum aromaticum</i>	benzoate	H <sub>2</sub>	1.4	33.8	0.042
<i>Nocardia</i> sp. CAR <sup>a</sup>	benzoate	NADPH	6.6	0.9	7.3
AOR from <i>Clostridium formicoaceticum</i> <sup>b</sup>	benzoate	TMV <sup>++</sup>	n.a.	16.7	n.a.
AOR from <i>Moorella thermoacetica</i> <sup>c</sup>	benzoate	CAV <sup>++</sup>	n.a.	53 ± 11	0.19
AOR from <i>Thermococcus paralvinellae</i> <sup>d</sup>	acetate	MV <sup>++</sup>	1.6	1.8	0.001

<sup>b</sup> - at 40° C, in 0.3M potassium phosphate pH 6.0, 60mM sodium propionate, 20mM semicarbazide, 0.8-0.9mM TMV<sup>++</sup> and 8-80 µg protein, data from White *et al.*<sup>178</sup>

<sup>c</sup> - at 40 °C, in 0.3 M citrate-phosphate buffer pH 5.5, containing 12 mM semicarbazide, 0.15 mM CAV<sup>++</sup>, 6–28 µg protein, data from Huber *et al.*<sup>76</sup>

<sup>d</sup> - at 85 °C in 500 mM potassium phosphate (pH5.5), data from Heider *et al.*<sup>65</sup>

## 6.7. Biocatalytic tests.

### 6.7.1. AOR and BaDH reactor for benzyl alcohol production.

Effective production of alcohols from carboxylic acids is a transformation pursued by biotechnologists and one of this work's main topics. The first aim of the work was to find feasible reductors that can push the AOR-catalyzed reduction of carboxylic acids and to couple that reaction to the further enzymatic reduction of the aldehyde. The discovery of AORs hydrogenase activity changed the perspective on the electron donors for the whole acid reduction transformation. The coupled assay used for AOR<sub>Aa</sub> kinetic studies can also be interpreted as a cascade to produce benzyl alcohol. In the example depicted in **Figure 26** the cascade successfully reduced benzoic acid to 0.12 mM of benzyl alcohol from 30 mM substrate using NADPH and hydrogen as electron donors. However, NADPH that was used in that experiment is a very expensive substrate. To make this

cascade economically practical, the NADPH should be exchanged for NAD<sup>+</sup> and an NADH regeneration system should be applied. Since AOR<sub>Aa</sub> is capable to simultaneously reducing carboxylic acids and NAD<sup>+</sup>, it could be used for both reactions in this cascade, and then BaDH would use the aldehyde and NADH to produce alcohol. Moreover, accounting for AOR<sub>Aa</sub> hydrogenase activity, hydrogen could be used as a sole net electron donor for the whole cascade, with very low NAD<sup>+</sup> concentration as a mediator of electrons (scheme of the cascade depicted in **Figure 47**).

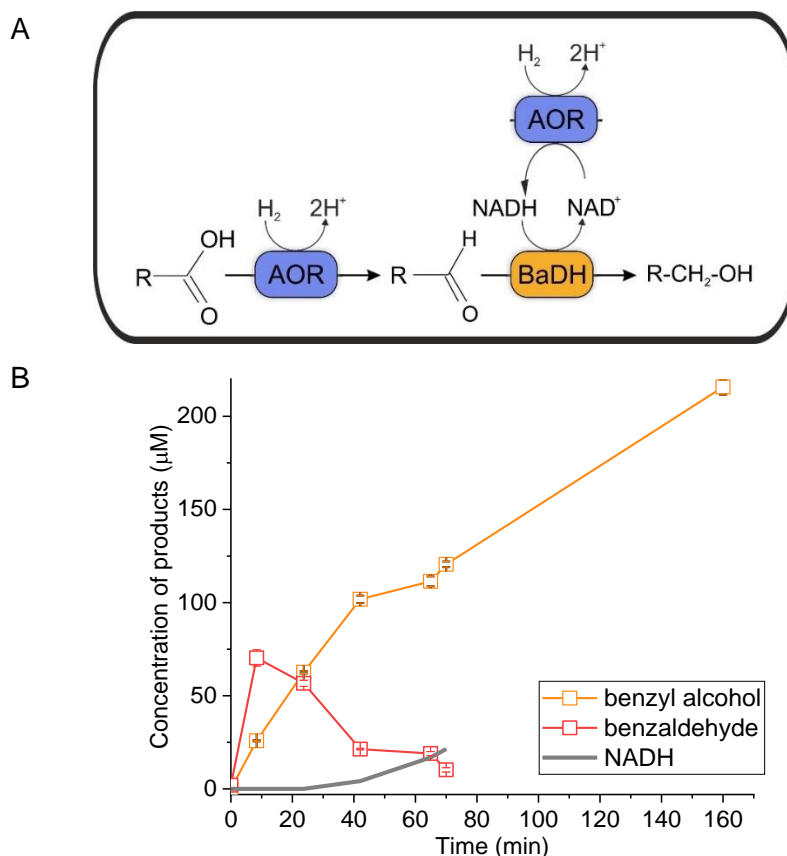


**Figure 47. A)** Scheme of enzymatic cascade for production of alcohols. **B)** Progress curves of enzymatic cascade catalyzed by 120 nM AOR<sub>Aa</sub> and 500 nM BaDH for production of benzyl alcohol from 30 mM benzoate with 0.1 mM NAD<sup>+</sup> and 2.5 % H<sub>2</sub> at pH 5.5.

The first attempt at the alcohol-producing cascade was meant to investigate if the production of alcohol can reach yields higher than benzaldehyde production without the cascade. In previous experiments, benzaldehyde reached an equilibrium concentration at around 100 μM. However, processing aldehyde further towards the alcohol should “pull” the reaction from equilibrium and the end product, benzyl alcohol, should be accumulated. To achieve that, the cascade was designed with unstoichiometric, higher BaDH activity than AOR activity. The result (**Figure 47.B**) shows that the initial high

concentration of benzaldehyde was promptly used to produce benzyl alcohol and then stayed at a marginal level as all produced aldehyde was converted by BaDH instantly. The initial lag time of the benzyl alcohol production was caused by initial slower production of NADH than aldehyde by AOR. Benzyl alcohol was obtained in a linearly increasing manner until the experiment was aborted after 2 h. Although the experiment was not followed to the end, the amount of product (0.2 mM benzyl alcohol) represented the highest yield of reduced aldehyde (further converted to alcohol) observed so far for AOR<sub>Aa</sub>.

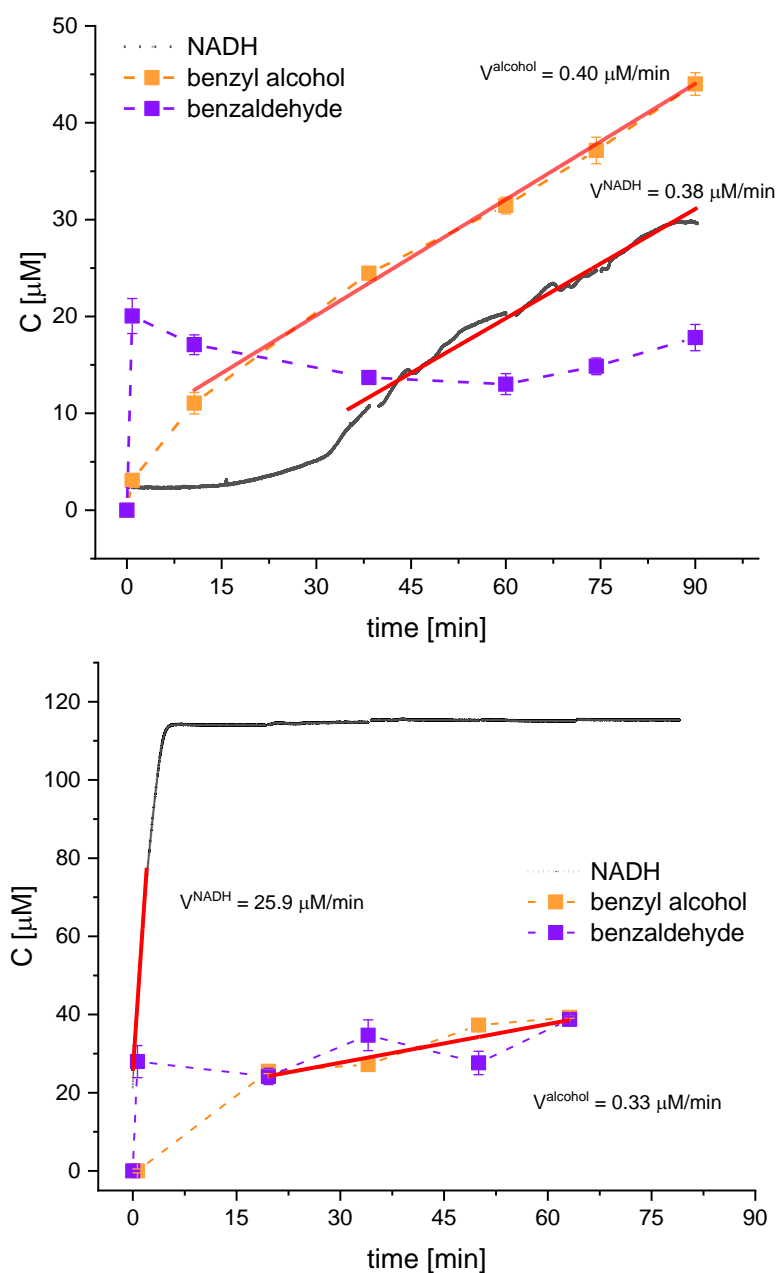


**Figure 48.** Progress curves of enzymatic cascade catalyzed by 60 nM AOR<sub>Aa</sub> and 500 nM BaDH for production of benzyl alcohol from 30 mM benzoate, 0.1 mM NAD<sup>+</sup>, in 2.5%

H<sub>2</sub>, pH 5.6 (top) and 7.0 (bottom). Rates for NADH and benzyl alcohol accumulation were fitted with linear function as indicated by red lines; the error bars represent SD.

**Table 21.** Rates of NADH and benzyl alcohol formation in cascade catalyzed by 60 nM AOR<sub>Aa</sub> and 500 nM BaDH.

	pH 7.0	pH 5.6
Rate of NADH accumulation (mU·mg <sup>-1</sup> )	1309.3±133.9	17.8±1.3
Rate of alcohol formation (mU·mg <sup>-1</sup> )	25.8±11.5	20.8±2.2
Average benzaldehyde concentration (μM)	26.5±3.1	15.9±0.4

Using only H<sub>2</sub> as an electron donor, AOR<sub>Aa</sub> was expected to catalyze both reductions of benzoic acid to benzaldehyde and of NAD<sup>+</sup> to NADH, which would be used by BaDH during the further reduction of benzaldehyde to benzyl alcohol.

This coupled test containing BaDH and NAD<sup>+</sup> was also intended to analyze the reaction stoichiometry. In an optimally coupled reaction cycle, an H<sub>2</sub>-dependent reduction of benzoate to benzyl alcohol should proceed without the accumulation of either benzaldehyde or NADH. The experiment was conducted at two pH values that support the occurrence of both reactions and represent different conditions: at acidic pH (5.6) and at neutral pH (7.0). The course of the reaction was illustrated by chosen example (**Figure 48**) and the rates of occurring reactions were shown in **Table 21**. In both conditions, the concentration of aldehyde quickly reached a quasi-equilibrium, which was on a moderately higher level in neutral pH, at approx. 27 μM. In acidic conditions, the concentration of alcohol established at the rate of 20.8 mU·mg<sup>-1</sup> after 15 min from start of reaction. Due to NADH's consumption due to aldehyde reduction, no NADH accumulation was observed during the first 30 minutes of the reaction. Later on, the concentration of NADH rose at the same rate as that of alcohol (17.8 mU·mg<sup>-1</sup>).

At neutral pH, the accumulation of NADH started immediately and with a rate significantly higher (1309 mU·mg<sup>-1</sup>) than in acidic conditions, whereas the alcohol was produced, again at a similar rate as at acidic pH (25.8 mU·mg<sup>-1</sup>). Interestingly, the applied cascade seems to work equally efficient in alcohol production at both acidic and neutral pH.

### 6.7.2. NADH regeneration system for R-HPED- catalyzed acetophenone reduction

A test reactor for synthesis of (R)-1-phenylethanol from acetophenone using NADH-dependent stereospecific short-chain alcohol dehydrogenase R-HPED from *A. aromaticum* was conducted to provide an example of the use of the AOR-catalyzed NADH regeneration system with hydrogen as an atom-efficient electron donor. R-HPED is an enzyme studied in our Laboratory as a catalyst for the stereospecific reduction of ketones with high optical purity of chiral product<sup>138</sup>. In those studies, R-HPED was also used for NADH regeneration as the enzyme reduced NAD<sup>+</sup> using propan-2-ol as a sacrificial substrate.

A crude cell extract of *A. evansii* with recombinant AOR<sub>Aa</sub> was used as the biocatalyst for NADH regeneration. The AOR was not enriched on the FPLC column, but instead, the soluble, non-proteinous ingredients of cell extract were washed *via* ultrafiltration. This approach to biocatalyst preparation has an economic advantage for industrial applications, as it introduces fewer steps and also prohibits the slow inactivation of AOR on contact with air, which was observed for the purified enzyme.

The course of the reaction was monitored by HPLC with DAD detection of the product-(R)-1-phenylethanol (**Figure 49**). The product was formed with an average rate of 9  $\mu\text{M}/\text{h}$ , which did not decrease during 48 h of reaction. After 48 hours, a conversion of acetophenone of 14.6% (0.43 mM) was observed.

The presented yield of the reactor using AOR-catalyzed NAD<sup>+</sup> reduction is not yet competitive to the previously established regeneration system based on the oxidation of propan-2-ol by bifunctional R-HPED. However, the experiment was set up with completely arbitrary conditions ( $\text{H}_2$ , NAD<sup>+</sup> concentration, pH) and can certainly be further optimized.

This experiment proved that the AOR-catalyzed NADH regeneration system can be applied in the form of crude extract preparations and that it remains fully active for a considerable amount of time (at least two days).

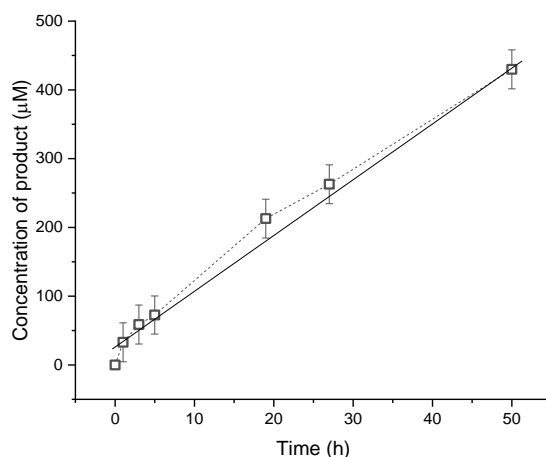


**Figure 49.** Progress curve of synthesis of (R)-1-phenylethanol from acetophenone by R-HPED, the NADH regeneration system used: AOR<sub>Aa</sub> with 2.5 % H<sub>2</sub>; analytical repetition average was shown with error bars representing SD.

### 6.7.3. Carbon monoxide inhibition test

Biomass gasification and methane reforming are examples of industrial methods of producing gaseous hydrogen-containing fuel (“blue hydrogen”). Apart from hydrogen, this fuel mostly contains relevant amounts of carbon monoxide, methane and nitrogen. Many known hydrogenases are inhibited by carbon monoxide and, therefore, “blue hydrogen” cannot be used with those biocatalysts<sup>97</sup>. AOR<sub>Aa</sub>, as a new type of hydrogenase, was expected to be also sensitive to this inhibitor.

To test the impact of carbon monoxide on the hydrogenase activity of AOR<sub>Aa</sub>, crude cell extract containing AOR<sub>Aa</sub> was incubated with a gas mixture prepared to mimic the content of syngas (containing (v / v) 59% nitrogen, 40% carbon monoxide, approx. 1% hydrogen and approx. 0.03% oxygen). After 1.5 h incubation, the activity of hydrogen-dependent NAD<sup>+</sup> reduction was measured and observed at the same level as for the control (crude cell extract incubated with 1% hydrogen). Therefore, the AOR<sub>Aa</sub> hydrogenase activity in NAD<sup>+</sup> reduction appears to be unaffected by CO, allowing efficient use of AOR<sub>Aa</sub> even with “blue hydrogen”.

## DISCUSSION OF PART II

The vast substrate spectrum of AOR<sub>Aa</sub> in aldehyde oxidation shown in this work (**Table 12**) may confirm the assumption presented in literature, that AORs are physiologically responsible for detoxification of the bacterial cell from toxic aldehydes by converting them to inert acids. On the other hand, the observed  $K_m$  values of aldehyde concentration were lower for AOR<sub>Mt</sub> and AOR<sub>Tp</sub> than for AOR<sub>Aa</sub>. The fact, that AOR<sub>Aa</sub> is less specific in

binding of the aldehydes as substrates may be beneficial for the application as catalyst in reduction of the carboxylic acids (in cascades shown in Chapter 6.7.).

The proved side-activity of AOR<sub>Aa</sub> as hydrogenase is first example of hydrogen activation by tungsten enzyme and only one other Mo-dependent enzyme, CO dehydrogenase, exhibit such activity. The activation of hydrogen in the latter case happens on copper atom in a MoCu-cofactor, while for AOR<sub>Aa</sub>, the responsible site is most probably tungsten cofactor.

The experiments shown in Chapter 6.5. demonstrated that the AOR<sub>Aa</sub> substrate spectrum is very similar to the one in aldehyde oxidation, as it is converting aromatic (benzoic acid, 4-hydroxybenzoic acid) and alkylaromatic (phenylacetic acid, *trans*-cinnamic acid), heterocyclic (nicotinic acid) or aliphatic acids (octanoic acid). Most of the produced aldehydes are listed as admitted flavoring agents.

The potential application of AOR<sub>Aa</sub> for H<sub>2</sub>-dependent NADH recycling was demonstrated in two coupled systems: with BaDH for the production of alcohols from acids and R-HPED for producing chiral alcohols from ketones. Using H<sub>2</sub> as an electron donor provides an atom-efficient and clean NADH recycling system, which is a general advantage of hydrogenases in this application. AOR<sub>Aa</sub> as an NADH recycling system is not as efficient as classical hydrogenases; however, it has some other advantages. “Blue hydrogen” is a suitable substrate source for AOR<sub>Aa</sub>, as it was shown to be insensitive to the presence of CO. In contrast to most hydrogenases, AOR<sub>Aa</sub> was shown to be stable throughout 48 h of catalyzed reaction and no significant drop of activity was observed in the experiment with R-HPED.

Moreover, the enzyme has a unique capability of simultaneously catalyzing both acid reduction and NADH regeneration. Considering the low equilibrium concentration of benzaldehyde without further derivatization, the enzyme has limited potential as a catalyst for producing pure aldehydes. On the other hand, the example of BaDH cascade demonstrates that if the aldehyde is only an intermediate, the cascade can achieve good yields. Surprisingly, cascade reactors were working with the same rates for alcohol production also in neutral pH even though acid reduction activity by AOR<sub>Aa</sub> is lower in these conditions. This finding provides a foundation for possible tests of *in vivo* reduction of acids.

The throughout study of AOR<sub>Aa</sub> hydrogenase activity, especially in coupling oxidation of hydrogen to acid reduction, showed a high application potential of the biocatalyst. The AOR<sub>Aa</sub>-based system can be used in production of high added-value compounds from carboxylic acids (also those derived from lignocellulosic biomass, e.g., 4-hydroxybenzoic



acid, vanillic acid), with use of hydrogen as an electron donor (possibly for whole biocatalytic cascade).

### **PART III. Structural studies**

## **7. Structural characterization of AOR**

### **7.1. Protein homogeneity**

The AOR<sub>Aa</sub> preparation by heterologous expression of a tagged protein in *A. Evansii* followed by purification on a Strep-tag column and subsequent gel filtration column yields, in comparison to native protein preparations, enzyme samples of higher purity and occupation of protein cofactors (ICP-MS data showed in Winiarska *et al.*<sup>179</sup>). Moreover, the purification protocol for recombinant AOR<sub>Aa</sub> was shortened from four stages on chromatographic columns to only two stages of purification, which minimized the risk of temperature or proteolytic degradation and oxygen exposure. Therefore, this method of purification should yield samples with a well-preserved structure of the protein. The HEPES buffer was proven by *ThermoFAD* assay to have no negative impact on protein stability. Therefore it was chosen as appropriate for cryoEM preparation.

The first stage of the structural project was the assessment of the homogeneity and stability of the protein by mass photometry (MP). The MP measurement for recombinant AOR<sub>Aa</sub> from the gel filtration pool showed that the sample was not homogenous but rather a combination of aggregates of masses 392, 306, 221, 133 and 79 kDa (**Figure 50**). The mass interspace between the four biggest complexes was regular and amounted to ca. 85 kDa. This mass pattern can be explained by the presence of different oligomers of the AOR complex, with repeating protomer of 85 kDa mass. The mass of the repeating subunit is in agreement with the stoichiometry of the AorAB protomer (86 kDa, 66 kDa for AorB and 20 kDa for AorA). The detected aggregate of mass 133 kDa might correspond to a heterotrimer AorABC (132 kDa). The three larger aggregates visible in MP consist of subsequently more AorAB protomers: Aor(AB)<sub>2</sub>C (218 kDa), Aor(AB)<sub>3</sub>C (304 kDa), and Aor(AB)<sub>4</sub>C (392 kDa). The most abundant higher-order aggregate in MP data was the presumed Aor(AB)<sub>2</sub>C complex. Nevertheless, the number of single protomers and small proteins was prevalent.

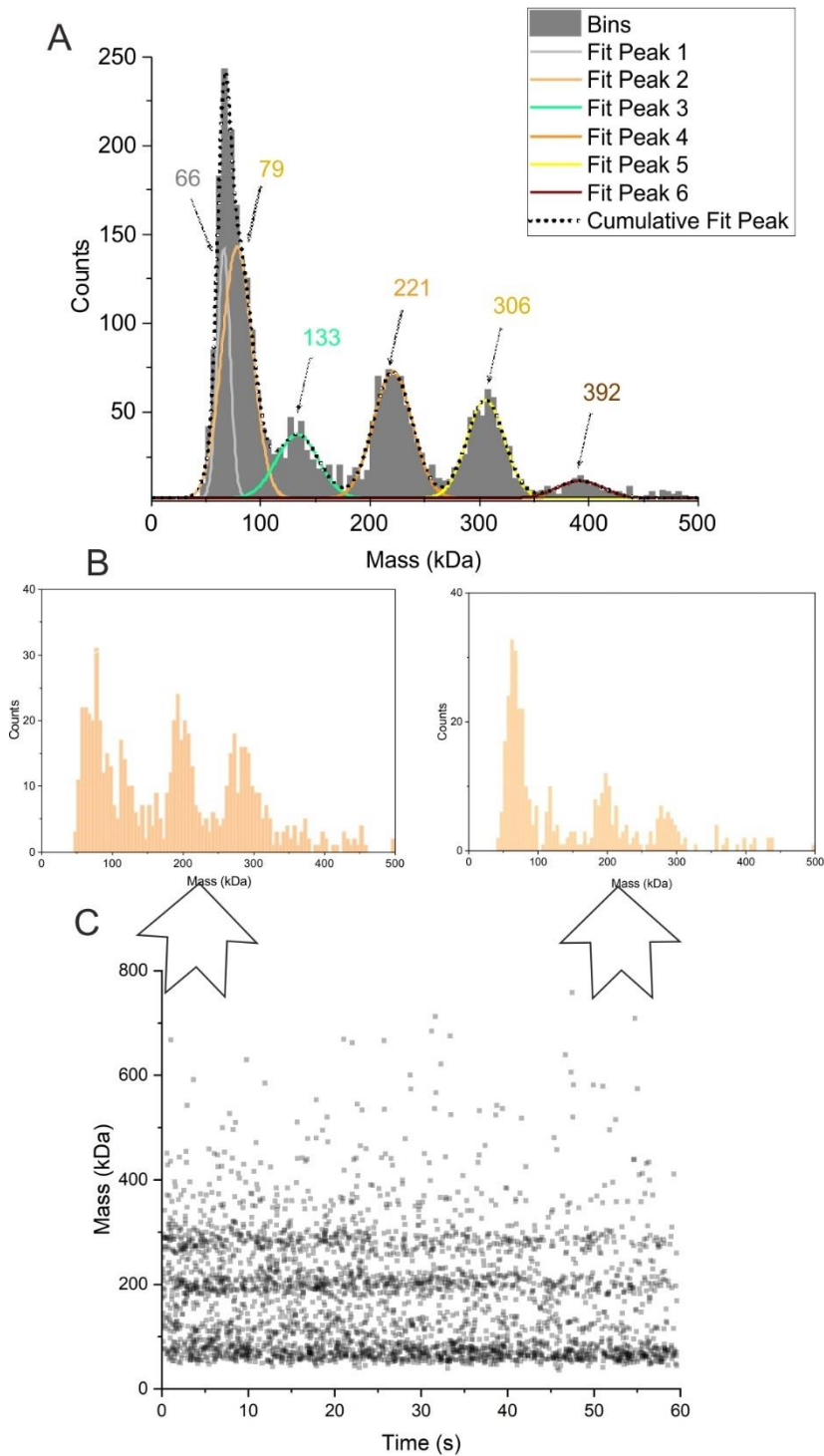


**Figure 50.** Results of mass photometry measurement for AOR preparation. **A)** Mass histogram of the recombinant AOR<sub>Aa</sub> from gel filtration pool of concentration of 50 nM, fitted with distribution peaks of Gaussian function. The average molecular mass of the distribution (kDa) was assigned for the maxima of the individual gauss functions. **B)** Mass histograms of the first and last 10 seconds of MP measurement of AOR<sub>Aa</sub> showed in **C)** scatter plot of single molecule binding events and their corresponding masses.

Mass photometry enables the observation of biomacromolecules in solution in a time-resolved manner, following stoichiometric changes in a complex structure. The time-resolved measurements of the protein sample by MP showed that the complex was not stable at very low concentrations. The histogram of mass counts collected in the first 10 seconds of measurement contained many counts for high masses (392, 306, 221 kDa), and after 40 s, the stoichiometry moved towards higher content of low-mass molecules (80 and 133 kDa), demonstrating dissociation of the complex in diluted samples (**Figure 50.B** and **C**). The structural study was aimed at resolving the complex at native composition. Therefore, the dissociation of the complex had to be prevented. That could be achieved by crosslinking the protein subunits with a mild and inert substance like bis(sulfosuccinimidyl)suberate (BS3). The amount of crosslinker was optimized in the range recommended by the manufacturer (0.5-3 mM) and the samples were screened on MP for stabilization of the higher-mass complexes. Already 1 mM of BS3 added as a crosslinker was sufficient to maintain the native stoichiometry of the complex and crosslinked samples were used to make EM grids.

## 7.2. Reconstruction of AOR<sub>Aa</sub> structure

The crosslinked AOR<sub>Aa</sub> complex was subjected to cryo-electron microscopy with single-particle analysis, which resulted in the reconstruction of the 3.3 Å density map of seven subunits of AOR<sub>Aa</sub> complex (**Table 22**). The density map (**Figure 51**) showed that the structurally characterized complex has a non-symmetric structure of stoichiometry Aor(AB)<sub>3</sub>C, which supports the observations from MP measurements. The reconstructed map enabled the generation of a model of Aor(AB)<sub>2</sub>C complex. Already at the heterogeneous refinement, two particle classes were identified: a more abundant class of particles of apparent stoichiometry Aor(AB)<sub>2</sub>C and a smaller class of Aor(AB)<sub>3</sub>C stoichiometry. The variable occupancy of the last AorAB protomer in the complex apparently impacted the local resolution of the corresponding map, as shown in **Figure 53**. No parts of the core structure were identified as flexible based on the local resolution. The model of Aor(AB)<sub>2</sub>C complex is annexed to this work in form of electronic supplement.

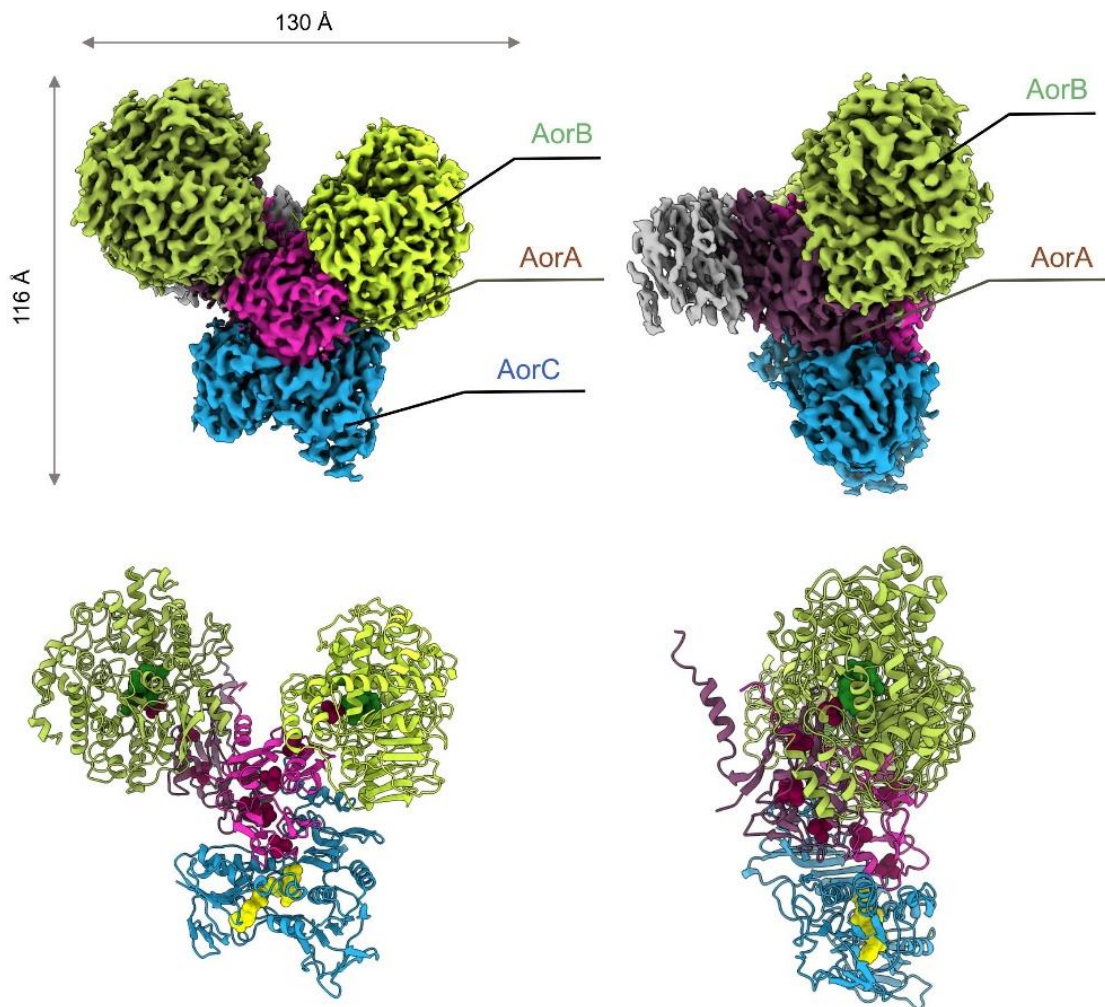


**Figure 51.** Representative three-dimensional cryo-EM reconstructed density of  $AOR_{Aa}$  (up) coloured by identified subunit. The low-resolution density was assigned to another (third) AorA" subunit and residual electron density (coloured in gray) may correspond to an additional (third) partially occupied AorB". Three-dimensional reconstruction of  $AOR_{Aa}$  consisting of two protomers: AorABC and AorAB.

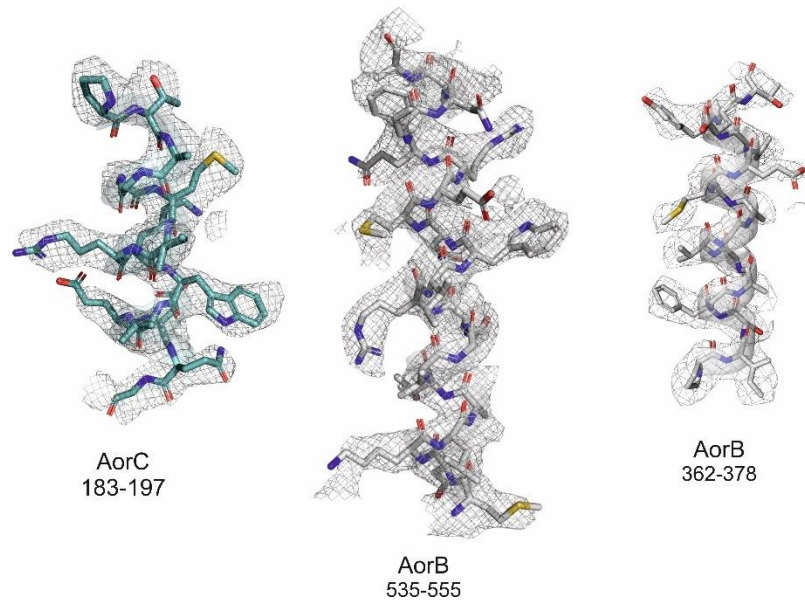


**Figure 52.** Fragments of the structure showing the fit of the model to electron density map.

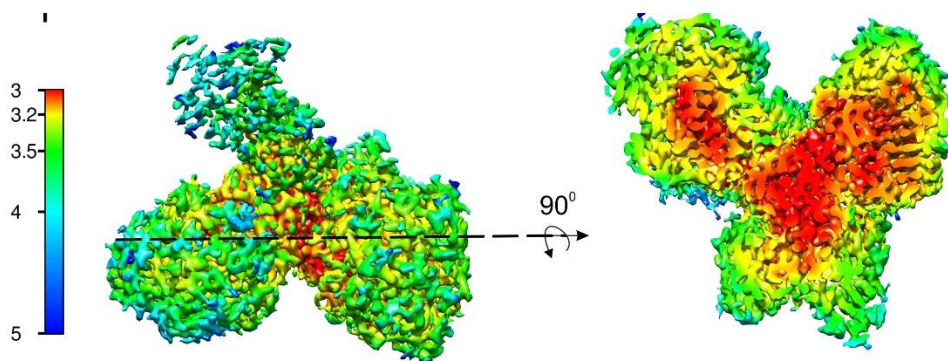


**Figure 53.** Density map of AOR<sub>Aa</sub> colored according to the local resolution calculated by cryoSPARC (left) and cut-open view of the central section tilted by  $90^\circ$  (right).

**Table 22.** Cryo-EM data collection, refinement and validation statistics of AOR<sub>Aa</sub> structure.

Protein	AOR <sub>Aa</sub>
<b>Data collection and processing</b>	
Microscope	Glacios Cryo-TEM
Voltage (kV)	200
Camera	Falcon 3
Total electron exposure (e <sup>-</sup> /Å <sup>2</sup> )	40
Defocus range (µm)	-0.5 to -2.0
Software	cryoSPARC
Raw pixel size (Å)	1.00
Symmetry imposed	C1
Micrographs (no.)	896
Initial extracted particles (no.)	273,728
Final extracted particles (no.)	62,731
Final map resolution (Å)	3.3
FSC threshold	0.143
Map sharpening B-factor (Å <sup>2</sup> )	137.2
<b>Refinement</b>	
Initial model used	AlphaFold
Model composition	
Chains	5
Non-hydrogen atoms	15,083
Protein residues	1972
Ligands	2 x Benzoate, 2 x Mg <sup>2+</sup> , 2 x W-co, 1 x FAD, 10 x Fe <sub>4</sub> -S <sub>4</sub>
B factors	
Protein	126.86
Ligand	64.52
R.M.S Deviations	
Bond lengths (Å)	0.004
Bond angles (°)	0.674
<b>Validation</b>	
MolProbity score	1.46
Clash score	2.69
Poor rotamers (%)	0.13
Ramachandran plot	
Favored (%)	93.93
Allowed (%)	5.91
Outliers (%)	0.15

### 7.3. Quaternary structure of the AOR<sub>Aa</sub> complex

The AorC subunit was identified only once in the density map. The model built into the observed electron density contains two AorA subunits in the center of the complex and

two AorB subunits binding to the complex, each by one of the AorAs. The reconstructed complex is not symmetrical; AorC has a large interface with only one of the AorA subunits, thus it can be assumed that with the connected AorB, those subunits are part of the AorABC complex detected in MP. To facilitate further discussion on AOR<sub>Aa</sub> structure and its oligomeric form, the following subunit pairs in the structure were named AorA' and AorB', AorA'' and AorB'', etc. The AorA'' and AorB'' subunits were recognized as hypothetical proteins building the third protomer of the complex, which was not included in the reconstructed model because of its rather low resolution.

The interactions between the subunits in Aor(AB)<sub>2</sub>C complex were analyzed, and the parameters of each formed interface in the complex were shown in **Table 23**.

**Table 23.** Properties of interfaces in Aor(AB)<sub>2</sub>C complex calculated in PDBePISA.

Structure 1			Structure 2			Interface area, (Å <sup>2</sup> )	Δ <sup>i</sup> G kcal/mol	N <sub>HB</sub>	N <sub>SB</sub>
Subunit 1	N <sub>res</sub>	Surface (Å <sup>2</sup> )	Subunit 2	N <sub>res</sub>	Surface (Å <sup>2</sup> )				
AorC	49	21 504	AorA	41	10 669	1 662.0	-19.7	6	3
AorA	31	10 669	AorA'	41	10 614	1 288.2	-13.5	13	0
AorA	27	10 669	AorB	37	23 335	961.8	-12.0	7	0
AorA'	25	10 614	AorB'	39	23 327	929.9	-11.8	8	0
AorC	15	21 504	AorA'	19	10 614	482.1	-2.6	4	2
AorC	15	21 504	AorB	17	23 335	431.7	0.7	4	1

N<sub>res</sub> - denotes the number of interacting residues in the subunit; N<sub>HB</sub> - denotes the number of possible hydrogen bonds across the interface; N<sub>SB</sub> - number of potential salt bridges across the interface; The interface area was determined by dividing the difference in total accessible surface areas of isolated and interacting structures by two.

Δ<sup>i</sup>G (kcal/M) indicates the solvation-free energy gain upon interface formation, calculated as the difference in total solvation energies of isolated and interfacing structures. Negative Δ<sup>i</sup>G corresponds to hydrophobic interfaces, or positive protein affinity. The influence of fulfilled hydrogen bonds and salt bridges across the contact is not included in this number.

The analysis of protein interfaces is used in X-ray crystallography to determine, if the interface is an actual macromolecular assembly or result of crystal packing. In cryo-EM, due to rapid freezing from the solution, the formation of crystal packing does not occur and such analysis is not necessary. Nevertheless, the observed varied stoichiometry of the complex might be caused by weak binding at interfaces that promotes dissociation of the complex in unfavourable conditions (low concentration of enzyme). Thus the analysis of interfaces formed in the complex was undertaken to explain the dissociation process.

The analysis is based on solvation-free energy gain upon the formation of the interface ( $\Delta^iG$ ) and the number of hydrogen bonds and salt bridges formed. As already mentioned, the AorC forms the largest interface in the complex ( $1\,662\text{ \AA}^2$ ), with a  $\Delta^iG$  value favouring this binding and three recognized salt bridges. The next very important interface is between AorA and AorA' ( $1\,288\text{ \AA}^2$ ), which constitutes most of the binding between the first protomer (forming AorABC complex) and second protomer (forming Aor(AB)<sub>2</sub>C complex). Binding within the protomer (AorA to AorB) in both analyzed cases is similarly relevant as between protomers. Interestingly, AorC forms an interface also with AorA' and AorB, which is less favourable in terms of  $\Delta^iG$ , however, it is also formed by hydrogen bonds and salt bridges.

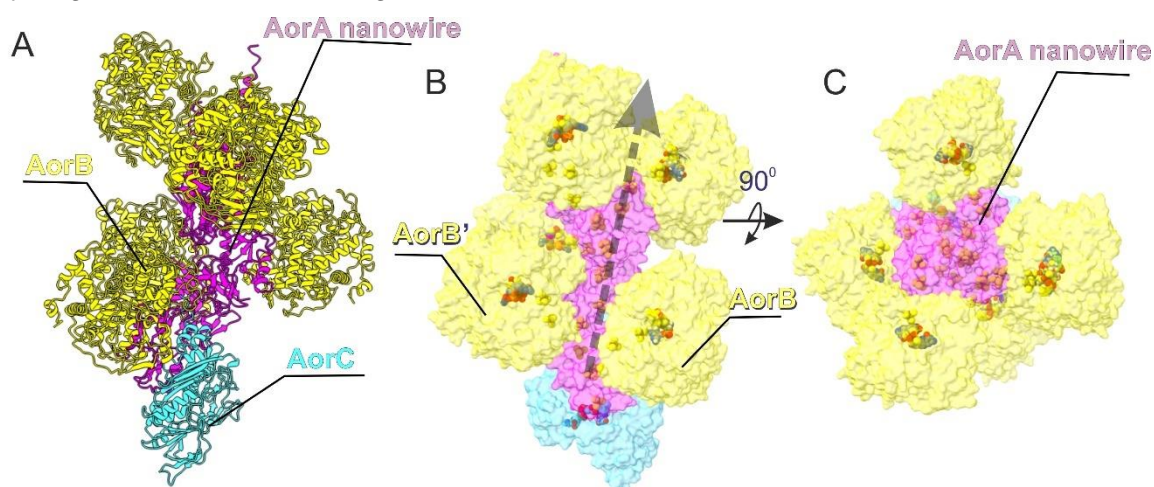


**Figure 54.** *In silico* prepared model of Aor(AB)<sub>5</sub>C complex. **A)** cartoon representation of structure, AorA subunits are depicted in magenta and form a nanowire on which AorB subunits are placed (yellow). **B,C)** The nanowire built from AorA subunits is decorated by AorB subunits and the last AorAB protomer of the complex has a free interface for binding of next subunit and filament can grow in direction marked on B.

The AorC subunit is a nucleation site for the complex, as it interacts with both protomers in Aor(AB)<sub>2</sub>C, which is the prevalent complex among all higher-order species shown in MP. The two AorB subunits resolved in the model are twisted about 70° around the axis formed by AorAA'. The binding motif between AorA and AorA' is most likely repeated for bigger oligomers, resulting in the binding of AorA' to AorA'' along the same axis, and AorB'' would be twisted by about another 70° relative to AorB'. This motif for oligomeric structure results in a filament of AorAB protomers, where the AorA subunits form a nanowire decorated by AorB subunits. The binding motif for the AorAA' interface is well-determined in the structure and the higher-order complex can be built *in silico* by simple superposition of subunits. Such a model was constructed for an Aor(AB)<sub>5</sub>C complex (matching the biggest complex identified by MP), which was possible without any steric



hindrances and is shown in **Figure 54**. Considering the absence of steric hindrances, the formation of even higher-order structures is possible as well.

#### **7.4. Electron transfer subunit AorA**

AorA subunits form the central part of the complex and in the oligomeric *in silico* model (**Figure 55**), those subunits form a nanowire. During analysis of the AorA sequence four conserved [CxxCxxCxxxC] motifs for binding of four ferredoxin-type  $\text{Fe}_4\text{S}_4$  clusters were found. The reconstructed protein model showed a double ferredoxin fold typical for electron-transfer subunits of large redox enzymes. The protein consists of three domains, as shown in **Figure 55.A**: two ferredoxin-like domains related by a twofold rotation and a C-terminal domain, which is an  $\alpha$ -helix protruding from the protein core. The first ferredoxin-like domain carries  $\text{Fe}_4\text{S}_4$  clusters FS-1 and FS-2, which are ligated by sequence motifs 1 and 4 (Cys12, 15, 18, and 126 for FS-1; Cys113, 116, 122, and 22 for FS-2), whereas FS-3 and FS-4 are present in the other ferredoxin-like domain and are ligated by sequence motifs 2 and 3 (Cys 53, 56, 61, 96 for FS-3, Cys 65, 86, 89, 92 for FS-4).

The AorA is structurally similar to known structures of subunits from Mo- and W-containing enzymes (as shown in **Table 24**). The closest homolog is a small subunit of  $\text{WOR5}_{Pf}$ , but AorA is also similar to many electron-transfer subunits in Mo-dependent formate dehydrogenases or formate hydrogenlyases as well as one of the ferredoxin-like subunits of BCR complex (the BamB-containing enzyme). The ferredoxin from *Gottschalkia acidurici* is very similar as measured by RMSD (1.5), although the Z-score for this pair is low as the smaller protein is only superimposed to part of AorA. A number of other ferredoxins were listed as similar structures. Among the tungsten enzymes, there is only one known example that forms oligomers and contains AorA-like subunits, namely hydrogen-dependent  $\text{CO}_2$  reductase (HDCR) from *Thermoanaerobacter kivui* (subunits HycB4 and HycB3)<sup>180</sup>.

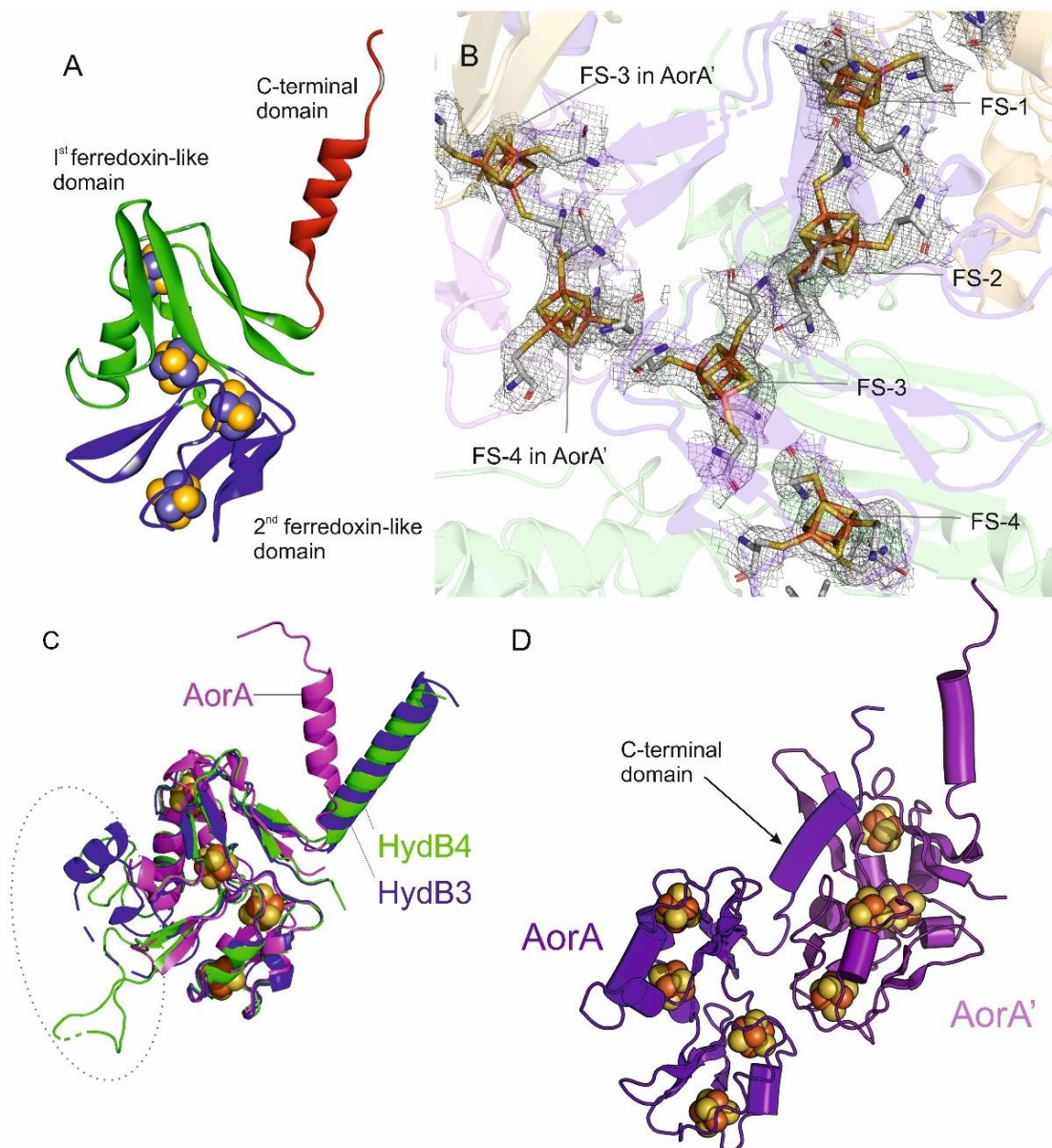


**Figure 55.** AorA subunit structural details. **A)** The structure of AorA can be divided into domains: the first ferredoxin-like domain (residues 1-52 and 113-136, coloured green) is interrupted in sequence by the second ferredoxin-like domain (residues 53-112, blue), and the last motif is C-terminal domain (residues 137-158, red). **B)** The Fe<sub>4</sub>S<sub>4</sub>-clusters and coordinating them cysteines depicted in corresponding electron density. **C)** Structural alignment between the electron carrier cores of AOR<sub>Aa</sub> (composed by AorA subunits, magenta) and HDCR from *T. kivui* (PDB ID: 7QV7; composed by HycB3 and HycB4 in blue and green, respectively). **D)** Cartoon depiction of subunits AorA and AorA'.

**Table 24.** Selected structurally similar proteins to AorA, with scores of quality of structural alignments.

Molecule	Z-score	RMSD	LALi	Nr res	% identity
WOR5 <sub>Pf</sub>	20.4	2	138	167	39
Formate Hydrogenlyase from <i>E. coli</i> , Subunit 3	17.5	1.9	129	170	41
HDCR HycB4	16.6	3.4	140	183	37
HDCR HycB3	16.5	4.9	149	174	31
Ferredoxin from <i>Gottschalkia acidurici</i>	7.0	1.5	49	55	33

% identity – the identity of sequences in the alignment, Nr res – total number of residues in the protein

The oligomerisation in the HDCR complex is mediated by the C-terminal domains in the form of  $\alpha$ -helix. This motif is very similar in AorA (**Figure 55.C**), where the C-terminal domain provides an additional surface to extend the interface with AorA' (**Figure 55.D**). Most of the identified hydrogen bridges between AorA and AorA' involve residues of the C-terminal domain of AorA (Asp137, Trp138, Gly140, Arg143, Met144, Trp147, Asn152). Therefore, it is likely that also in AOR<sub>Aa</sub> the C-terminal helix of AorA is responsible for oligomerisation.

### 7.5. Structural details of AorC subunit

AorC is a FAD-containing protein structurally similar to FAD-containing reductases from *Pseudomonas* sp. (see **Table 25**). No important structural similarity was found to any known structures of Mo- and W-containing protein complexes. AorC can be divided into domains characteristic for FAD-containing, NAD-dependent proteins: FAD-binding domain, NAD-binding domain and C-terminal domain (depicted in **Figure 56.C**)<sup>181</sup>.

The FAD-binding domain and the NAD-binding domain form characteristic Rossmann folds, consisting of parallel  $\beta$ -strands interspersed by  $\alpha$ -helices, a motif used in proteins to bind nucleotide cofactors<sup>183</sup>. The FAD-binding domain is not coded consecutively in the sequence. Therefore, it is divided into two parts, which together give a motif of three helices placed on a large  $\beta$ -sheet formed by six  $\beta$ -strands (**Figure 56.C**). The NAD-binding domain structure mirrors the former domain. The C-terminal domain consists of a large  $\beta$ -sheet followed by three  $\alpha$ -helices, in especially elongated motif. This domain might be responsible for the important task of AorC as a nucleation subunit. The residues present in the C-terminal domain form interactions with all of the subunits that

AorC binds, including the main contact site with AorB (Arg424) and the only apparent contact site with AorA” (Val423).

**Table 25** Selected structurally similar proteins to AorC, with scores of quality of structural alignments.

Molecule	Z-score	RMSD	LALi	Nr res	% identity
FAD-containing reductase, a subunit of toluene dioxygenase from <i>Pseudomonas putida</i>	40	2.5	400	406	26
ferredoxin reductase from <i>Rhodopseudomonas palustris</i>	39.2	2.5	396	404	27
ferredoxin reductase from <i>Pseudomonas sp.</i>	38.7	2.4	389	402	25
putidaredoxin reductase from <i>Pseudomonas putida</i>	38.4	3.1	414	422	21

% identity – the identity of sequences in the alignment, Nr res – total number of residues in the protein

There are a few conserved motifs present in AorC for binding of the FAD cofactor. A motif of highly conserved three glycines (Gly7, Gly9 and Gly11) at the N-terminal part of the sequence that enable binding of FAD cofactor in protein. Gly7 interacts with an oxygen atom of the ribose ring of the adenosine fragment of FAD. Because of the absence of side chains, Gly7 and Gly9 also permit close contact of the pyrophosphate group of FAD with the  $\alpha$ -helix for charge compensation, specifically to oxygen atoms  $O_{P1}$  or  $O_{P2}$ <sup>182</sup>. The third glycine (Gly11) allows close packing of the helix with the  $\beta$ -sheet.<sup>183</sup> The second motif is a conserved Arg41, which bonds via a salt bridge with the 2'-phosphates. Lastly, Glu294 interacts with the ribitol hydroxyl group of FAD via a hydrogen bond.

Met42 is most likely engaged in electron transport since it closely interacts with FAD and two AorA cysteines that coordinate the FS-4 cluster. The FAD cofactor's isoalloxazine ring is accessible to NAD-type substrates via a binding pocket conserved among FAD-dependent oxidoreductases. A highly conserved polar residue, Arg179, is located near the entrance to the FAD-containing cavity, providing an apparent binding site for the NAD<sup>+</sup> cofactor's phosphates (see **Figure 56**).

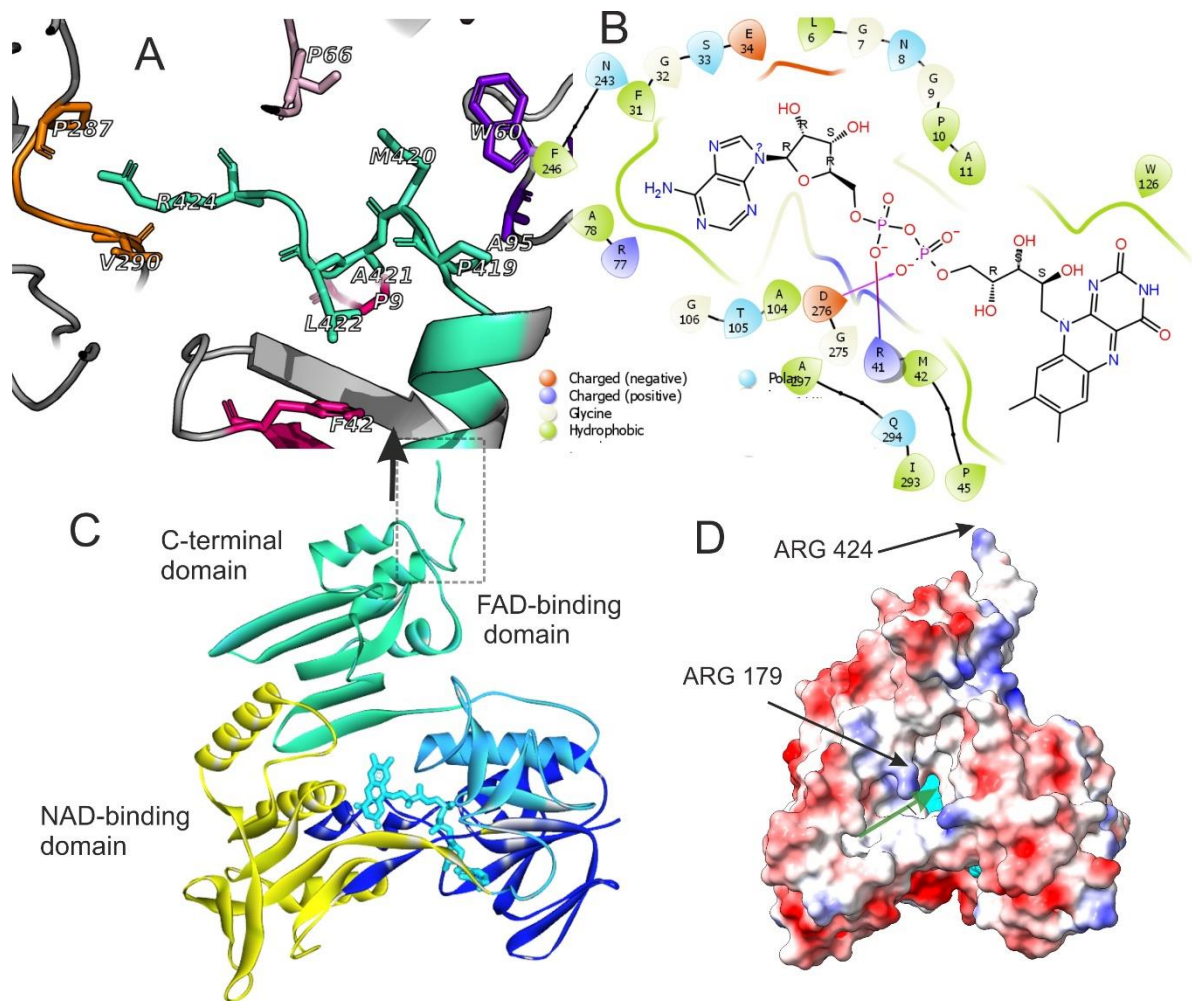


**Figure 56.** AorC subunit structural details. **A)** C-terminal loop of AorC (depicted in cyan). Atoms show amino acids responsible for interactions with other subunits. AorC Arg424 forms a hydrogen bond with AorB (Pro287) and has hydrophobic interactions with Val290. AorC Met420 interacts with AorA' by weak hydrophobic interactions (Phe42 and Pro9 residues in AorA'). Finally, Met420 and Phe419 in the AorC helix interact even with AorA' (Trp60 and Ala95). **B)** FAD-protein interactions diagram. Depicted bonds with Gln294 (H-bond) and Arg41 (salt bridge); **C)** The N-terminal FAD-binding domain (residues 1-126) is coloured in dark blue, the apparent NAD-binding domain (residues 126–240) is shown in yellow, the C-terminal FAD-binding domain (residues 241 –317) is depicted in light blue, and the C-terminal domain (residues 318 – 424) is coloured in teal. FAD is depicted as blue sticks; **D)** FAD subunit surface coloured by electrostatic potential (blue- positive, red – negative, FAD is shown in teal). A green arrow marks NADH binding pocket, a positively charged, highly conserved Arg179 at the entrance to the binding pocket might facilitate NADH binding.

## 7.6. The catalytic subunit

The catalytic subunit AorB is structurally very similar to the monomer of AOR from *P. furiosus* (RMSD of 1.4). It also exhibits a considerable similarity to the FOR and WOR5 catalytic subunits from *P. furiosus* (RMSD 2.0 and 2.2, respectively). The similar fold of the protein is not surprising, considering their close relation and high sequence identity (at about 49%, 34% and 31% identity to AorB, respectively for AOR<sub>Pf</sub>, FOR and WOR5, more details shown in **Table 26**). Similarly to AOR<sub>Pf</sub> and FOR, the tungsten cofactor and Fe<sub>4</sub>S<sub>4</sub>-cluster are localized in a binding pocket formed between three domains of AorB. The first domain forms a regular  $\beta$ -sandwich consisting of two six-stranded  $\beta$  sheets (residues 1 to 211) on which the W-co is anchored through the magnesium ion binding site. Above the W-co, two very similar  $\alpha$ -domains (domain 2. consisting of residues 212 to 418 and domain 3. of residues 419 to 616) are positioned, closing the active site cavity. The entrance to the active site cavity is provided by two broad and short channels with a neutral charge on their surfaces, allowing the entrance of bulky molecules to the tungsten cofactor.

**Table 26.** Selected structurally similar proteins to AorB, with scores of quality of structural alignments.

Molecule	Z-score	RMSD	LALi	Nr res	% identity
AOR <sub>Pf</sub>	50.6	1.4	597	605	49
FOR <sub>Pf</sub>	44	2	583	611	34
WOR5 <sub>Pf</sub>	39.4	2.2	570	624	31
BamB from <i>Geobacter metallireducens</i>	36.5	2.5	567	653	27

% identity – the identity of sequences in the alignment, Nr res – total number of residues in the protein

The W-co was recognized in electron density as expected, in *W-bis*-MPT pyranopterin form and the resolution allowed tracing the position of both pterins, magnesium and phosphate residues (as shown in **Figure 57.B**). The four dithiolenes from pterins were confirmed to be binding the tungsten. The existence of two more ligands above the tungsten was indicated by an additional high excessive electron density, but the acquired resolution was insufficient to identify them properly. Any protein-derived ligand of tungsten has been ruled out based on the resolved density of AorB sidechains. A study shown in Chapter 8 resulted in proposing the most probable W-co structure as W(VI) with two oxo ligands and geometry shown in **Figure 57**.

Residues Cys295, Cys298, Cys302 from domain 2 and Cys509 from domain 3 bind to Fe atoms from the  $Fe_4S_4$  cluster, which was named FS-0 to distinguish it from clusters in AorA. Each of the domains binds the W-co by highly conserved residues: in domain 1 Asn92 and Ala182 form coordination bonds with the magnesium ion, from domain 2, Arg75, Gly94, Arg181, Asp361 form H-bonds and salt bridge interactions with the MPT distal from the FS-0, whereas residues from domain 3, Asp504, Ile508, Cys509, Val510, interact with the proximal MPT. The residues employed in cofactor binding are conserved in AOR<sub>Pf</sub>, but not in FOR<sub>Pf</sub>. In contrast to the known structures of AOR<sub>Pf</sub> (with a sodium cation in the active site pocket)<sup>49</sup>, FOR<sub>Pf</sub> (with a calcium cation bound to pyranopterin)<sup>83</sup> and WOR5<sub>Pf</sub> (containing two additional magnesium ions)<sup>70</sup>, no additional metal ion was found in close proximity to any of the pterins in AOR<sub>Aa</sub>.

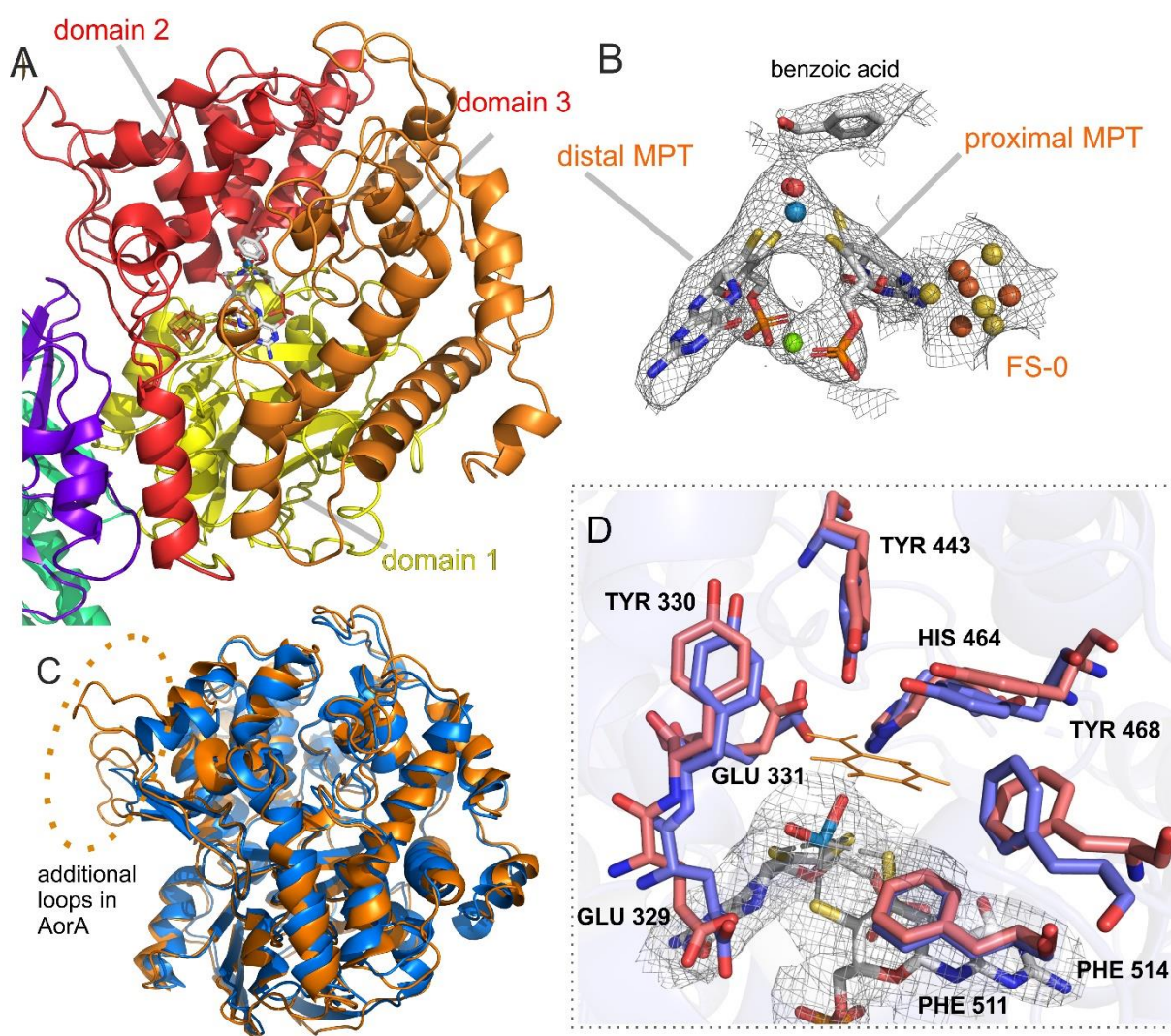


**Figure 57.** Structural properties of AorB. **A)** AorB secondary structure divided into domains: domain 1 depicted in yellow, domain 2 shown in red and domain 3 in orange; **B)** The W-co, FS-0 and benzoic acid in corresponding density; **C)** superimposed

structures of AorB (orange) and monomer of AOR<sub>Pf</sub> (blue); **D**) comparison of active site cavity in AorB (red) and AOR<sub>Pf</sub> (blue).

The active site cavity in AorB has an identical composition as in AOR<sub>Pf</sub>. Even the positions of side chains are almost perfectly conserved (as shown in **Figure 57.D**). The main differences in the sequence and structure of both enzymes are represented in **Figure 57.C**. The AorB has two prolonged loops that are not present in AOR<sub>Pf</sub> and this motif of the AOR<sub>Aa</sub> structure apparently improves binding to AorA.

From the conserved amino acids positioned close to W-co, Glu331 and His464 are most probably catalytically active residues, as already suggested by Liao *et al.* for analogous residues in FOR<sub>Pf</sub>.<sup>87</sup> The hydrophobic conserved amino acids Tyr330, Tyr443, Tyr468, Phe511 and Phe514 may be responsible for stabilizing the binding of aromatic and bulkier aliphatic aldehydes in the active site. The protonation of amino acids in the active site of AorB was predicted based on the pK<sub>a</sub> values calculated according to the PROPKA procedure<sup>148</sup>. The tyrosines Tyr330, 443, 468 are supposedly protonated within the pH range of enzyme stability (pH 5 to 8.5), as they had very high predicted pK<sub>a</sub> (13.6-19.7). The glutamate has pK<sub>a</sub> (7.0) in the middle of the catalytic range of AOR, thus is probably residue engaged in acid-base catalysis. The His464 was predicted to have a lower pK<sub>a</sub> (3.67) than the model pK<sub>a</sub> of histidines (6.5), which implies that in the conditions of assays (i.e. at pH 8.0), it is neutral but may become charged at acidic conditions at which carboxylic acids were reduced with hydrogen by AOR<sub>Aa</sub>. Nonetheless, these predictions are biased by the electrostatic microenvironment introduced by a neighbouring, highly-charged W-co, which is not considered by the PROPKA procedure. Thus, it is reasonable to assume that the pK<sub>a</sub> of His464 may not be correctly predicted, as in case of ethylbenzene dehydrogenase from the DMSO-reductase family, a histidine in the active site occurs most likely in doubly-protonated form<sup>184</sup>. This hypothesis is supported by visual inspection of the His464 position, which implies the potential formation of H-bond interaction with one of the W=O ligands (the distance of His-Nε---O=W is 3.4 Å).

An apparent aromatic product, which was assumed to be benzoic acid, was identified as bound to W-co active site. The identification of the bound molecule was supported by its apparent availability - the presence of benzoic acid in the growth media of bacteria (the carbon source for *A. Evansii* was sodium benzoate). The acid molecule is apparently bound in the active site by interactions with protein, as shown in **Figure 58**. His464 is potentially deprotonated (based on PROPKA analysis of pK<sub>a</sub>) and the apparent hydrogen bond (distance nitrogen to oxygen 2.6 Å) could be formed with the hydroxy group of protonated benzoic acid (pK<sub>a</sub> =4.2). Furthermore, the carboxylic group of Glu331 is close



(2.9 Å) to putatively protonated benzoic acid, also enabling H-bond interaction. Finally, Tyr443 is able to form an additional H-bond interaction from the other side with the carbonyl oxygen of benzoic acid (3.7 Å). The benzoic acid is also bound close to the cofactor W(VI) with two oxo ligands, with a distance between the closer oxo ligand and the carbonyl carbon of 3.0 Å. The CryoEM grid was prepared in aerobic conditions, thus the cofactor is expected to be in the oxidized state. Therefore, the product (acid) bound to this cofactor appears to be a stable, non-reactive form of a complex (i.e. E<sup>ox</sup> : P).

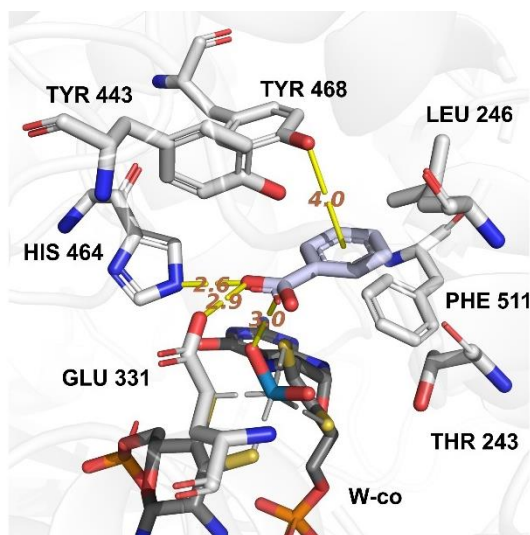


**Figure 58.** Anticipated interactions of benzoic acid with residues in the active site.

### 7.7. Electron transfer chain in AOR<sub>Aa</sub> complex

The NAD-dependent catalysis can be performed by AOR<sub>Aa</sub> thanks to the connection between W-co and FAD cofactor provided by Fe<sub>4</sub>S<sub>4</sub> clusters forming an electron transfer chain. The Fe<sub>4</sub>S<sub>4</sub>-clusters in proteins are responsible for electron transfer and the location of all clusters and cofactors in protein within short distances is the key to understanding the flow of electrons<sup>185</sup>.

In the reconstructed Aor(AB)<sub>2</sub>C complex, there are four Fe<sub>4</sub>S<sub>4</sub> in each AorA, one Fe<sub>4</sub>S<sub>4</sub> and one tungsten cofactor in each AorB. The AorC carries only the FAD cofactor. As shown in **Figure 59**, the Fe<sub>4</sub>S<sub>4</sub> clusters form a clear pathway (from FS-0 to FS-4) between W-co in AorA and FAD cofactor in AorC, allowing electron flow during the catalytic cycle. The FS-0 is bound in AorB in van-der-Waals distance to the proximal pterin of W-co (3.5 Å edge-to-edge, and 8.3 Å to W atom). The Fe<sub>4</sub>S<sub>4</sub> clusters FS-0 to FS-4 are arranged in the protein, maintaining short distances between subsequent cofactors (10.2 to 11.9 Å). The FS-4 of AorA is located 9.5 Å from the FAD cofactor. The small distances between all redox cofactors (much below 15 Å) are predicted to facilitate electron transfer within microseconds through quantum tunnelling<sup>186</sup>. Furthermore, FS-3

of AorA is also in close contact with FS-4 from AorA' (10.1 Å), thus allowing the electron flow from AorB' (and further distal protomers of the extended nanowire) to the FAD cofactor.

In the *in silico* model Aor(AB)<sub>5</sub>C (**Figure 59**) this connection between the AorA subunits constituting an electron pathway between protomers via FS-3 and FS-4 is repeated. A macromolecular view on the FS cofactors in Aor(AB)<sub>5</sub>C model reveals that the FS-3 and FS-4 clusters of the subsequent AorA subunits of the nanowire form a regular helix-like motif. The FS-2 and FS-1 cofactors are protruding from the core of the helix at a 90° angle (formed between FS-4, FS-3 and FS-2 of the individual AorAs). The region of AorA' forming the interface with the preceding AorA that allows the contact between Fe<sub>4</sub>S<sub>4</sub> clusters from both subunits is the exact same surface that is involved in binding AorA to AorC in the proximity of FAD. This feature of quaternary structure implies that AorC can be bound to the structure only once in the complex, as no other binding site for this subunit would be available on the AorA-type subunit.

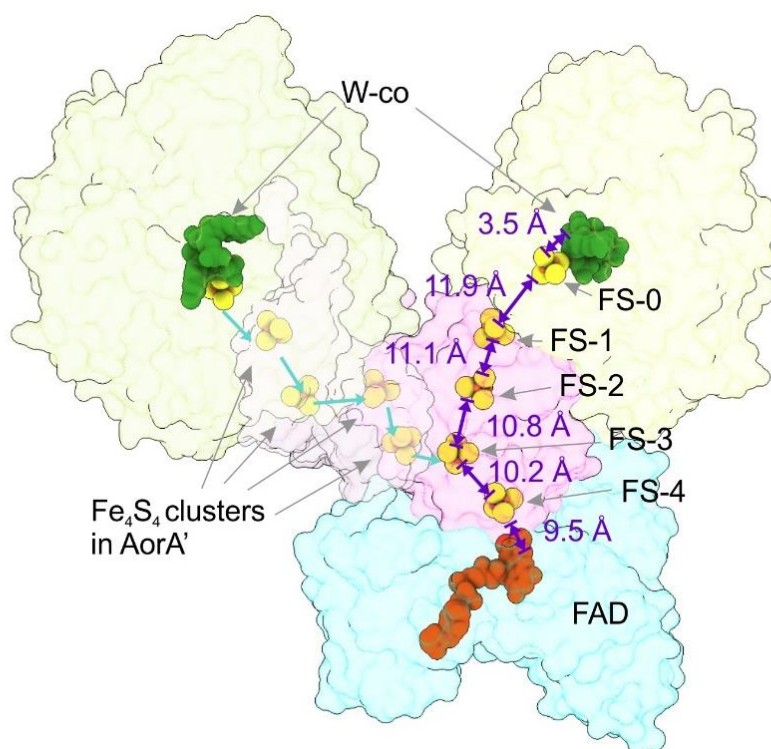


**Figure 59.** The electron-transfer pathway of AOR<sub>Aa</sub>. Both acid reduction and hydrogen oxidation hypothetically can occur on one of the two tungsten cofactors (bisWPT). The Fe<sub>4</sub>S<sub>4</sub> clusters chain transfers the electrons from the tungsten cofactor to the FAD, where NAD<sup>+</sup> is reduced. The distal protomer electron chain (blue) links to the main electron pathway (violet) at FS-3.

### DISCUSSION OF PART III

The reconstructed structure of AOR<sub>Aa</sub> shows for the first time structural details for a multi-subunit bacterial AOR. Moreover, it is the first study of AOR by cryoEM single-particle approach, a method which offers much more reliable information on the quaternary structure and complex assembly than X-ray crystallography. The data from cryoEM structure combined with mass photometry results give unequivocal proof for the formation of oligomeric structures by AOR<sub>Aa</sub>.

The structural details of Aor(AB)<sub>2</sub>C complex revealed that all of the protomers are connected by poly-AorA subunits as electron-transfer wire. The two structurally characterized AorA subunits are bound to each other so that the Fe<sub>4</sub>S<sub>4</sub> cluster chain of AorA' can link with the AorA Fe<sub>4</sub>S<sub>4</sub> clusters. This facilitates electron flow from the distant AorB(s) to the FAD containing AorC (in **Figure 59** the pathway from distant AorBs is marked as blue arrows). This feature presumably could also be working for further AorBs, allowing electron flow within the filamentous structure. That phenomenon could impact the kinetics of the enzyme as the direct link between two tungsten cofactors is one of the features enabling the cooperativity of the active sites. The binding of the substrate in the active site of one subunit could influence the affinity of the other active sites. As discussed previously (in Chapter 4.2), the AOR<sub>Aa</sub> kinetics show some deviation from hyperbolic function kinetics, resulting with not so perfect fit of the kinetic data with the Michaelis-Menten model. The impact of cooperativity on kinetics is possible. However, it could also be partially explained by substrate inhibition by a high concentration of aldehydes, as observed for other AORs.

A method to test the hypothesis of cooperativity of active sites would be to compare the kinetics (dependence of activity from substrate concentration) of a trimeric (AorABC) and multimeric (Aor(AB)<sub>n</sub>C) form of the enzyme. This could be achieved by a mutation of the protein that would change the binding properties between subunits, and consequently, the quaternary structure of the complex. Based on the structure analysis, it can be concluded that this effect can be achieved by truncating the terminal  $\alpha$ -helix of AorA, which is most probably crucial for binding higher-order protomers.

While the actual oligomerisation grade of AOR<sub>Aa</sub> *in vivo* is unknown, it is probably higher than experimentally observed two to four protomer complexes. The *in silico* model (shown in **Figure 54**) indicates that there are no steric hindrances for the binding of more AorAB protomers. Moreover, in the MP analysis of the AOR<sub>Aa</sub> preparation, a large amount of isolated AorAB protomers was detected, which probably originate from the dissociation of larger complexes. Thus in higher concentrations, the larger complexes

are still intact, possibly even larger than the detected Aor(AB)<sub>5</sub>C and there is no argument disproving the occurrence of even higher oligomerisation grades *in vivo*.

The presence of a free binding site for next AorA at the “AorA end” of filament, may be the reason for exchange of the subunits between AOR<sub>Aa</sub> and AOR<sub>Ae</sub> complexes noticed in enzyme preparation (Chapter 2.). During purification of AOR<sub>Aa</sub> on affinity column, a fraction of the multimeric complexes probably has an additional AorAB protomer from AOR<sub>Ae</sub> bound. The affinity tag must be present in at least one of the protomers (i.e. the tagged AorA from AOR<sub>Aa</sub>) in the complex, thus also AOR<sub>Ae</sub> complex with at least one protomer from AOR<sub>Aa</sub> will be bound on the column and then present in eluate.

The formation of high-order oligomeric quaternary structures by complexes of metabolic enzymes has seldom been seen. Nonetheless, it was demonstrated that the quaternary structure has a significant influence on enzymatic activity<sup>187</sup>. For example, an acetyl-CoA carboxylase from several higher eukaryotes and yeast has been demonstrated to form multimeric structures as a way to control enzyme activity, as the polymerized enzyme was more active than the monomeric form of the enzyme<sup>188,189</sup>. AdhE, *E. coli*'s bifunctional CoA-dependent acetaldehyde and alcohol dehydrogenase, exhibits a similar behaviour<sup>187,190</sup>. A comparable impact has been seen for the HDCR, a crucial enzyme in *A. woodii*'s catabolic metabolism<sup>180</sup>. Considering the high similarity of HDCR subunits of the corresponding function to AorA, it is reasonable to suspect that in the case of AOR<sub>Aa</sub> the filamentation also can lead to increased or even changed activity.

The formation of larger complexes was previously reported for AOR from *C. thermoaceticum*, for which multisubunit Aor(AB)<sub>3</sub>C complexes were characterized in subsequent reports<sup>75,78</sup>. Therefore, filamentation may be a common feature of multi-subunit AORs.

Reconstruction of the AOR<sub>Aa</sub> structure opens the possibility for mechanistic studies aided by site-directed mutagenesis. The importance of amino acids potentially taking part in the catalytic cycle, e.g., His464 and Glu331, can be tested by exchanging them for amino acids with side chains unable to perform acid-base catalysis. The drop of such mutants' activity compared to native protein should prove that the amino acid is catalytically important. Moreover, attempts to change AOR<sub>Aa</sub> selectivity can be made, i.e. by exchanging the Phe511 and Phe514 for polar amino acids, the hydrophobic aldehydes should not be stabilized in the active site anymore.

In contrast to other known structures from enzymes of the AOR family, AOR<sub>Aa</sub> lack additional cations in the active site cavity. However it may be an artefact caused by the method. The presence of cations in the vicinity of the pterins would neutralize the

phosphate charge and the overall charge of the cofactor (as in the assumed oxidized state, its charge is -2).

## PART IV. Studies of W-co.

### 8. Geometry of W-co

The central tungsten atom in the active site of AORs is coordinated by two pyranopterin cofactors and additional, unidentified ligands, which could not be reliably resolved from the spectral and structural data available for either AOR<sub>Pf</sub> or AOR<sub>Aa</sub> (see **Figure 60**). The intrinsic features of tungsten were the main problem for the clear interpretation of spectroscopic studies, as mentioned already in the Chapter 4.4. of Literature Review. A solution for this common for tungstoenzymes problem was proposed previously by Culka *et al.*<sup>191</sup> in a theoretical study of BamB, where one of the ligands (ligand X) was unsolved. In the BamB example, a series of models were prepared with different possible candidates for ligand X (S<sup>2-</sup>; SH<sup>-</sup>; SH<sub>2</sub>O<sup>2-</sup>; OH<sup>-</sup>; OH<sub>2</sub>; CN<sup>-</sup>; CNH; NCH, and CO) and different oxidation states of tungsten (W IV/V/VI) were considered. In this study problem concerned two unknown ligands; therefore, the solution had to be reasonably simplified based on the available data. The reasoning was as follows:

- The oxidation state of the tungsten cofactor in structural data was assumed to contain either reduced (W(IV) or oxidized (W(VI)) tungsten atom. The analysis of EPR W(V) signals both for AOR<sub>Pf</sub> or AOR<sub>Aa</sub> showed that this state is present only in a low quantity in the samples. Therefore, the intermediate oxidation state could be ruled out<sup>192 193</sup>
- The ligands are most probably changing during the catalytic cycle as the enzyme catalyzes oxygen transfer reaction. In consequence, the composition of the oxidized models should allow for the formation of the reduced state.
- The EXAFS data for AOR<sub>Pf</sub> showed the presence of 3-4 single bonds between the W atom and sulfurs and additional 2-3 other ligands<sup>84</sup>.

Therefore only the following models were prepared: for the oxidized cofactor [W(VI)(O)<sub>2</sub>(MPT)<sub>2</sub>Mg(H<sub>2</sub>O)<sub>4</sub>]<sup>2-</sup>, [W(VI)SO(MPT)<sub>2</sub>Mg(H<sub>2</sub>O)<sub>4</sub>]<sup>2-</sup>, and for the reduced cofactor: [W(IV)O(MPT)<sub>2</sub>Mg(H<sub>2</sub>O)<sub>4</sub>]<sup>2-</sup>, [W(IV)(OH)<sub>2</sub>(MPT)<sub>2</sub>Mg(H<sub>2</sub>O)<sub>4</sub>]<sup>2-</sup>, [W(IV)O(OH)(MPT)<sub>2</sub>Mg(H<sub>2</sub>O)<sub>4</sub>]<sup>2-</sup>, [W(IV)O(H<sub>2</sub>O)(MPT)<sub>2</sub>Mg(H<sub>2</sub>O)<sub>4</sub>]<sup>2-</sup>, where MPT ligand was additionally protonated at the phosphate group. In the further description of the result, for brevity reasons, the Mg(H<sub>2</sub>O)<sub>4</sub> part was omitted.

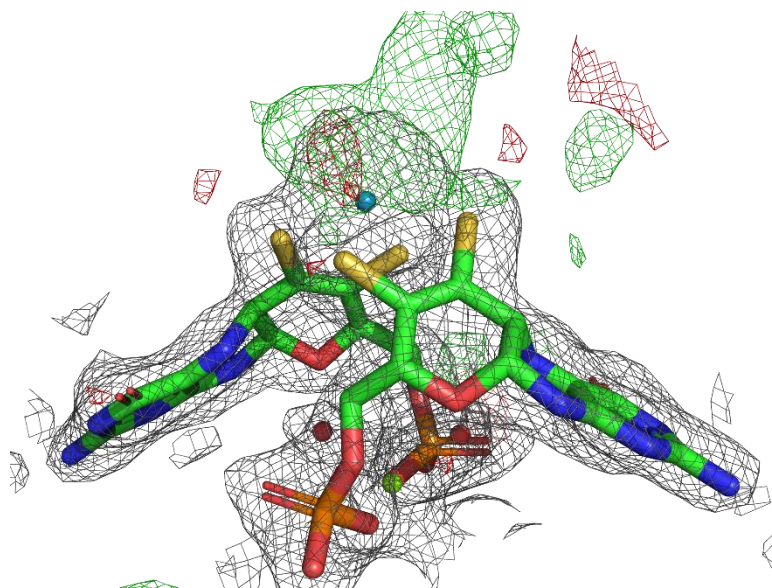


**Figure 60.** The difference map of  $AOR_{Pf}$  calculated from crystallographic data of the deposited structure. The excess electron density of the model is shown in red, and the deficient electron density of the model is shown in green.

### 8.1. QM-only study of W-co

In the first step of the study, the geometries of molecular models of W-co were minimized in the gas phase by the QM method and obtained coordinates were analyzed in search of models fitting the experimental data. A comparison of bonds and angles in first shell of tungsten coordination in DFT optimized models was confronted with data from the literature and gathered in **Table 28**.

#### *Model W(VI)(O)<sub>2</sub>(MPT)<sub>2</sub>*

The optimized structure of  $W(VI)O_2(MPT)_2$  (**Figure 61**) showed distorted octahedral coordination of tungsten, with the shortest two bonds between  $W=O$  (1.76 Å), and uneven length of  $W-S$  bonds. The  $W-S$  distances *trans* to the  $W=O$  bond were longer (2.739 and 2.688 Å) than in *cis* configuration (2.477 and 2.501 Å). Such distortion involving the elongation of *trans* bonds for Mo- and W-complexes was assigned in the literature to the *trans* influence in the ground state of W (VI) complex<sup>194</sup>. The analysis of Mulliken charges showed that tungsten was positively charged (0.283), and the two oxygen ligands had equal negative charges (-0.51). The four sulfur ligands were negatively charged, the two *trans* sulfur atoms with lower charge than *cis* sulfur atoms. It is worth noting that the sulfur – tungsten bonds and charges are not equal in the *cis/trans* pairs and the longer the bond, the lower charge on sulfur.

In the literature, synthetic models of the tungsten cofactor are reported that correspond to the theoretical model presented in this thesis. An example is a complex of

$[\text{Ph}_4\text{P}]_2[\text{W}(\text{VI})\text{O}_2(\text{mnt})_2] \cdot 2\text{H}_2\text{O}$  that was synthesized as one of the possible models for the tungsten cofactor of  $\text{AOR}_{\text{Pfl}}$  and its geometry was elucidated by X-ray diffraction spectroscopy<sup>195</sup>. The synthetic model consisted of tungsten ion coordinated by 1,2-dicyanoethylenedithiolate ( $\text{mnt}^{2-}$ ) ligand simulating dithiolene pterin ligands and respective other ligands (oxo). The synthetic complex shows two-fold symmetry and only half of the model was characterized. The overall geometry showed distorted octahedral tungsten coordination with resolved bond lengths somewhat shorter (0.032-0.126Å) than those obtained in the DFT  $\text{W}(\text{VI})\text{O}_2(\text{MPT})_2$  model.

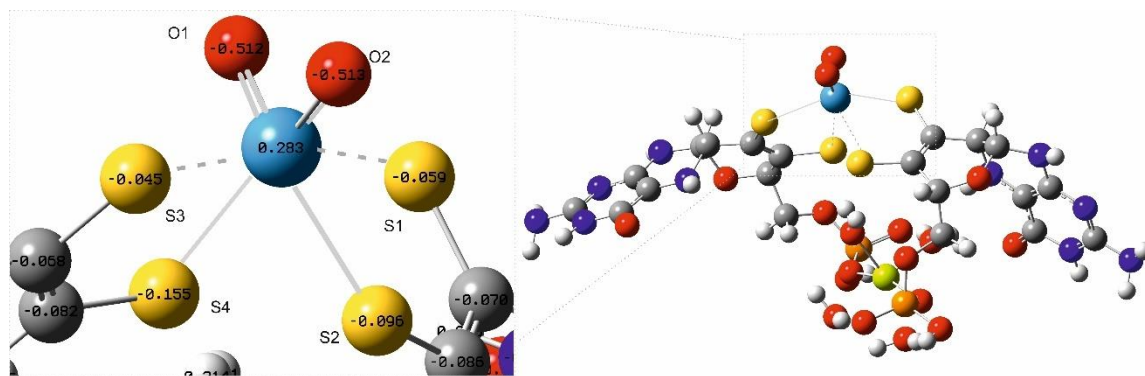


**Figure 61.** Optimized  $\text{W}(\text{VI})\text{O}_2(\text{MPT})_2$  model and its fragment showing tungsten atom and its ligand with Mulliken charges assigned to atoms. Bonds between tungsten and *cis* to  $\text{W}=\text{O}$  sulfurs (S1, S3) are presented by dashed lines, the O1 and S2, and the O2 and S4 are in *trans* positions.

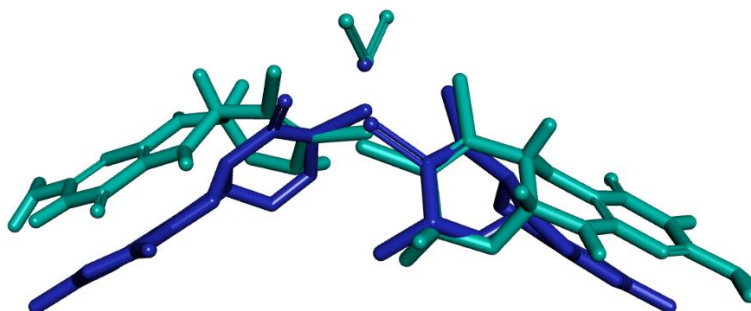


**Figure 62.** Superposition of cofactor models. DFT optimized  $\text{W}(\text{VI})\text{O}_2(\text{MPT})_2$  shown in teal, the crystal structure of  $\text{W-co}$  (PTE from 1AOR) without hydrogen atoms, shown in blue. The phosphates in both cofactors were hidden to simplify the interpretation of pterin coordination.

The superposition of  $\text{W}(\text{VI})\text{O}_2(\text{MPT})_2$  model with the PTE cofactor (see **Figure 62**) revealed that the optimization has considerably changed the geometry of the cofactor. The pterins in  $\text{W}(\text{VI})\text{O}_2(\text{MPT})_2$  are more planar than in the crystal structure (1AOR). This is probably caused by the lack of steric constraints imposed by the protein milieu as the

structure geometry was optimized in a vacuum. Nevertheless, the obtained geometry shows the intrinsic geometry of  $W(VI)(O)_2(MPT)_2$ .

**Table 27.** Bond lengths between tungsten and oxygen ligands in DFT optimized models of the oxidized cofactor, the synthetic model and derived from EXAFS of oxidized AOR<sub>Pf</sub>.

Bond length (Å)	Crystal structure (1AOR)	EXAFS (oxidized AOR <sub>Pf</sub> ) <sup>a</sup>	$W(VI)O_2(MPT)_2$ DFT	$W(VI)O S(MPT)_2$ DFT	$[W(VI)O_2(mnt)_2]^{2-}$ synthetic model <sup>195</sup>
W-S1	2.363	2.40	2.501	2.480	2.445
W-S2	2.342	2.40	2.688	2.748	2.622
W-S3	2.333	2.40	2.477	2.471	n.a.
W-S4	2.346	2.40	2.739	2.681	n.a.
W=O1	n.a.	1.75	1.762	1.763	1.701
W=O2	n.a.	1.75	1.761	2.210 W=S	n.a.
S2-W-S4	113.97	n.a.	82.05	87.13	n.a.
S1-W-S3	144.09	n.a.	161.56	152.4	n.a.

<sup>a</sup> data presented in Pushie *et al.*<sup>84</sup> show possible additional single bond with oxygen (only 0.6 occupation of oxygen) at 2.06 Å, the presence of less than four (3.4) W-S bonds was noted; n.a. – not available

#### Model $W(VI)SO(MPT)_2$

The optimization of  $W(VI)SO(MPT)_2$  model yielded a very similar structure to  $W(VI)O_2(MPT)_2$  model, with distorted octahedral tungsten coordination. The shortest bond was detected between W and oxo ligand (1.763 Å), and a longer bond with the sulfido ligand (2.210 Å). The bond with the pterin *trans* to W=S is shorter (2.681 Å) than *trans* to W=O (2.748 Å).



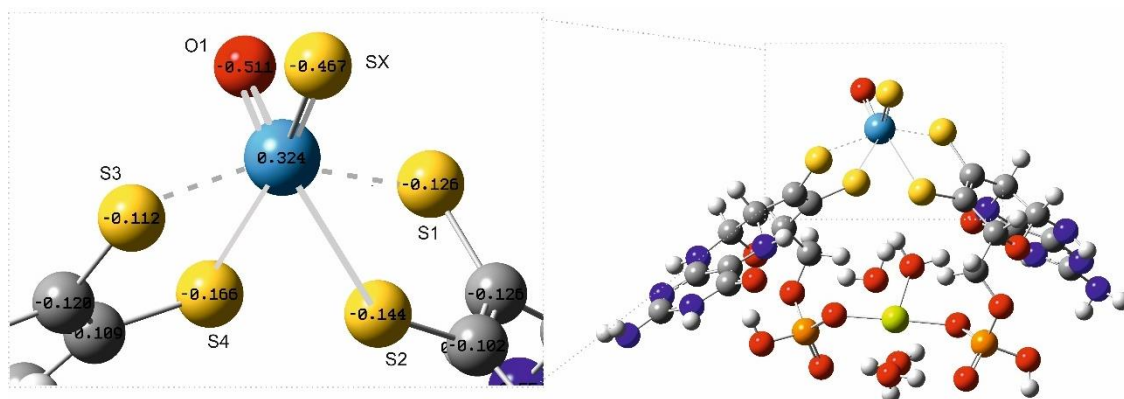


**Figure 63.** Fragment of optimized  $W(VI)SO(MPT)_2$  model with Mulliken charges assigned to atoms. Bonds between tungsten and *cis* to  $W=O$  sulfurs (S1, S3) are presented by dashed lines, the O1 and S2, and the O2 and S4 are in *trans* positions.

The DFT models of the oxidized ( $W(VI)$ ) cofactor show a distorted octahedral tungsten coordination, which is consistent with synthetic models geometry. The  $AOR_{Pf}$  EXAFS data show less than 4 W-S bonds of 2.4 Å length. Therefore, the model with an additional sulfido ligand does not fit to the experimental data. The  $W(VI)O_2(MPT)_2$  model, which is more consistent with the EXAFS data for  $AOR_{Pf}$ , was chosen for the next step of the study – the QM:MM optimization of the structure.

#### *Models of the reduced cofactor*

Das and coworkers also studied a synthetic model of reduced ( $W(IV)$ ) cofactor. A complex of  $[Et_4N]_2[W(IV)O(mnt)_2] \cdot 2H_2O$  that was synthesized as a possible model for the reduced tungsten cofactor of  $AOR_{Pf}$  and its geometry was elucidated by X-ray diffraction spectroscopy<sup>195</sup>. The model contained two  $mnt^{2-}$  ligands coordinating tungsten atom in a distorted square pyramid geometry. The W-S bonds in the reduced synthetic model were shorter than the corresponding bonds in the oxidized model.

The optimization of the  $W(IV)(OH)_2(MPT)_2$  model yielded a trigonal prismatic coordination geometry of tungsten complex, with the sulfur atoms localized in equatorial positions of a distorted square pyramid. The Mulliken charges shown for atoms in **Figure 64** reveal that this model is more polarised than both of the oxidized models. The tungsten atom was very positively charged (0.466) and the oxygens of hydroxo ligands were strongly negatively charged (about -0.65). All W-S bonds have similar length of about 2.4 Å and both W-O bonds of about 2.0 Å. This observation does not match the results from EXAFS, where two different bonds between W and O atoms were identified for the reduced  $AOR_{Pf}$  sample.

**Table 28.** Bond lengths and angles between tungsten and oxygen ligands in DFT optimized models of the reduced cofactor, the synthetic model and derived from EXAFS of oxidized AOR<sub>Pf</sub>.

Bond length (Å)	Crystal structure	EXAFS (reduced AOR <sub>Pf</sub> ) <sup>a</sup>	W(IV)(OH) <sub>2</sub> (MPT) <sub>2</sub> QM-only	W(IV)O(MPT) <sub>2</sub> QM-only	[W(IV)O(mnt) <sub>2</sub> ] <sup>2-</sup>
W-S1	2.363	2.39	2.423	2.443	2.368(9)
W-S2	2.342	2.39	2.462	2.453	2.392(7)
W-S3	2.333	2.39	2.420	2.430	2.370
W-S4	2.346	2.39	2.451	2.451	2.362
W=O1	n.a.	1.75	2.010	1.718	1.73
W-O2	n.a.	1.97	1.955	n.a.	n.a.
S2-W-S4	113.97	n.a.	122.5		140.7(2)
S1-W-S3	144.09	n.a.	146.2		147.7(2)

<sup>a</sup> data presented in Pushie *et al.* from W L<sub>III</sub> EXAFS of AOR<sub>Pf</sub> show 1 W–O at 1.75 Å, 4 W–S at 2.39 Å, and 1 W–O at 1.97 Å.; <sup>b</sup> the water dissociated from the complex,

Model W(IV)(OH)<sub>2</sub>(MPT)<sub>2</sub>

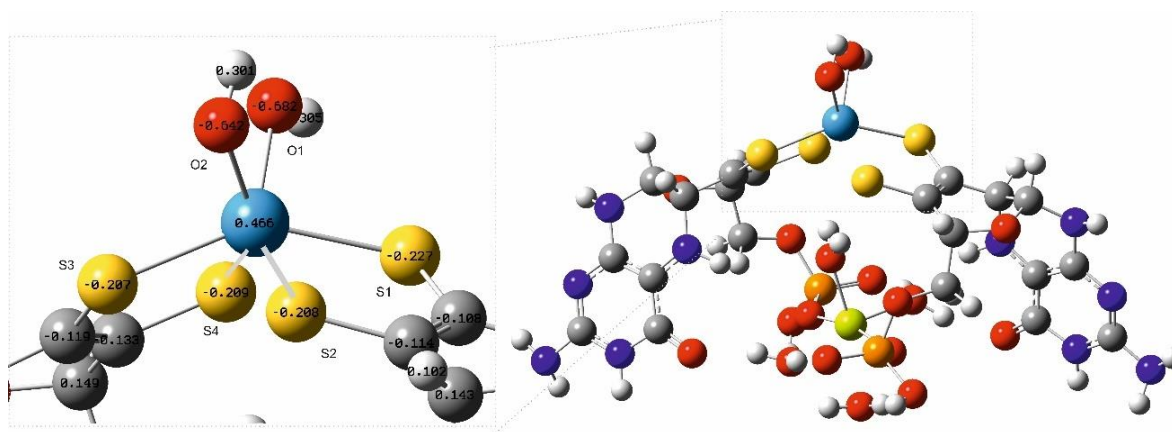


**Figure 64.** Fragment of optimized W(IV)(OH)<sub>2</sub>(MPT)<sub>2</sub> model with Mulliken charges assigned to atoms.

Model W(IV)O(MPT)<sub>2</sub>

The reduced model of W-co with one oxo ligand (W(IV)O(MPT)<sub>2</sub>) was optimized to a distorted square pyramid coordination of tungsten, with all W-S bonds of about 2.4 Å length and a double bond with the oxo ligand of 1.72 Å, similar to the dimensions of the synthetic model. Although the geometry of the cofactor fits the EXAFS data, the lack of one additional ligand rules out this model from further consideration.

### Model $W(IV)O(H_2O)(MPT)_2$

During the geometry optimization of  $W(IV)O(H_2O)(MPT)_2$  the water molecule broke the coordination bond with the tungsten atom and left the first coordination sphere (**Figure 65**). Instead, it formed a hydrogen bond with the oxo ligand at a distance of 1.97 Å. The resulting geometry of the cofactor was the same as for  $W(IV)=O$  model.

This result shows that direct binding of water to the reduced tungsten cofactor, if other ligands are present, is not energetically preferable and the binding is not associated with an energy barrier. On the other hand, the single bond with a water molecule and double bond with oxygen should yield bond lengths similar to those disclosed by EXAFS of reduced  $AOR_{Pf}$  (1.95 and 1.75 Å, respectively). Therefore, to test if the dissociation of water was erroneously caused by the chosen optimization methodology (in the gas phase), this model was also optimized by the QM:MM approach.

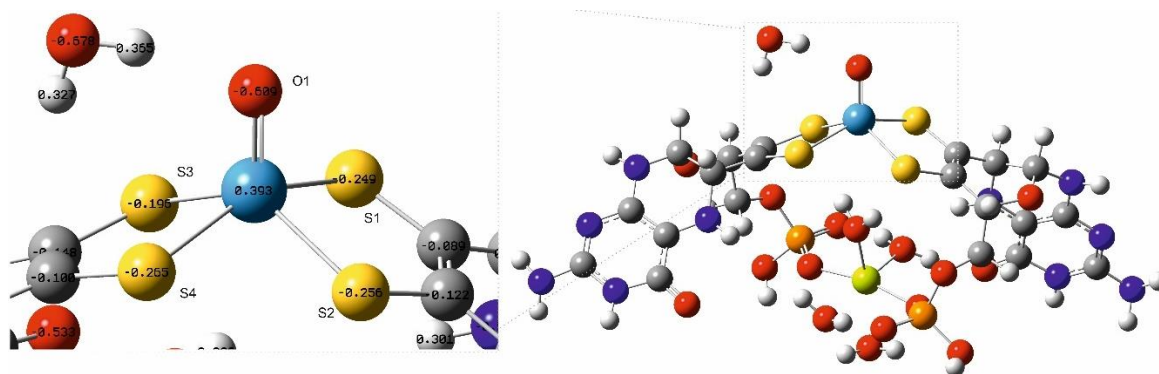


**Figure 65.** Fragment of optimized  $W(IV)O(H_2O)(MPT)_2$  model with Mulliken charges assigned to atoms.

### Model $W(IV)O(OH)(MPT)_2$

During the optimization of the geometry of the reduced cofactor with one oxo and one hydroxo ligand, one of the coordination bonds between sulfur and tungsten atom broke, resulting in a drastic change in cofactor geometry (**Figure 66**). The resulting geometry was not a satisfactory candidate for fit into the density, as the pterins no longer formed a typical  $W$ -co structure. It was assumed, however, that with restraints from protein surroundings, the cofactor may retain its geometry. Therefore, this model was also chosen for the next step of optimization as QM:MM model.

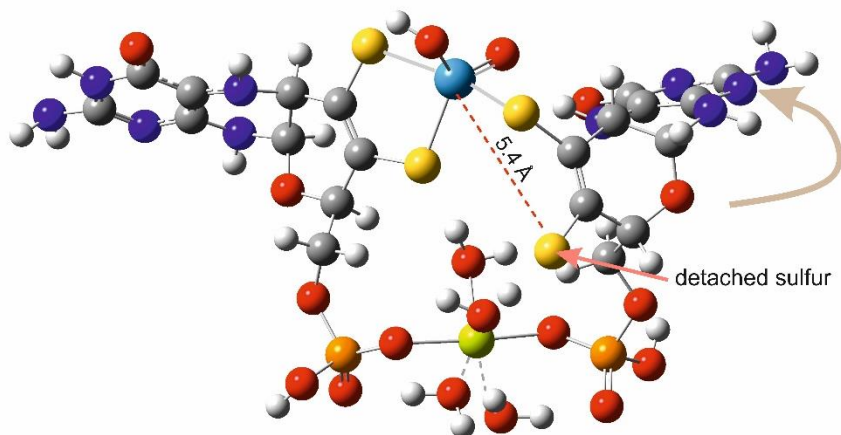


**Figure 66.** The optimized model  $W(IV)O(OH)(MPT)_2$ . The sulfur atom marked on figure at the beginning of optimization had a bond with tungsten atom and in optimized model the distance between this sulfur and tungsten was 5.4 Å, the connected MPT moved behind the cofactor (as marked).

## 8.2. QM:MM models of W-co

Only three candidate models of W-co compositions were selected for further QM:MM study: i)  $W(VI)O_2(MPT)_2$ ; ii)  $W(IV)O(H_2O)(MPT)_2$ ; iii)  $W(IV)O(OH)(MPT)_2$  (in naming of the cofactor other ligands were omitted for brevity and clarity reasons). Geometry optimization was performed for  $W(IV)O(H_2O)(MPT)_2$  just with mechanical embedding and for  $W(VI)O_2(MPT)_2$  and  $W(IV)O(OH)(MPT)_2$  with an additional electronic embedding optimization step. As in QM:MM protein provided the H-bond and salt bridge partners for the phosphate groups, the MPT ligands were in the completely deprotonated state ( $MPT^{4-}$ ). Considering the unexpected results of QM-only optimization (especially for the reduced models), the optimized geometries were compared with experimental data and then fitted to the electron density map of  $AOR_{Pf}$ .

The geometry optimization by QM:MM method took into account the steric boundaries and electrostatic interactions imposed by the protein. This important difference between QM-only and QM:MM optimization resulted in changes in the final geometries of the cofactor models (**Figure 67**). The cofactor was more planar in QM-only models, while in QM:MM models, the pterins formed a steeper, pyramid-like form. The pyramid-like geometry was rather similar to the geometry of the pterins in the deposited PDB structure of W-co in  $AOR_{Pf}$  (superposition shown in **Figure 67.D**).

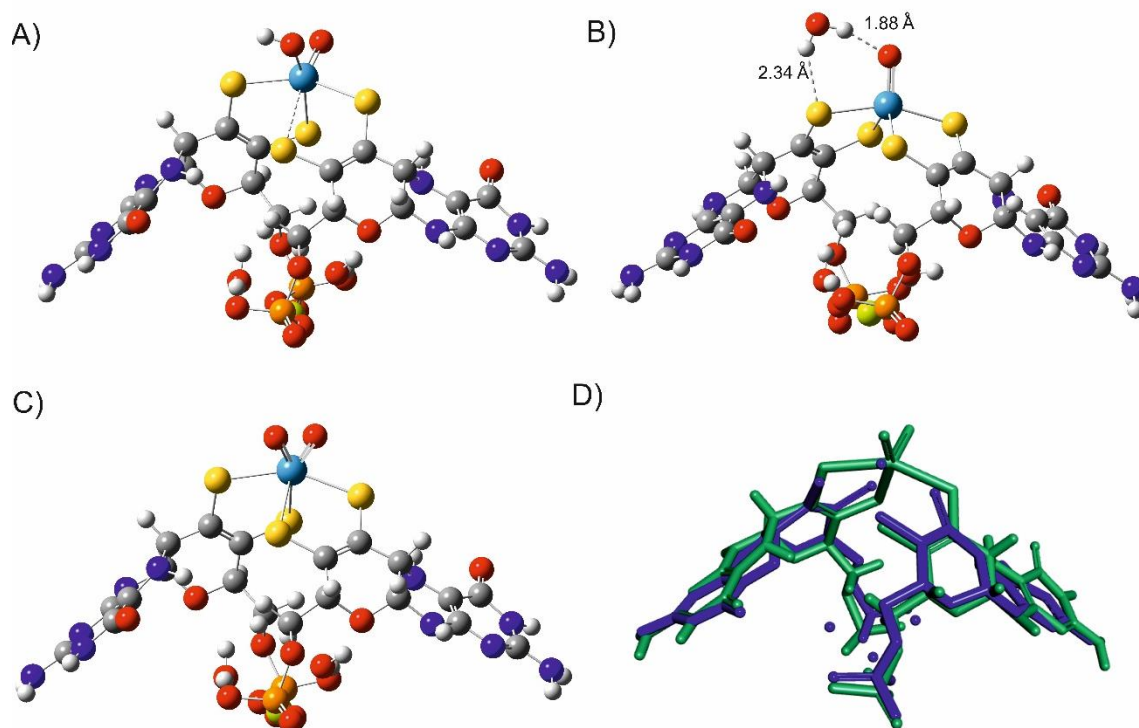


**Figure 67.** Optimized QM:MM models of cofactor A)  $W(IV)O(OH)(MPT)_2$ , B)  $W(IV)O(H_2O)(MPT)_2$ , C)  $W(VI)O_2(MPT)_2$ , D) Superposition of cofactor models.  $W(VI)O_2(MPT)_2$  shown in teal, the crystal structure of W-co (from PDB ID:1AOR) do not have hydrogens, shown in blue.

#### Model $W(VI)O_2(MPT)_2$

In contrast to the QM-only gas phase model, the bonds between the W atom and the two oxo ligands also turned out not to be totally equal. A small difference in the lengths of those bonds may be due to the apparent hydrogen bond that was formed between His448 and the oxo ligand (O2) further removed from the W atom. The difference in oxo ligand geometry also impacted the *trans* sulfurs, resulting in much more different bond lengths (shorter bond of 2.591 Å *trans* to O2, longer bond of 2.746 Å to O1).

#### Model $W(IV)O(OH)(MPT)_2$

The optimized structure of the reduced cofactor model  $W(IV)O(OH)(MPT)_2$  (**Figure 67.A**) exhibited a profoundly distorted octahedral geometry. The W-S bond in *trans* position to oxo ligand was calculated to be very long (3.195 Å), beyond the distance for a covalent bond. This sulfur seems to be weakly bound by electrostatic interaction with a positively charged W atom and might not be noticed by spectroscopic methods like EXAFS. In contrast to the corresponding QM-only model, the cofactor retained its geometry.

**Table 29.** Bond lengths and angles between tungsten and oxygen ligands in optimized selected QM:MM models of the cofactor.

Bond length (Å)	Crystal structure (1AOR)	EXAFS (oxidized AOR <sub>PF</sub> ) <sup>a</sup>	W(VI)O <sub>2</sub> (MPT) <sub>2</sub> QM:MM	W(IV)O(OH) (MPT) <sub>2</sub> QM:MM	W(IV)O(H <sub>2</sub> O) (MPT) <sub>2</sub> QM:MM
W-S1	2.363	2.40	2.496	2.422	2.455
W-S2	2.342	2.40	2.591	2.432	2.381
W-S3	2.333	2.40	2.485	2.587	2.475
W-S4	2.346	2.40	2.746	3.195 <sup>a</sup>	2.408
W=O1	n.a.	1.75	1.751	2.057	1.744
W=O2	n.a.	1.75	1.742	1.727	n.a. <sup>a</sup>
S2-W-S4	113.97	n.a.	87.4	76.82	115.73
S1-W-S3	144.09	n.a.	151.61	148.47	156.96

<sup>a</sup> water molecule in the optimized model is not bound to the W atom

#### *Model W(IV)O(H<sub>2</sub>O)(MPT)<sub>2</sub>*

Similarly to the corresponding QM-only model, the bond between the W atom and the water ligand was spontaneously cleaved during QM:MM optimization of W(IV)O(H<sub>2</sub>O)(MPT)<sub>2</sub> model and water molecule formed hydrogen bonds with oxo ligand and one of sulfur (**Figure 67.B**). The bond cleavage during QM:MM geometry optimization confirms that the effect observed in the gas phase was not an artefact and can not be mended by the presence of the protein. Furthermore, it excludes this model from candidate structures used to interpret the 1AOR density map. The tungsten coordination sphere showed distorted square pyramid geometry. The bonds between the W atom and all four sulfur atoms varied more than in the QM-only model, which shows the impact of protein surrounding on cofactor geometry.

### **8.3. Fit of optimized W-co models to electron density of AORs**

#### *Model W(IV)O(OH)(MPT)<sub>2</sub>*

Fitting of the W(IV)O(OH)(MPT)<sub>2</sub> model to the electron density map of AOR<sub>PF</sub> resulted in the difference map shown in **Figure 68**. The occupancy of the tungsten atom in the cofactor was optimized to 0.89 during refinement. The map shows that one of the pterins (on the left in **Figure 68**) fits well to the electron density. On the other hand, the other pterin and phosphate residues positions exhibited much deviation from the available map. The tungsten coordination sphere also did not fit the map well. The hydroxy ligand

of tungsten brought in excess density to the model, while the mono oxo ligand provided insufficient density. An additional excess of electron density over the oxo ligand might correspond to a water molecule missing in the model. The overall fit of the  $W(IV)O(OH)(MPT)_2$  model to the experimental density map was unsatisfactory.

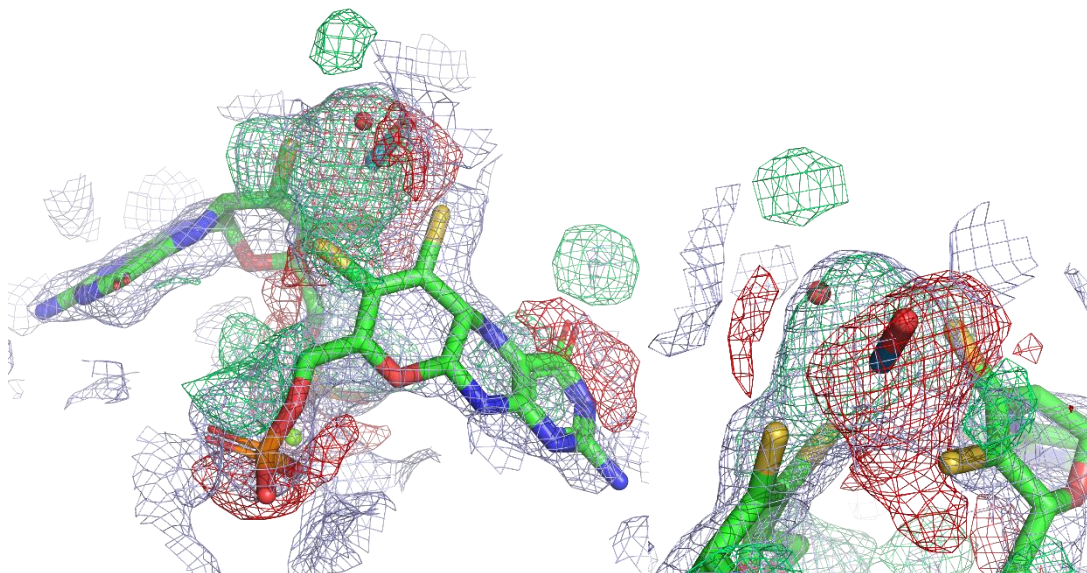


**Figure 68.** Difference map of  $AOR_{Pf}$  calculated from crystallographic data and reduced  $W(IV)O(OH)(MPT)_2$  model prepared by QM:MM modelling. The excess of electron density of the model is shown in red, the deficient electron density of the model is shown in green.

#### *Model $W(VI)O_2(MPT)_2$*

In comparison to the previous model, refinement of the  $W(VI)O_2(MPT)_2$  model to the electron density map of  $AOR_{Pf}$  resulted in a better quality of fit, as shown in the difference map in **Figure 69**. The occupancy of the tungsten atom in the cofactor was optimized to be almost full (0.97) during refinement. The difference map shows that the most outliers of the model from the map occur at the phosphate residues and the pyrimidine ring of the pterin as in the previous model. Those two parts of the cofactor could be mobile and may have variable conformations in the crystal, which could explain the inconsistency in the fit. The tungsten ligands fit the map correctly. Only small inconsistencies in electron density were detected near the W atom, which could correspond to a discrete error in occupancy optimization of the cofactor or the oxidation of the sample with X-ray damage. Above the oxo ligand, there is still an additional excess electron density that might correspond to a water molecule missing in the model.

This model was also used in the refinement of the  $AOR_{Aa}$  structure and the quality of fit is shown in **Figure 69**. The lower resolution of the  $AOR_{Aa}$  map and lacking possibility to

prepare the difference map (property of the cryo-EM electron density maps) made these data less valuable for the assessment of the model. The visual assessment of the model fit to AOR<sub>Aa</sub> electron density (**Figure 57**) shows minor inconsistencies in pterin geometry and position on phosphates, similar to the features of the AOR<sub>Pf</sub> map. The tungsten cofactor and its ligands (except for S1 sulfur) are fitting the electron density. The good quality of fit of this model to the electron density map of AOR<sub>Pf</sub> and to AOR<sub>Aa</sub> allows drawing a conclusion that the most probable geometry of oxidized cofactor in both structures is represented by the W(VI)O<sub>2</sub>(MPT)<sub>2</sub> model.

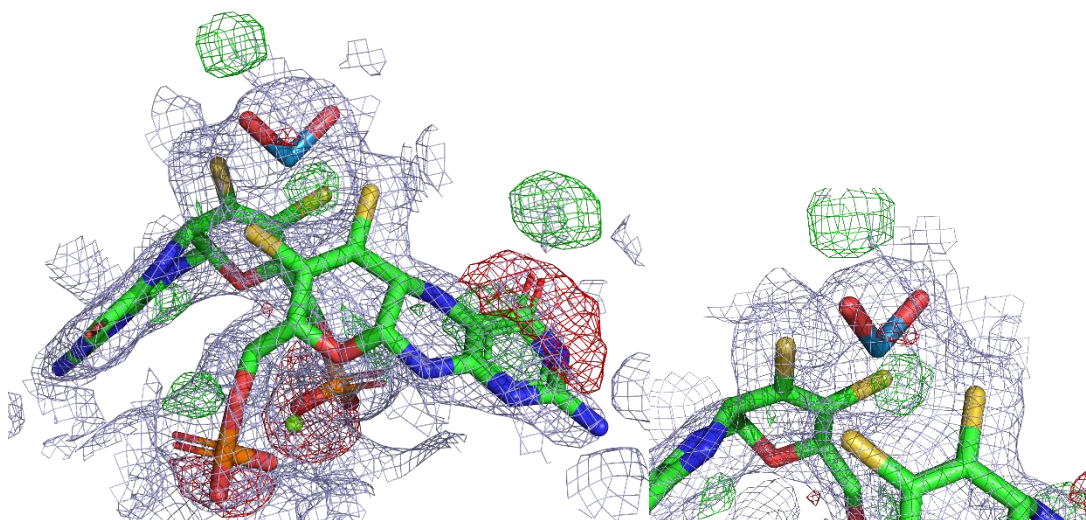


**Figure 69.** Difference map of AOR<sub>Pf</sub> calculated from crystallographic data and oxidized W(VI)O<sub>2</sub>(MPT)<sub>2</sub> model prepared by QM:MM modelling. The excess electron density of the model is shown in red, and the deficient electron density of the model is shown in green.

## 9. EXAFS of AOR<sub>Aa</sub>

The QM-only and QM:MM models of W-co prepared in the previous chapter aided the interpretation of X-ray absorption spectra for studied samples of AOR<sub>Aa</sub>. The data collected for samples with reduced, oxidized and ‘as isolated’ AOR<sub>Aa</sub> are shown in **Figure 70**. All datasets are burdened with high noise, and the dataset for the ‘as isolated’ sample is discontinued at higher wave numbers (k). The Fourier transforms were fitted with models of W-co and the best fits were presented in **Table 30**.

For the reduced sample, two possible compositions of cofactor were found. The number of W-S bonds in the sample was the main difference in the model and both three or four coordination numbers were deemed possible. The model containing three W-S bonds had a lower value of the fit-error Fisher function and therefore was selected as more probable. The reduced AOR<sub>Aa</sub> had substantial sulfur coordination with an average W-S



bond length of 2.38 Å and two additional oxygen ligands, bound at 1.79 and 2.00 Å. This result fits the QM:MM model  $W(IV)O(OH)(MPT)_2$ , where the hydroxo group was bound at 2.06 Å and oxo at 1.73 Å. The coordination number of sulfurs and bond lengths are also matching if the fourth sulfur in QM:MM model would be assumed to be too distant to exhibit a relevant signal in the EXAFS spectrum. The comparable results of the experimental and theoretical study of reduced cofactor strongly point to a conclusion that its composition is indeed as in  $W(IV)O(OH)(MPT)_2$  model.

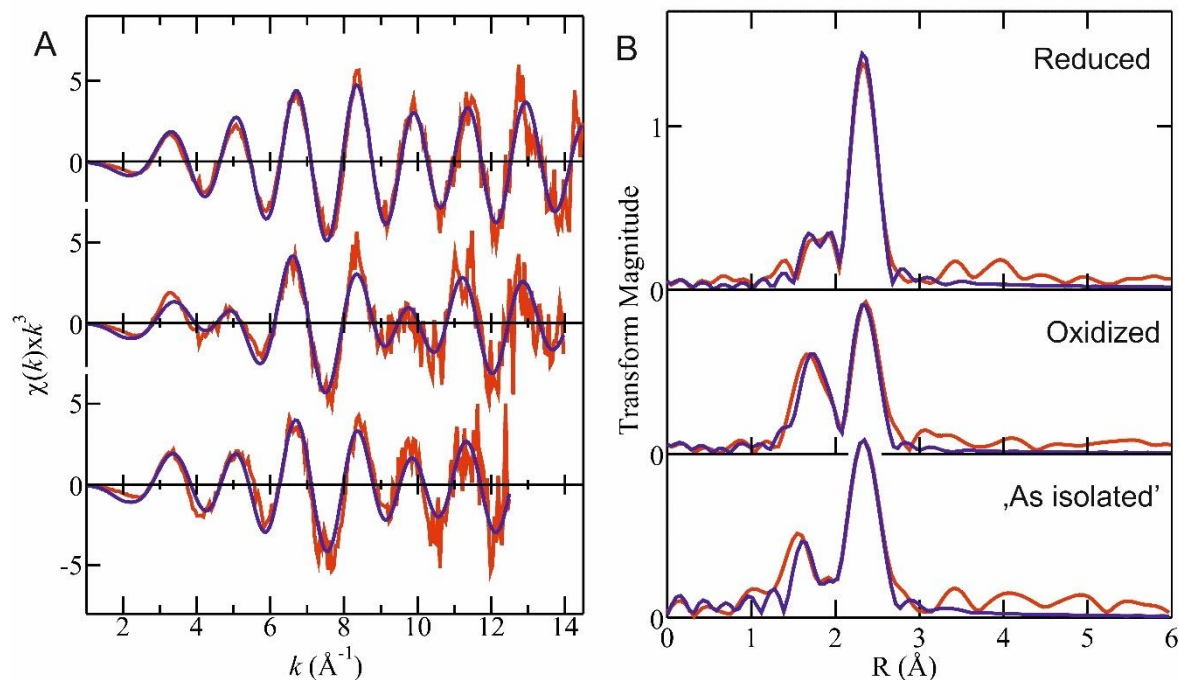


**Figure 70.** **A)** EXAFS oscillations as a function of photo-electron wave vector  $k$ , and weighted by  $k^3$ ; **B)** W  $L_{III}$ -edge EXAFS Fourier transform (WS phase-corrected) of  $AOR_{Aa}$  for samples in order from the top: reduced with sodium dithionite, oxidized with ferrocenium tetrafluoroborate, 'as isolated'.

The results for both oxidized and 'as isolated' samples were surprising, as they show that only two sulfurs are coordinating the tungsten in the cofactor. These results contradict the previous studies for  $AOR_{Pf}$  (EXAFS, X-ray structure) and  $AOR_{Aa}$  (structure in Chapter 7) and do not fit the models shown in Chapter 8. On the other hand, there are three identified bonds between oxygens and the W atom, two short (double bonds corresponding to oxo ligand) and one longer bond (single bond corresponding to water or hydroxo ligand). The identified oxygen ligands are similar to those detected in EXAFS of oxidized  $AOR_{Pf}$ . A possible explanation for the unexpected result may be a decomposition of the sample, i.e., from treatment with the rather harsh oxidant. Another

case where the readings could be true is that the cofactor is in a new state, which has not been noted before in AOR. To resolve this uncertainty, the experiment needs to be repeated with better enzyme samples.

**Table 30.** EXAFS curve-fitting analysis of the three samples of AOR<sub>Aa</sub>. The data for the reduced sample were fitted using two W-co models of different compositions.

Sample	Interaction	N	R	$\sigma^2$	$\Delta E_0$	F	k-range
reduced	W-S	3	2.380(3)	0.0035(1)	-11.5(7)	0.3498	1-14.5
	W-O	1	1.793(6)	0.0027(5)			
	W-O	1	2.003(9)	0.0044(11)			
alternative fit for reduced	W-S	4	2.380(3)	0.0051(2)	-11.3(7)	0.3929	
	W-O	1	1.803(6)	0.0020(5)			
	W-O	1	1.998(7)	0.0019(7)			
oxidized	W-S	2	2.398(5)	0.0038(3)	-12.1(9)	0.5057	1-14
	W-O	2	1.771(5)	0.0045(5)			
	W-O	1	2.021(18)	0.0068(2)			
as-isolated	W-S	2	2.337(3)	0.0053(3)	-12.1	0.5223	1-12.5
	W-O	2	1.785(8)	0.0069(10)			
	W-O	1	2.012(11)	0.0018(9)			

Values given in parentheses are the estimated standard deviations obtained from the diagonal elements of the variance–covariance matrix. N is the coordination number and  $\sigma^2$  is the mean-square-displacement in the bond distance R. The fit–error function F. N was fixed to an integer value.

## DISCUSSION OF PART IV

The prepared series of QM-only optimized models allowed for the comparison of structural details, such as bond lengths and angles, with experimental data on the W-co cofactor in AORs. The QM-only optimized models did not represent the enzyme active site correctly, which was a consequence of the chosen level of model detail, as the calculations were conducted in a vacuum and did not account for the restraints from the protein. The resulting W-co geometries showed pterins in a more planar position than in the AOR<sub>Pf</sub> crystal structure. The extent of distortion from octahedral geometry introduced by the protein suggests modulation of the tungsten cofactor redox potential toward a reduced state (by elevation of W(VI) energy)<sup>57</sup>.

In contrast to the QM-only model, in the QM:MM models the optimized W-co geometry is positioned in the protein (protein was treated in MM). The QM:MM optimized models of

the cofactor have a pterin geometry resembling the density of pterins in the crystal structure of AOR<sub>Pf</sub>. On the other hand, the protein residues surrounding the W-co can interact with it and influence its geometry. These interactions, like hydrogen bonds, are formed during the optimization because both cofactor and neighbouring residues are flexible. However, the interactions are not necessarily present in the protein (as too many assumptions like protonation state are made during the model building and optimization) and can add error to the geometry. Considering the possible errors in both QM-only and QM:MM methods and the calculation cost of QM:MM method, the presented two-stage optimization approach allows reinterpreting the structural data of AOR<sub>Pf</sub> and provides reasonable proof for solving the structure of W-co.

All optimized models of oxidized W-co shown distorted octahedral geometry of the tungsten coordination sphere. Meanwhile, in most reduced structures, the W atom forms a square pyramid with dithiolene ligands. This drastic change in geometry with the oxidation state of the metal was explained by Stein and coworkers by a pseudo-Jahn-Teller (PJT) effect. The PJT effect arises from the mixing of the ground electronic and excited electronic states and causes distortion of the octahedral formed by W ligands. The PJT effect minimizes the reorganizational energy of cycling between W(IV) and W(VI) as the pterins move when the oxidation state changes. This effect was also suggested to impact the reduction potentials and catalytic reactivity of Mo- and W-enzymes<sup>196</sup>.

The theoretical approach showed that from studied models, the most probable candidate for cofactor present in both AOR<sub>Pf</sub> and AOR<sub>Aa</sub> is the oxidized W-co with two oxo ligands. This model fits well the AOR<sub>Pf</sub> EXAFS results, the electron density map of AOR<sub>Pf</sub> and, with a satisfactory match, fits the cofactor in AOR<sub>Aa</sub> electron map. The minor differences with the structural data might be the result of a non-homogenous sample of the isolated enzyme (this phenomenon was explained by Cotelasagne *et al.*<sup>81</sup>), while the theoretical models have the exact structures.

The experiments shown in this work provided a vast insight into AOR<sub>Aa</sub> – catalyzed reactions and the general conclusions should be discussed in the context of the reaction mechanism. The structural study shows that the active site of AOR<sub>Aa</sub> is strikingly similar to that of AOR<sub>Pf</sub> and the conserved amino acids that might take part in catalysis are His464, Glu331 and Tyr443. Previous studies lacked information on ligands present at the W-co in AOR. In this work, the best candidate structures of oxidized and reduced cofactors were determined. The theoretical study shown in the Chapter 8 concludes that

the oxidized cofactor has two oxo ligands. The EXAFS data show that the reduced W-co has one oxo ligand and one hydroxo ligand (structure, as shown by model W(IV)=O-OH).

In this work, the substrate spectrum of AOR<sub>Aa</sub> in aldehyde oxidation was shown to be vast and numerous examples of the shown oxidations were proved to be reversible. The reduction of carboxylic acids by AOR<sub>Aa</sub> was shown to be possible even with low-redox potential electron donors like hydrogen.

In reaction with D<sub>2</sub> as an electron donor, the d<sup>1</sup>-benzaldehyde content is low, but its presence implies that the acid reduction and hydrogen oxidation reactions take place in close vicinity enabling the transfer of a proton from D<sub>2</sub>, probably on the same cofactor – W-co.

In light of those facts, two probable reaction mechanisms can be proposed. The first proposed mechanism is based on previous suggestions made by prof. Martin Kirk on conferences (although never published) and partially inspired by the mechanism suggested for FOR by Liao *et al.*<sup>87</sup>. This mechanism (**Figure 71**) includes first-shell coordination of the substrate to tungsten atom in W-co. This mechanism was adjusted to include the oxidized and reduced states that were identified in this work. The aldehyde is coordinated by His464 via a hydrogen bond with α-hydrogen of a carbonyl group and the oxo ligand from W-co conducts a nucleophilic attack on α-carbon. This attack activates oxygen at the carbonyl group to bind to tungsten. The conformational change at the carbonyl group lowers the energy necessary to abstract the proton from α-carbon. The intermediate is hydrolyzed by water, which results in the release of carboxylic acid. The W-co is left in a reduced state with one oxo ligand and one hydroxo ligand.

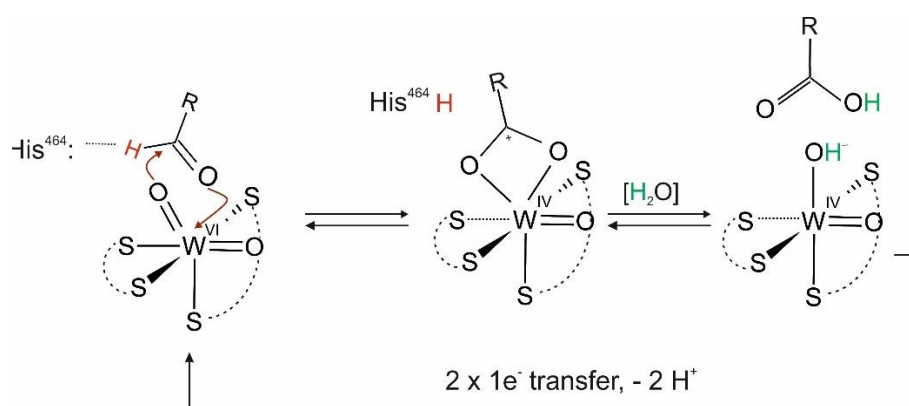


**Figure 71.** The reaction mechanism hypothesis for aldehyde oxidation by AOR, based on M.Kirk and Liao works<sup>87</sup>, adapted to include geometries of W-co solved in this work.

This mechanism assumes that breaking the bond between tungsten and oxygen (in the product) is relatively easy as the release of acid is promoted by hydrolysis. Moreover, this mechanism assumes that aldehyde reacts in carbonyl form, while one of the main substrates (formaldehyde) occurs in water almost exclusively in the form of geminal diol. Therefore, another mechanism was also proposed, taking into consideration the hydrated form of the aldehydes and proposing that the reaction proceeds in the second coordination sphere of the W atom.

In this alternate mechanism (**Figure 72**), the substrate binds to the active site in the form of geminal diol. The benzoate resolved in the AOR structure is also bound in a position that would resemble the binding of a geminal diol. The hydroxo group would be stabilized by H-bond interaction with His464 and Glu331, while the  $\alpha$ -hydrogen of hydrated aldehyde would form a hydrogen bond with the oxo ligand of the W atom. A hydride moiety may then be transferred from the carbonyl atom to the W-co concomitantly or sequentially, with the OH-proton transferred to Glu331 (acting as a base), yielding a carboxylic acid as a product. The transferred hydride on the W-co would immediately lead to a two-electron reduction of W(VI) to W(IV), while the proton would still remain bound to the (former) oxo group, creating a hydroxy ligand at W.

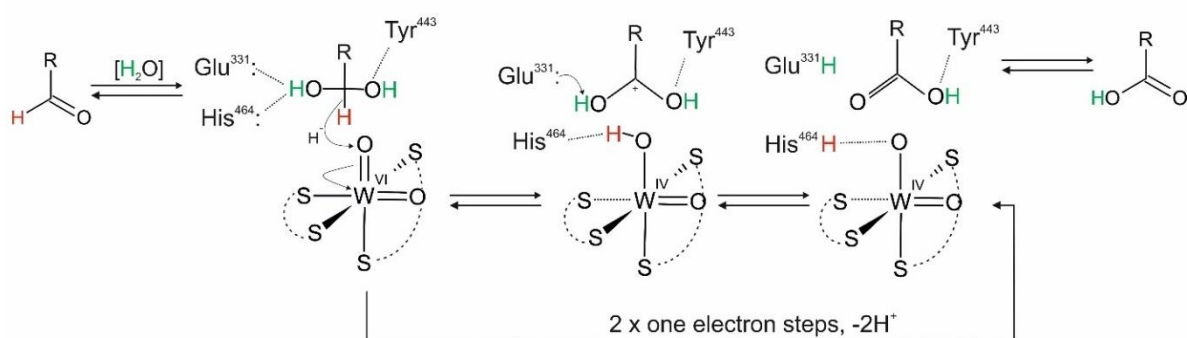


**Figure 72.** Proposed mechanism of aldehyde oxidation by AOR<sub>Aa</sub>. Aldehyde undergoes spontaneous addition of water to form respective geminal diol. Deprotonated Glu 331 and His464 and protonated Tyr443 bind the geminal diol in a position where the  $\alpha$ -hydrogen forms a hydrogen bond with oxo ligand coordinating W-co. This hydride is abstracted and the proton from the hydroxy group is intercepted by the Glu331 and acid is formed.

The two proposed mechanisms can be further tested by QM:MM modeling. Moreover, the role of the amino acids mentioned in those mechanisms can be tested by directed mutagenesis. These studies are currently conducted in cooperation with prof. Maciej Szaleniec and partners from Marburg University.

## SUMMARY OF THE RESULTS

In this thesis, a throughout characteristic of aldehyde oxidoreductase from *Aromatoleum aromaticum* was shown. A summary of the results achieved in this work is listed below.

1. A number of homogenous preparations of aldehyde oxidoreductase from *Aromatoleum aromaticum* have been obtained by:

a. Fermentation of *A.aromaticum* SR7 $\Delta$ *pdh* strain and multi-step chromatography protocol.

b. Fermentation of *A.evansii* heterologously expressing AOR<sub>Aa</sub> and affinity chromatography.

An additional gel filtration step for the latter method yielded active protein preparations of the highest purity noted so-far.

2. The purity of enzyme preparation from a heterologous system was assessed by mass spectroscopy analysis and the only **identified impurity** was assigned to a small admixture of three subunits of the close AOR<sub>Aa</sub> homolog **AOR<sub>Ae</sub> from *A.evansii***. The proteins are highly similar with the sequence identity of each subunit of 92% for AorA, 83% for AorB and 85% for AorC. Therefore, the presence AOR<sub>Ae</sub> should not change the activity of AOR<sub>Aa</sub>. However, the admixture of AOR<sub>Ae</sub> could have had a negative impact on the resolution of the structural studies.

3. **The stability of AOR<sub>Aa</sub>** in a range of pH was tested based on AorC unfolding. The enzyme was shown to be stable in the pH range of 4.5-7.5, and the stability decreased in pH above 8.0. Several buffers were tested and no negative impact of buffer type on enzyme stability was noted.

4. The activity of AOR<sub>Aa</sub> in aldehyde oxidation was confirmed by UV-vis kinetic test with NAD<sup>+</sup> as an electron acceptor for a range of new substrates, including 4-substituted benzaldehyde derivatives and heterocyclic aldehydes (furfural and 2-thiophenecarboxaldehyde). Moreover, the kinetic parameters for benzaldehyde, acetaldehyde and phenylacetaldehyde were established.

5. An activity of AOR<sub>Aa</sub> as **hydrogenase** was shown in this work, which is **unprecedented for tungsten enzymes**. AOR<sub>Aa</sub> was proven to reduce NAD<sup>+</sup>, BV<sup>2+</sup> and carboxylic acids with electrons from hydrogen oxidation. The **substrate spectrum** of AOR<sub>Aa</sub> was established by the detection of aldehydes by LC-MS/MS and GC-MS methods. It was demonstrated that aliphatic, aromatic and heterocyclic acids are converted. The kinetic parameters for hydrogen-dependent benzoic acid reduction and reduction of NAD<sup>+</sup> and BV<sup>2+</sup> were established.

6. A coupled assay for measuring AOR<sub>Aa</sub> activity in benzoic acid reduction with hydrogen as an electron donor was established with BaDH reducing further the AOR-reduced benzaldehyde to benzyl alcohol with NADPH as an electron donor, which concentration was measured by UV-vis.
7. The pH optimum for H<sub>2</sub>-dependent NAD<sup>+</sup> reduction by AOR<sub>Aa</sub> was established to be 8.0, whereas for benzoic acid reduction, the lower the pH, the higher activity was observed.
8. AOR<sub>Aa</sub> was shown to simultaneously reduce NAD<sup>+</sup> and benzoic acid in the presence of hydrogen **without electron bifurcation**. When a benzyl alcohol dehydrogenase (BaDH) was additionally applied in the above reactor, the **production of benzyl alcohol** with electrons derived solely from hydrogen was shown, both in acidic and neutral pH.
9. Partial isotopic enrichment of produced benzaldehyde with deuterium in reduction driven by deuterium gas suggested that both hydrogen oxidation and acid reduction are catalyzed in the same active site.
10. Application of AOR<sub>Aa</sub> as an **NADH-regenerating system** was additionally shown in the reactor with R-HPED producing (*R*)-1-phenylethanol. The applicability of blue hydrogen for AOR<sub>Aa</sub>-catalyzed reductions was demonstrated by the NAD<sup>+</sup> reduction test with a gas mix containing carbon monoxide.
11. **Cryo-electron microscopy** investigation of AOR<sub>Aa</sub> resulted in a reconstruction of a **3.3 Å** global resolution density map of seven subunits of an **Aor(AB)<sub>2</sub>C complex**. The structural data, together with mass photometry data, shown, that AOR<sub>Aa</sub> has an oligomeric structure with AorAB as a repeating protomer (Aor(AB)<sub>n</sub>C, where highest observed n=5). The quality of the map allowed for tracing of the main chain and sidechains for Aor(AB)<sub>2</sub>C complex and the next two subunits are clearly visible in the map. The reconstructed structure revealed that:
  - a. In AorB the W-co has a similar structure as the cofactor identified in other AORs and the Fe<sub>4</sub>S<sub>4</sub> cluster is in close vicinity of W-co;
  - b. The AorA subunit carries four Fe<sub>4</sub>S<sub>4</sub> clusters, which are within a short distance of each other and the neighbouring cofactors, enabling fast electron flow. The AorA subunits in the oligomeric complex are responsible for forming a nanowire and linking the protomers.
  - c. The AorC carries the FAD cofactor and is a probable nucleation subunit for the complex.
12. A QM-only and QM:MM study of potential cofactor geometries allowed us to determine that the most probable composition of oxidized AOR cofactor contains two oxo ligands.

13. W L<sub>III</sub>-edge EXAFS of AOR<sub>Aa</sub> points to the coordination of reduced W-co similar to QM:MM model with W(IV) coordinated by one oxo and one hydroxo ligand.

14. The proposed structures of reduced and oxidized cofactor and other new data on catalyzed reactions allowed the formulation of two new hypothetical reaction mechanisms:

- a. A hypothetical mechanism with first-shell coordination of the substrate to tungsten atom in W-co;
- b. Second-shell catalysis with an aldehyde in the form of geminal diol.

In terms of the two main aims of the thesis, the achievements of this work might be summarized as follows:

- The solved structure of AOR<sub>Aa</sub> and details of active site geometry and occupancy (structure of cofactor and position of the substrate in active site) are important milestones in solving the aldehyde oxidation reaction mechanism.
- The discovered new activity of AOR<sub>Aa</sub> as hydrogenase became an unplanned (at the beginning of this work) extension of the aim to develop the biotechnological application of the enzyme in carboxylic acid reduction. The profound characterization of the biocatalyst covered by this work resulted in development of two biotechnological methods of application potential. The developed methods of acid reduction and NADH regeneration with the use of hydrogen and AOR<sub>Aa</sub> were covered in two Polish Patent Applications and a joint European Patent Application.



## References

- (1) Hollmann, F.; Arends, I. W. C. E.; Holtmann, D. Enzymatic Reductions for the Chemist. *Green Chemistry* **2011**, 13 (9), 2285–2314. <https://doi.org/10.1039/c1gc15424a>.
- (2) Garzón-Posse, F.; Becerra-Figueroa, L.; Hernández-Arias, J.; Gamba-Sánchez, D. Whole Cells as Biocatalysts in Organic Transformations. *Molecules* **2018**, 23 (6), 1265. <https://doi.org/10.3390/molecules23061265>.
- (3) Zhou, N.; Thilakarathna, W. P. D. W.; He, Q. S.; Rupasinghe, H. P. V. A Review: Depolymerization of Lignin to Generate High-Value Bio-Products: Opportunities, Challenges, and Prospects. *Front Energy Res* **2022**, 9. <https://doi.org/10.3389/fenrg.2021.758744>.
- (4) Nielsen, J.; Larsson, C.; van Maris, A.; Pronk, J. Metabolic Engineering of Yeast for Production of Fuels and Chemicals. *Current Opinion in Biotechnology*. **2013**, 24 (3) 398–404. <https://doi.org/10.1016/j.copbio.2013.03.023>.
- (5) Weizmann, C. Improvements in the Bacterial Fermentation of Carbohydrates and in Bacterial Cultures for the Same. GB Patent GB191504845, **1919**.
- (6) Nissen, L. S.; Basen, M. The Emerging Role of Aldehyde:Ferredoxin Oxidoreductases in Microbially-Catalyzed Alcohol Production. *J Biotechnol* **2019**, 306, 105–117. <https://doi.org/10.1016/j.jbiotec.2019.09.005>.
- (7) Liew, F.; Henstra, A. M.; Köpke, M.; Winzer, K.; Simpson, S. D.; Minton, N. P. Metabolic Engineering of *Clostridium Autoethanogenum* for Selective Alcohol Production. *Metab Eng* **2017**, 40, 104–114. <https://doi.org/10.1016/j.ymben.2017.01.007>.
- (8) Keller, M. W.; Lipscomb, G. L.; Nguyen, D. M.; Crowley, A. T.; Schut, G. J.; Scott, I.; Kelly, R. M.; Adams, M. W. W. Ethanol Production by the Hyperthermophilic Archaeon *Pyrococcus Furiosus* by Expression of Bacterial Bifunctional Alcohol Dehydrogenases. *Microb Biotechnol* **2017**, 10 (6), 1535–1545. <https://doi.org/10.1111/1751-7915.12486>.
- (9) Basen, M.; Schut, G. J.; Nguyen, D. M.; Lipscomb, G. L.; Benn, R. A.; Prybol, C. J.; Vaccaro, B. J.; Poole, F. L.; Kelly, R. M.; Adams, M. W. W. Single Gene Insertion Drives Bioalcohol Production by a Thermophilic Archaeon. *Proceedings of the National Academy of Sciences* **2014**, 111 (49), 17618–17623. <https://doi.org/10.1073/pnas.1413789111>.
- (10) Fiala, G.; Stetter, K. O. *Pyrococcus Furiosus* Sp. Nov. Represents a Novel Genus of Marine Heterotrophic Archaeobacteria Growing Optimally at 100C. *Arch Microbiol* **1986**, 145 (1), 56–61. <https://doi.org/10.1007/BF00413027>.
- (11) McMurry, J.; Boczoń, W. *Chemia Organiczna*; PWN, Warszawa **2007**; Vol. 4.
- (12) Wade, L. G. Jr. *Organic Chemistry*; Prentice-Hall: Englewood Cliffs, NJ, **1987**; Chapter 18.
- (13) Bochwic, B. *Preparatyka Organiczna*; PWN, Warszawa 1967.

- (14) McMurry, J. *Organic Chemistry*, 6th ed.; Brooks Cole, Ed.; **2007**.
- (15) Baekeland, L. H. The Synthesis, Constitution, and Uses of Bakelite. *J of Industrial & Engineering Chemistry* **1909**, 1 (3), 149–161. <https://doi.org/10.1021/ie50003a004>.
- (16) Adopting the List of Flavouring Substances Provided for by Regulation (EC) No 2232/96 of the European Parliament and of the Council, Introducing It in Annex I to Regulation (EC) No 1334/2008 of the European Parliament and of the Council and Repealing Commission Regulation (EC) No 1565/2000 and Commission Decision 1999/217/EC; *Official J of the European Union*, **2012**; 1–161.
- (17) United States in the Code of Federal Regulations (CFR) at 21CFR182.60.
- (18) Final Report on the Safety Assessment of Benzaldehyde. *Int J Toxicol* **2006**, 25 (1\_suppl), 11–27. <https://doi.org/10.1080/10915810600716612>.
- (19) Karumathil, D. P.; Nair, M. S.; Gaffney, J.; Kollanoor-Johny, A.; Venkitanarayanan, K. Trans-Cinnamaldehyde and Eugenol Increase *Acinetobacter Baumannii* Sensitivity to Beta-Lactam Antibiotics. *Front Microbiol* **2018**, 9. <https://doi.org/10.3389/fmicb.2018.01011>.
- (20) Michlig Gonzalez, S.; Meylan Merlini, J.; Camacho, S.; le Coutre, J. Compositions and Methods Using P-Anisaldehyde. Patent WO2015011036A1, Washington, DC, **2015**.
- (21) Yu, T.; Yin, Y.; Ge, Y.; Cheng, S.; Zhang, X.; Feng, Z.; Zhang, J. Enzymatic Production of 4-Hydroxyphenylacetaldehyde by Oxidation of the Amino Group of Tyramine with a Recombinant Primary Amine Oxidase. *Process Biochemistry* **2020**, 92, 105–112. <https://doi.org/10.1016/j.procbio.2020.03.007>.
- (22) O'Brien, J.; Morrissey, P. A.; Ames, J. M. Nutritional and Toxicological Aspects of the Maillard Browning Reaction in Foods. *Crit Rev Food Sci Nutr* **1989**, 28 (3), 211–248. <https://doi.org/10.1080/10408398909527499>.
- (23) Wu, J.-Y.; Shi, Z.-G.; Feng, Y.-Q. Determination of 5-Hydroxymethylfurfural Using Derivatization Combined with Polymer Monolith Microextraction by High-Performance Liquid Chromatography. *J Agric Food Chem* **2009**, 57 (10), 3981–3988. <https://doi.org/10.1021/jf900434n>.
- (24) Bedenbaugh, A. O.; Bedenbaugh, J. H.; Bergin, W. A.; Adkins, J. D. Synthesis of Aldehydes and Secondary Amines from Carboxylic Acids via Imines. *J Am Chem Soc* **1970**, 92 (19), 5774–5775. <https://doi.org/10.1021/ja00722a060>.
- (25) Magano, J.; Dunetz, J. R. Large-Scale Carbonyl Reductions in the Pharmaceutical Industry. *Org Process Res Dev* **2012**, 16 (6), 1156–1184. <https://doi.org/10.1021/op2003826>.
- (26) Rosenmund, K. W. Über Eine Neue Methode Zur Darstellung von Aldehyden. 1. Mitteilung. *Berichte der deutschen chemischen Gesellschaft* **1918**, 51 (1), 585–593. <https://doi.org/10.1002/cber.19180510170>.

- (27) Tokuyama, H.; Yokoshima, S.; Yamashita, T.; Shao-Cheng, L.; Leping, L.; Fukuyama, T. Facile Palladium-Mediated Conversion of Ethanethiol Esters to Aldehydes and Ketones. *J Braz Chem Soc* **1998**, *9* (4). <https://doi.org/10.1590/S0103-50531998000400011>.
- (28) Tojo, G., Fernández, M., *Oxidation of Alcohols to Aldehydes and Ketones: A Guide to Current Common Practice*, Springer, New York, **2006**.
- (29) Kazimírová, V.; Rebroš, M. Production of Aldehydes by Biocatalysis. *Int J Mol Sci* **2021**, *22* (9), 4949. <https://doi.org/10.3390/ijms22094949>.
- (30) Napora-Wijata, K.; Strohmeier, G. A.; Winkler, M. *Biocatalytic Reduction of Carboxylic Acids*. Biotechnology J. Wiley-VCH Verlag 2014, pp 822–843. <https://doi.org/10.1002/biot.201400012>.
- (31) Correia, H. D.; Marangon, J.; Brondino, C. D.; Moura, J. J. G.; Romão, M. J.; González, P. J.; Santos-Silva, T. Aromatic Aldehydes at the Active Site of Aldehyde Oxidoreductase from *Desulfovibrio Gigas*: Reactivity and Molecular Details of the Enzyme–Substrate and Enzyme–Product Interaction. *JBIC J of Biological Inorganic Chemistry* **2015**, *20* (2), 219–229. <https://doi.org/10.1007/s00775-014-1196-4>.
- (32) Winkler, M. Carboxylic Acid Reductase Enzymes (CARs). *Current Opinion in Chemical Biology*. Elsevier Ltd April 1, 2018, pp 23–29. <https://doi.org/10.1016/j.cbpa.2017.10.006>.
- (33) Gahloth, D.; Aleku, G. A.; Leys, D. Carboxylic Acid Reductase: Structure and Mechanism. *J Biotechnol* **2020**, *307*, 107–113. <https://doi.org/10.1016/j.jbiotec.2019.10.010>.
- (34) Venkitasubramanian, P.; Daniels, L.; Rosazza, J. P. N. Reduction of Carboxylic Acids by *Nocardia* Aldehyde Oxidoreductase Requires a Phosphopantetheinylated Enzyme. *J of Biological Chemistry* **2007**, *282* (1), 478–485. <https://doi.org/10.1074/jbc.M607980200>.
- (35) Kunjapur, A. M.; Tarasova, Y.; Prather, K. L. J. Synthesis and Accumulation of Aromatic Aldehydes in an Engineered Strain of *Escherichia Coli*. *J Am Chem Soc* **2014**, *136* (33), 11644–11654. <https://doi.org/10.1021/ja506664a>.
- (36) Fraatz, M. A.; Goldmann, M.; Geissler, T.; Gross, E.; Backes, M.; Hilmer, J.-M.; Ley, J.; Rost, J.; Francke, A.; Zorn, H. Biotechnological Production of Methyl-Branched Aldehydes. *J Agric Food Chem* **2018**, *66* (10), 2387–2392. <https://doi.org/10.1021/acs.jafc.6b04793>.
- (37) Venkitasubramanian, P.; Daniels, L.; Das, S.; Lamm, A. S.; Rosazza, J. P. N. Aldehyde Oxidoreductase as a Biocatalyst: Reductions of Vanillic Acid. *Enzyme Microb Technol* **2008**, *42* (2), 130–137. <https://doi.org/10.1016/j.enzmictec.2007.08.009>.
- (38) Horvat, M.; Fritsche, S.; Kourist, R.; Winkler, M. Characterization of Type IV Carboxylate Reductases (CARs) for Whole Cell-Mediated Preparation of 3-Hydroxytyrosol. *ChemCatChem* **2019**, *11* (16), 4171–4181. <https://doi.org/10.1002/cctc.201900333>.

- (39) Johnson, M. K.; Rees, D. C.; Adams, M. W. W. Tungstoenzymes. *Chem Rev* **1996**, 96, 2817–2839.
- (40) Rollinson C.L., Chromium, molybdenum and tungsten. In: Bailar, J.C., Emeleus, H.J., Nyholm, S., Trotman-Dickenson A.F. (eds) *Comprehensive inorganic chemistry*, Pergamon Press, Oxford **1973**, 3:742–769
- (41) Kletzin, A.; Adams, M. W. W. Tungsten in Biological Systems. *FEMS Microbiol Rev* **2006**, 18 (1), 5–63. <https://doi.org/10.1111/j.1574-6976.1996.tb00226.x>.
- (42) Lassner, E.; Schubert, W.-D. *Tungsten*; Springer US: Boston, MA, 1999. <https://doi.org/10.1007/978-1-4615-4907-9>.
- (43) Fiala, G.; Stetter, K. O. *Pyrococcus Furiosus* Sp. Nov. Represents a Novel Genus of Marine Heterotrophic Archaeobacteria Growing Optimally at 100C. *Arch Microbiol* **1986**, 145 (1), 56–61. <https://doi.org/10.1007/BF00413027>.
- (44) Misko, A. L.; Liang, Y.; Kohl, J. B.; Eichler, F. Delineating the Phenotypic Spectrum of Sulfite Oxidase and Molybdenum Cofactor Deficiency. *Neurol Genet* **2020**, 6 (4), e486. <https://doi.org/10.1212/NXG.0000000000000486>.
- (45) Hille, R., Schulzke, C., Kirk, M. L., *Molybdenum and Tungsten Enzymes*; Eds.; Royal Society of Chemistry: Cambridge, **2016**. <https://doi.org/10.1039/9781782628828>.
- (46) Maia, L. B.; Moura, J. J. G. How Biology Handles Nitrite. *Chemical Reviews*. American Chemical Society May 28, 2014, pp 5273–5357. <https://doi.org/10.1021/cr400518y>.
- (47) Canfield, D. E.; Glazer, A. N.; Falkowski, P. G. The Evolution and Future of Earth's Nitrogen Cycle. *Science* (1979) **2010**, 330 (6001), 192–196. <https://doi.org/10.1126/science.1186120>.
- (48) Seelmann, C. S.; Willstein, M.; Heider, J.; Boll, M. *Tungstoenzymes: Occurrence, Catalytic Diversity and Cofactor Synthesis*, *Inorganics*. MDPI, **2020**, 8(8), 44. <https://doi.org/10.3390/INORGANICS8080044>.
- (49) Chan M.K., Mukund S., Kletzin A., Adams M.W.W., Rees D.C. Structure of a hyperthermophilic tungstopterin enzyme. Aldehyde:ferredoxin oxidoreductase. *Science*. **1995** (267) 1463–1469. doi: 10.1126/science.7878465.
- (50) Matz, K. G.; Mtei, R. P.; Leung, B.; Burgmayer, S. J. N.; Kirk, M. L. Noninnocent Dithiolene Ligands: A New Oxomolybdenum Complex Possessing a Donor–Acceptor Dithiolene Ligand. *J Am Chem Soc* **2010**, 132 (23), 7830–7831. <https://doi.org/10.1021/ja100220x>.
- (51) Dong, C.; Yang, J.; Leimkühler, S.; Kirk, M. L. Pyranopterin Dithiolene Distortions Relevant to Electron Transfer in Xanthine Oxidase/Dehydrogenase. *Inorg Chem* **2014**, 53 (14), 7077–7079. <https://doi.org/10.1021/ic500873y>.
- (52) Rothery, R. A.; Stein, B.; Solomonson, M.; Kirk, M. L.; Weiner, J. H. Pyranopterin Conformation Defines the Function of Molybdenum and Tungsten Enzymes.

- Proceedings of the National Academy of Sciences **2012**, 109 (37), 14773–14778. <https://doi.org/10.1073/pnas.1200671109>.
- (53) Bevers, L. E.; Hagedoorn, P.-L.; Hagen, W. R. The Bioinorganic Chemistry of Tungsten. *Coord Chem Rev* **2009**, 253 (3–4), 269–290. <https://doi.org/10.1016/j.ccr.2008.01.017>.
- (54) Seiffert, G. B.; Ullmann, G. M.; Messerschmidt, A.; Schink, B.; Kroneck, P. M. H.; Einsle, O. Structure of the Non-Redox-Active Tungsten/[4Fe:4S] Enzyme Acetylene Hydratase. *Proceedings of the National Academy of Sciences* **2007**, 104 (9), 3073–3077. <https://doi.org/10.1073/pnas.0610407104>.
- (55) Hille, R.; Hall, J.; Basu, P. The Mononuclear Molybdenum Enzymes. *Chem Rev* **2014**, 114 (7), 3963–4038. <https://doi.org/10.1021/cr400443z>.
- (56) Reschke, S.; Duffus, B. R.; Schrapers, P.; Mebs, S.; Teutloff, C.; Dau, H.; Haumann, M.; Leimkühler, S. Identification of YdhV as the First Molybdoenzyme Binding a Bis-Mo-MPT Cofactor in *Escherichia Coli*. *Biochemistry* **2019**, 58 (17), 2228–2242. <https://doi.org/10.1021/acs.biochem.9b00078>.
- (57) Borowski, T.; Szaleniec, M. Challenges in Modelling Metalloenzymes. In *Transition Metals in Coordination Environments*; Broclawik, E., Ed.; Springer, 2019; 503–526.
- (58) Meckenstock, R. U.; Krieger, R.; Ensign, S.; Kroneck, P. M. H.; Schink, B. Acetylene Hydratase of *Pelobacter Acetylenicus*. Molecular and Spectroscopic Properties of the Tungsten Iron-Sulfur Enzyme. *Eur J Biochem* **1999**, 264 (1), 176–182. <https://doi.org/10.1046/j.1432-1327.1999.00600.x>.
- (59) Mendel, R. R.; Hercher, T. W.; Zupok, A.; Hasnat, M. A.; Leimkühler, S. The Requirement of Inorganic Fe-S Clusters for the Biosynthesis of the Organometallic Molybdenum Cofactor. *Inorganics* **2020**, 8 (7), 43. <https://doi.org/10.3390/inorganics8070043>.
- (60) Weinert, T.; Huwiler, S. G.; Kung, J. W.; Weidenweber, S.; Hellwig, P.; Stärk, H. J.; Biskup, T.; Weber, S.; Cotelesage, J. J. H.; George, G. N.; Ermler, U.; Boll, M. Structural Basis of Enzymatic Benzene Ring Reduction. *Nat Chem Biol* **2015**, 11 (8), 586–591. <https://doi.org/10.1038/nchembio.1849>.
- (61) Mukund, S.; Adams, M. W. Molybdenum and Vanadium Do Not Replace Tungsten in the Catalytically Active Forms of the Three Tungstoenzymes in the Hyperthermophilic Archaeon *Pyrococcus Furiosus*. *J Bacteriol* **1996**, 178 (1), 163–167. <https://doi.org/10.1128/jb.178.1.163-167.1996>.
- (62) Schut, G. J.; Thorgersen, M. P.; Poole, F. L.; Haja, D. K.; Putumbaka, S.; Adams, M. W. W. Tungsten Enzymes Play a Role in Detoxifying Food and Antimicrobial Aldehydes in the Human Gut Microbiome. *Proceedings of the National Academy of Sciences* **2021**, 118 (43), e2109008118. <https://doi.org/10.1073/pnas.2109008118>.
- (63) White, H.; Feicht, R.; Huber, C.; Lottspeich, F.; Simon, H. Purification and Some Properties of the Tungsten-Containing Carboxylic Acid Reductase from

- Clostridium formicoaceticum*; **1991**; 372(11):999-1005, [https://doi:10.1515/bchm3.1991.372.2.999](https://doi.org/10.1515/bchm3.1991.372.2.999)
- (64) Debnar-Daumler, C.; Seubert, A.; Schmitt, G.; Heider, J. Simultaneous Involvement of a Tungsten-Containing Aldehyde:Ferredoxin Oxidoreductase and a Phenylacetaldehyde Dehydrogenase in Anaerobic Phenylalanine Metabolism. *J Bacteriol* **2014**, 196 (2), 483–492. <https://doi.org/10.1128/JB.00980-13>.
- (65) Heider, J.; Ma, K.; Adams, M. W. W. Purification, Characterization, and Metabolic Function of Tungsten-Containing Aldehyde Ferredoxin Oxidoreductase from the Hyperthermophilic and Proteolytic Archaeon *Thermococcus* Strain ES-1; *J Bacteriol* **1995**; 177(16):4757-64, doi: 10.1128/jb.177.16.4757-4764.1995
- (66) Roy, R.; Mukund, S.; Schut, G. J.; Dunn, D. M.; Weiss, R.; Adams, M. W. W. Purification and Molecular Characterization of the Tungsten-Containing Formaldehyde Ferredoxin Oxidoreductase from the Hyperthermophilic Archaeon *Pyrococcus Furiosus*: The Third of a Putative Five-Member Tungstoenzyme Family. *J Bacteriol* **1999**, 181 (4), 1171–1180. <https://doi.org/10.1128/JB.181.4.1171-1180.1999>.
- (67) Thorgersen, M. P.; Schut, G. J.; Poole, F. L.; Haja, D. K.; Putumbaka, S.; Mycroft, H. I.; de Vries, W. J.; Adams, M. W. W. Obligately Aerobic Human Gut Microbe Expresses an Oxygen Resistant Tungsten-Containing Oxidoreductase for Detoxifying Gut Aldehydes. *Front Microbiol* **2022**, 13. <https://doi.org/10.3389/fmicb.2022.965625>.
- (68) Mukund, S.; Adams, M. W. W. Glyceraldehyde-3-Phosphate Ferredoxin Oxidoreductase, a Novel Tungsten-Containing Enzyme with a Potential Glycolytic Role in the Hyperthermophilic Archaeon *Pyrococcus Furiosus*. *J of Biological Chemistry* **1995**, 270 (15), 8389–8392. <https://doi.org/10.1074/jbc.270.15.8389>.
- (69) Bevers, L. E.; Bol, E.; Hagedoorn, P.-L.; Hagen, W. R. WOR5, a Novel Tungsten-Containing Aldehyde Oxidoreductase from *Pyrococcus Furiosus* with a Broad Substrate Specificity. *J Bacteriol* **2005**, 187 (20), 7056–7061. <https://doi.org/10.1128/JB.187.20.7056-7061.2005>.
- (70) Mathew, L. G.; Haja, D. K.; Pritchett, C.; McCormick, W.; Zeineddine, R.; Fontenot, L. S.; Rivera, M. E.; Glushka, J.; Adams, M. W. W.; Lanzilotta, W. N. An Unprecedented Function for a Tungsten-Containing Oxidoreductase. *JBIC J of Biological Inorganic Chemistry* **2022**, 27 (8), 747–758. <https://doi.org/10.1007/s00775-022-01965-0>.
- (71) Roy, R.; Adams, M. W. W. Characterization of a Fourth Tungsten-Containing Enzyme from the Hyperthermophilic Archaeon *Pyrococcus Furiosus*. *J Bacteriol* **2002**, 184 (24), 6952–6956. <https://doi.org/10.1128/JB.184.24.6952-6956.2002>.
- (72) Mukund, S.; Adams, M. W. Characterization of a Tungsten-Iron-Sulfur Protein Exhibiting Novel Spectroscopic and Redox Properties from the Hyperthermophilic Archaeobacterium *Pyrococcus Furiosus*. *J of Biological Chemistry* **1990**, 265 (20), 11508–11516. [https://doi.org/10.1016/S0021-9258\(19\)38426-1](https://doi.org/10.1016/S0021-9258(19)38426-1).

- (73) Mukund, S.; Adams, M. W. W. The Novel Tungsten-Iron-Sulfur Protein of the Hyperthermophilic Archaeobacterium, *Pyrococcus Furiosus*, Is an Aldehyde Ferredoxin Oxidoreductase: Evidence for Its Participation in a Unique Glycolytic Pathway. *J of Biological Chemistry* **1991**, 266 (22), 14208–14216. [https://doi.org/10.1016/s0021-9258\(18\)98669-2](https://doi.org/10.1016/s0021-9258(18)98669-2).
- (74) Arndt, F.; Schmitt, G.; Winiarska, A.; Saft, M.; Seubert, A.; Kahnt, J.; Heider, J. Characterization of an Aldehyde Oxidoreductase From the Mesophilic Bacterium *Aromatoleum Aromaticum* EbN1, a Member of a New Subfamily of Tungsten-Containing Enzymes. *Front Microbiol* **2019**, 10. <https://doi.org/10.3389/fmicb.2019.00071>.
- (75) Strobl, G.; Feicht, R.; White, H.; Lottspeich, F.; Simon, H. The Tungsten-Containing Aldehyde Oxidoreductase from *Clostridium Thermoaceticum* and Its Complex with a Mologen-Accepting NADPH Oxidoreductase; **1992**; 373(3):123-32. doi: 10.1515/bchm3.1992.373.1.123
- (76) Huber, C.; Skopan, H.; Feicht, R.; White, H.; Simon, H. Pterin Cofactor, Substrate Specificity, and Observations on the Kinetics of the Reversible Tungsten-Containing Aldehyde Oxidoreductase from *Clostridium Thermoaceticum*. *Arch Microbiol* **1995**, No. 164, 110–118.
- (77) Huber, C., Caldeira, J., Jongejan, J.A. et al. Further characterization of two different, reversible aldehyde oxidoreductases from *Clostridium formicoaceticum*, one containing tungsten and the other molybdenum. *Arch. Microbiol.* **1994**, 162, 303–309. <https://doi.org/10.1007/BF00263776>
- (78) White, H.; Strobl, G.; Feicht, R.; Simon, H. Carboxylic Acid Reductase: A New Tungsten Enzyme Catalyses the Reduction of Non-Activated Carboxylic Acids to Aldehydes. *Eur J Biochem* **1989**, 184 (1), 89–96. <https://doi.org/10.1111/j.1432-1033.1989.tb14993.x>.
- (79) Schut, G. J.; Adams, M. W. W. The Iron-Hydrogenase of *Thermotoga Maritima* Utilizes Ferredoxin and NADH Synergistically: A New Perspective on Anaerobic Hydrogen Production. *J Bacteriol* **2009**, 191 (13), 4451–4457. <https://doi.org/10.1128/JB.01582-08>.
- (80) Ammam, F.; Tremblay, P.-L.; Lizak, D. M.; Zhang, T. Effect of Tungstate on Acetate and Ethanol Production by the Electrosynthetic Bacterium *Sporomusa Ovata*. *Biotechnol Biofuels* **2016**, 9 (1), 163. <https://doi.org/10.1186/s13068-016-0576-0>.
- (81) Cotelesage, J. J. H.; Pushie, M. J.; Grochulski, P.; Pickering, I. J.; George, G. N. Metalloprotein Active Site Structure Determination: Synergy between X-Ray Absorption Spectroscopy and X-Ray Crystallography. *J Inorg Biochem* **2012**, 115, 127–137. <https://doi.org/10.1016/j.jinorgbio.2012.06.019>.
- (82) Pushie, M. J.; Cotelesage, J. J.; George, G. N. Molybdenum and Tungsten Oxygen Transferases-Structural and Functional Diversity within a Common Active Site Motif. *Metallomics*. **2014**, 6(1):15-24. <https://doi.org/10.1039/c3mt00177f>.

- (83) Hu, Y.; Faham, S.; Roy, R.; Adams, M. W. W.; Rees, D. C. Formaldehyde Ferredoxin Oxidoreductase from *Pyrococcus Furiosus*: The 1.85 Å Resolution Crystal Structure and Its Mechanistic Implications. *JMB* **1999**, 266, 899–914. <https://doi.org/https://doi.org/10.1006/jmbi.1998.2488>.
- (84) Pushie, M. J.; George, G. N. Spectroscopic Studies of Molybdenum and Tungsten Enzymes. *Coordination Chemistry Reviews*. **2011**, (225) 1055–1084. <https://doi.org/10.1016/j.ccr.2011.01.056>.
- (85) Koehler, B. P.; Mukund, S.; Conover, R. C.; Dhawan, I. K.; Roy, R.; Adams, M. W. W.; Johnson, M. K. Spectroscopic Characterization of the Tungsten and Iron Centers in Aldehyde Ferredoxin Oxidoreductases from Two Hyperthermophilic Archaea. *J Am Chem Soc* **1996**, 118 (49), 12391–12405. <https://doi.org/10.1021/ja962197u>.
- (86) Metz, S.; Wang, D.; Thiel, W. Reductive Half-Reaction of Aldehyde Oxidoreductase toward Acetaldehyde: A Combined QM/MM Study. *J Am Chem Soc* **2009**, 131 (13), 4628–4640. <https://doi.org/10.1021/ja805938w>.
- (87) Liao, R. Z.; Yu, J. G.; Himo, F. Tungsten-Dependent Formaldehyde Ferredoxin Oxidoreductase: Reaction Mechanism from Quantum Chemical Calculations. *J Inorg Biochem* **2011**, 105 (7), 927–936. <https://doi.org/10.1016/j.jinorgbio.2011.03.020>.
- (88) Liao, R.-Z.; Yu, J.-G.; Himo, F. Mechanism of Tungsten-Dependent Acetylene Hydratase from Quantum Chemical Calculations. *Proceedings of the National Academy of Sciences* **2010**, 107 (52), 22523–22527. <https://doi.org/10.1073/pnas.1014060108>.
- (89) Fuchs, G. Anaerobic Metabolism of Aromatic Compounds. *Ann N Y Acad Sci* **2008**, 1125 (1), 82–99. <https://doi.org/10.1196/annals.1419.010>.
- (90) Schmitt, G.; Arndt, F.; Kahnt, J.; Heider, J. Adaptations to a Loss-of-Function Mutation in the Betaproteobacterium *Aromatoleum Aromaticum*: Recruitment of Alternative Enzymes for Anaerobic Phenylalanine Degradation. *J Bacteriol* **2017**, 199 (20). <https://doi.org/10.1128/JB.00383-17>.
- (91) Rabus, R.; Kube, M.; Heider, J.; Beck, A.; Heitmann, K.; Widdel, F.; Reinhardt, R. The Genome Sequence of an Anaerobic Aromatic-Degrading Denitrifying Bacterium, Strain EbN1. *Arch Microbiol* **2005**, 183 (1), 27–36. <https://doi.org/10.1007/s00203-004-0742-9>.
- (92) Saba, T.; Burnett, J. W. H.; Li, J.; Wang, X.; Anderson, J. A.; Kechagiopoulos, P. N.; Wang, X. Assessing the Environmental Performance of NADH Regeneration Methods: A Cleaner Process Using Recyclable Pt/Fe<sub>3</sub>O<sub>4</sub> and Hydrogen. *Catal Today* **2020**, 339, 281–288. <https://doi.org/10.1016/j.cattod.2019.01.049>.
- (93) Wang, X.; Saba, T.; Yiu, H. H. P.; Howe, R. F.; Anderson, J. A.; Shi, J. Cofactor NAD(P)H Regeneration Inspired by Heterogeneous Pathways. *Chem. Elsevier Inc* **2017**, 2 (5) 621–654. <https://doi.org/10.1016/j.chempr.2017.04.009>.



- (94) Lauterbach, L.; Lenz, O.; Vincent, K. A. H<sub>2</sub>-Driven Cofactor Regeneration with NAD(P)<sup>+</sup>-Reducing Hydrogenases. *FEBS J*; **2013**; 280, 3058–3068. <https://doi.org/10.1111/febs.12245>.
- (95) Lubitz, W.; Ogata, H.; Rüdiger, O.; Reijerse, E. Hydrogenases. *Chem Rev* **2014**, 114 (8), 4081–4148. <https://doi.org/10.1021/cr4005814>.
- (96) Wilcoxon, J.; Hille, R. The Hydrogenase Activity of the Molybdenum/Copper-Containing Carbon Monoxide Dehydrogenase of *Oligotropha Carboxidovorans*. *J of Biological Chemistry* **2013**, 288 (50), 36052–36060. <https://doi.org/10.1074/jbc.M113.522441>.
- (97) Pandelia, M.-E.; Ogata, H.; Currell, L. J.; Flores, M.; Lubitz, W. Inhibition of the [NiFe] Hydrogenase from *Desulfovibrio Vulgaris* Miyazaki F by Carbon Monoxide: An FTIR and EPR Spectroscopic Study. *Biochimica et Biophysica Acta (BBA) - Bioenergetics* **2010**, 1797 (2), 304–313. <https://doi.org/10.1016/j.bbabi.2009.11.002>.
- (98) de Lacey, A. L.; Fernández, V. M.; Rousset, M.; Cammack, R. Activation and Inactivation of Hydrogenase Function and the Catalytic Cycle: Spectroelectrochemical Studies. *Chem Rev* **2007**, 107 (10), 4304–4330. <https://doi.org/10.1021/cr0501947>.
- (99) Zhang, B.; Hemann, C. F.; Hille, R. Kinetic and Spectroscopic Studies of the Molybdenum-Copper CO Dehydrogenase from *Oligotropha Carboxidovorans*. *J of Biological Chemistry* **2010**, 285 (17), 12571–12578. <https://doi.org/10.1074/jbc.M109.076851>.
- (100) Rovaletti, A.; Bruschi, M.; Moro, G.; Cosentino, U.; Greco, C.; Ryde, U. Theoretical Insights into the Aerobic Hydrogenase Activity of Molybdenum–Copper CO Dehydrogenase. *Inorganics* **2019**, 7 (11), 135. <https://doi.org/10.3390/inorganics7110135>.
- (101) Wang, S.; Huang, H.; Kahnt, J.; Thauer, R. K. A Reversible Electron-Bifurcating Ferredoxin- and NAD-Dependent [FeFe]-Hydrogenase (HydABC) in *Moorella thermoacetica*. *J Bacteriol* **2013**, 195 (6), 1267–1275. <https://doi.org/10.1128/JB.02158-12>.
- (102) Lenz, O.; Lauterbach, L.; Frielingsdorf, S. O<sub>2</sub>-Tolerant [NiFe]-Hydrogenases of *Ralstonia Eutropha* H16: Physiology, Molecular Biology, Purification, and Biochemical Analysis; **2018**; 613, 117–151. <https://doi.org/10.1016/bs.mie.2018.10.008>.
- (103) Brugna-Guiral, M.; Tron, P.; Nitschke, W.; Stetter, K.-O.; Burlat, B.; Guigliarelli, B.; Bruschi, M.; Giudici-Ortoni, M. T. [NiFe] Hydrogenases from the Hyperthermophilic Bacterium *Aquifex Aeolicus*: Properties, Function, and Phylogenetics. *Extremophiles* **2003**, 7 (2), 145–157. <https://doi.org/10.1007/s00792-002-0306-3>.
- (104) Peters, J. W.; Miller, A.-F.; Jones, A. K.; King, P. W.; Adams, M. W. Electron Bifurcation. *Curr Opin Chem Biol* **2016**, 31, 146–152. <https://doi.org/10.1016/j.cbpa.2016.03.007>.

- (105) Buckel, W.; Thauer, R. K. Flavin-Based Electron Bifurcation, A New Mechanism of Biological Energy Coupling. *Chem Rev* **2018**, 118 (7), 3862–3886. <https://doi.org/10.1021/acs.chemrev.7b00707>.
- (106) Buckel, W.; Thauer, R. K. Flavin-Based Electron Bifurcation, Ferredoxin, Flavodoxin, and Anaerobic Respiration With Protons (Ech) or NAD<sup>+</sup> (Rnf) as Electron Acceptors: A Historical Review. *Front Microbiol* **2018**, 9. <https://doi.org/10.3389/fmicb.2018.00401>.
- (107) Wang, S.; Huang, H.; Kahnt, J.; Mueller, A. P.; Köpke, M.; Thauer, R. K. NADP-Specific Electron-Bifurcating [FeFe]-Hydrogenase in a Functional Complex with Formate Dehydrogenase in *Clostridium Autoethanogenum* Grown on CO. *J Bacteriol* **2013**, 195 (19), 4373–4386. <https://doi.org/10.1128/JB.00678-13>.
- (108) Yu, H. Extending the Size Limit of Protein Nuclear Magnetic Resonance. *Proceedings of the National Academy of Sciences* **1999**, 96 (2), 332–334. <https://doi.org/10.1073/pnas.96.2.332>.
- (109) Campbell, M. G.; Veessler, D.; Cheng, A.; Potter, C. S.; Carragher, B. 2.8 Å Resolution Reconstruction of the *Thermoplasma Acidophilum* 20S Proteasome Using Cryo-Electron Microscopy. *Elife* **2015**, 4. <https://doi.org/10.7554/eLife.06380>.
- (110) Noble, A. J.; Dandey, V. P.; Wei, H.; Brasch, J.; Chase, J.; Acharya, P.; Tan, Y. Z.; Zhang, Z.; Kim, L. Y.; Scapin, G.; Rapp, M.; Eng, E. T.; Rice, W. J.; Cheng, A.; Negro, C. J.; Shapiro, L.; Kwong, P. D.; Jeruzalmi, D.; des Georges, A.; Potter, C. S.; Carragher, B. Routine Single Particle CryoEM Sample and Grid Characterization by Tomography. *Elife* **2018**, 7. <https://doi.org/10.7554/eLife.34257>.
- (111) Zuo, J. M.; Spence, J. C. H. *Advanced Transmission Electron Microscopy*; Springer New York: **2017**. <https://doi.org/10.1007/978-1-4939-6607-3>.
- (112) Passmore, L. A.; Russo, C. J. Specimen Preparation for High-Resolution Cryo-EM; **2016**; 579, 51–86. <https://doi.org/10.1016/bs.mie.2016.04.011>.
- (113) Kastner, B.; Fischer, N.; Golas, M. M.; Sander, B.; Dube, P.; Boehringer, D.; Hartmuth, K.; Deckert, J.; Hauer, F.; Wolf, E.; Uchtenhagen, H.; Urlaub, H.; Herzog, F.; Peters, J. M.; Poerschke, D.; Lüthmann, R.; Stark, H. GraFix: Sample Preparation for Single-Particle Electron Cryomicroscopy. *Nat Methods* **2008**, 5 (1), 53–55. <https://doi.org/10.1038/nmeth1139>.
- (114) Dubochet, J.; Adrian, M.; Chang, J.-J.; Homo, J.-C.; Lepault, J.; McDowell, A. W.; Schultz, P. Cryo-Electron Microscopy of Vitrified Specimens. *Q Rev Biophys* **1988**, 21 (2), 129–228. <https://doi.org/10.1017/S0033583500004297>.
- (115) Orlova, E. v.; Saibil, H. R. Structural Analysis of Macromolecular Assemblies by Electron Microscopy. *Chem Rev* **2011**, 111 (12), 7710–7748. <https://doi.org/10.1021/cr100353t>.
- (116) Ludtke, S. J.; Baldwin, P. R.; Chiu, W. EMAN: Semiautomated Software for High-Resolution Single-Particle Reconstructions. *J Struct Biol* **1999**, 128 (1), 82–97. <https://doi.org/10.1006/jsbi.1999.4174>.

- (117) Yuanxin Zhu; Carragher, B.; Mouche, F.; Potter, C. S. Automatic Particle Detection through Efficient Hough Transforms. *IEEE Trans Med Imaging* **2003**, 22 (9), 1053–1062. <https://doi.org/10.1109/TMI.2003.816947>.
- (118) Bepler, T.; Morin, A.; Rapp, M.; Brasch, J.; Shapiro, L.; Noble, A. J.; Berger, B. Positive-Unlabeled Convolutional Neural Networks for Particle Picking in Cryo-Electron Micrographs. *Nat Methods* **2019**, 16 (11), 1153–1160. <https://doi.org/10.1038/s41592-019-0575-8>.
- (119) Rabus, R.; Widdel, F. Anaerobic Degradation of Ethylbenzene and Other Aromatic Hydrocarbons by New Denitrifying Bacteria; *Arch Microbiol*, **1995**; 163(2):96-103. doi: 10.1007/BF00381782.
- (120) Saliı, I.; Szaleniec, M.; Zein, A. A.; Seyhan, D.; Sekuła, A.; Schühle, K.; Kaplieva-Dudek, I.; Linne, U.; Meckenstock, R. U.; Heider, J. Determinants for Substrate Recognition in the Glycyl Radical Enzyme Benzylsuccinate Synthase Revealed by Targeted Mutagenesis. *ACS Catal* **2021**, 11 (6), 3361–3370. <https://doi.org/10.1021/acscatal.0c04954>.
- (121) Dehio, C.; Meyer, M. Maintenance of Broad-Host-Range Incompatibility Group P and Group Q Plasmids and Transposition of Tn5 in *Bartonella Henselae* Following Conjugal Plasmid Transfer from *Escherichia Coli*. *J Bacteriol* **1997**, 179 (2), 538–540. <https://doi.org/10.1128/jb.179.2.538-540.1997>.
- (122) Bradford, M. M. A Rapid and Sensitive Method for the Quantitation of Microgram Quantities of Protein Utilizing the Principle of Protein-Dye Binding. *Anal Biochem* **1976**, 72 (1–2), 248–254. [https://doi.org/10.1016/0003-2697\(76\)90527-3](https://doi.org/10.1016/0003-2697(76)90527-3).
- (123) Laemmli, U. K. Cleavage of Structural Proteins during the Assembly of the Head of Bacteriophage T4. *Nature* **1970**, 227 (5259), 680–685. <https://doi.org/10.1038/227680a0>.
- (124) Forneris, F.; Orru, R.; Bonivento, D.; Chiarelli, L. R.; Mattevi, A. ThermoFAD, a ThermoFluor®-Adapted Flavin Ad Hoc Detection System for Protein Folding and Ligand Binding. *FEBS J* **2009**, 276 (10), 2833–2840. <https://doi.org/10.1111/j.1742-4658.2009.07006.x>.
- (125) Pantoliano, M. W.; Petrella, E. C.; Kwasnoski, J. D.; Lobanov, V. S.; Myslik, J.; Graf, E.; Carver, T.; Asel, E.; Springer, B. A.; Lane, P.; Salemme, F. R. High-Density Miniaturized Thermal Shift Assays as a General Strategy for Drug Discovery. *SLAS Discovery* **2001**, 6 (6), 429–440. <https://doi.org/10.1177/108705710100600609>.
- (126) Luo, L.; Gu, C.; Li, M.; Zheng, X.; Zheng, F. Determination of Residual 4-Nitrobenzaldehyde in Chloramphenicol and Its Pharmaceutical Formulation by HPLC with UV/Vis Detection after Derivatization with 3-Nitrophenylhydrazine. *J Pharm Biomed Anal* **2018**, 156, 307–312. <https://doi.org/10.1016/j.jpba.2018.04.024>.
- (127) Kim, H.-J.; Shin, H.-S. Simple Derivatization of Aldehydes with D-Cysteine and Their Determination in Beverages by Liquid Chromatography–Tandem Mass

- Spectrometry. *Anal Chim Acta* **2011**, 702 (2), 225–232. <https://doi.org/10.1016/j.aca.2011.07.006>.
- (128) Burgers, P. C.; Terlouw, J. K. Ion Structures in Mass Spectrometry. In *Encyclopedia of Spectroscopy and Spectrometry*; Elsevier, **2017**; 322–329. <https://doi.org/10.1016/B978-0-12-803224-4.00182-5>.
- (129) Briggs, G. E.; Haldane, J. B. S. A Note on the Kinetics of Enzyme Action. *Biochemical J* **1925**, 19 (2), 338–339. <https://doi.org/10.1042/bj0190338>.
- (130) Somvanshi, P. R.; Venkatesh, K. Hill Equation. In *Encyclopedia of Systems Biology*; Springer New York: New York, NY, **2013**; 892–895. [https://doi.org/10.1007/978-1-4419-9863-7\\_946](https://doi.org/10.1007/978-1-4419-9863-7_946).
- (131) Michaelis, L.; Hill, E. S. The Viologen Indicators. *J of General Physiology* **1933**, 16 (6), 859–873. <https://doi.org/10.1085/jgp.16.6.859>.
- (132) Dean, J. A., *Lange's Handbook of Chemistry*, 12th ed.; McGraw-Hill Inc.: New York, **1979**; 68. <https://doi.org/10.1002/jps.2600680645>.
- (133) Copeland, R. *Enzymes: A Practical Introduction to Structure, Mechanism, and Data Analysis*, 2nd Edition. Wiley-VCH; **2000**.
- (134) Storer, A. C.; Cornish-Bowden, A. The Kinetics of Coupled Enzyme Reactions. Applications to the Assay of Glucokinase, with Glucose 6-Phosphate Dehydrogenase as Coupling Enzyme. *Biochemical J* **1974**, 141 (1), 205–209. <https://doi.org/10.1042/bj1410205>.
- (135) Lee, C. C.; Hu, Y.; Ribbe, M. W. ATP-Independent Substrate Reduction by Nitrogenase P-Cluster Variant. *Proc Natl Acad Sci U S A* **2012**, 109 (18), 6922–6926. <https://doi.org/10.1073/pnas.1202429109>.
- (136) Muhr, E.; Schühle, K.; Clermont, L.; Sünwoldt, K.; Kleinsorge, D.; Seyhan, D.; Kahnt, J.; Schall, I.; Cordero, P. R.; Schmitt, G.; Heider, J. Enzymes of Anaerobic Ethylbenzene and P-Ethylphenol Catabolism in 'Aromatoleum Aromaticum': Differentiation and Differential Induction. *Arch Microbiol* **2015**, 197 (9), 1051–1062. <https://doi.org/10.1007/s00203-015-1142-z>.
- (137) Büsing, I.; Höffken, H. W.; Breuer, M.; Wöhlbrand, L.; Hauer, B.; Rabus, R. Molecular Genetic and Crystal Structural Analysis of 1-(4-Hydroxyphenyl)-Ethanol Dehydrogenase from 'Aromatoleum Aromaticum'; EbN1. *J Mol Microbiol Biotechnol* **2015**, 25 (5), 327–339. <https://doi.org/10.1159/000439113>.
- (138) Borowiecki, P.; Telatycka, N.; Tataruch, M.; Źądło-Dobrowolska, A.; Reiter, T.; Schühle, K.; Heider, J.; Szaleniec, M.; Kroutil, W. Biocatalytic Asymmetric Reduction of  $\gamma$ -Keto Esters to Access Optically Active  $\gamma$ -Aryl- $\gamma$ -Butyrolactones. *Adv Synth Catal* **2020**, 362 (10), 2012–2029. <https://doi.org/10.1002/adsc.201901483>.
- (139) Shi, J.-M.; Pei, J.; Liu, E.-Q.; Zhang, L. Bis(Sulfosuccinimidyl) Suberate (BS3) Crosslinking Analysis of the Behavior of Amyloid- $\beta$  Peptide in Solution and in Phospholipid Membranes. *PLoS One* **2017**, 12 (3), e0173871. <https://doi.org/10.1371/j.pone.0173871>.

- (140) Afonine, P. v.; Klaholz, B. P.; Moriarty, N. W.; Poon, B. K.; Sobolev, O. v.; Terwilliger, T. C.; Adams, P. D.; Urzhumtsev, A. New Tools for the Analysis and Validation of Cryo-EM Maps and Atomic Models. *Acta Crystallogr D Struct Biol* **2018**, 74 (9), 814–840. <https://doi.org/10.1107/S2059798318009324>.
- (141) Orlova, E. v.; Saibil, H. R. Structural Analysis of Macromolecular Assemblies by Electron Microscopy. *Chem Rev* **2011**, 111 (12), 7710–7748. <https://doi.org/10.1021/cr100353t>.
- (142) Jumper, J.; Evans, R.; Pritzel, A.; Green, T.; Figurnov, M.; Ronneberger, O.; Tunyasuvunakool, K.; Bates, R.; Žídek, A.; Potapenko, A.; Bridgland, A.; Meyer, C.; Kohl, S. A. A.; Ballard, A. J.; Cowie, A.; Romera-Paredes, B.; Nikolov, S.; Jain, R.; Adler, J.; Back, T.; Petersen, S.; Reiman, D.; Clancy, E.; Zielinski, M.; Steinegger, M.; Pacholska, M.; Berghammer, T.; Bodenstein, S.; Silver, D.; Vinyals, O.; Senior, A. W.; Kavukcuoglu, K.; Kohli, P.; Hassabis, D. Highly Accurate Protein Structure Prediction with AlphaFold. *Nature* **2021**, 596 (7873), 583–589. <https://doi.org/10.1038/s41586-021-03819-2>.
- (143) Pettersen, E. F.; Goddard, T. D.; Huang, C. C.; Couch, G. S.; Greenblatt, D. M.; Meng, E. C.; Ferrin, T. E. UCSF Chimera: A Visualization System for Exploratory Research and Analysis. *J Comput Chem* **2004**, 25 (13), 1605–1612. <https://doi.org/10.1002/jcc.20084>.
- (144) Emsley, P.; Lohkamp, B.; Scott, W. G.; Cowtan, K. Features and Development of Coot. *Acta Crystallogr D Biol Crystallogr* **2010**, 66 (4), 486–501. <https://doi.org/10.1107/S0907444910007493>.
- (145) The PyMOL Molecular Graphics System, Version 2.6.0a0, Schrödinger, LLC.
- (146) Goddard, T. D.; Huang, C. C.; Meng, E. C.; Pettersen, E. F.; Couch, G. S.; Morris, J. H.; Ferrin, T. E. UCSF ChimeraX: Meeting Modern Challenges in Visualization and Analysis. *Protein Science* **2018**, 27 (1), 14–25. <https://doi.org/10.1002/pro.3235>.
- (147) Krissinel, E.; Henrick, K. Inference of Macromolecular Assemblies from Crystalline State. *J Mol Biol* **2007**, 372 (3), 774–797. <https://doi.org/10.1016/j.jmb.2007.05.022>.
- (148) Li, H.; Robertson, A. D.; Jensen, J. H. Very Fast Empirical Prediction and Rationalization of Protein pKa Values. *Proteins: Structure, Function, and Bioinformatics* **2005**, 61 (4), 704–721. <https://doi.org/10.1002/prot.20660>.
- (149) Holm, L. Using Dali for Protein Structure Comparison; In *Structural Bioinformatics*, Springer New York **2020**; 29–42. [https://doi.org/10.1007/978-1-0716-0270-6\\_3](https://doi.org/10.1007/978-1-0716-0270-6_3).
- (150) Young, G.; Hundt, N.; Cole, D.; Fineberg, A.; Andrecka, J.; Tyler, A.; Olerinyova, A.; Ansari, A.; Marklund, E. G.; Collier, M. P.; Chandler, S. A.; Tkachenko, O.; Allen, J.; Crispin, M.; Billington, N.; Takagi, Y.; Sellers, J. R.; Eichmann, C.; Selenko, P.; Frey, L.; Riek, R.; Galpin, M. R.; Struwe, W. B.; Benesch, J. L. P.; Kukura, P. Quantitative Mass Imaging of Single Biological Macromolecules. *Science* (1979) **2018**, 360 (6387), 423–427. <https://doi.org/10.1126/science.aar5839>.

- (151) Sonn-Segev, A.; Belacic, K.; Bodrug, T.; Young, G.; VanderLinden, R. T.; Schulman, B. A.; Schimpf, J.; Friedrich, T.; Dip, P. V.; Schwartz, T. U.; Bauer, B.; Peters, J.-M.; Struwe, W. B.; Benesch, J. L. P.; Brown, N. G.; Haselbach, D.; Kukura, P. Quantifying the Heterogeneity of Macromolecular Machines by Mass Photometry. *Nat Commun* **2020**, 11 (1), 1772. <https://doi.org/10.1038/s41467-020-15642-w>.
- (152) Head-Gordon, M. Quantum Chemistry and Molecular Processes. *J. Phys. Chem.* **1996**, 100, 13213–13225.
- (153) Hohenberg, P.; Kohn, W. Inhomogeneous Electron Gas. *Physical Review* **1964**, 136 (3B), B864–B871. <https://doi.org/10.1103/PhysRev.136.B864>.
- (154) Kohn, W.; Sham, L. J. Self-Consistent Equations Including Exchange and Correlation Effects. *Physical Review* **1965**, 140 (4A), A1133–A1138. <https://doi.org/10.1103/PhysRev.140.A1133>.
- (155) Siegbahn, P. E. M.; Blomberg, M. R. A. Transition-Metal Systems in Biochemistry Studied by High-Accuracy Quantum Chemical Methods. *Chem Rev* **2000**, 100 (2), 421–438. <https://doi.org/10.1021/cr980390w>.
- (156) Gaussian 09, Revision A.02, M. J. Frisch, G. W. Trucks, H. B. Schlegel, G. E. Scuseria, M. A. Robb, J. R. Cheeseman, G. Scalmani, V. Barone, G. A. Petersson, H. Nakatsuji, X. Li, M. Caricato, A. Marenich, J. Bloino, B. G. Janesko, R. Gomperts, B. Mennucci, H. P. Hratchian, J. V. Ortiz, A. F. Izmaylov, J. L. Sonnenberg, D. Williams-Young, F. Ding, F. Lipparini, F. Egidi, J. Goings, B. Peng, A. Petrone, T. Henderson, D. Ranasinghe, V. G. Zakrzewski, J. Gao, N. Rega, G. Zheng, W. Liang, M. Hada, M. Ehara, K. Toyota, R. Fukuda, J. Hasegawa, M. Ishida, T. Nakajima, Y. Honda, O. Kitao, H. Nakai, T. Vreven, K. Throssell, J. A. Montgomery, Jr., J. E. Peralta, F. Ogliaro, M. Bearpark, J. J. Heyd, E. Brothers, K. N. Kudin, V. N. Staroverov, T. Keith, R. Kobayashi, J. Normand, K. Raghavachari, A. Rendell, J. C. Burant, S. S. Iyengar, J. Tomasi, M. Cossi, J. M. Millam, M. Klene, C. Adamo, R. Cammi, J. W. Ochterski, R. L. Martin, K. Morokuma, O. Farkas, J. B. Foresman, and D. J. Fox, Gaussian, Inc., Wallingford CT, **2016**.
- (157) Becke, A. D. Density-functional Thermochemistry. III. The Role of Exact Exchange. *J Chem Phys* **1993**, 98 (7), 5648–5652. <https://doi.org/10.1063/1.464913>.
- (158) Rugor, A.; Wójcik-Augustyn, A.; Niedzialkowska, E.; Mordalski, S.; Staroń, J.; Bojarski, A.; Szalaniec, M. Reaction Mechanism of Sterol Hydroxylation by Steroid C25 Dehydrogenase – Homology Model, Reactivity and Isoenzymatic Diversity. *J Inorg Biochem* **2017**, 173, 28–43. <https://doi.org/10.1016/j.jinorgbio.2017.04.027>.
- (159) Schlegel, H. B. Optimization of Equilibrium Geometries and Transition Structures. *J Comput Chem* **1982**, 3 (2), 214–218. <https://doi.org/https://doi.org/10.1002/jcc.540030212>.
- (160) Salomon-Ferrer, R.; Case, D. A.; Walker, R. C. An Overview of the Amber Biomolecular Simulation Package. *Wiley Interdiscip Rev Comput Mol Sci* **2013**, 3 (2), 198–210. <https://doi.org/10.1002/wcms.1121>.

- (161) Seminario, J. M. Calculation of Intramolecular Force Fields from Second-Derivative Tensors. *Int J Quantum Chem* **1996**, 60 (7), 1271–1277.
- (162) Singh, U. C.; Kollman, P. A. An Approach to Computing Electrostatic Charges for Molecules. *J Comput Chem* **1984**, 5 (2), 129–145. <https://doi.org/10.1002/jcc.540050204>.
- (163) Wang, J.; Wang, W.; Kollman, P. A.; Case, D. A. Automatic Atom Type and Bond Type Perception in Molecular Mechanical Calculations. *J Mol Graph Model* **2006**, 25 (2), 247–260. <https://doi.org/10.1016/j.jmgm.2005.12.005>.
- (164) Wang, J.; Wolf, R. M.; Caldwell, J. W.; Kollman, P. A.; Case, D. A. Development and Testing of a General Amber Force Field. *J Comput Chem* **2004**, 25 (9), 1157–1174. <https://doi.org/10.1002/jcc.20035>.
- (165) Carvalho, A. T. P.; Swart, M. Electronic Structure Investigation and Parametrization of Biologically Relevant Iron-Sulfur Clusters. *J Chem Inf Model* **2014**, 54 (2), 613–620. <https://doi.org/10.1021/ci400718m>.
- (166) Duan, Y.; Wu, C.; Chowdhury, S.; Lee, M. C.; Xiong, G.; Zhang, W.; Yang, R.; Cieplak, P.; Luo, R.; Lee, T.; Caldwell, J.; Wang, J.; Kollman, P. A Point-Charge Force Field for Molecular Mechanics Simulations of Proteins Based on Condensed-Phase Quantum Mechanical Calculations. *J Comput Chem* **2003**, 24 (16), 1999–2012. <https://doi.org/10.1002/jcc.10349>.
- (167) Joung, I. S.; Cheatham, T. E. Determination of Alkali and Halide Monovalent Ion Parameters for Use in Explicitly Solvated Biomolecular Simulations. *J Phys Chem B* **2008**, 112 (30), 9020–9041. <https://doi.org/10.1021/jp8001614>.
- (168) Dapprich, S.; Komáromi, I.; Byun, K. S.; Morokuma, K.; Frisch, M. J. A New ONIOM Implementation in Gaussian98. Part I. The Calculation of Energies, Gradients, Vibrational Frequencies and Electric Field Derivatives. *J of Molecular Structure*: **1999**, 461–462, 1–21. [https://doi.org/10.1016/S0166-1280\(98\)00475-8](https://doi.org/10.1016/S0166-1280(98)00475-8).
- (169) Orozco, M.; Marchn, I.; Soteras, I.; Vreven, T.; Morokuma, K.; Mikkelsen, K. v.; Milani, A.; Tommasini, M.; Zoppo, M. del; Castiglioni, C.; Aguilar, M. A.; Snchez, M. L.; Martn, M. E.; Galvn, I. Fdez.; Sato, H. Beyond the Continuum Approach. In *Continuum Solvation Models in Chemical Physics*; John Wiley & Sons, Ltd: Chichester, UK, **2007**; 499–605. <https://doi.org/10.1002/9780470515235.ch4>.
- (170) Vreven, T.; Byun, K. S.; Komáromi, I.; Dapprich, S.; Montgomery, J. A.; Morokuma, K.; Frisch, M. J. Combining Quantum Mechanics Methods with Molecular Mechanics Methods in ONIOM. *J Chem Theory Comput* **2006**, 2 (3), 815–826. <https://doi.org/10.1021/ct050289g>.
- (171) Reichart, O.; Szakmár, K.; Jozwiak, Á.; Felföldi, J.; Baranyai, L. Redox Potential Measurement as a Rapid Method for Microbiological Testing and Its Validation for Coliform Determination. *Int J Food Microbiol* **2007**, 114 (2), 143–148. <https://doi.org/10.1016/j.ijfoodmicro.2006.08.016>.
- (172) Rabus, R.; Wöhlbrand, L.; Thies, D.; Meyer, M.; Reinhold-Hurek, B.; Kämpfer, P. *Aromatoleum Gen. Nov.*, a Novel Genus Accommodating the Phylogenetic Lineage Including *Azoarcus Evansii* and Related Species, and Proposal of

- Aromatoleum Aromaticum Sp. Nov., Aromatoleum Petrolei Sp. Nov., Aromatoleum Bremense Sp. Nov., Aromatoleum Toluolicum Sp. Nov. and Aromatoleum Diolicum Sp. Nov. *Int J Syst Evol Microbiol* **2019**, 69 (4), 982–997. <https://doi.org/10.1099/ijsem.0.003244>.
- (173) Samuelsen, L.; Holm, R.; Lathuile, A.; Schönbeck, C. Buffer Solutions in Drug Formulation and Processing: How PK a Values Depend on Temperature, Pressure and Ionic Strength. *Int J Pharm* **2019**, 560, 357–364. <https://doi.org/10.1016/j.ijpharm.2019.02.019>.
- (174) Bruins, M. E.; Matser, A. M.; Janssen, A. E. M.; Boom, R. M. Buffer Selection for HP Treatment of Biomaterials and Its Consequences for Enzyme Inactivation Studies. *High Press Res* **2007**, 27 (1), 101–107. <https://doi.org/10.1080/08957950601082573>.
- (175) Wilcoxon, J.; Hille, R. The Hydrogenase Activity of the Molybdenum/Copper-Containing Carbon Monoxide Dehydrogenase of *Oligotropha Carboxidovorans*. *J of Biological Chemistry* **2013**, 288 (50), 36052–36060. <https://doi.org/10.1074/jbc.M113.522441>.
- (176) Sankar, M.; Nowicka, E.; Carter, E.; Murphy, D. M.; Knight, D. W.; Bethell, D.; Hutchings, G. J. The Benzaldehyde Oxidation Paradox Explained by the Interception of Peroxy Radical by Benzyl Alcohol. *Nat Commun* **2014**, 5 (1), 3332. <https://doi.org/10.1038/ncomms4332>.
- (177) Praestgaard, E.; Elmerdahl, J.; Murphy, L.; Nymand, S.; McFarland, K. C.; Borch, K.; Westh, P. A Kinetic Model for the Burst Phase of Processive Cellulases. *FEBS J* **2011**, 278 (9), 1547–1560. <https://doi.org/10.1111/j.1742-4658.2011.08078.x>.
- (178) White, H.; Feicht, R.; Huber, C.; Lottspeich, F.; Simon, H. Purification and Some Properties of the Tungsten-Containing Carboxylic Acid Reductase from *Clostridium Formicoaceticum*. *Biol Chem Hoppe Seyler* **1991**, 372 (2), 999–1006. <https://doi.org/10.1515/bchm3.1991.372.2.999>.
- (179) Winiarska, A.; Hege, D.; Gemmecker, Y.; Kryściak-Czerwenka, J.; Seubert, A.; Heider, J.; Szalaniec, M. Tungsten Enzyme Using Hydrogen as an Electron Donor to Reduce Carboxylic Acids and NAD<sup>+</sup>. *ACS Catal* **2022**, 12 (14), 8707–8717. <https://doi.org/10.1021/acscatal.2c02147>.
- (180) Dietrich, H. M.; Righetto, R. D.; Kumar, A.; Wietrzynski, W.; Trischler, R.; Schuller, S. K.; Wagner, J.; Schwarz, F. M.; Engel, B. D.; Müller, V.; Schuller, J. M. Membrane-Anchored HDCR Nanowires Drive Hydrogen-Powered CO<sub>2</sub> Fixation. *Nature* **2022**, 607 (7920), 823–830. <https://doi.org/10.1038/s41586-022-04971-z>.
- (181) Lin, T.-Y.; Werther, T.; Jeoung, J.-H.; Dobbek, H. Suppression of Electron Transfer to Dioxygen by Charge Transfer and Electron Transfer Complexes in the FAD-Dependent Reductase Component of Toluene Dioxygenase. *J of Biological Chemistry* **2012**, 287 (45), 38338–38346. <https://doi.org/10.1074/jbc.M112.374918>.



- (182) Wierenga, R. K.; Terpstra, P.; Hol, W. G. J. Prediction of the Occurrence of the ADP-Binding  $\beta\alpha\beta$ -Fold in Proteins, Using an Amino Acid Sequence Fingerprint. *J Mol Biol* **1986**, 187 (1), 101–107. [https://doi.org/10.1016/0022-2836\(86\)90409-2](https://doi.org/10.1016/0022-2836(86)90409-2).
- (183) Dym, O.; Eisenberg, D. Sequence-Structure Analysis of FAD-Containing Proteins. *Protein Science* **2001**, 10, 1712. <https://doi.org/10.1101/ps.12801>.
- (184) Szaleniec, M.; Dudzik, A.; Kozik, B.; Borowski, T.; Heider, J.; Witko, M. Mechanistic Basis for the Enantioselectivity of the Anaerobic Hydroxylation of Alkylaromatic Compounds by Ethylbenzene Dehydrogenase. *J Inorg Biochem* **2014**, 139, 9–20. <https://doi.org/10.1016/j.jinorgbio.2014.05.006>.
- (185) Brzóška, K.; Meczyńska, S.; Kruszewski, M. Iron-Sulfur Cluster Proteins: Electron Transfer and Beyond. *Acta Biochim Pol* **2006**, 53 (4), 685–691.
- (186) Winkler, J. R.; Gray, H. B. Electron Flow through Metalloproteins. *Chem Rev* **2014**, 114 (7), 3369–3380. <https://doi.org/10.1021/cr4004715>.
- (187) Schuchmann, K.; Vonck, J.; Müller, V. A Bacterial Hydrogen-Dependent CO<sub>2</sub> Reductase Forms Filamentous Structures. *FEBS J* **2016**, 283 (7), 1311–1322. <https://doi.org/10.1111/febs.13670>.
- (188) Kim, C.-W.; Moon, Y.-A.; Park, S. W.; Cheng, D.; Kwon, H. J.; Horton, J. D. Induced Polymerization of Mammalian Acetyl-CoA Carboxylase by MIG12 Provides a Tertiary Level of Regulation of Fatty Acid Synthesis. *Proceedings of the National Academy of Sciences* **2010**, 107 (21), 9626–9631. <https://doi.org/10.1073/pnas.1001292107>.
- (189) Kleinschmidt, A. K.; Moss, J.; Lane, M. D. Acetyl Coenzyme A Carboxylase: Filamentous Nature of the Animal Enzymes. *Science* (1979) **1969**, 166 (3910), 1276–1278. <https://doi.org/10.1126/science.166.3910.1276>.
- (190) Kessler, D.; Leibrecht, I.; Knappe, J. Pyruvate-Formate-Lyase-Deactivase and Acetyl-CoA Reductase Activities of Escherichia Coli Reside on a Polymeric Protein Particle Encoded by AdhE. *FEBS Lett* **1991**, 281 (1–2), 59–63. [https://doi.org/10.1016/0014-5793\(91\)80358-A](https://doi.org/10.1016/0014-5793(91)80358-A).
- (191) Culka, M.; Huwiler, S. G.; Boll, M.; Ullmann, G. M. Breaking Benzene Aromaticity - Computational Insights into the Mechanism of the Tungsten-Containing Benzoyl-CoA Reductase. *J Am Chem Soc* **2017**, 139 (41), 14488–14500. <https://doi.org/10.1021/jacs.7b07012>.
- (192) Koehler, B. P.; Mukund, S.; Conover, R. C.; Dhawan, I. K.; Roy, R.; Adams, M. W. W.; Johnson, M. K. Spectroscopic Characterization of the Tungsten and Iron Centers in Aldehyde Ferredoxin Oxidoreductases from Two Hyperthermophilic Archaea. *J Am Chem Soc* **1996**, 118 (49), 12391–12405. <https://doi.org/10.1021/ja962197u>.
- (193) Fabian Arndt. Wolframabhängige Aldehyd-Oxidoreduktase (AOR): Katalytische Eigenschaften Und Maturation, PhD Thesis, Philipps-Universität Marburg, Marburg, **2020**.

- (194) Ueyama, N.; Oku, H.; Kondo, M.; Okamura, T.; Yoshinaga, N.; Nakamura, A. Trans Influence of Oxo and Dithiolene Coordination in Oxidized Models of Molybdenum Oxidoreductase: Synthesis, Structures, and Properties of  $Q_2 [Mo^{VI} O_2 (1,2\text{-Benzenedithiolato})_2]$  ( $Q = NEt_4, PPh_4$ ) and Related Complexes. *Inorg Chem* **1996**, 35 (3), 643–650. <https://doi.org/10.1021/ic950204u>.
- (195) Das, S. K.; Biswas, D.; Maiti, R.; Sarkar, S. Modeling the Tungsten Sites of Inactive and Active Forms of Hyperthermophilic *Pyrococcus Furiosus* Aldehyde Ferredoxin Oxidoreductase. *J Am Chem Soc* **1996**, 118 (6), 1387–1397. <https://doi.org/10.1021/ja9511580>.
- (196) Stein, B. W.; Yang, J.; Mtei, R.; Wiebelhaus, N. J.; Kersi, D. K.; LePluart, J.; Lichtenberger, D. L.; Enemark, J. H.; Kirk, M. L. Vibrational Control of Covalency Effects Related to the Active Sites of Molybdenum Enzymes. *J Am Chem Soc* **2018**, 140 (44), 14777–14788. <https://doi.org/10.1021/jacs.8b08254>.